



MID-AMERICA TRANSPORTATION CENTER

Report # MATC-UNL: 220

Final Report



Development of Advanced Finite Element Material Models for Cable Barrier Wire Rope

John D. Reid, Ph.D.

Professor

Nebraska Transportation Center

University of Nebraska-Lincoln

Karla A. Lechtenberg, M.S.M.E., E.I.T.

Cody S. Stolle, M.S.M.E., E.I.T.



2010

A Cooperative Research Project sponsored by the
U.S. Department of Transportation Research and
Innovative Technology Administration

The contents of this report reflect the views of the authors, who are responsible for the facts and the accuracy of the information presented herein. This document is disseminated under the sponsorship of the Department of Transportation University Transportation Centers Program, in the interest of information exchange.

The U.S. Government assumes no liability for the contents or use thereof.

MATC



Development of Advanced Finite Element Material Models for Cable Barrier Wire Rope

Cody S. Stolle, M.S.M.E., E.I.T.
Graduate Research Assistant
University of Nebraska-Lincoln

John D. Reid, Ph.D.
Professor
Mechanical Engineering Department
University of Nebraska-Lincoln

Karla A. Lechtenberg, M.S.M.E., E.I.T.
Research Associate Engineer
University of Nebraska-Lincoln

Midwest Roadside Safety Facility
Nebraska Transportation Center
University of Nebraska-Lincoln
130 Whittier Building
Lincoln, Nebraska 68583-0853
(402) 472-0965

Submitted to

Mid-America Transportation Center
U.S. Department of Transportation
Region VII University Transportation Center
University of Nebraska-Lincoln
2200 Vine Street
262 Whittier Building
Lincoln, Nebraska 68583-0853

MwRSF Research Report No. TRP-03-233-10
August 2, 2010

TECHNICAL REPORT DOCUMENTATION PAGE

1. Report No. TRP-03-233-10	2.	3. Recipient's Accession No.	
4. Title and Subtitle Development of Advanced Finite Element Material Models for Cable Barrier Wire Rope		5. Report Date August 2, 2010	
		6.	
7. Author(s) Stolle, C.S., Reid, J.D., and Lechtenberg, K.A.		8. Performing Organization Report No. TRP-03-233-10	
9. Performing Organization Name and Address Midwest Roadside Safety Facility (MwRSF) University of Nebraska-Lincoln 130 Whittier Building Lincoln, Nebraska 68583-0853		10. Project/Task/Work Unit No.	
		11. Contract © or Grant (G) No.	
12. Sponsoring Organization Name and Address Mid-America Transportation Center U.S. Department of Transportation Region VII University Transportation Center University of Nebraska-Lincoln 2200 Vine Street 262 Whittier Building Lincoln, Nebraska 68583		13. Type of Report and Period Covered Final Report (2008-2010)	
		14. Sponsoring Agency Code MATC TRB RiP No. 18463 25-1121-0001-220	
15. Supplementary Notes Prepared in cooperation with U.S. Department of Transportation, Federal Highway Administration.			
16. Abstract (Limit: 200 words) <p>An improved LS-DYNA model of ¾-in. (19-mm) diameter 3x7 wire rope commonly used in roadside cable guardrail installations has been developed. A Belytschko-Schwer beam element was selected along with material *MAT_166. Numerical noise was reduced using part stiffness damping with a coefficient of 2%, and frequency range damping with a coefficient of 12%. The optimum element length based on timestep, accuracy, and computational cost was determined to be between 0.4 and 0.8 in. (10-20 mm).</p> <p>Dynamic component tests were conducted on wire rope to determine material properties. These tests were simulated and the results compared to the physical tests. The new proposed wire rope model more accurately simulated the wire rope tension and bogie vehicle motion than other previously-developed wire rope models.</p> <p>The wire rope was also modeled in full-scale crash test models using a Chevrolet C2500 pickup model, consistent with NCHRP Report No. 350 TL-3 impact conditions. Results of the crash test and simulation were compared, and the wire rope response was determined to be accurate. Therefore the new wire rope model was determined to be an improvement over existing models of wire rope and is recommended for use in cable guardrail simulations.</p>			
17. Document Analysis/Descriptors Highway Safety, Roadside Appurtenances, Cable Guardrail, Cables, Computer Modeling, LS-DYNA		18. Availability Statement No restrictions. Document available from: National Technical Information Services, Springfield, Virginia 22161	
19. Security Class (this report) Unclassified	20. Security Class (this page) Unclassified	21. No. of Pages 352	22. Price

Disclaimer Statement

The contents of this report reflect the views and opinions of the authors who are responsible for the facts and the accuracy of the data presented herein. This document is disseminated under the sponsorship of the Department of Transportation University Transportation Centers Program, in the interest of information exchange. The contents do not necessarily reflect the official views or policies of the Mid-America Transportation Center nor the Federal Highway Administration or U.S. Department of Transportation. This report does not constitute a standard, specification, regulation, product endorsement, or an endorsement of manufacturers.

Uncertainty of Measurement Statement

The Midwest Roadside Safety Facility (MwRSF) has determined the uncertainty of measurements for several parameters involved in standard full-scale crash testing and non-standard testing of roadside safety features. All tests conducted on the wire rope in this study were non-certified component tests conducted for research and development purposes only.

Acknowledgements

The authors wish to acknowledge several sources that made a contribution to this project:

(1) MwRSF personnel for conducting and overseeing component testing; and (2) the U.S. Department of Transportation, University Transportation Center (UTC) research grant provided through the Mid-America Transportation Center (MATC).

Acknowledgement is also given to the following individuals who made a contribution to the completion of this research project.

Midwest Roadside Safety Facility

D.L. Sicking, Ph.D., P.E., Professor and MwRSF Director
R.K. Faller, Ph.D., P.E., Research Assistant Professor
J.C. Holloway, M.S.C.E., E.I.T., Test Site Manager
R.W. Bielenberg, M.S.M.E., E.I.T., Research Associate Engineer
C.L. Meyer, B.S.M.E., E.I.T., Research Associate Engineer
A.T. Russell, B.S.B.A., Shop Manager
K.L. Krenk, B.S.M.A, Maintenance Mechanic
A.T. McMaster, Laboratory Mechanic
Undergraduate and Graduate Research Assistants

TABLE OF CONTENTS

TECHNICAL REPORT DOCUMENTATION PAGE	i
Disclaimer Statement	ii
Uncertainty of Measurement Statement.....	ii
Acknowledgements.....	iii
TABLE OF CONTENTS.....	iv
LIST OF FIGURES	viii
LIST OF TABLES	xiii
1 INTRODUCTION	1
1.1 Background.....	1
1.2 Research Objective	2
1.3 Research Approach.....	2
1.3.1 Selection of Wire Rope to be Modeled.....	2
1.3.2 Determination of Required Tests	3
2 CHARACTERISTICS OF WIRE ROPE.....	6
2.1 Terminology.....	6
2.2 Wire Rope Construction	6
2.3 Characteristics of Wire Rope	8
3 LITERATURE REVIEW	10
3.1 Analytical Model	10
3.1.1 Single Wire Model.....	10
3.1.2 Simple Straight Strand.....	11
3.1.3 Wire Rope	12
3.2 Isolated Parameter Models.....	13
3.3 Simplified Models.....	15
3.4 Detailed Models	17
3.5 Discussion.....	20
4 PROPOSED MODEL.....	21
4.1 Selection of Wire Rope.....	21
4.2 Model Composition	21
4.3 Selection of Beam Element Cross-section.....	24
4.4 Material Selection	26
4.5 Proposed Model	26
5 QUASI-STATIC TENSILE TESTING	30
5.1 Testing Methodology	30
5.2 Equipment and Test Setup	31

5.2.1 Extensometers	32
5.2.2 String Pots	33
5.2.3 Wire Rope End Fittings	35
5.2.4 Voltmeters, Power Supply, and Video Cameras.....	36
5.2.5 Load Frame	37
5.3 Prestretching	42
5.4 Test Results.....	42
5.4.1 Raw Data.....	42
5.4.2 Processed Tensile Test Data	46
5.4.2.1 Force vs. Strain Plots	46
5.4.2.2 Engineering Stress vs. Strain Plots	52
5.5 Discussion	54
5.6 Conclusions.....	61
6 MODELING WIRE ROPE IN QUASI-STATIC TENSION	63
6.1 Motivation of Quasi-Static Tensile Test Simulations.....	63
6.2 Single Beam Element Simulations.....	63
6.2.1 Non-Prestretched Wire Rope	63
6.2.2 Prestretched Wire Rope	70
6.3 Mesh Sensitivity Analysis.....	71
6.4 Discussion.....	72
7 DYNAMIC TENSILE TESTING.....	76
7.1 Test Methodology	76
7.2 Test Setup.....	76
7.3 Test No. DTC-1	99
7.4 Test No. DTC-2	112
7.5 Test No. DTC-3	118
7.6 Discussion.....	123
7.7 Summary	123
7.8 Future Work	124
8 MODELING WIRE ROPE IN DYNAMIC TENSION	126
8.1 Motivation.....	126
8.2 General Model Description.....	126
8.3 Baseline Model	128
8.4 Curved Test Rope	130
8.5 Curved and Gravitationally-Initialized Model.....	133
8.6 Discussion.....	137
8.7 Summary.....	138
8.8 Future Work	139
9 QUASI-STATIC BENDING TESTING	140
9.1 Introduction.....	140
9.2 Beam Theory.....	141
9.3 Quasi-Static Bending Tests.....	146
9.4 Curvature Approximation	149
9.5 Discussion.....	153

9.6 Conclusions.....	154
9.7 Future Work.....	155
10 MODELING WIRE ROPE IN QUASI-STATIC BENDING.....	156
10.1 Purpose.....	156
10.2 Beam Element Constitutive Assumptions	156
10.3 Modeling an I-Beam in Bending.....	159
10.3.1 Model Description	159
10.3.2 Analytical Results	162
10.3.3 Simulation Results	162
10.4 Modeling Wire Rope in Bending.....	164
10.4.1 Model Description	165
10.4.2 Baseline Model	167
10.4.3 Optimized Element Length	168
10.5 Discussion.....	172
10.6 Conclusions.....	173
11 WIRE ROPE RESPONSE TO DYNAMIC IMPULSE.....	175
11.1 Purpose.....	175
11.2 The 1-Dimensional Wave Equation for Tensioned Strings	175
11.3 The 1-Dimensional Wave Equation for Stiff Bars.....	177
11.4 Discussion.....	180
12 DYNAMIC BENDING TESTING.....	183
12.1 Test Methodology	183
12.2 Description of Tests	183
12.3 Data Collection	192
12.4 Test Results.....	195
12.4.1 Component Test Nos. DBC-1 and DBC-2.....	195
12.4.2 Component Test Nos. DBC-3 and DBC-4.....	209
12.4.3 Component Test Nos. DBC-5 and DBC-6.....	224
12.5 Discussion.....	238
12.6 Summary.....	241
12.7 Future Work	242
13 MODELING WIRE ROPE IN DYNAMIC BENDING	243
13.1 Purpose.....	243
13.2 Modeling Test No. DBC-1.....	243
13.2.1 Baseline Model	243
13.2.2 Gravity and Slack in the Wire Rope	249
13.2.3 Complete Model.....	253
13.2.3.1 Bogie Model with Gravitationally-Loaded Wire Rope	255
13.2.3.2 Effect of Other MAT_166 Parameters.....	260
13.3 Evaluation of Test No. DBC-1.....	266
13.4 Modeling Test No. DBC-2.....	273
13.5 Modeling Test No. DBC-4.....	276
13.6 Modeling Test No. DBC-6.....	283
13.7 Discussion.....	290

13.8 Summary 293
13.9 Future Work 293
14 FULL-SCALE TEST SIMULATION 295
 14.1 Motivation..... 295
 14.2 Test Description 295
 14.2.1 System Description 295
 14.2.2 Instrumentation 303
 14.3 Test Results 304
 14.4 New Wire Rope Model 310
 14.5 Simulation Results 313
 14.5.1 Simulation Event Timeline 321
 14.5.2 Simulation Analysis 321
 14.6 Summary, Discussion, and Future Work 328
15 DISCUSSION 331
16 CONCLUSIONS..... 339
17 RECOMMENDATIONS 341
18 FUTURE WORK..... 342
19 REFERENCES 344
20 APPENDICES 348

LIST OF FIGURES

Figure 1. Section Classifications for Wire Rope [2].....	7
Figure 2. Solid Element Model of ¾-in. (19-mm) Wire Rope	24
Figure 3. Tension Load Curve (Load Curve No. 1), Proposed Wire Rope Model.....	28
Figure 4. Moment-Curvature Curve (Load Curve No. 2), Proposed Wire Rope Model	29
Figure 5. Torque-Rate of Twist Curve (Load Curve No. 3), Proposed Wire Rope Model	29
Figure 6. Quasi-Static Tensile Test Setup (a) Non-Prestretched (b) Prestretched.....	32
Figure 7. Extensometer Used in Tensile Testing.....	33
Figure 8. String Pot Setup and Gauge Length	35
Figure 9. Wire Rope End Terminations (a) Non-Prestretched (b) Prestretched.....	36
Figure 10. Data Acquisition System	37
Figure 11. Load Frame Assembly After Prestretched Wire Rope Test	38
Figure 12. Pin Support Bracket Details	39
Figure 13. Part Details, Quasi-Static Tensile Tests	40
Figure 14. Rib Details, Quasi-Static Tensile Test.....	41
Figure 15. Fracture Location at String Pot U-bolt, Non-Prestretched Wire Rope Test.....	43
Figure 16. Load and Elongation, Non-Prestretched Tensile Test.....	44
Figure 17. String Pot Output Voltage, Non-Prestretched Tensile Test.....	44
Figure 18. Prestretching Test Load and Extensometer Prestretching Strain	45
Figure 19. Fracture Location in Center of Wire Rope, Prestretched Tensile Test.....	47
Figure 20. Ductile Fracture Surfaces with Necking, Prestretched Wire Rope	48
Figure 21. Load and Elongation, Prestretched Tensile Test	49
Figure 22. String Pot Output Voltage, Prestretched Tensile Test.....	49
Figure 23. Load and Engineering Strain, Non-Prestretched Tensile Test	50
Figure 24. Correlated String Pot Strain and Extensometer Data, Prestretched Tensile Test.....	51
Figure 25. Force and Engineering Strain, Prestretched Tensile Test.....	52
Figure 26. Stress and Strain, Non-Prestretched Tensile Test.....	53
Figure 27. Stress and Strain, Prestretched Tensile Test.....	54
Figure 28. String Pot and Extensometer Configuration, Non-Prestretched Tensile Test	57
Figure 29. Force-Displacement Comparison, Type 1 and Type 2 Beam Elements.....	67
Figure 30. Plastic Strain Comparison, Type 1 Beam Element	68
Figure 31. Ratio of ELOUT Plastic Strain to Calculated Plastic Strains.....	69
Figure 32. Calculated Engineering Stress vs. Calculated Engineering Strain	70
Figure 33. Prestretched Wire Rope Simulation Model and Test Results	71
Figure 34. Recommended Tensile Curves for Wire Rope Modeling	75
Figure 35. Test Setup, Test No. DTC-1	77
Figure 36. DTC Tow Cable Arrangement, Test Nos. DTC-1 and DTC-3.....	78
Figure 37. Sway Resistance Pipe Details.....	79
Figure 38. Sway Resistance Pipe Part Details	80
Figure 39. Load Frame Details	81
Figure 40. Test Setup, Test Nos. DTC-1 and DTC-3	82
Figure 41. Test Setup, Test No. DTC-2	83
Figure 42. Bogie Test Vehicle, Test Nos. DTC-1 through DTC-3.....	84
Figure 43. Load Frame Details	87
Figure 44. Load Frame Details	88
Figure 45. Load Cell Assembly Details.....	89

Figure 46. Load Bracket and Load Cell Details	90
Figure 47. Rotator Pipe Assembly Part Details	91
Figure 48. Lower Connector Rod and Neoprene Bearing Pad Details	92
Figure 49. Load Frame Tube Details	93
Figure 50. Load Frame Tube Details	94
Figure 51. Load Pipe Assembly Details	95
Figure 52. Load Frame, Test Nos. DTC 1-3	96
Figure 53. String Potentiometer Alignment and Configuration Details, Test No. DTC-1	98
Figure 54. Sequential Photographs, Test No. DTC-1	101
Figure 55. Bogie and Wire Rope Final Position, Test No. DTC-1	102
Figure 56. Upstream Wire Rope Damage at Socket, Test No. DTC-1	103
Figure 57. Upstream Wire Rope Damage, Test No. DTC-1	104
Figure 58. Downstream Wire Rope Damage, Test No. DTC-1	105
Figure 59. Downstream Wire Rope Damage, Fracture Locations, Test No. DTC-1	106
Figure 60. Load Cell Data, Test No. DTC-1	107
Figure 61. Bogie Displacement, Test No. DTC-1	108
Figure 62. Bogie Velocity, Test No. DTC-1	109
Figure 63. Bogie Acceleration, Test No. DTC-1	109
Figure 64. String Potentiometer Strain Calculation, Test No. DTC-1	110
Figure 65. Force-Strain Comparison of Test No. DTC-1 and Quasi-Static Tensile Testing.....	111
Figure 66. Sequential Photographs, Test No. DTC-2	114
Figure 67. Final Position of Wire Rope, Test No. DTC-2	115
Figure 68. Downstream Wire Rope Pullout, Test No. DTC-2	116
Figure 69. Pullout of Downstream Wire Rope Socket, Test No. DTC-2	117
Figure 70. Load Cell Results, Test No. DTC-2	118
Figure 71. Sequential Photographs, Test No. DTC-3	119
Figure 72. Wire Rope Pullout of Downstream Socket, Test No. DTC-3	120
Figure 73. Upstream Wire Rope Socket, Test No. DTC-3	121
Figure 74. Load Cell Comparison, Test Nos. DTC-1 and DTC-3	122
Figure 75. Rotator Pipe Assembly, Test and Modeled, Test No. DTC 1-3	127
Figure 76. Baseline Model, Test No. DTC-1	128
Figure 77. Wire Rope Axial Load Comparison, Test and Simulation, Test No. DTC-1	129
Figure 78. Wire Rope Axial Load Comparison, Test and Simulation, Test No. DTC-1	131
Figure 79. Curved Wire Rope Geometry, Curved Wire Rope Simulation	131
Figure 80. Bogie Acceleration Comparison, Test and Simulation, Test No. DTC-1	133
Figure 81. Wire Rope Axial Load Comparison, Test and Simulation, Test No. DTC-1	134
Figure 82. Bogie Velocity, Test and Simulation, Test No. DTC-1	135
Figure 83. Bogie Acceleration, Test and Simulation, Test No. DTC-1	136
Figure 84. Prismatic Beam Subject to Applied Moment	141
Figure 85. Clamped Configuration of Long Wire Rope Quasi-Static Bending Test.....	147
Figure 86. Reference Line and Surface for Vertical and Horizontal Measurements	148
Figure 87. Loading Configuration and Method of Applying Discrete Weights	150
Figure 88. Long Wire Rope Deflection by Applied Moment	150
Figure 89. Medium-Length Wire Rope Deflection by Applied Moment	151
Figure 90. Short-Length Wire Rope Deflection by Applied Moment	151
Figure 91. Example Beam Cross-Section Definition with Major S-S and T-T Axes.....	157
Figure 92. Possible Deformation Modes of Beams	158

Figure 93. Modeled W14x132 (W360x196) Beam in LS-DYNA.....	159
Figure 94. Applied End Load Conditions on Cantilever Beam.....	160
Figure 95. Moment-Curvature Input Curve for W14x132 (W360x196) Beam.....	161
Figure 96. Analytical and Simulated Results.....	163
Figure 97. Moment-Curvature Curve Estimation Obtained Using Gravitational Models.....	165
Figure 98. Measured Initial Radius of Curvature of Wire Rope.....	166
Figure 99. Long Wire Rope Test and Simulation Comparison	169
Figure 100. Short Cable Test and Simulation Comparison	169
Figure 101. Mesh Sensitivity Analysis for Long Wire Rope Loaded at C Position.....	172
Figure 102. Moment-Curvature Input Curve for Use with Wire Rope Model	174
Figure 103. Tensioned String Model and Reaction Forces.....	175
Figure 104. Stiff Rod Subjected to Bending	177
Figure 105. Bending Test Details, Test Nos. DBC-1 through DBC-6	184
Figure 106. Load Frame and Rotator Pipe End Assembly, Test Nos. DBC-1 through DBC-6 .	185
Figure 107. Load Frame and Rotator Pipe End Assembly Details, Test Nos. DBC-1 through DBC-6.....	186
Figure 108. Concrete Wall Reinforcement Details, Test No. DBC-1 through DBC-6	187
Figure 109. Bogie Head Attachment, Test Nos. DBC-1 through DBC-6.....	188
Figure 110. Impact Head Mount, Test Nos. DBC 1-6.....	189
Figure 111. Bogie Vehicle, Component Test Nos. DBC-1 through DBC-6.....	190
Figure 112. Impact Head and Mounting Post, Component Test Nos. DBC 1-6.....	191
Figure 113. Sequential Photographs, Test Nos. DBC 1 and DBC-2	196
Figure 114. Bogie Impact Location, Component Test Nos. DBC 1 through DBC-4	197
Figure 115. Final Position of Wire Rope and Bogie Vehicle, Test No. DBC-1	198
Figure 116. Final Position of Wire Rope and Bogie Vehicle, Test No. DBC-2.....	199
Figure 117. Wire Rope Damage, Test No. DBC-1	200
Figure 118. Wire Rope Damage, Test No. DBC-2	201
Figure 119. Impact Head Damage and Wire Rope Pull-Through, Test No. DBC-1	202
Figure 120. Wire Rope Pull-Through, Test No. DBC-2.....	203
Figure 121. Load Cell Results, Component Test Nos. DBC 1-2.....	205
Figure 122. Bogie Displacement, Component Test Nos. DBC 1-2	206
Figure 123. Bogie Velocity, Component Test Nos. DBC 1-2	207
Figure 124. Bogie Acceleration, Component Test Nos. DBC 1-2.....	207
Figure 125. Spectral Frequency Analysis, Test Nos. DBC 1-2	208
Figure 126. Sequential Photographs, Test Nos. DBC-3 and DBC-4.....	212
Figure 127. Final Position of Bogie Vehicle and Wire Rope, Test No. DBC-3.....	213
Figure 128. Wire Rope Pullout, Test No. DBC-3.....	214
Figure 129. Wire Rope Pullout Through Epoxy, Test No. DBC-3.....	215
Figure 130. Load Cell Cushion Design Modification, Test No. DBC-4	216
Figure 131. Final Position of Bogie and Wire Rope, Test No. DBC-4	217
Figure 132. Wire Rope Damage, Test No. DBC-4.....	218
Figure 133. Wire Rope Damage, Test No. DBC-4	219
Figure 134. Wire Rope Damage, Test No. DBC-4	220
Figure 135. Final Position for Load Frames, Test No. DBC-4.....	221
Figure 136. Load Cell Results, Test Nos. DBC-3 and DBC-4	222
Figure 137. Bogie Displacement, Test Nos. DBC 3 and DBC-4.....	222
Figure 138. Bogie Velocity, Test No. DBC-4	223

Figure 139. Bogie Acceleration, Test No. DBC-4.....	224
Figure 140. Sequential Photographs, Test Nos. DBC-5 and DBC-6.....	225
Figure 141. Test Setup and Impact Location, Test No. DBC-5.....	226
Figure 142. Final Position of Bogie and Wire Rope, Test No. DBC-5	227
Figure 143. Wire Rope Damage, Test No. DBC-5.....	228
Figure 144. Wire Rope End Fitter Damage, Test No. DBC-5.....	229
Figure 145. Final Position of Bogie and Wire Rope, Test No. DBC-6	230
Figure 146. Wire Rope Damage, Test No. DBC-6.....	231
Figure 147. Wire Rope Damage, Test No. DBC-6.....	232
Figure 148. Load Cell Data, Test No. DBC-6	234
Figure 149. Bogie Displacement, Test Nos. DBC-5 and DBC-6	235
Figure 150. Bogie Velocity, Test Nos. DBC-5 and DBC-6.....	235
Figure 151. Bogie Acceleration, Test Nos. DBC-5 and DBC-6.....	236
Figure 152. Spectral Acceleration Frequency Analysis for Test No. DBC 6.....	237
Figure 153. Baseline Model, Test No. DBC-1.....	244
Figure 154. Rotator Pipe End Assembly, Test and Baseline Model, Test No. DBC-1	244
Figure 155. Impact Head, Tested and Modeled, Test No. DBC-1.....	247
Figure 156. Wire Rope Axial Load Comparison, Test No. DBC-1 and Baseline Simulation....	248
Figure 157. Bogie Displacement Comparison, Test No. DBC-1 and Baseline Model.....	249
Figure 158. Methods of Generating Slack in Wire Rope, Test No. DBC-1	251
Figure 159. Wire Rope Tension Comparison, Test Data and Methods of Including Slack	252
Figure 160. Bogie Acceleration Comparison, Test Data and Methods of Simulating Slack.....	253
Figure 161. Bogie Vehicle Comparison, Test and Model, Test No. DBC-1	254
Figure 162. Sequential Photographs, Test and Simulation, Test No. DBC 1	256
Figure 163. Wire Rope Tension Comparison, Test and Simulation, Test No. DBC-1.....	257
Figure 164. Bogie Displacement Comparison, Test and Simulation, Test No. DBC-1	258
Figure 165. Bogie Velocity Comparison, Test and Simulation, Test No. DBC-1.....	259
Figure 166. Bogie Acceleration Comparison, Test and Simulation, Test No. DBC-1	259
Figure 167. Bending Stiffness Curves Evaluated for Sensitivity Study	260
Figure 168. Wire Rope Tension Comparison, Varying Bending Stiffness Models.....	261
Figure 169. Bogie Velocity Comparison, Varying Bending Stiffness Models.....	263
Figure 170. Bogie Acceleration Comparison, Varying Bending Stiffness Models	263
Figure 171. Effect of CFA on Non-Linear Tensile Curve Models of Test No. DBC-1	264
Figure 172. Effect of CFA on Linearized Tensile Curve Models of Test No. DBC-1	265
Figure 173. Wire Rope Model Comparison.....	266
Figure 174. Wire Rope Axial Load Comparison, Test and Simulation, Test No. DBC-1	269
Figure 175. Wire Rope Length, Beam-and-Shell Model, Test No. DBC-1.....	270
Figure 176. Bogie Displacement Comparison, Test and Simulations, Test No. DBC-1	271
Figure 177. Bogie Velocity Comparison, Test and Simulations, Test No. DBC-1	272
Figure 178. Bogie Acceleration Comparison, Test and Simulations, Test No. DBC-1	273
Figure 179. Wire Rope Axial Load, Test and Simulation, Test No. DBC-2	274
Figure 180. Bogie Displacement, Test and Simulation, Test No. DBC-2	275
Figure 181. Bogie Velocity, Test and Simulation, Test No. DBC-2	275
Figure 182. Bogie Acceleration, Test and Simulation, Test No. DBC-2.....	276
Figure 183. Sequential Photographs, Test and Simulation, Test No. DBC 4.....	278
Figure 184. Wire Rope Tension, Test and Simulations, Test No. DBC-4.....	279
Figure 185. Simulated Wire Rope Tension, CFA Greater than 1.0, Test No. DBC-4.....	280

Figure 186. Bogie Displacement, Test and Simulation, Test No. DBC-4	281
Figure 187. Bogie Velocity, Test and Simulations, Test No. DBC-4.....	282
Figure 188. Bogie Acceleration, Test and Simulations, Test No. DBC-4.....	283
Figure 189. Sequential Photographs, Test and Simulation, Test No. DBC-6.....	285
Figure 190. Wire Rope Tension, Test and Simulation, Test No. DBC-6	286
Figure 191. Wire Rope Bend and Tension Transmission	287
Figure 192. Bogie Displacement Comparison, Test and Simulation, Test No. DBC-6	288
Figure 193. Bogie Velocity Comparison, Test and Simulation, Test No. DBC-6.....	289
Figure 194. Bogie Acceleration, Test and Simulation, Test No. DBC-6.....	289
Figure 195. Cable Guardrail System Details, Test No. CS-1 [44].....	296
Figure 196. End Post and Compensator Assembly Details, Test No. CS-1 [44].....	297
Figure 197. Anchor Post Details, Test No. CS-1 [44]	298
Figure 198. Line Post Details, Test No. CS-1 [44].....	299
Figure 199. Slip Base Post Details, Test No. CS-1 [44].....	300
Figure 200. System Details and Impact Location, Test No. CS-1	301
Figure 201. Line Posts and Cable Compensator, Test No. CS-1	302
Figure 202. Test Summary and Sequential Photographs, Test No. CS-1 [44]	305
Figure 203. Sequential Photographs, Test No. CS-1	306
Figure 204. Sequential Photographs, Test No. CS-1	307
Figure 205. Vehicle Damage, Test No. CS-1	308
Figure 206. System Damage, Test No. CS-1	309
Figure 207. Modeled System, Test No. CS-1	310
Figure 208. C2500 Pickup Model with Wheel Well Covers, Left Side	311
Figure 209. Post Model and Hook Bolts.....	312
Figure 210. Hook Bolt Modeling.....	313
Figure 211. Sequential Photographs, Test and Simulation, Test No. CS-1	314
Figure 211 (cont). Sequential Photographs, Test and Simulation, Test No. CS-1	315
Figure 211 (cont). Sequential Photographs, Test and Simulation, Test No. CS-1	316
Figure 212. Sequential Photographs, Test and Simulation, Test No. CS-1	317
Figure 213. Sequential Photographs, Test and Simulation, Test No. CS-1	318
Figure 214. Post Deformation, Test and Simulation, Test No. CS-1.....	322
Figure 215. Total Wire Rope Tensile Loads, Three Ropes, Test and Simulation	324
Figure 216. Wire Rope Tensile Load, Full-Scale Test and Updated Model, Test No. CS-1.....	325
Figure 217. Vehicle Longitudinal Displacement, Test and Simulation, Test No. CS-1.....	327
Figure 218. Vehicle Velocity, Test and Simulation, Test No. CS-1.....	329

LIST OF TABLES

Table 1. Bulk Physical Testing Properties Required for Characterization	4
Table 2. Wire Rope Terminology	6
Table 3. Characteristics of Lagrangian Elements in LS-DYNA.....	22
Table 4. Relevant Parameters for Proposed Cable Material Model.....	27
Table 5. Recommended Tensile Load Curves for Load Curve No. 1.....	28
Table 6. Mesh Density Comparison, Tensile Test Simulation	72
Table 7. Recommended Tensile Curves for Prestretched and Non-Prestretched Wire Ropes	75
Table 8. Computational Time and Accuracy, Stiff I-Beam Model.....	164
Table 9. Moment-Curvature Input Curve	170
Table 10. Beam Element Percent Error in Bending.....	170
Table 11. Comparison of Wire Rope Mesh Density Results	172
Table 12. Final Low Axial Load Moment-Curvature Input Curve.....	174
Table 13. Summary of Modeling Parameters for Wire Rope Models Investigated.....	267
Table 14. Results Comparisons, Test and Simulation Data, Test No. DBC-1	269

1 INTRODUCTION

1.1 Background

Wire rope is a versatile, flexible, high-strength member that is used in many mechanical systems to provide excellent tensile strength while remaining flexible. It is also used in power transmission applications components which are physically separated or not collinear. Wire rope is typically classified by four parameters: (1) nominal diameter; (2) rope construction; (3) core type; and (4) breaking load. Variations in the make of the wire rope affect physical properties, such as flexibility, rupture strength, and service life.

Researchers have modeled wire rope using finite element analysis in an attempt to understand the complex physical system and wire interactions. These models are computationally expensive, since the accurate treatment of a wire typically requires a minimum of 9 to 12 solid elements within the cross-section. In addition, many wire rope types contain more than 50 wires, and common structural strand ropes contain more than 100 wires. Explicit solid modeling of these ropes is challenging since each wire is helically wound in a strand, and the strands are helically wound around cores. Furthermore, many mechanical systems implement wire ropes that are very long. Costello noted that wire ropes which are miles long are used in mining operations in Africa [1]. Detailed modeling of a long wire rope, such as the ropes used in roadside cable guardrail systems, is prohibitively computationally expensive.

Though previously-created wire rope material models for wire rope have been developed and used with some success, there is a need for a simplified, validated model of wire rope with low computational cost to accurately model wire rope under impact conditions. There are many applications for the use of a validated wire rope model, including simulation of cable median barrier penetration events. Furthermore, a validated material model for the generalized behavior

of a wire rope can then be used to evaluate more detailed models of a similar rope for future modeling applications.

1.2 Research Objective

The objective of this research project was to develop an improved material model of wire rope for use in LS-DYNA. The following criteria were used to judge the progress of the research objective: (1) the simulated tensile and bending behavior of wire rope should be within 5% of the results of physical component testing and are acceptable within 10%; (2) the proposed model should demonstrate improvement over existing models of wire rope when simulated in physical systems; (3) the model must be concise and easily constructed; and (4) the model must be stable and not prone to non-physical modeling results. In addition, the limitations of and future work on the model required consideration.

1.3 Research Approach

The research objective was to be completed in four steps: (1) identify methods for simplifying wire rope into a computationally cost-effective model; (2) conduct physical testing to determine the material properties of the wire rope; (3) construct models of physical component testing to capture bulk material properties; and (4) implement the simplified model into full-scale models to consider dynamic impact under complicated impact conditions.

1.3.1 Selection of Wire Rope to be Modeled

Since many types of wire ropes are currently in use throughout the world, it is impossible to accurately model every make and material used in the construction of wire rope. Thus, one rope size and make was selected, and an analysis procedure was created to aid in the generation of bulk material properties for other types of wire ropes used in alternative applications.

One wire rope which is commonly used in highway cable guardrail systems is the ¾-in. diameter (19-mm) 3x7 wire rope, with a minimum breaking strength of approximately 39,000 lb

(39 kip, or 173.5 kN). This rope size and configuration is of particular interest to researchers in highway safety fields because field experience demonstrated that this wire rope has great abrasion resistance, is relatively stiff, and often remains elastic when subjected to most vehicular impacts. As a result, the ropes often may be reused. Additionally, the wire rope has a relatively simple cross-section, with three strands of seven wires each, and all wires have the same diameter. Thus, this wire rope selection has both a relatively simple construction for ease of modeling and immediate application in the field of roadside safety engineering.

1.3.2 Determination of Required Tests

Characterization of the behavior of wire rope requires a total of 13 parameters, which are shown in Table 1. Due to limitations on funding for analysis of the wire rope, five of the thirteen parameters were selected for component testing and evaluation, with greatest consideration given to usefulness of resulting data, ease of test construction, and uniqueness of results. Parameters which were considered essential to the characterization of wire rope used in cable guardrail systems consisted of: (1) tensile load curve; (2) tensile dynamic magnification factor; (3) bending moment curve; (4) bending moment dynamic magnification factor; and (5) damping factors for bending. The remaining material parameters were estimated based on engineering knowledge. The indicated physical properties are sufficient to create a reduced, computationally-efficient model of wire rope for use in cable guardrail modeling.

Table 1. Bulk Physical Testing Properties Required for Characterization

Tension	Elastic-Plastic Load Curve Dynamic Magnification Factor
Compression	Elastic-Plastic Load Curve Critical Load Point to Prevent Birdcaging Dynamic Magnification Factor
Bending	Quasi-Static Elastic-Plastic Moment Curvature Curve Dynamic Magnification Factor
Torsion	Torque-Twist Static (both twist directions) Torque-Twist Under Load (both twist directions) Dynamic Magnification Factor
Damping	Axial Bending Torsion

It should be noted that wire rope rarely undergoes compression during vehicular impact. The ¾-in. (19-mm) diameter 3x7 wire rope used in cable guardrail systems is pre-tensioned with a static load. Longitudinal tension waves are generated in the wire rope, but since the ropes are generally constrained at the ends, tension waves are reflected and not inverted to compression waves. Furthermore, because wire ropes expand during compression, slight unwinding of the wire rope and loss in wire contact tends to damp out any dynamic compression waves in tensioned rope impacts. In severe cases the compression waves and strand unwinding can lead to birdcaging—a permanent condition causing separation of the strands and deformation of the core [2]. Birdcaging rarely (if ever) occurs in cable guardrail systems; therefore the compressive load curve on wire rope was not pursued.

During vehicle impacts, wire rope may also experience some torsion upstream and downstream of impact due to the extensional-torsional coupling in wire rope [3], but friction with the vehicle constrains the rope and prevents axial rotations in the impact region. The torque acting on a wire rope does not cause warping and is only manifested as internal shear stress. If

the total wire rope stress is less than the yield load, the torsional contributions are believed to be negligible. However, further studies may be required to validate this assumption.

For the aforementioned reasons, tests on wire rope were structured to evaluate the tensile and bending behavior, dynamic magnification factors in tension and bending, and bending damping factors.

2 CHARACTERISTICS OF WIRE ROPE

2.1 Terminology

There are many specific terms which apply to wire rope. Wire rope discussions utilize jargon which must be recognized and understood. Some of the wire rope terminology is shown in Table 2.

Table 2. Wire Rope Terminology

Term	Definition
Wire	Basic unit of wire rope; small diameter cylinder, usually comprised of steel
Strand	Uniform helical wrapping of wires to form cohesive cylinder
Core Wire	Central wire about which other wires are wrapped in a strand
Wire Rope	Helical wrapping of strands
Core	Central unit about which the outer strands of a rope are wrapped
IWRC	Independent wire rope core; smaller wire rope around which outer strands are wrapped, which may have a different strand construction than the remainder of the wire rope
Fiber Core	Fibrous strand (often solid) around which outer strands are wrapped in a rope
Strand x Wires	Nominal designation of the number of strands by the number of wires in a strand e.g., 3x7 refers to 3 strands by 7 wires per strand; other types include 6x19, 6x37, and 7x25
Lay	Orientation of wires with respect to the axial (long) direction of the rope May be regular, lang, or combined (also known as "alternate" or "reverse")
Lay Direction	Direction of strand helix around the rope core
Lay Length	Axial length required for a single strand to complete one revolution in a rope
Birdcaging	Condition where strands are forced in compression and bulge away from the core Permanent deformation occurs
Kink	Residual bend in wire rope following a high-curvature deformation
Breaking Strength	Nominal lower limit of load a wire rope can sustain before fracture
Operating Load	Recommended limit of axial load on a wire rope; usually $\leq 20\%$ of breaking strength
Coarse vs. Fine	Refers to the number of wires in a strand; coarse ropes are stiff, fine ropes are flexible
Plow Steels	Material commonly-used in construction of wire rope; selections are iron, mild plow steel, plow steel, improved plow steel, and extra-improved plow steel
Sheathed Ropes	Wire rope with exterior coating; the exterior coatings are commonly plastic
Compacted Strand	Strands are compressed to increase strand wire contact and make external rope surface circular

2.2 Wire Rope Construction

Wire ropes are constructed from a series of wires helically wound together. A collection of wires wrapped helically around a central core wire is called a strand, and strands are wrapped

around the core to complete a wire rope. Multiple layers of strands may be specified, different diameters of wires may be present within a single strand.

Many types of wire rope are classified under generalized cross-sections, but wire ropes do not always have the same number of wires designated in the wire rope construction. Rope sections are shown in Figure 1. Wire rope may be configured with one of many subclasses: 7-Wire, Warrington, Seale, Warrington Seale, and Filler Wire. Wire rope specified with an independent wire rope core (IWRC) may have a core strand which is different from the outer strands, and often has a different number of wires [2].

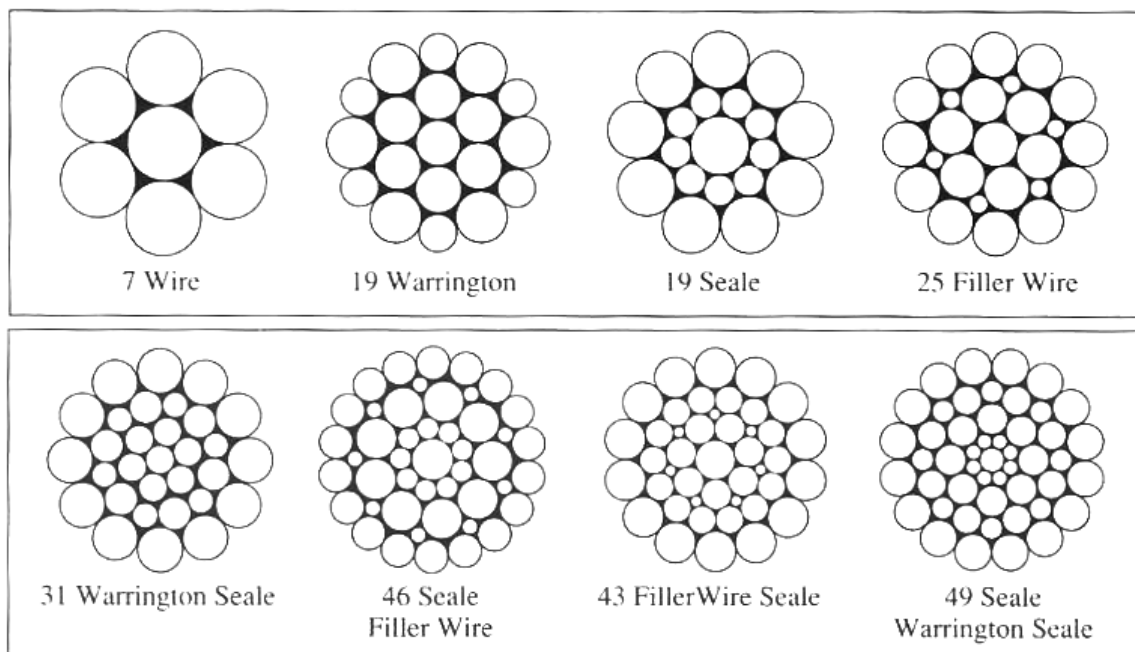


Figure 1. Section Classifications for Wire Rope [2]

The most basic strand section is the 7-wire. The 7-wire section is composed of six wires wrapped around a single wire core, all of which are the same diameter. The 19-wire Warrington consists of a 7-Wire section with an additional 12 wires wrapped around the seven-wire strand. The Seale classification incorporates large wires on the outer diameter for improved abrasive wear, with a large wire core and smaller wires in the gaps between outer wires and wire core.

The Filler Wire section is similar to the Warrington section, but with the smaller wires shifted into the gaps between outer wires and the interior 7-wire section. For large section constructions, the Warrington, Seale, and Filler sections may be combined to form more complicated sections.

2.3 Characteristics of Wire Rope

Wire rope has a complicated wire-to-wire interaction inside of the strands. Wire-to-wire contact creates bearing stresses, and the extension of a wire rope under tension creates a torsional coupling [3]. Furthermore, the load carried by any given wire is dependent on its distance from the center of the strand, the strand's position in the wire rope, and size of the wire relative to adjacent wires [1, 4-5].

General physical characteristics of wire rope include bending, crushing, fatigue, and abrasion resistance, as well as the minimum breaking strength. In general, stranded wire ropes with large wires on the outside of the rope have good crushing and abrasion resistance, but often have less flexibility and fatigue resistance. By contrast, stranded wire ropes with small wires generally have good fatigue resistance and flexibility, and less crushing and abrasion resistance.

There are three lays of a wire rope: regular lay, lang lay, and combined (aka alternate or reverse) lay. The regular lay incorporates strands with wires oriented along the axis of the rope, such that the wire is pulled in tension mostly along the long axis of the wire. Regular lay can come in right or left direction, but the left is rarely used in structural wire rope. Regular lay is the most commonly used lay in wire rope.

Lang lay is intended to increase the flexibility of a wire rope by orienting the wires in a strand at an angle to the long axis of the rope. Wires in strands designated with lang lay sections are more like springs and deflect more under axial load since the helical winding of the wire is more pronounced in the axial direction. While this increases the flexibility of the rope and

decreases bending stresses, this rope is generally weaker in tension, and may become unwound if wrapped too tightly over a sheave. The lang lay may be manufactured in right or left lay directions.

Combined lay uses alternating strands of the straight and lang lay and helically winds the strands around a central core, usually an independent wire rope core (IWRC). This configuration is rarely used, but possesses characteristics of balanced axial strength and bending strength, while resisting unwinding on a sheave. This lay is only manufactured with right direction, and is used in specialized circumstances.

Because the rope is wound with many wires and frictional interaction of the wires prevents large relative motion, fracture of individual wires does not preclude imminent failure of the wire rope. In fact, it has been stated that every wire in the wire rope may be fractured and the rope will still operate satisfactorily, so long as wire fractures are spaced far enough apart [1]. However, the length of rope required to prevent failure is not specified, and the breaking load of wire rope will be reduced as a result of compounded wire fractures.

3 LITERATURE REVIEW

Though wire rope is often considered as a singular, controlled-response component of a mechanical system, wire rope is truly composed of many individual component wires which have a combined effect.

3.1 Analytical Model

The analytical model of wire rope which is widely known and used in the wire rope industry was presented by Costello [1]. The analytical model proposed considered three cases: (1) a helically-wound wire, which was evaluated according to elasticity principles; (2) a helically-wound strand, which was approximated; and (3) a wire rope, which expanded on the strand model.

3.1.1 Single Wire Model

The kinematics of a single wire was described by considering a cylindrical curved beam, such that the radius of curvature and axial length of the beam were large with respect to cross-sectional dimensions—this was the fundamental mathematical definition of a thin wire. Three fibers attached to the end of the wire were oriented parallel with the principal cross-sectional moments of inertia of the wire cross-section. Each cross-section is assumed to initially be dimensionally identical.

In the deformed configuration, cross-sectional distortion and 3-axis deformation may occur in which case the three fibers may no longer form an orthogonal coordinate trio. Costello defined the wire in such a way that the Z-axis of the section was at every cross-section tangent to the line connecting the centroids of each wire cross-section. Then, at every cross-section, an X-axis is defined such that the X-axis is in the plane formed between the Z-axis and one of the deformed fibers, which was originally oriented with the "lateral" principle axis of the cross-

section. Though the location of the "lateral" axis is arbitrary, consistency must be used along the axis of the wire such that the X-axis is defined in the same way for every cross-section. Finally, the remaining coordinate axis Y is located orthogonally to both Z and X axes.

To follow the wire, a particle is created at one end of the beam. This particle is projected and travels along the centroidal axis of the wire with a velocity that encircles the Z-axis. The components of curvature in the X, Y, and Z directions are $\kappa_x, \kappa_y,$ and $\tau_z,$ respectively. A projection of the $\vec{\omega}$ onto the original undeformed coordinates provides $\kappa_x^o, \kappa_y^o,$ and $\tau_z^o.$ Note that τ_z and τ_z' are twists per unit length.

Using a force and moment balance for a static response of a wire, Costello generated the following relationships:

$$M_y = EI_{xx}(\kappa_x - \kappa_x^o); M_x = EI_{yy}(\kappa_y - \kappa_y^o); T_z = C(\tau_z - \tau_z^o) \quad [1]$$

where: M = Moment
 E = Young's Modulus
 I = Area Moment of Inertia
 κ = Curvature
 T = Torque;
 τ = Twist Rate
 C = Torsional Rigidity

This exactly treats the load and moment relationships of a single wire.

3.1.2 Simple Straight Strand

The strand is composed of a collection of wires helically wrapped around a wire core. Costello developed a relationship for the section such that in the undeformed configuration the helically-wound outer wires do not touch. This allows evaluation of the strand without additional subjugation of bearing contact between outer wires in the strand. Costello postulated that a cross-sectional plane normal to the axis of the straight core wire would cause a transverse axial elongation normal to the radius from the center wire [1, 5].

Applied forces, moments, and torques in the strand may be summed, and wire stresses were related to the helix angle, center distance, and poisson's ratio of the material. The relations developed by Costello were calculated using the small-angle assumption, and assumed small displacements from applied loads. The stresses were related to the applied forces and moments on the strand for various positions within the strand.

Costello observed a single strand subjected to axial loads, twisting moments, and bending moments does not have a uniform distribution of stress throughout the strand. Instead, the outer wires, which (since they are helically wound around the center wire) are longer than the core wire, experience lower loads that are concentrated at the location closest to the center wire. Contact stresses were also observed to be very large with respect to the axial stresses.

3.1.3 Wire Rope

A wire rope was evaluated using an extension of the strand theory, such that additional consideration for the helical position of the outer strand was generated. Plots of the outer wire stress as a function of the nominal stress, determined from geometry, were presented. The plots indicated that the outer wire stress could become very large if the radius of curvature was small and the outer wire diameter was large.

In addition to internal stress analysis, the wire rope was evaluated to determine what effects friction had on tension, and birdcaging was also addressed. It was observed that friction had very little effect on tension when the outer strands were not in contact with each other (and even less when the outer wires of the strands did not contact each other). By contrast, wire ropes with strands and wires that were in contact with adjacent wires that were not radially-directed had frictional contributions, as did ropes with fiber cores.

3.2 Isolated Parameter Models

The simplest efforts to model the bulk behavior of wire rope have largely been focused in transportation roadside safety research. The earliest efforts to model wire rope were conducted in New York [6-7] and the Department of Highways in Canada [8-9]. Cable models were used as preliminary estimates of cable guardrail performance under a variety of circumstances, which could then be iterated and converge in a solution which could be tested.

The cable barrier models proposed in New York considered the wire ropes (which are commonly referred to as cables in roadside safety engineering literature) as tensioned springs capable only of elastically stretching under impact loads. The impacting vehicle was typically a rigid vehicle model that was planar and often rectangular, and post release algorithms were used to determine when the cables released from the posts. The cables were elastic and the axial strain in the cables was related proportionately to effective average cable stress. Coulomb friction was specified between the cables and the flanges of the posts. This model was used for many years after its introduction in 1969.

The New York model was used to predict maximum deflection of an impacting vehicle, propensity for snag on posts, and to approximate wire rope tension. Variables which were used to iterate and investigate design options included post size, spacing, and strength, as well as wire rope elastic modulus and contact friction coefficients. Since each variable could be independently controlled, this model was used in parameter studies.

The Department of Highways in Ontario, Canada, desired a validated computer model for evaluating vehicle impacts with cable barriers [8-9]. The research approach was similar to the model presented by New York, and was created at nearly the same time. The vehicle model was a rigid rectangular shape with a chamfered corner that was placed on the impacting front corner

to simulate the damage to the vehicle by a cable barrier. The yaw moment of inertia of the vehicle was an input parameter, which was utilized to simulate the vehicle resistance to yaw. Posts were placed in a modeled soil environment and were deleted when failure criteria were met.

Cables used in the model were considered perfectly-elastic springs with no bending strength. Using the rigid vehicle assumption, the modeled wire rope was assumed to be in contact with the vehicle at a maximum of 3 locations: two points at the front chamfered corner and one point at the rear corner of the vehicle. Similar to the New York model, the Canadian cable barrier model incorporated friction between the cable and posts, and the cable and vehicle. The friction that was defined by this experiment followed the Coulomb model.

A variety of organizations contributed to simplistic designs of cable guardrail, also using discrete spring-like cables and friction between impacting vehicles and the wire rope [e.g. 10]. The impacting vehicles in the simulations were rectangular and deformable. The model was based on the concept of discrete *bays*, which are the sections of wire rope contained between adjacent posts. The wire rope was assumed to release from a post when a bending wave was reflected off of the post twice.

The proposed wire rope model did very well in predicting maximum dynamic vehicle displacement, as well as maximum wire rope tension and vehicle velocity. Parameter studies were conducted on friction, post release schemes for alternative post attachment hardware. Later, this code was updated and distributed for use in optimizing cable guardrail systems through the BrifSim and BrifSim II programs.

3.3 Simplified Models

Wire rope guardrail simulations conducted at the Midwest Roadside Safety Facility (MwRSF) at the University of Nebraska-Lincoln were used to evaluate cable barrier systems prior to crash testing using LS-DYNA [11]. The wire rope guardrail system consisted of a G1 guardrail system with the center of the posts located at the slope break point of a 1.5:1 slope. The posts were S3x5.7 (S76x8.5) sections, and extended 33 in. (838 mm) above ground.

The wire rope model was a beam-and-solid model. The major load-carrying part of the wire rope was a continuous length of beam elements, defined with *MAT_CABLE_DISCRETE_BEAM and elastic modulus of 18.3 Mpsi (126 GPa). Wrapped around the outside of the beam elements was a shroud of eight solid wedge-shaped elements. The wedge-shaped elements were defined with an elastic-highly-plastic material, so that the elastic resistance would be very weak. The secondary benefit to the solid element shroud was the introduction of both bending strength and compressive strength, both of which are necessary for stable models.

The beam-and-solid model indicated that the vehicle would likely be redirected on the slope. However, in the test, the pickup truck rolled onto its side and down into the ditch. In addition, significant hourglassing and torsional warping occurred to the wire rope around the pickup due to the low resistance of the solid elements.

The beam-and-solid wire rope model in LS-DYNA used by MwRSF was again utilized to simulate the response of a cable guardrail end terminal system [12]. The low-tension cable guardrail system had three cables, mounted at 30 in., 27 in. and 24 in. (762 mm, 686 mm, and 610 mm). Strand-splitting wedge end anchors were used at the terminal.

Significant effort went into the simulation of the end terminal components. Hiser and Reid conducted many studies to accurately simulate the cable barrier end terminal system [13-

20]. The end terminal system consisted of a rigid cable anchor bracket modeled with shells, a slip-base post developed by Hiser with a cable router, and downstream line posts. This model was very accurate when impacted in end-on impact situations.

The National Crash Analysis Center (NCAC) also worked with the simulation of cable guardrail impacts using simulation models. The wire rope model used by NCAC consisted of a beam-and-shell approach. The beam-and-shell model of wire rope was a center series of type 1 beam elements defined with an elastic material and cross-sectional stiffness properties consistent with a 3/4-in. (19-mm) diameter solid bar. Nodal rigid bodies were defined at each beam element node, and the nodal rigid bodies connected null shells surrounding the beam elements. The null shells provided a contact surface which was more favorable than the beam elements themselves.

A test of the Washington 3-strand cable median barrier conducted at TTI was simulated using the cable posts, cables, hook bolts, and soil meshes [21-22]. The simulations were tuned until the model accurately reflected the full-scale testing, both in vehicle redirection and system reaction. Once the model was validated, researchers examined median barrier placement in medians.

Bumper trajectories of three vehicles were simulated and evaluated for vehicle departures into V-ditch medians with 6:1 side slopes. The three vehicles evaluated were a Ford Crown Victoria sedan, Mitsubishi Mirage small car, and Chevrolet C2500 pickup. The trajectories of the vehicles were simulated using the Human Vehicle Environment (HVE) software package and evaluated under a variety of impact speeds and angles. Based on the evaluations, it was observed that the vehicle bumpers of most small vehicles and sedans would underride a cable barrier when placed 4 ft (1.2 m) from the center of the V-ditch, but that the bumper of the test vehicles were

within the cable heights when the system was installed 1 ft (0.3 m) from the center of the median.

In addition to cable guardrail impact simulations, NCAC conducted an investigation to determine the effect of end anchor spacing and cable pretension on vehicle redirection and maximum deflection [23]. The same wire rope model was used, and it was noted that with longer system lengths, deflections increase as well, though this effect was finite. Pretension could reduce the vehicle dynamic deflection, but reducing the tension by 40% led to an increase in deflection of approximately 5%.

Non-linear finite element analysis using MADYMO was conducted on motorcycle impacts with cable barrier systems in Germany [24]. The wire rope was modeled using a single octagonal solid element to represent the cross-section. Motorcyclists were modeled using ellipsoids. Wire ropes were modeled in slots in the posts, and the posts were defined to be rigid. The wire rope area was approximately the same as the actual area of the 3x7 wire rope.

Analysis of the motorcyclist impacts with the barriers indicated that the posts caused significant damage to the riders and the motorcycles, whereas the wire ropes were more flexible. Damage to motorcyclists was limited from impact with the wire ropes since the ropes tended to distribute loads on the impacting body. However, as in the other simplified models, the geometry of the cross-section of the wire rope was approximated, and did not have the same flexural or tensile characteristics as actual wire rope.

3.4 Detailed Models

In recent years, with the growth of computer processing power and computational speed, researchers have turned to detailed models of wire rope to understand the complicated interaction between wires in the cross-section. Furthermore, the load sharing between wires, prediction of

birdcaging and wire fracture, and induced contact stresses between adjacent wires have been investigated using full, detailed wire rope models.

Y.J. Chiang studied the stress intensity factor of a simple, 8-wire chord [25]. In Chiang's analysis the six outer wires of the chord did not touch, but the outer wires did touch the larger center wire. The outer wires were composed of 8-node solid isoparametric elements with a 21-element mesh cross-section. The center wire utilized 20 elements with horizontal and vertical axes of symmetry and trapezoidal prismatic solid elements were used throughout the center wire.

A modulus of elasticity of 28.63 Mpsi (197.4 GPa) was used to simulate the wire rope elastic strength, and a Poisson's ratio of 0.28 was used to calculate cross-sectional distortions from axial loads. A uniform displacement of 3.9 $\mu\text{in.}$ (0.00010 mm) was applied to the end of the chord, while the other end remained fixed. Stress intensity factors, which are defined as stresses which deviate from the nominal average stress on a cross-section, were monitored and recorded. It was observed that the typical stress riser in a steel cable due to contact friction, wire winding, and load transfer between adjacent wires was approximately 35%.

Later, wire deformation within stranded wire ropes was investigated using a short-length model of wire rope with solid wire meshing [26]. A $\frac{3}{8}$ -in. (10-mm) diameter 6x19 wire rope was modeled over a length of $\frac{7}{16}$ in. (11 mm). The modulus of elasticity of the steel material was 26.1 Mpsi (180 GPa), and a Poisson's ratio of 0.3 was used. The wire rope was loaded by fixing one end against all rotation and translation, and applying a tensile load to the other end of the rope.

Spatial dependence was observed on wire rope deformation, total elongation, and wire rope load. This ultimately led to differences in wire rope deflections at different positions within a strand, such that greater elongations (and thus axial strains) occurred at locations near the

center of the wire rope, and smaller elongations occurred near the outside boundary of the rope. This indicated that the lowest stresses were present near the outside of the wire rope while a larger portion of the tensile stress was sustained in the center of the rope. Physical testing conducted in support of the modeling indicated good correlation to simulated test data, though the presence of friction in real wire rope was neglected in the wire rope model and thus the simulation differed slightly from the test.

A different approach was taken by Jiang, Henshall, and Walton [27]. A single strand of wire rope with three layers of wires in the strand was analyzed using solid elements. The geometry of the wires was helical, and only a singular symmetrical slice was evaluated, with continuity (symmetric) boundary conditions on both sides. Researchers applied fixed and free-rotating boundary conditions to the lower side of the modeled wire rope, and loads and displacements were applied to the opposite ends. Wire load, stresses, and displacements were created, and it was observed that when twist and tension loads were applied to the wire rope stresses were fairly uniform throughout the wire rope. However, when the wire rope had a free end the stress in the outermost wire was reduced by a factor of 3 to 5.

Jiang conducted an additional study on a reduced explicit model of wire rope by examining a 1/12th section of the wire rope (cut through the center of the outside wire of a 7-wire strand). An analytical determination of the stress in the wire due to load acting on the strand was used to estimate contact stresses. The results of the simulation confirmed the analytical results. Jiang also confirmed that if wire rope is loaded beyond a critical tensile load, residual bearing stresses will occur in the wires due to a Poisson effect.

3.5 Discussion

Models of wire rope generally consisted of parameterized or simplified models if the wire ropes are used over very long lengths (e.g., cable guardrail systems). For shorter lengths or for wire rope models in which specific internal reactions of the wires were desired, solid elements were used and the wires were independently modeled and simulated in physical scenarios. No one model works best in all situations; there are distinct advantages and disadvantages to each modeling approach. Future modeling efforts may hybridize the simplified and detailed (or explicit) methods of modeling wire rope by replacing the solid element wires in the cross-sections with individual beams for each wire. This will reduce the overall computational expense footprint that is required when using the detailed (explicit) method, while still offering a much more sophisticated and physically accurate approach than the single beam element method.

4 PROPOSED MODEL

4.1 Selection of Wire Rope

Wire ropes are constructed in a vast array of sizes, strand shapes and constructions, and with many different numbers of wires. Applications for wire rope include stranded electrical wires and power transmission lines to crane and mine shaft hoists. There is application for the modeling of many types of wire rope, but testing all of the wire rope to create concise models for each would be prohibitively expensive and time consuming. Furthermore, differences in make, size, and stiffness of wire ropes mean that a generalized wire rope model with minor material or size variations is virtually impossible to create.

One type of wire rope which has both immediate need and application for a computer simulation model is the wire rope used in cable guardrail systems. The $\frac{3}{4}$ -in. (19-mm) diameter 3x7 wire rope has a very good strength to weight ratio, excellent abrasive resistance, and large bending resistance, but currently it has not been validated in roadside barrier modeling. Since roadside engineers are increasingly turning to finite element analysis for design and evaluation prior to full-scale testing, a validated model of wire rope used in cable guardrail is necessary. The validation of a new wire rope model will provide an excellent opportunity for roadside engineers to address difficult problems pertaining to roadside cable barrier applications.

4.2 Model Composition

In order to develop a concise and accurate material model of wire rope, researchers considered three evaluation criteria:

- Accuracy: Does the model replicate quasi-static and dynamic loading?
- Simplicity: Can the new wire rope model be implemented quickly and with ease?
- Robustness: Does the model remain stable and accurate during impact applications?

When the new wire rope model satisfactorily met the three evaluation criteria, it was determined to be acceptable. It was intended that the model be used in LS-DYNA; however, with appropriate modifications, this model may be applied to alternative finite element analysis programs.

There are five unique Lagrangian (i.e., mesh-based cohesive model) elements in LS-DYNA: (1) discrete masses, (2) discrete elements (springs and dashpots), (3) beam elements, (4) shell elements, and (5) solid elements. Characteristics of the element types are shown in Table 3. Clearly, discrete masses cannot physically represent the reaction of wire rope, since elements are disjoint. Likewise, discrete elements typically lack the degree of complexity required to fully characterize the behavior of many real components.

Table 3. Characteristics of Lagrangian Elements in LS-DYNA

Element Type	Material Model Complexity	Computational Expense	Mesh Sensitivity	Accurately Represents:
Discrete Mass	-	Lowest	Lowest	1-D Motion of massive bodies
Discrete Spring/Damper	Low	Low	Low	Springs, dampers, strings
Beam	Low/High	Medium	Medium	Wires, structural shapes, tether, rebar
Shell	Low/High	High	High	Most thin-structured or hollow pieces; walls
Solid	Low/High	Highest	Highest	All physical structures

Shell elements can be more accurate than discrete elements in many applications. However, since most wire ropes are approximately circular, shell elements are not applicable to the proposed wire rope model, and would be difficult to implement. Addition of shells onto a beam or discrete element model is difficult and physically do not represent wire rope very well.

Beams were a clearly advantageous choice for modeling wire rope. Since beams are simplified elements based on classical beam equations, modeling with beams would be both simple and tailored toward the bulk properties of wire rope. Generally, beams are computationally inexpensive, and a fine mesh may be obtained at a modest computational cost.

Advanced material models are applicable to many beam element types. Additionally, the existing simplified models of wire rope used in cable guardrail systems were created using beam elements. This allows for a swift and easy transition to the new wire rope model proposed in this study.

In many applications solid elements can more accurately capture physical responses to loading. This is because stresses and strains are captured in 3-D space with few assumptions required for computation, and the generated model most closely matches theoretical analyses. Geometrical detail can also be approximated more accurately using solid elements. However, individual computation of the stresses at each point in each wire of each strand is more information than is needed for roadside cable barrier modeling. To accurately capture the deformation and response of one increment of wire rope measuring 0.50-in. (12.7-mm) long using solid elements with 9 elements in a wire cross-section and with solid element lengths of 0.10 in. (2.5 mm), more than 945 elements are required. Comparatively, a single beam element was found in this study to accurately represent the same length of wire rope. Most roadside safety facilities do not have the computational resources necessary to evaluate a solid element model of a three-cable barrier system with a length of 300 ft (91 m), as it would require millions of elements. This is a notable increase in computational cost, modeling difficulty, number of elements in a model, and required effort by the researcher. Additional difficulties in utilization of a solid element model of wire rope include contact definitions between each wire in the section and any impacting structure, initial penetrations, snagging of nodes on contact surfaces, and a limited range of elements. An example of a solid element-model of $\frac{3}{4}$ -in. (19-mm) diameter 3x7 wire rope is shown in Figure 2.



Figure 2. Solid Element Model of $\frac{3}{4}$ -in. (19-mm) Wire Rope

Though solid element models of wire rope are useful for understanding the physics and interaction of the wires and strands within a wire rope, the model cannot be applied to wire rope used in cable barrier systems due to the tremendous computational expense and difficulty currently required. Therefore, the beam element was selected to model wire rope.

4.3 Selection of Beam Element Cross-section

There are eleven classified beam sections available for modeling beam elements, which may be categorized into four major groups: 2-D or axisymmetric beams, discrete beams, resultant beams, and beams with integrated cross-sections. Fundamental calculation of forces, moments, stresses, strains, and displacements vary between section types [28]. Though computational costs are generally less for the resultant-type beam elements, there is some advantage to cross-section integration in integrated elements.

Beam elements generally follow three assumptions: (1) cross-sectional distortions do not occur in loading conditions (i.e., plane sections remain planar and have a Poisson's ratio of zero); (2) angular displacements between adjacent beams are small; and (3) no warping occurs due to bending or torsion [28]. However, newer beam elements incorporate non-linearities due to warping and buckling [29].

Wire rope, though principally very complex, has relatively simple bulk reactions. Wire rope cannot sustain large compressive loads, and if loaded in compression over a long axial length, the wire rope will bend and buckle instead of compressing. The Euler buckling load of a 3 ft – 3 in. (1.0 m) length of ¾-in. (19-mm) diameter wire rope is only 25 lb (0.11 kN) based on classical buckling analysis [30]—the weight of the wire rope alone is nearly 2.7 lb (1.2 kg). Further, though there is an extensional-torsional coupling in wire rope [3], the torsion does not affect the bending reaction nor does it interact with external loads on the wire rope. The advanced warping beam types were not selected because of the increased difficulty in analyzing beams with "buckling degrees of freedom" and due to the fact that wire rope, as a primarily tension-based member, rarely experiences elastic or plastic buckling.

Existing models of wire rope used in cable guardrail incorporated discrete beams as the cable elements. However, discrete beams have no bending strength, and do not accurately capture the bending stiffness of the cable. Moreover, the discrete cables have no resistance to torsion and rotate freely. Though bulk cable reaction may be approximated with the discrete beams in some cases, they also were not selected for analysis in this project.

Two types of beams were evaluated for use in the proposed wire rope model: the Hughes-Liu integrated (type 1) beam and the Belytshcko-Schwer (type 2) beam. The type 1 element has received general acceptance due to ease of application and the advantageous *INTEGRATION_BEAM command, which allows the user to define an arbitrary cross-section to the beam for analysis [31]. The type 2 beam element was selected since it has a wide range of materials that can be applied to the element, and it was a widely-used and thoroughly-evaluated element type. Additionally, the type 2 beam element had a distinct advantage of decreased computational cost and simplicity over the type 1 element.

4.4 Material Selection

Beam element materials are provided in the LS-DYNA Keyword Manual for different section types [32]. The type 2 beam element only shares one material type with the type 1 element: *MAT_ELASTIC.

The type 1 element has most of the elastic-plastic materials applicable to shells and solids since it was derived from a solid element formulation. Materials applicable include linear-elastic, non-linear elastic, plastic-kinematic, piecewise linear plasticity, and viscoelastic models. Material models incorporating damage, non-isotropic behavior, or cracking are not applicable to the type 1 beam element.

The type 2 beam element is a resultant formulation, and requires use of resultant material models. As a result, material models applicable to the type 2 element are limited. Material models applicable to the type 2 element include elastic, rigid, resultant plastic, simplified Johnson-Cook viscoelastic, force-limited, moment-curvature beam, steel concentric brace, and seismic beam.

Due to problems in the determination of the actual displacement and the effective strain in the type 1 beam using the piecewise linear plasticity model, the type 2 beam using the moment curvature material model was selected to refine and evaluate. This problem will be discussed in detail in a later section.

4.5 Proposed Model

Cards defined for the proposed model are shown in Table 4. LS-DYNA implementation of the proposed model is shown in Table 5 and Figures 3 through 5. The development of the implementation is detailed in the following sections. Material parameters are specified in metric units (kg, mm, ms) for ease of input into LS-DYNA decks.

Table 4. Relevant Parameters for Proposed Cable Material Model

*SECTION	elform	Element Formulation	2	
	a	Cross-Sectional Area	285.0227	mm ²
*MAT_ MOMENT_ CURVATURE_ BEAM	ro	Density	4.309E-06	kg/mm ³
	e	Modulus of Elasticity	56.4	kN/mm ² (Non-Prestretched)
			62.9	kN/mm ² (Prestretched)
	elaf	Tension-Compression Load Curve	1	Load Curve No.
	lcms1-8	Moment-Curvature Curve in S-S Direction	2	Load Curve No.
	lcmt1-8	Moment-Curvature Curve in T-T Direction	2	Load Curve No.
	lct1-8	Torsion-Twist per Unit Length Curve	3	Load Curve No.
	reps	Rupture Effective Plastic Strain	0.01625	Linearized Non-Prestretched
			0.0230	Non-Linear Non-Prestretched
0.0185			Prestretched	
cfa	Dynamic Magnification Factor for Axial Loads	0.97		
cfb	Dynamic Magnification Factor for Bending Loads	1.00		
*DAMPING_ FREQUENCY_ RANGE	cdamp	Coefficient of Damping (Fraction of Critical)	11%	
	flow	Lower Frequency Bound	***	Based on Characteristic Frequency: post spacing divided by the characteristic bending wave speed, 340 m/s
	fhigh	Upper Frequency Bound	***	

** L_{free} refers to cantilever length or half of the length of the fundamental waveform

Table 5. Recommended Tensile Load Curves for Load Curve No. 1

Non-Prestretched Baseline		Non-Prestretched With Geometrical Stretch		Prestretched	
True Strain	Axial Force (kN)	True Strain	Axial Force (kN)	True Strain	Axial Force (kN)
0.00000000	0.00000000	0.00000000	0.00000000	0.00000000	0.00000000
0.008937121	110.398594105	0.000010000	0.145143150	0.004795620	83.619521342
0.009870041	121.813154169	0.000130000	0.774254827	0.006443918	104.867031688
0.011651737	136.049084775	0.000220000	1.085736654	0.008081977	119.626820549
0.013076832	143.858764574	0.000300000	1.459514847	0.009222070	126.604013475
0.014862910	151.164162192	0.000350000	1.646403943	0.013720171	146.756887686
0.016897369	157.585950324	0.000450000	2.198171751	0.015948646	156.684258488
0.024654681	172.995564236	0.000580000	2.910130213	0.018486490	162.384375923
0.034179644	182.817583777	0.000690000	3.595390232	0.021997547	169.210277676
0.039568289	188.164193743	0.000770000	4.267301031	0.024989359	174.358627303
0.046628261	191.823858320	0.000850000	4.859116502	0.025965115	175.822591890
0.049911007	194.385161537	0.001000000	6.118393031	0.028367689	178.541383266
0.059994686	197.000000000	0.001170000	7.689151388	0.039924366	189.274157078
		0.001290000	9.024073504	0.041177608	190.026163203
		0.009496593	110.398594105	0.047103248	192.602562887
		0.010423865	121.813154169	0.054227610	194.974274513
		0.012204576	136.049084775	0.061906827	196.860964437
		0.013628883	143.858764574	0.071521621	198.471770457
		0.015413976	151.164162192	0.093020967	201.439747295
		0.017447316	157.585950324	0.096687353	201.600000000
		0.020166744	162.477820471		
		0.027534677	175.003839659		
		0.030515308	179.667262121		
		0.039801059	188.164193743		
		0.047162102	191.823858320		
		0.060521441	197.000000000		

Recommended Tensile Curves

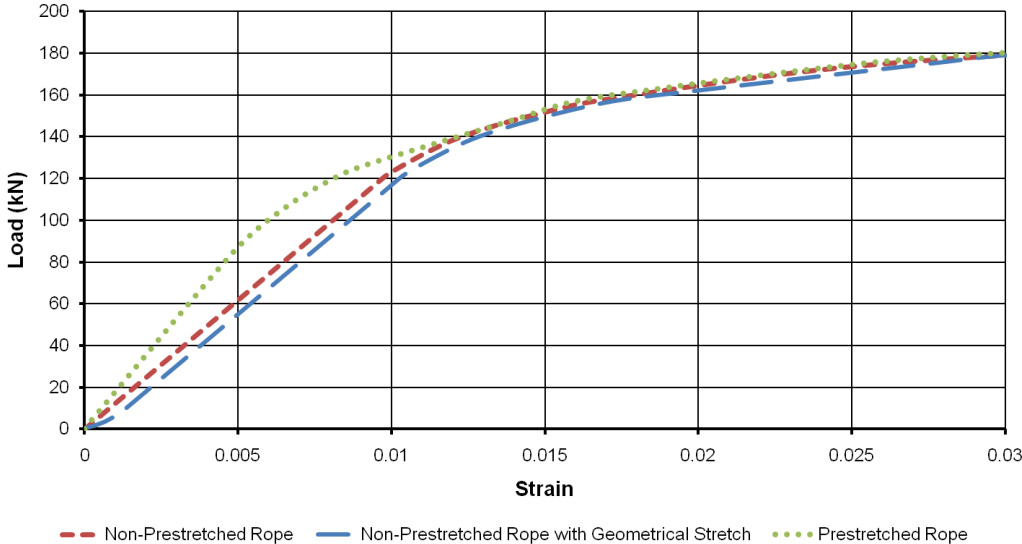


Figure 3. Tension Load Curve (Load Curve No. 1), Proposed Wire Rope Model

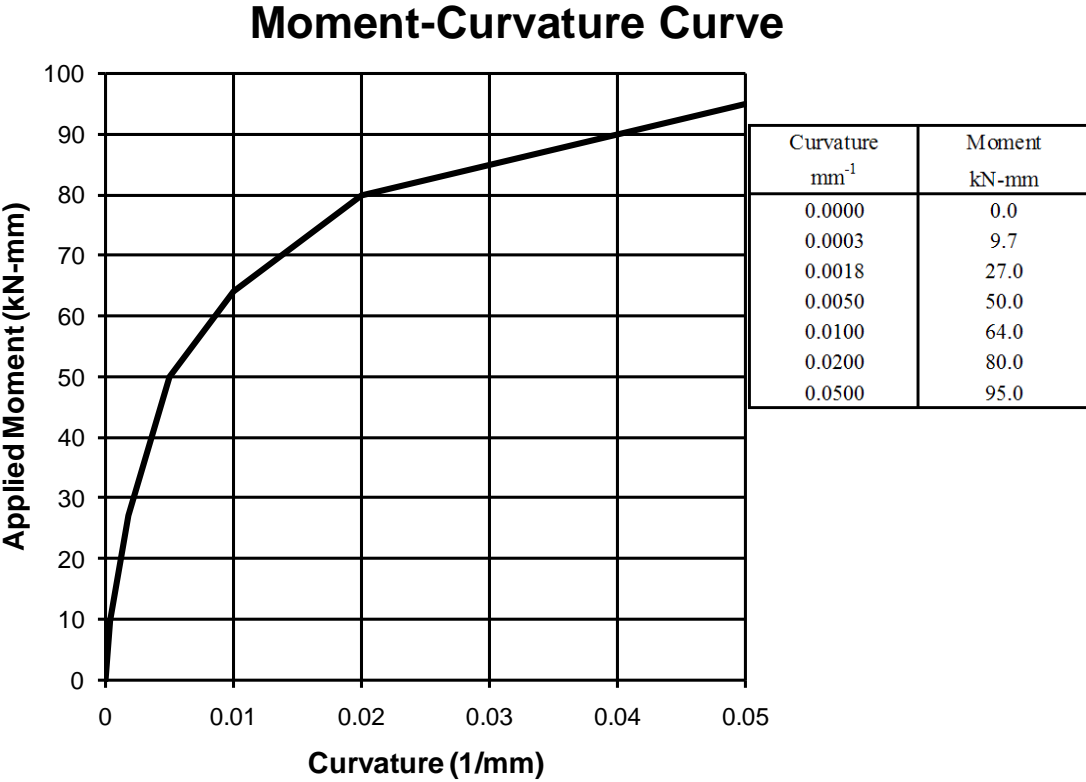


Figure 4. Moment-Curvature Curve (Load Curve No. 2), Proposed Wire Rope Model

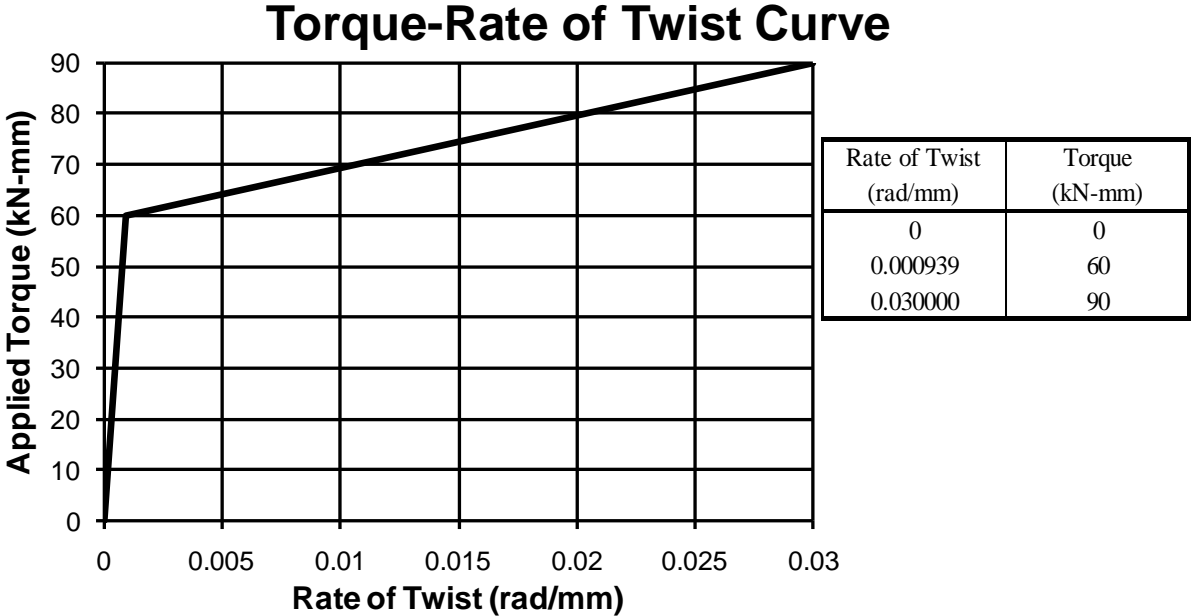


Figure 5. Torque-Rate of Twist Curve (Load Curve No. 3), Proposed Wire Rope Model

5 QUASI-STATIC TENSILE TESTING

5.1 Testing Methodology

Quasi-static tensile tests are conducted on wire rope to determine the breaking strength, modulus of elasticity, and ultimate stretch of wire rope. Ultimately, these results from the quasi-static tensile tests would be used to generate axial force curves for the new wire rope model. Once the tensile behavior of wire rope is determined, dynamic magnification factors may be calculated based on dynamic component testing. Two tensile tests were planned: one for non-prestretched wire rope, and one for prestretched wire rope.

Uniaxial tensile testing requires that both ends of the tested ropes be constrained against rotation and lateral motion. A displacement-controlled boundary condition was applied to end of the wire rope. The rate of wire rope displacement in time was controlled such that strain rate effects would have a negligible influence on the resulting tensile loading of the wire rope.

Due to the inherent difficulty in accurately determining the stress and strain in the cable, two quasi-static tensile tests were prepared, with the first test used to refine testing procedures for the second test. In the first test a non-prestretched cable was to be tested to failure. The non-prestretched wire rope was a rope which had not been loaded since manufacturing.

The first test was successful in generating useful material data. Consequently, it was decided that the second rope should be tested to failure using a prestretched rope in order to observe differences and make comparative judgments. In both tests strain was measured using a known gauge length and was videotaped, while the load was monitored using load cells in the testing equipment. Tensile tests were conducted according to ASTM A 931-96 [33]. The ¾-in. (19-mm) diameter 3x7 wire rope was in compliance with ASTM A 741-98 [34-37].

5.2 Equipment and Test Setup

The tests were configured as follows. Two string pots and one extensometer were used to measure gauge length displacements during each of the tests. Voltmeters displayed the output voltage from the string pots throughout the test, and were videotaped for data logging. The extensometer voltage output was recorded and processed by a MATS II NuVision processor. Load monitoring was measured by the onboard load cell of the SATEC 440-kip (1,958-kN) testing machine, and recorded by the SATEC computer. Data was exported and processed for further analysis.

The specified minimum breaking strength for wire rope used in cable guardrail is 25,000 lb (111.2 kN) [34]. However, tensile tests conducted on $\frac{3}{4}$ -in. (19-mm) diameter 3x7 wire rope indicated a breaking load closer to 40,000 lb (178 kN). Catastrophic release of this load could lead to test equipment damage and hazard to experimenters. Therefore, a safe radius was employed around the machine, and the load frame was secured using $\frac{1}{2}$ -in. (13-mm) diameter polyethylene rope with constraint bolts to ensure the load frame remained in place following rope fracture. In addition, measurement equipment was wrapped with polystyrene blocks to prevent damage if the rope should fracture suddenly. Tensile test setup photos are shown in Figure 6.

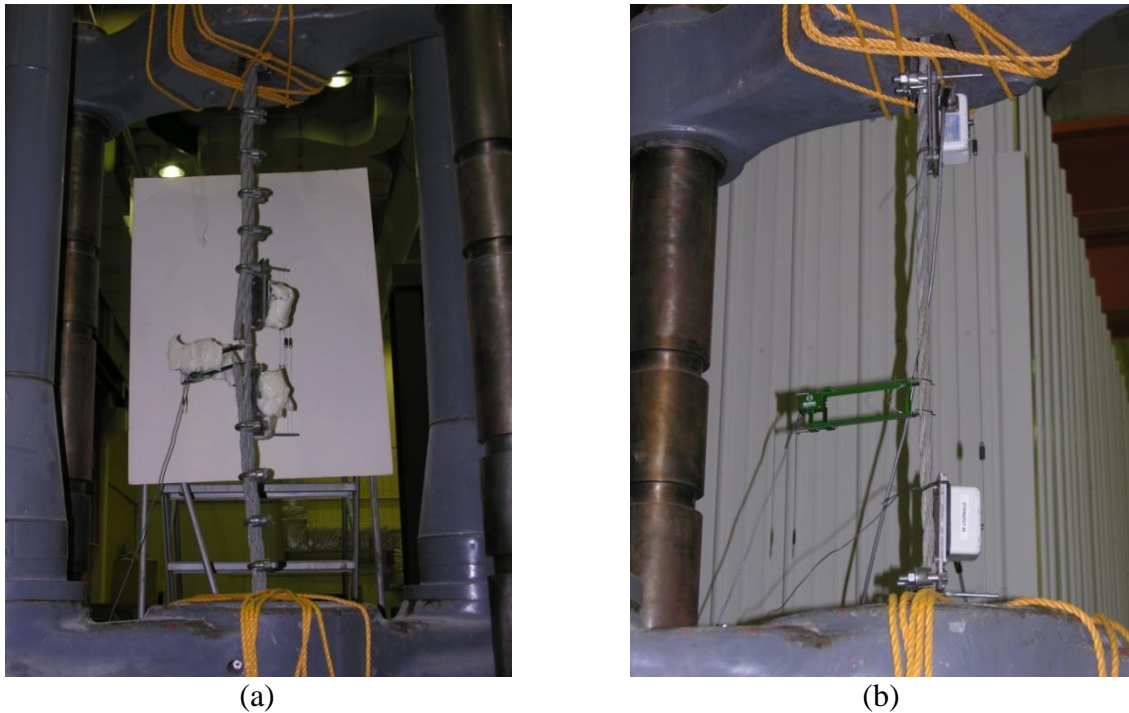


Figure 6. Quasi-Static Tensile Test Setup (a) Non-Prestretched (b) Prestretched

5.2.1 Extensometers

The extensometer was mounted on the wire rope at a gauge length of 1.9545 ± 0.0005 in. (49.644 ± 0.013 mm) and 1.9975 in. ± 0.0005 in. (50.737 mm ± 0.013 mm) for the non-prestretched and prestretched tensile tests, respectively. Since the lay length of the rope was 7.7 in. (196 mm), the extensometer did not measure the stretch of one strand but rather the relative stretch between two different strands. Although the measurement of displacement of the wire rope along a single strand is useful for determining the stretch of individual wires, the lay length of the rope prevented measurement in the direction of the strand lay. Furthermore, the axial stretch, which was measured, was more desirable than the strand stretch.

The extensometers were attached to the wire ropes in the non-prestretched wire rope test using cylindrical blade gauges and rubber bands to apply a small contact force. The string pots were mounted at cable clip locations using U-bolts. Clamping force applied to the U-bolts in the

non-prestretched wire rope test was higher than the proof load of the bolts. The U-bolt clamping load for the second test was very small, to ensure that the U-bolts would not create a stress concentration.

The extensometers used in the tensile tests were 2.00-in. long (50.8-mm) gauge-length extensometers with a travel of +1.000/-0.200 in. (+25.40/-5.08 mm). The extensometers had a linearity of 0.056%, with an average voltage output of 20.092 mV/in. (0.79102 mV/mm). The actual gauge lengths of the extensometer in the non-prestretched and prestretched tensile tests were 1.9545 in. (49.644 mm) and 1.9975 in. (50.737 mm), respectively. This was determined by averaging three independent measurements of the gauge length using a pair of digital calipers with a precision of 500 μ m. (13 μ m). The excitation voltage to the extensometers was 5 V, with a gain of 20. The extensometer used in the tensile tests is shown in Figure 7.

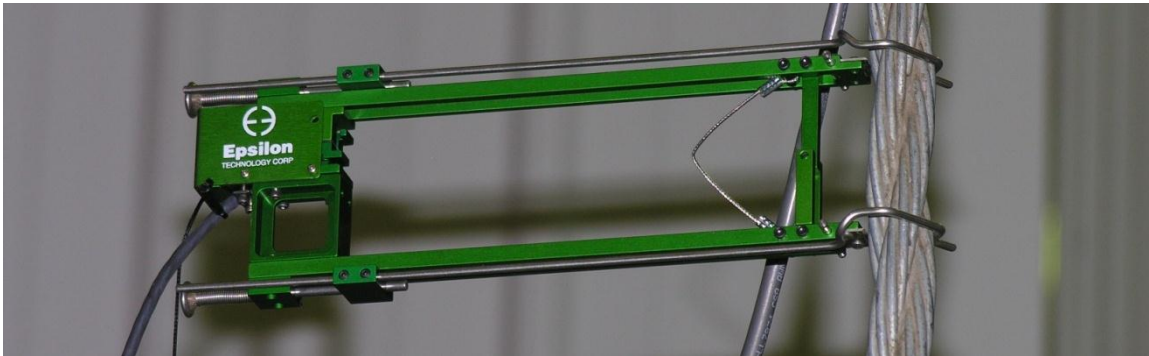


Figure 7. Extensometer Used in Tensile Testing

5.2.2 String Pots

String pots were secured to the wire ropes in both tests. The string pots were made by Unimeasure, Inc. and had gauge lengths of 16 in. (406 mm) and $33\frac{5}{16}$ in. (846.1 mm) for the non-prestretched and prestretched wire ropes, respectively. A pulley system was developed for use in the prestretched test to provide a mechanical measurement advantage to the string pots,

due to the low resolution observed in the non-prestretched wire rope test and prestretching process.

String pot displacements were calculated using the known gauge lengths and recording the voltage change from the extension of the string pot measurement wires. Two string pots were mounted opposed to one another, such that the tensioned measurement wire in one string pot measured the displacement of the second string pot location. Small rubber guides were placed on the outside of the string pot at the tensioned wire outlet to help guide the string from the string pot out from the internal coil so that tension in the wire would result in smooth string pot wire extension. Since the string pot tension, the length of the curve in the string pot string, and the pulley wrap locations were approximately constant, they could be factored out of the resulting displacement as a constant.

String pots were mounted on 1/4-in. (6-mm) thick plates near the leading edge. Two holes for the U-bolt shank were cut near the back end of the string pot. At the rear edge of the plate, a stiff 3/8-in. (10-mm) diameter rod was welded to the plate, and a hole was drilled at the approximate height of the string pot to mount a tension wire. The factor of safety against yielding in the rods was approximately 4.0 based on string pot tension.

Due to the low resolution of the string pots in the non-prestretched wire rope test, the wire mount system was modified for the prestretched test by wrapping the tension wire around the outside of the stiff rods in a pulley fashion, and greasing the wires to reduce friction. The total pulley system consisted of three wrappings, such that the effective gauge length was tripled. Since the deflection of the pulley strings when tensioned remained very nearly constant throughout the loading, this deflection was automatically factored out when relative displacements were calculated. String pot setup is shown in Figure 8.



Figure 8. String Pot Setup and Gauge Length

5.2.3 Wire Rope End Fittings

The wire rope terminations for both non-prestretched and prestretched tensile tests are shown in Figure 9. Two types of wire rope end fittings were used in the non-prestretched and prestretched tests of the wire rope. In the non-prestretched rope test, a thimble termination with clamped U-bolts was used. Use of U-bolts in wire rope terminations is generally not recommended for high-load applications, since the termination is only rated to approximately 80% of the ultimate strength of the wire rope, and U-bolts induce stress concentrations [2,35]. However, the extensometer was mounted more than 10 wire rope diameters from the U-bolt clamps, and using St. Venant's principles, the displacement of the extensometer and load through the wire rope were very nearly equivalent to a single wire rope at the measured location.

The prestretched wire rope termination was fitted with Crosby G417 galvanized closed spelter sockets and Crosby Wirelock socket resin compound. Socketing of the ends of the wire rope were conducted in compliance with Crosby guidelines and widely-accepted socketing procedures [2, 34-35].

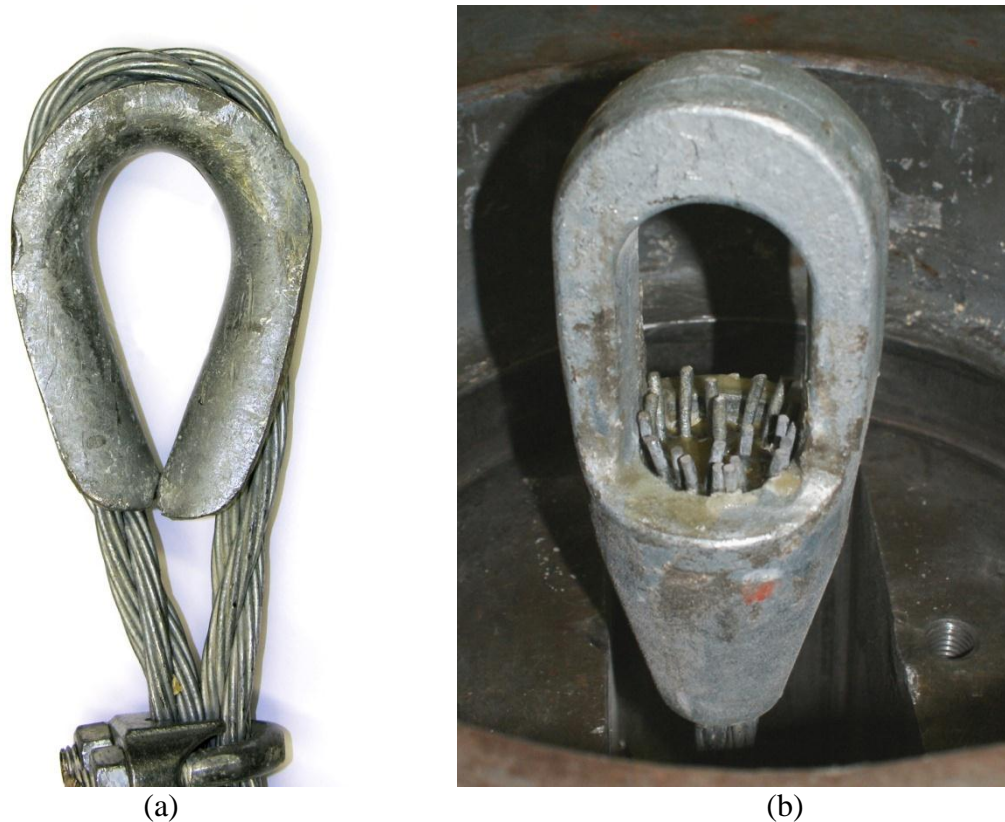


Figure 9. Wire Rope End Terminations (a) Non-Prestretched (b) Prestretched

5.2.4 Voltmeters, Power Supply, and Video Cameras

Three voltmeters were used in both tensile tests. One voltmeter measured the output voltage across the power supply, which provided power for the string pots. This voltmeter served as a calibration for the test to observe any fluctuation in the input voltage which would affect the output voltage of the string pots. The other two voltmeters were used to measure output voltage from the string pots.

Two digital video cameras were also used in both tests. One digital video camera recorded the control station to track the voltage measured from the output of the string pots and power supply, and the other recorded the motion of the wire rope throughout the test. Both digital video cameras had a recording speed of 29.97 frames/sec. The voltmeter, power supply, tracking video camera, and test control station are shown in Figure 10.



Figure 10. Data Acquisition System

5.2.5 Load Frame

A load frame was constructed to support the wire rope in the tensile testing machine, as shown in Figure 11. The load frame consisted of two symmetrical brackets supporting a 1½-in. (38-mm) diameter load bearing pin. The load bearing pin material was unknown at the time of the test but was believed to be at least ASTM A36 steel. The factor of safety in pure shear of the load bearing pin was approximately 3.00. Bending was not considered since the free beam length of the pin was less than ¼ in. (6 mm).

In order to minimize bending stresses imposed in the pin, the brackets were constructed with a pin sleeve flush with the face of the bracket. Two vertical ribs, each ½-in. (13-mm) thick, were welded to a 6 ¼ in. long x 2½ in. wide by ½ in. thick (159 mm x 64 mm by 13 mm) base plate. The pin sleeve consisted of a 2½ in. diameter x 2½ in. long by ¼ in. thick (64 mm x 64 mm x 6 mm) pipe, and the ribs were 5¾ in. long x 3½ in. tall by ½ in. thick (146 mm x 89 mm x

13 mm), with a $\frac{7}{8}$ -in. x $3\frac{1}{2}$ -in. (22-mm x 89-mm) chamfer on either side. Drawings are shown in Figures 12 through 14.

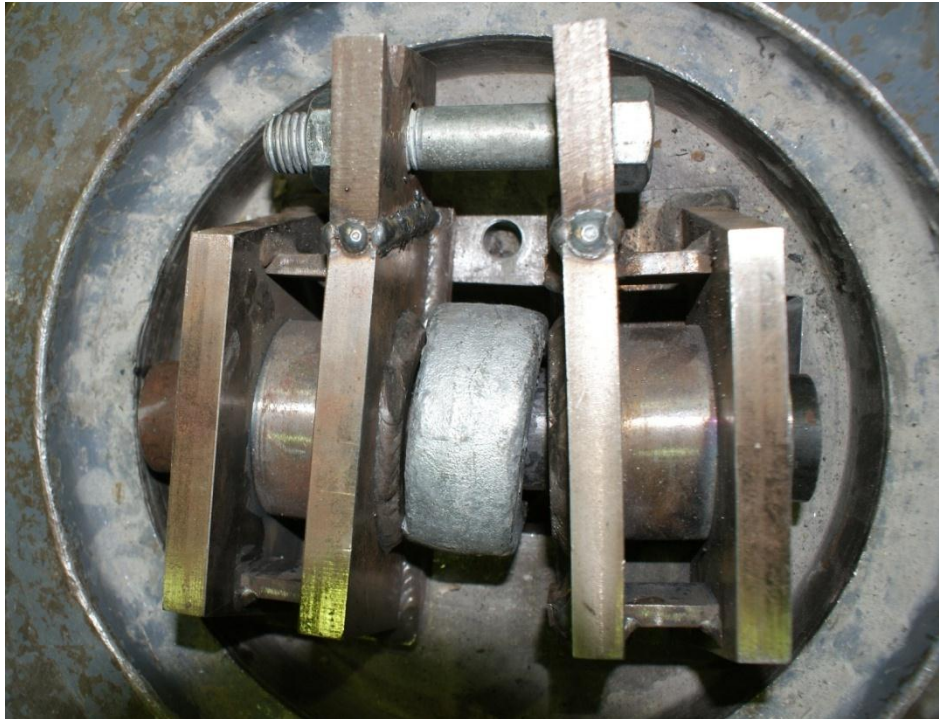
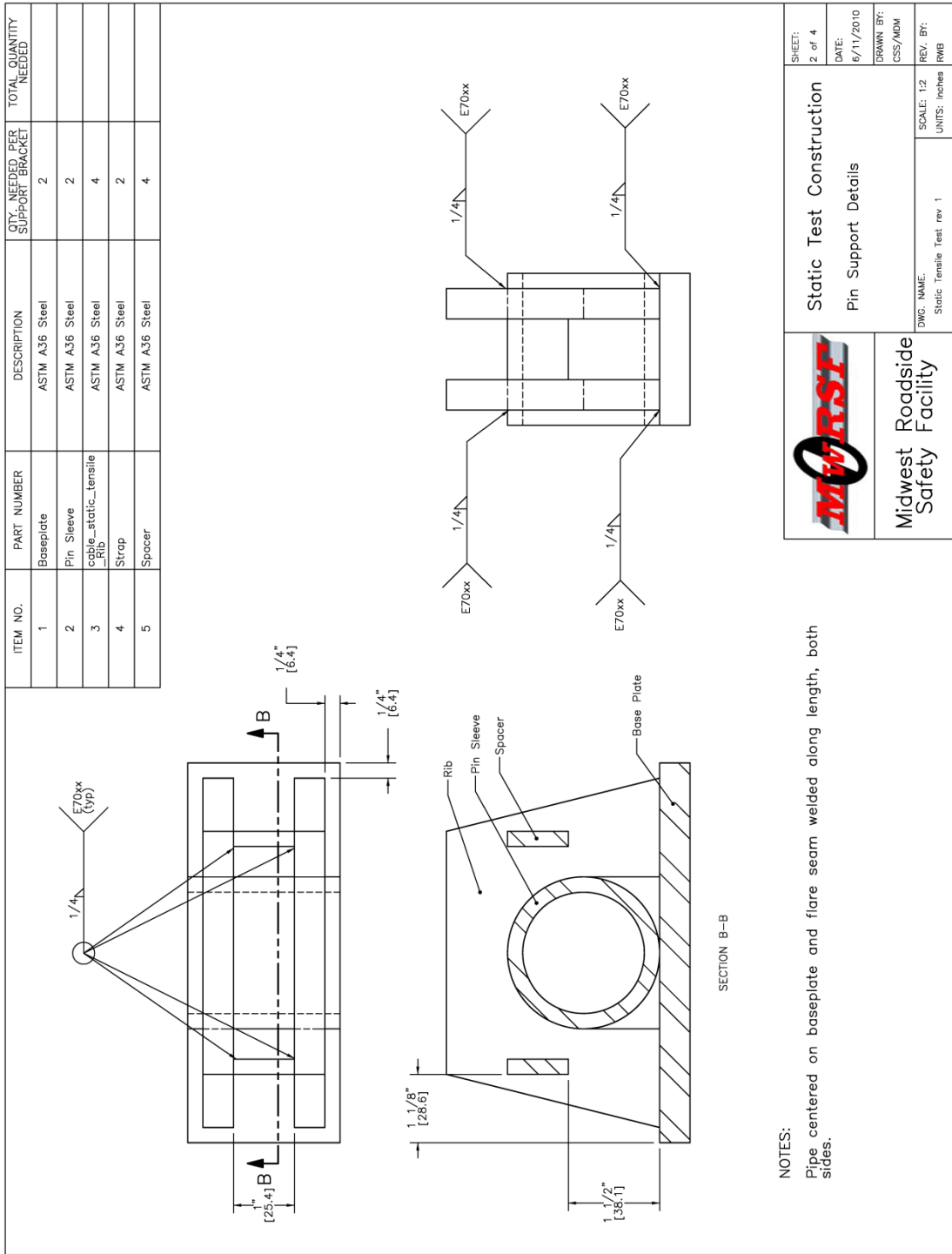


Figure 11. Load Frame Assembly After Prestretched Wire Rope Test

The load frames were used on the top and bottom of the tensile testing machine to secure the ends of the wire ropes. The load frame was tied to the tensile testing machine with $\frac{1}{2}$ -in. (13-mm) diameter polyester rope and a security bolt, to prevent the load brackets from disengaging from the machine and becoming projectiles after the wire rope fractured.




	Static Test Construction Pin Support Details	SHEET: 2 of 4 DATE: 6/11/2010 DRAWN BY: CSS/MDM REV. BY: RMB
	Midwest Roadside Safety Facility	DWG. NAME: Static Tensile Test rev 1 SCALE: 1:2 UNITS: inches

Figure 12. Pin Support Bracket Details

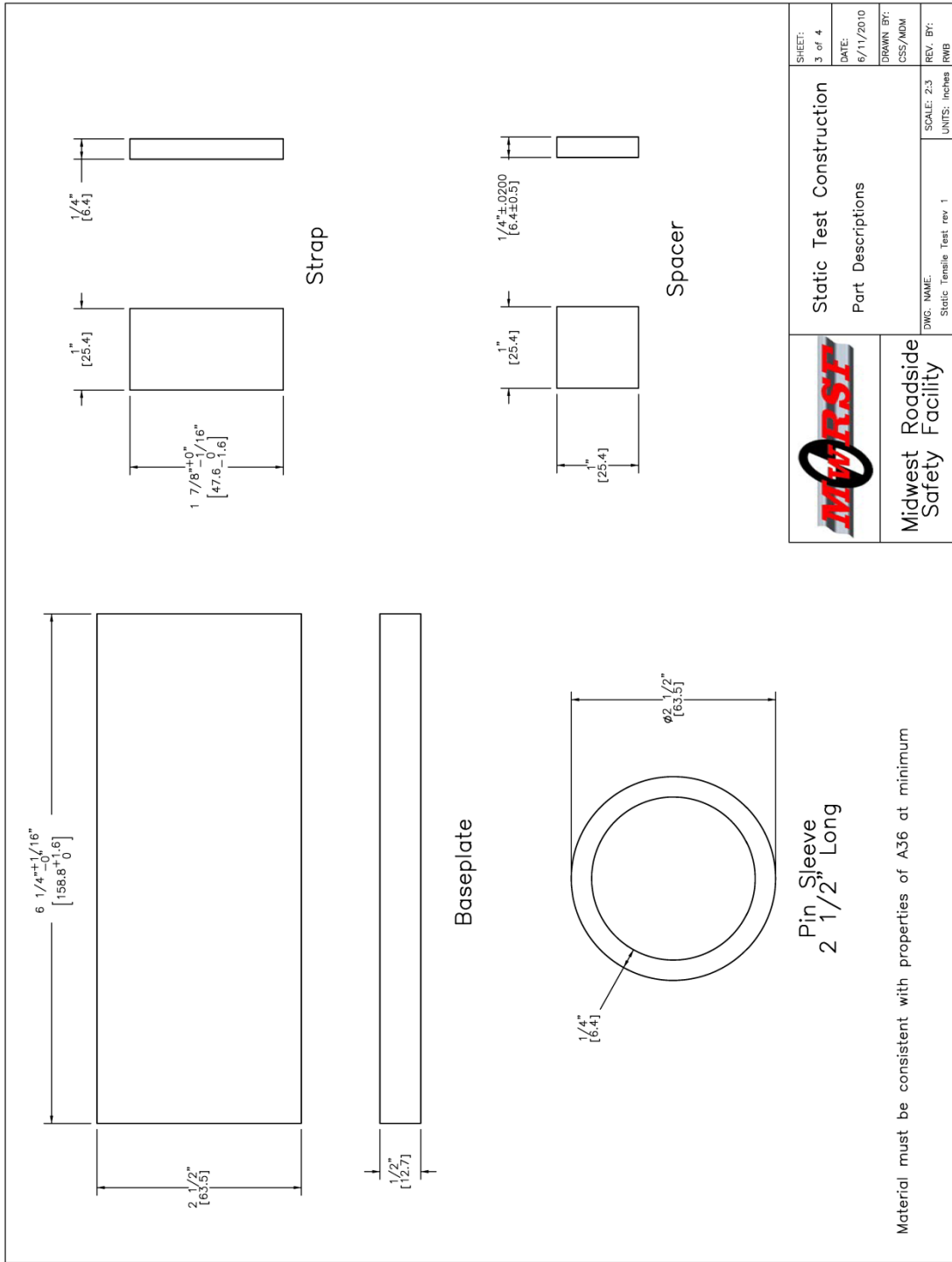


Figure 13. Part Details, Quasi-Static Tensile Tests

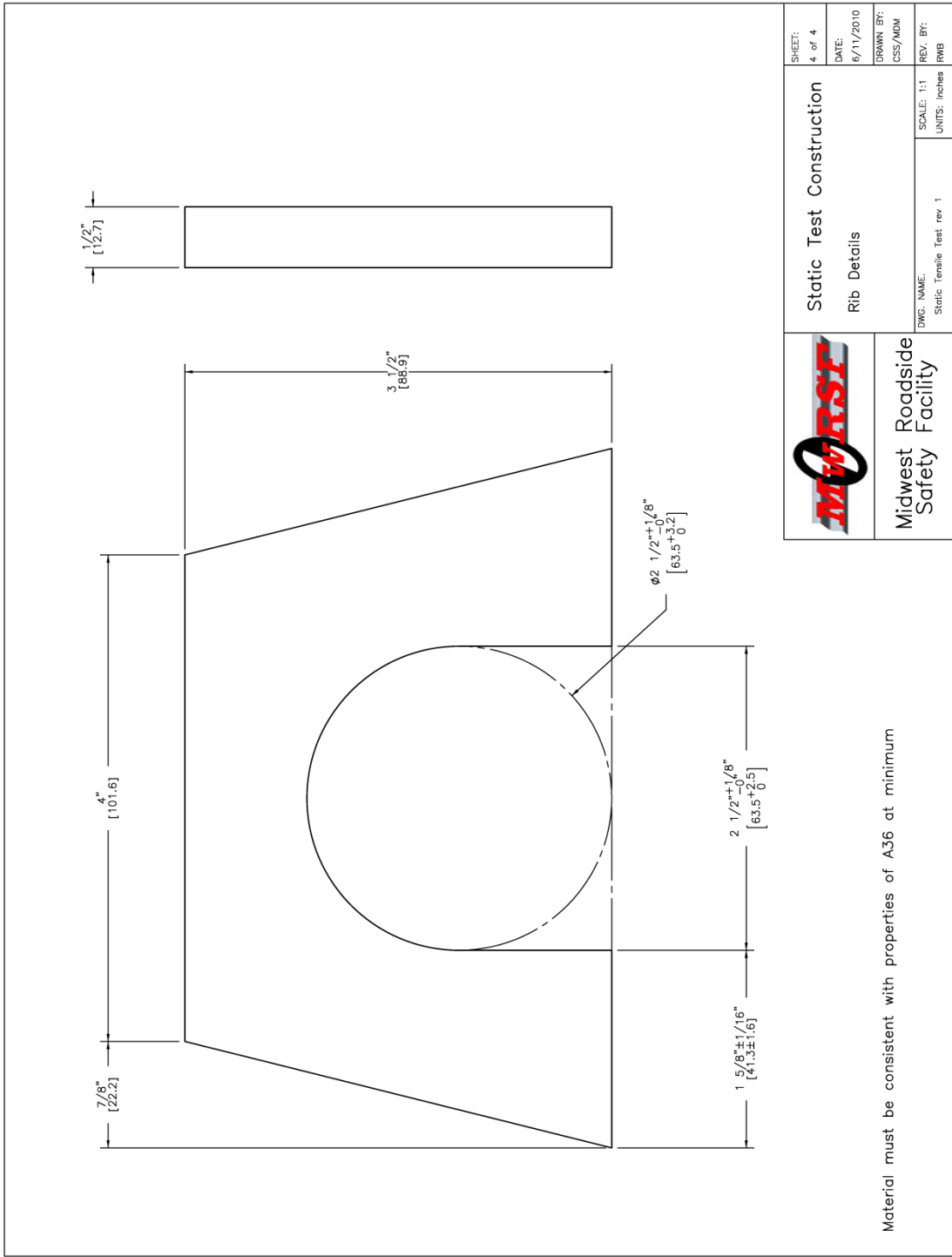


Figure 14. Rib Details, Quasi-Static Tensile Test

5.3 Prestretching

The wire rope in the prestretched tensile test was prestretched using a method adapted from recommendations provided by the Army Corps of Engineers, as well as federal guidelines [35-37]. Using a nominal breaking load of 39,000 lb (173 kN) for ¾-in. (19-mm) diameter 3x7 wire rope, the rope was loaded up to 40 percent of the nominal breaking load at 15,500 lb (68.9 kN), held for 5 minutes, then unloaded to 5,000 lb (22.2 kN). This was conducted three times, and each phase was timed for 5 minute increments.

5.4 Test Results

Two tensile tests were conducted, one on a non-prestretched wire rope and the other on a prestretched wire rope. Load and strain histories were plotted and the voltage results from the string pots were filtered and analyzed. These results were used to build force-strain plots for use in LS-DYNA.

5.4.1 Raw Data

Photos of the fracture location of the non-prestretched tensile test is shown in Figure 15. The raw force and elongation data extracted from the non-prestretched tensile test is shown in Figure 16, and string pot output voltage is shown in Figure 17. An internal conversion in the SATEC MATS II controller converted displacements to strain, based on the internal monitoring of extensometer output voltage and the input gauge length of the extensometer.

The displacement curve of the extensometer did not increase linearly in time, as was expected. Instead, the extensometer displacement curve was almost parabolic, curving upward near the time that the force curve tapered off. Though a constant strain rate was specified throughout the test, the machine was unable to maintain a uniform, constant strain rate due to

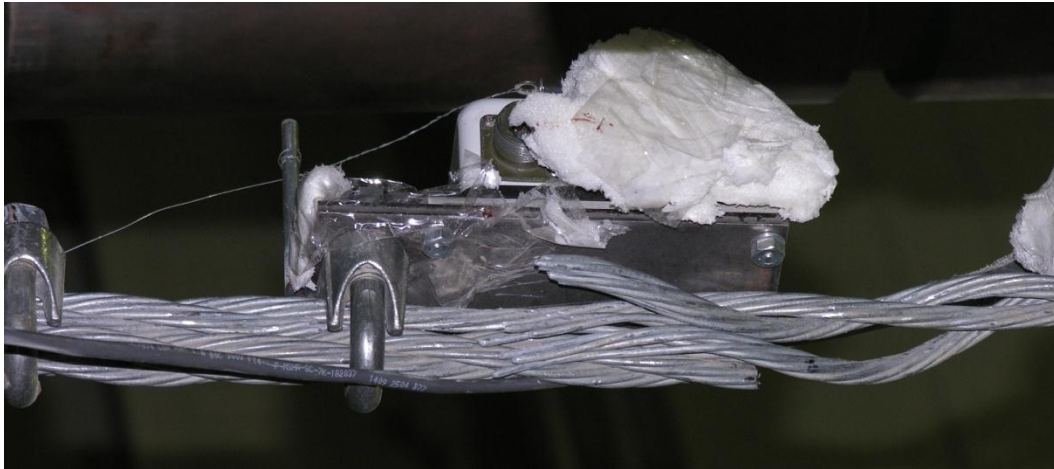


Figure 15. Fracture Location at String Pot U-bolt, Non-Prestretched Wire Rope Test

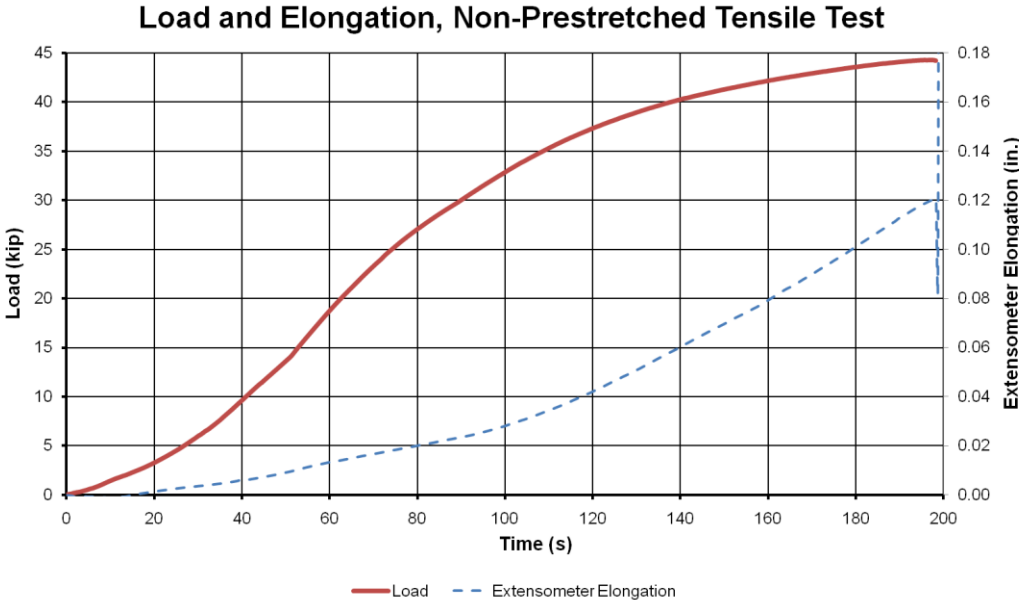


Figure 16. Load and Elongation, Non-Prestretched Tensile Test

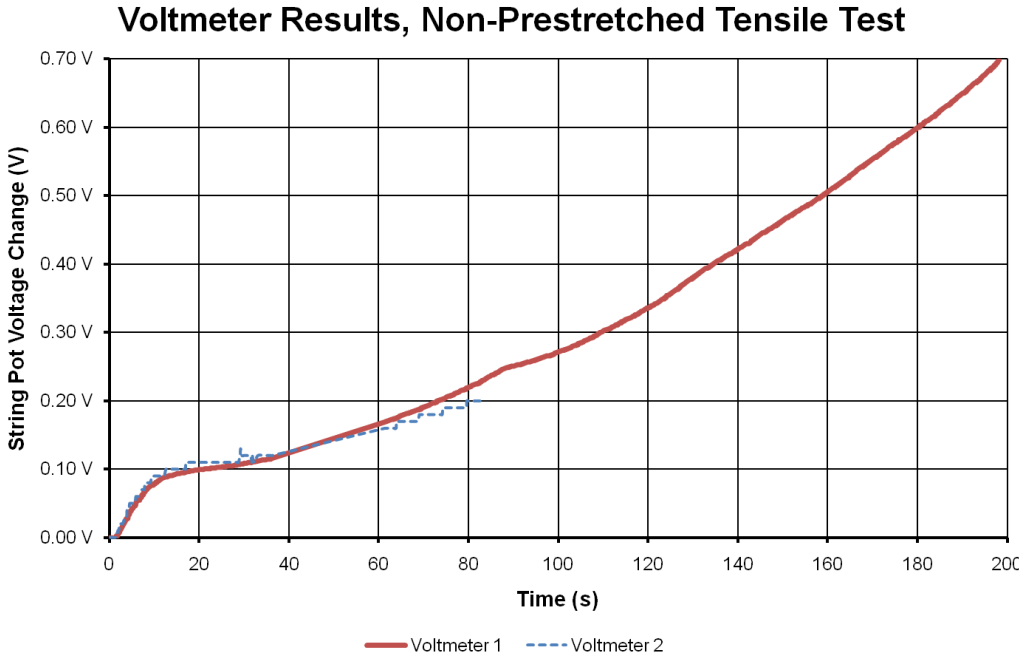


Figure 17. String Pot Output Voltage, Non-Prestretched Tensile Test

the changes in load transferred by the wire rope. Though the duration of the non-prestretched tensile test was relatively brief, the strain rate was not believed to affect tensile test results.

Wire rope tensile load vs. prestretching strain results are shown in Figure 18. The load was ramped from a 5,000-lb (22.2 kN) holding level to a nominal maximum of 15,500 lb (68.9 kN) based on prestretching to a nominal of 40% of the expected breaking load.

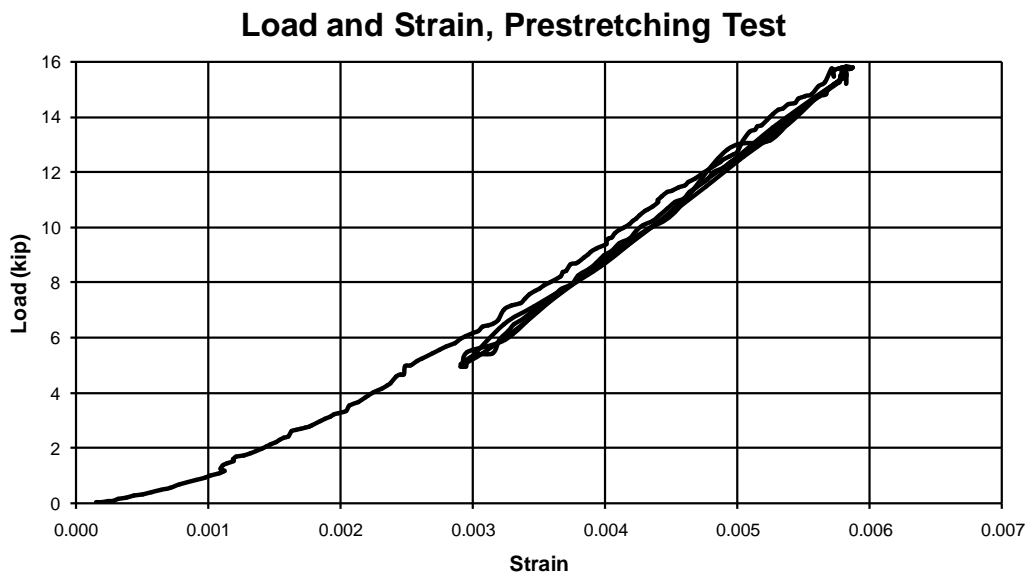


Figure 18. Prestretching Test Load and Extensometer Prestretching Strain

String pot, extensometer, and load cell results were tracked in time using captured video of the results screen. The string pot data was analyzed, and the results noted. Low resolution of the string pot was noted in the test, which led to inconsistent results. By contrast, the extensometer data provided useful evaluation tools for considering the prestretching of the wire rope.

Shortly after conducting the prestretching tensile test, a quasi-static test on the prestretched wire rope was conducted. The fracture location of the prestretched wire rope is shown in Figures 19 and 20. Load and displacement recorded during the test are shown in

Figures 21 and 22. The average strain rate throughout the test was $1.67(10^{-5})$ per minute and this caused the test to be approximately two hours long.

The prestretching test was stopped and restarted at a much higher load rate above a tensile load of 45 kip (200 kN) because time constraints on the use of test equipment in the lab did not allow for the continuation of the test. The strain rate was increased to approximately 0.01 per minute to determine the breaking load of the wire rope, but the strain and displacement data were not considered valid for the remainder of the test.

5.4.2 Processed Tensile Test Data

5.4.2.1 Force vs. Strain Plots

Displacements of the string pots and extensometers were converted to engineering strains to evaluate strain vs. tensile force in the wire ropes. The engineering strains are determined via

$$\epsilon = \frac{\Delta l}{l_0} \quad [2]$$

for Δl the change in the measured gauge length of the device and l the initial gauge length. The engineering strains were converted to true strains using the relation

$$\epsilon_T = \ln(1 + \epsilon) \quad [3]$$

Forces plotted against the calculated engineering strain of both the extensometer and string pots in the non-prestretched tensile test are shown in Figure 23. The curves show some similar attributes, but near the beginning of the test non-linear force-deflection relationship is evident. The extensometer strain followed a negative strain-force relationship until -0.00054, then began to increase. Thereafter, the force and strain became fairly linear until approximately 28,000 lb (124.6 kN). Following this point, the wire rope exhibited plastic behavior until fracture at 0.0618 strain and 44,146 lb (196.4 kN). It should be noted that data from only one of the string pots was captured during the test.

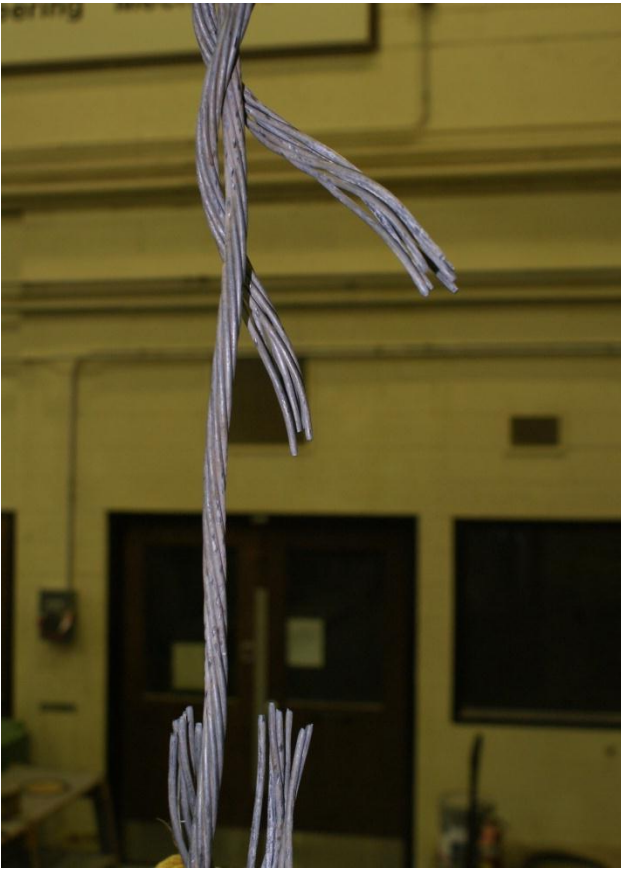


Figure 19. Fracture Location in Center of Wire Rope, Prestretched Tensile Test

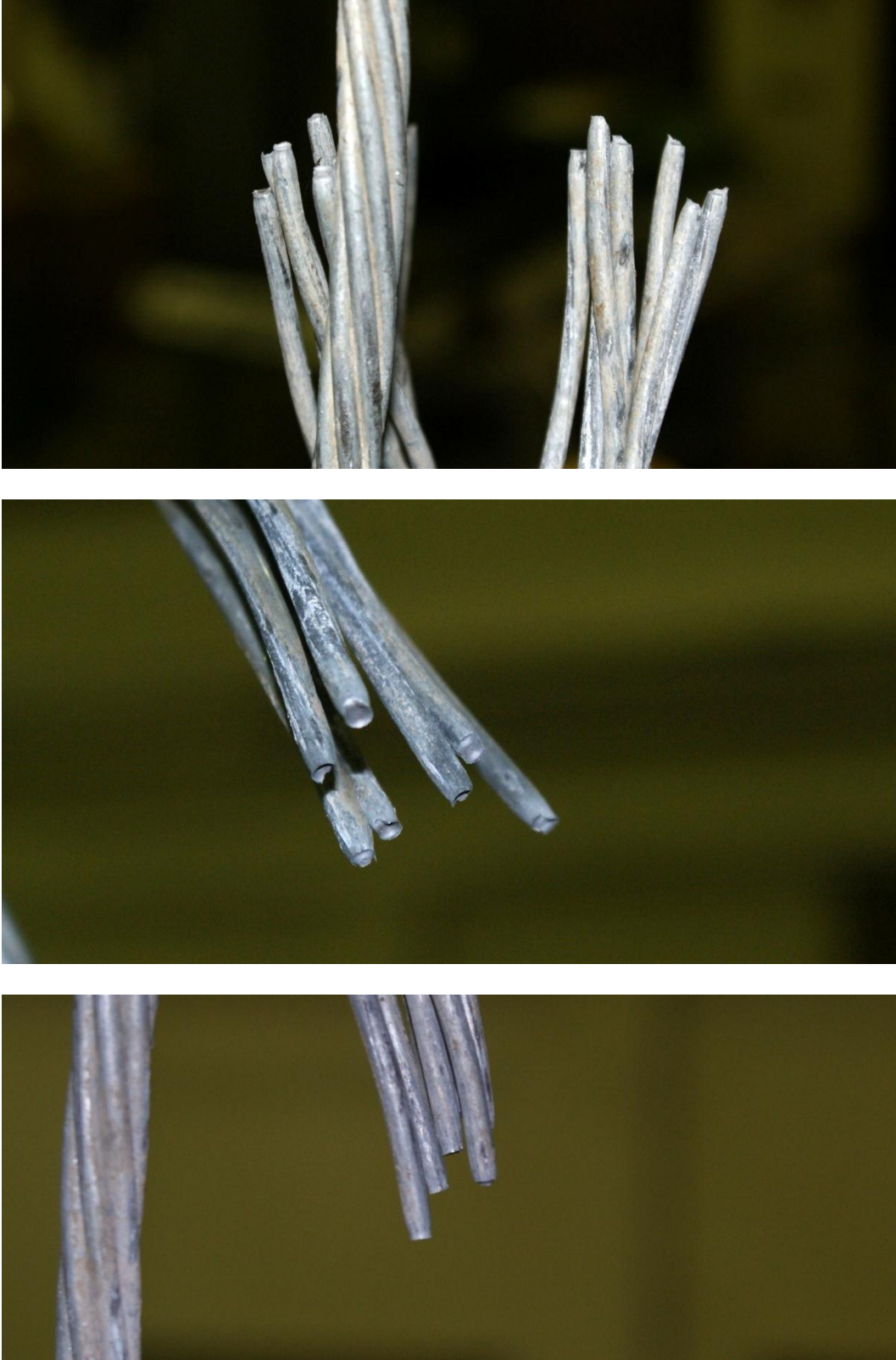


Figure 20. Ductile Fracture Surfaces with Necking, Prestretched Wire Rope

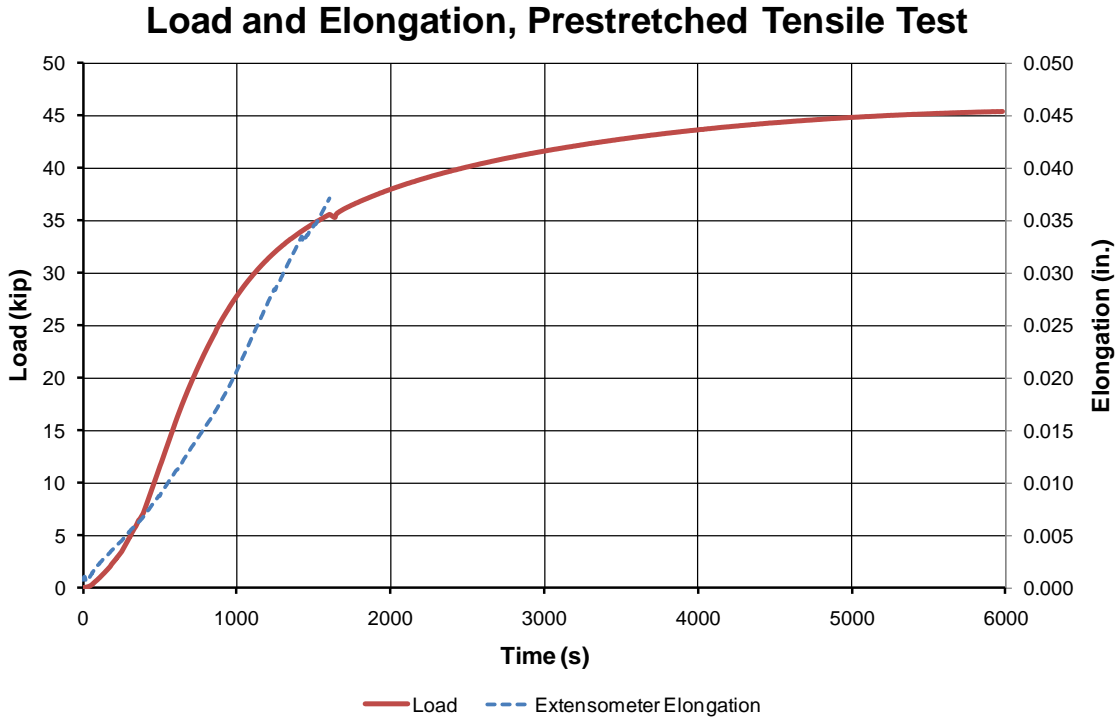


Figure 21. Load and Elongation, Prestretched Tensile Test

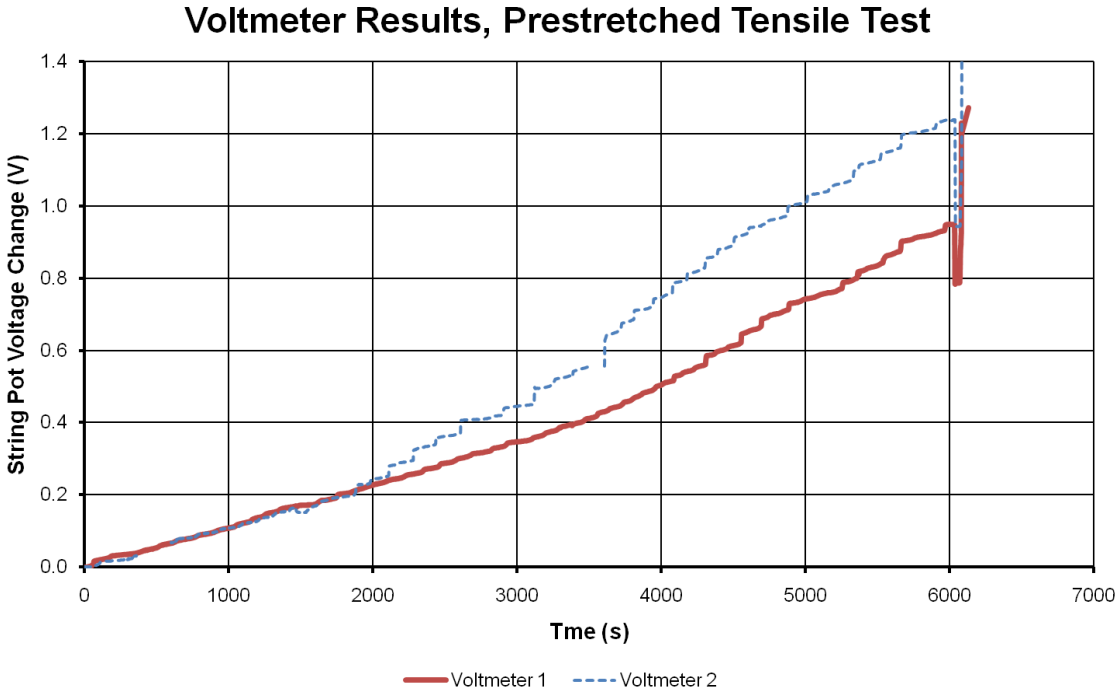


Figure 22. String Pot Output Voltage, Prestretched Tensile Test

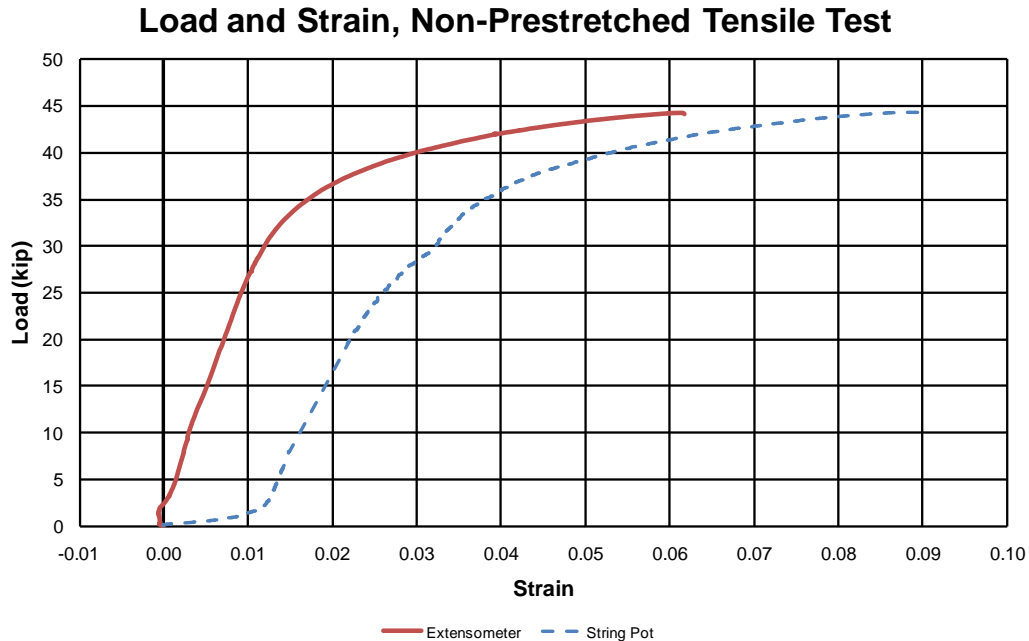


Figure 23. Load and Engineering Strain, Non-Prestretched Tensile Test

The string pots were configured in the prestretched tensile test by wrapping the output wires from the string pots around a measurement post to form a pulley system with a 3-times mechanical advantage. The gauge length between the measurement sticks was $33 \frac{5}{16}$ -in. (846-mm) long, but the output of the string pots was not located at the exact location of the first measurement stick. This affects the true gauge length of the string pot. Furthermore, the sensitivity of the string pots of 0.04848 V/V/in. (0.00191 V/V/mm) was modified due to the geometry of the tested wire rope. Small non-linearities due to very small angular offsets of the string pot mounts, curvature of the string pot measurement wires around the pulley supports, and a small initial curvature of the tested wire rope contributed to accumulation of error, which was amplified by the mechanical advantage of 3.0. As a result, the true string pot sensitivity could not be analytically, defensibly determined.

Strain was also calculated in the prestretched wire rope. In both string pot and extensometer strain measurements, an initial non-linear stretch occurred in the wire rope.

However, the strain in the string pot was not as clearly defined as in the extensometer. Due to the small angular offset of the string pot mounts on the prestretched wire rope, a very small initial curvature in the measured length of the rope, and the mechanical advantage gained using a pulley-type system, the calibration factor on the string pot mount varied from the nominal calibration factor of 0.04848 V/V/in. (0.00191 V/V/mm) for measuring relative displacement between the mounts.

The effective calibration factor was calculated by generating the predicted engineering strain data using the nominal gauge length divided by the mechanical advantage and comparing it to the engineering strain obtained using the extensometer. A deviation factor was multiplied to the effective string pot sensitivity factor such that a best-fit was obtained between 0.010 and 0.018 strain. Using the modified resulting strain values, the strain was multiplied by the nominal gauge length to obtain effective string pot displacement. Strain calibration efforts are shown in Figure 24.

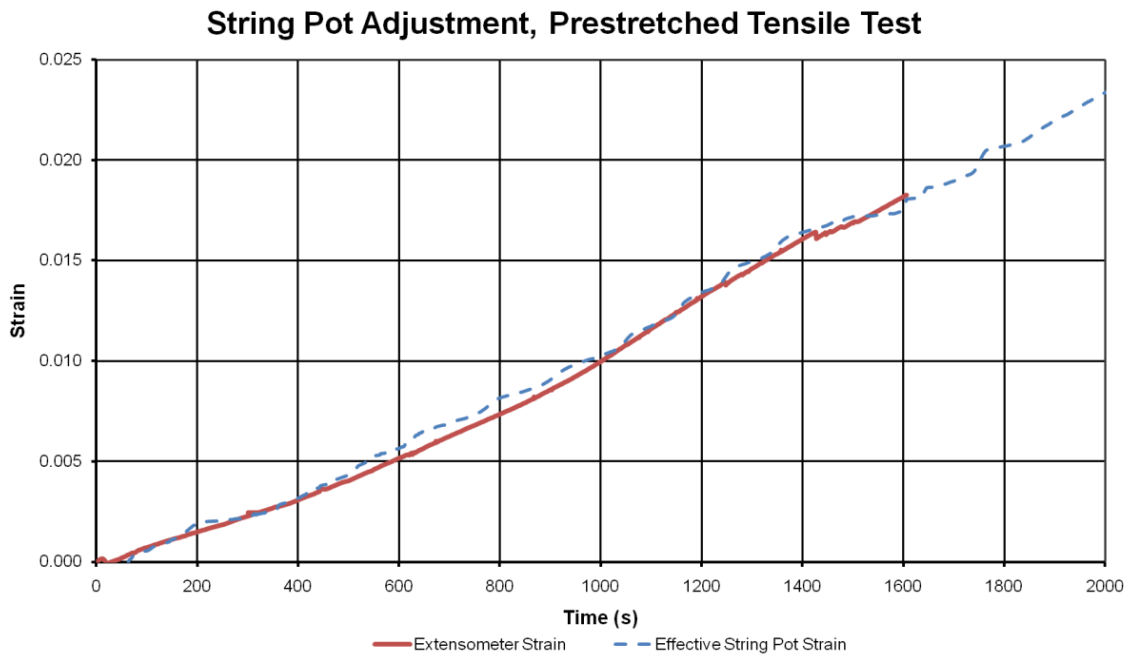


Figure 24. Correlated String Pot Strain and Extensometer Data, Prestretched Tensile Test

Prestretched wire rope load and strain plots for both the extensometer and string pots are shown in Figure 25. To protect the extensometer in the prestretched test, the extensometer was removed at a load of approximately 35 kips (156 kN). Though this represented only approximately 1/3 of the strain before fracture, sufficient data was obtained to ensure equivalence between the string pots and extensometer. It should also be noted that the strain data from string pot no. 2 was disregarded, since it was inconsistent and oscillated frequently throughout the test.

Force and Strain, Prestretched Tensile Test

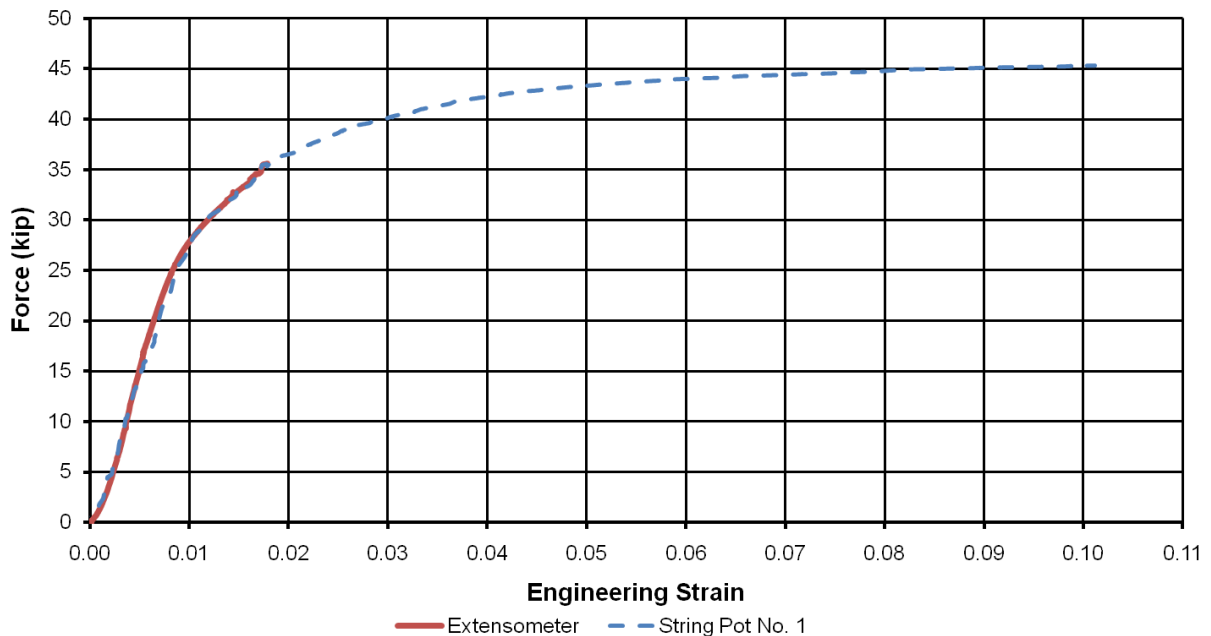


Figure 25. Force and Engineering Strain, Prestretched Tensile Test

5.4.2.2 Engineering Stress vs. Strain Plots

Stresses were also calculated for both the non-prestretched and prestretched tensile tests.

Engineering stress is defined to be:

$$\sigma = \frac{F}{A} \quad [4]$$

Since beam elements assume cross-sectional deformations do not occur, the area remains constant throughout the simulation; therefore, only engineering stresses require consideration.

Cross-sectional areas were estimated by assuming that each wire in the cross-section had a circular shape when cut on the normal plane to the axis of the wire rope. Since 21 wires are used in 3x7 wire rope, and the nominal diameter of the wires is 0.1205 in. (3.061 mm), the resulting approximate area of the wire rope is 0.2395 in.² (154.5 mm²). Engineering stress vs. engineering strain plots for the non-prestretched and prestretched tensile tests are shown in Figures 26 and 27.

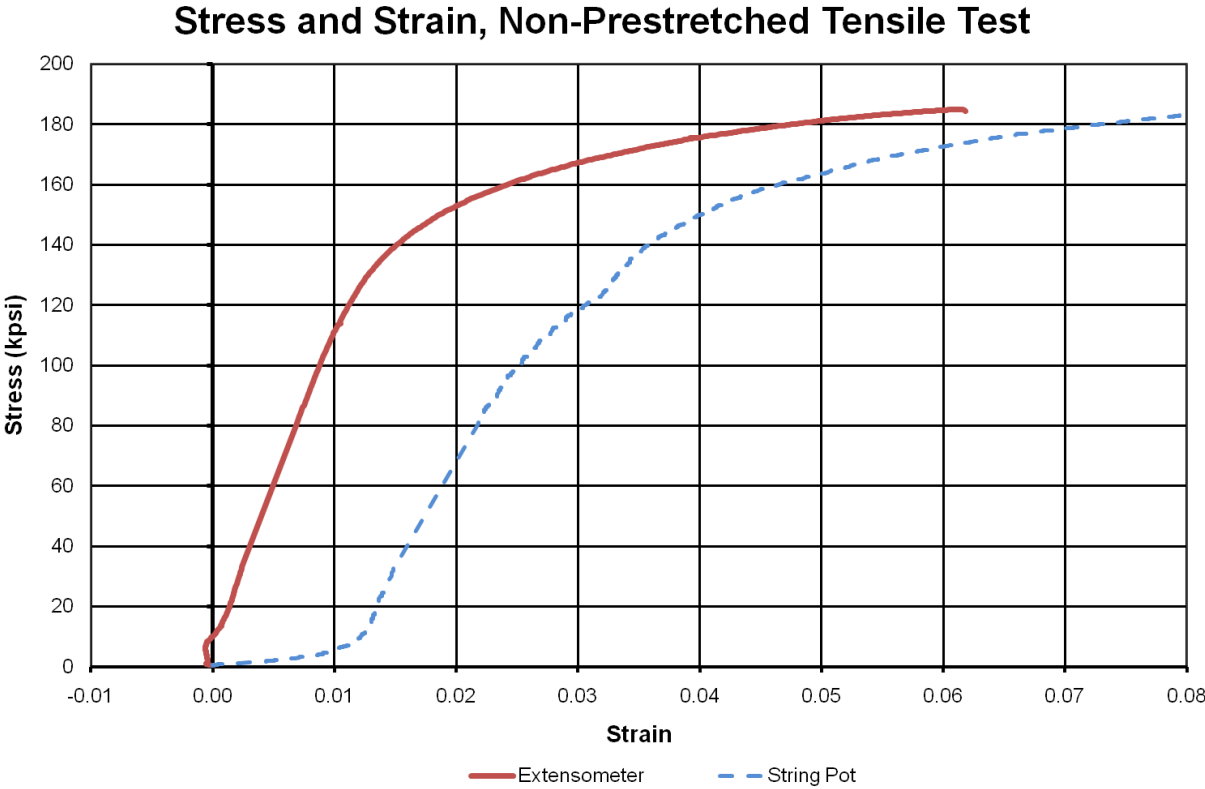


Figure 26. Stress and Strain, Non-Prestretched Tensile Test

Stress and Strain, Prestretched Tensile Test

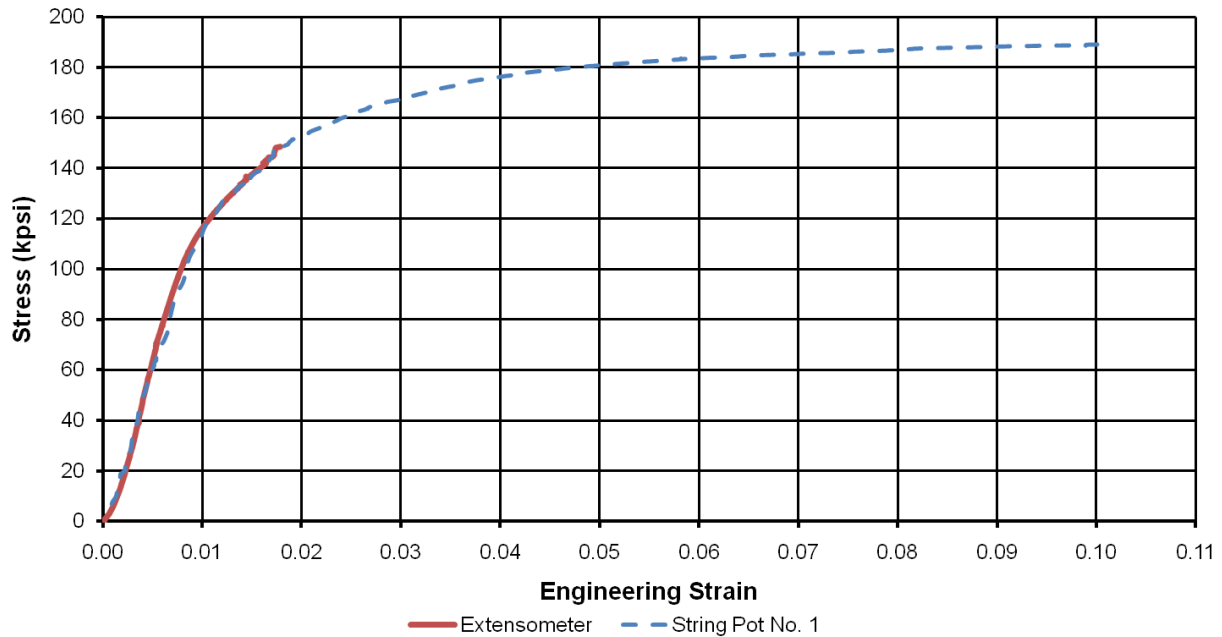


Figure 27. Stress and Strain, Prestretched Tensile Test

5.5 Discussion

Determination of the non-linear initial geometrical strain of the non-prestretched wire rope was difficult because the string pot and extensometer data were not similar until a load of approximately 5,000 lb (22.2 kN). Furthermore, the extensometer predicted negative initial strain, which was physically impossible. Generally, the modulus of elasticity is defined as

$$E = \frac{d\sigma}{d\epsilon} \approx \frac{\Delta\sigma}{\Delta\epsilon} \quad [5]$$

for small values of engineering strain and stress. In the linear region of the stress-strain curve, the modulus of elasticity may be calculated between any two points within the linear region. However, the negative initial strain recorded by the extensometer precluded use of low-force strain data for determination of the modulus of elasticity. Instead, an approximate modulus of elasticity of the non-prestretched wire rope was generated using stress and the strain data

between 17 and 23 kip (75.6 and 102.3 kN). The calculated modulus of elasticity of non-prestretched wire rope was 11.59 Mpsi (79.9 GPa). This effective modulus is lower than the modulus of steels, which is expected since the wires are pulled in a helix and thus greater displacements result from axial loading.

Extensometer and string pot strain measurements for the non-prestretched tensile had substantial differences in recorded displacement below 5 kip (22.2 kN). This is due to several compounding problems using the string pot secured firmly to the wire rope at discrete clamping locations. Since the non-prestretched wire rope used a thimble end termination, twelve $\frac{5}{8}$ -in. (16-mm) diameter U-bolts were used to effectively swage a bent end of the wire rope onto itself. The string pots were secured to the wire rope at the two U-bolts closest to the tested central length of the rope. At these locations, there was a transition in stiffness between two wire ropes pulled in tension and a single wire rope cross-section. The extensometer was placed in the center of the test length, and was not subject to end-condition variations. Using St. Venant's principles, since the extensometer was approximately 10 diameters away from the U-bolt on either side, it would not be affected by variations in the bolted stress conditions.

Though differences were expected between the string pot and extensometer measurements of strain in the wire rope, the very large difference evident at the onset of the test led to concern for predicting any non-linear initial prestretching to remove geometrical stretch. Here, "geometrical stretch" is defined as the initial non-linear strain in a wire rope as it is loaded prior to loading elastically. In this regard, geometrical stretch may be considered as the non-linear part of the initial displacement of the wire rope, which is summed with the initial elastic strain.

Geometrical stretch occurs in wire rope due to constructional tolerances between and within the strands in the wire rope. As the wire rope is loaded, the strands are pulled tight and the load is distributed across the wires in the strand, allowing relative displacement of individual wires to occur. Further, due to the helical winding of the wires within strands, axial loading produces an unwinding effect in the wire rope. As a result of the wire rope's tendency to unwind, the rope is torsionally loaded when it is stretched, producing twisting along the length of the rope. The extensional-torsional coupling which occurs in wire rope is noted by Rochinha and Mattos [3].

The two string pots and the extensometer were mounted at nearly the same locations on opposite positions around the wire rope, as shown in Figure 28. The wire rope had an initial curvature which led to a slight convex bending displacement on the side of the extensometer. This is likely the cause of the initial negative strain of the extensometer; as the wire rope was straightened, the reduction in gauge length of the extensometer due to the straightening of the curvature was greater than the increase in strain as a result of the applied loading. It is possible that a very small degree of slippage occurred at the razor edges of the extensometer due to the odd geometry of the wire rope. Since wire rope grips were not available at the time of the test, a cylindrical grip was used and this led to difficulty in securely attaching the grips.

Likewise, the string pots were subject to several problems at the onset of the test: (1) the string pots were mounted on the concave side of the curvature of the wire rope, leading to artificial increases in strain; (2) very small grip-slippage occurred at the U-bolt locations due to shifting loads and increasing loads in the free end of the wire rope; and (3) sensitivity of the string pots was insufficient to accurately capture the displacement over the very low gauge length.

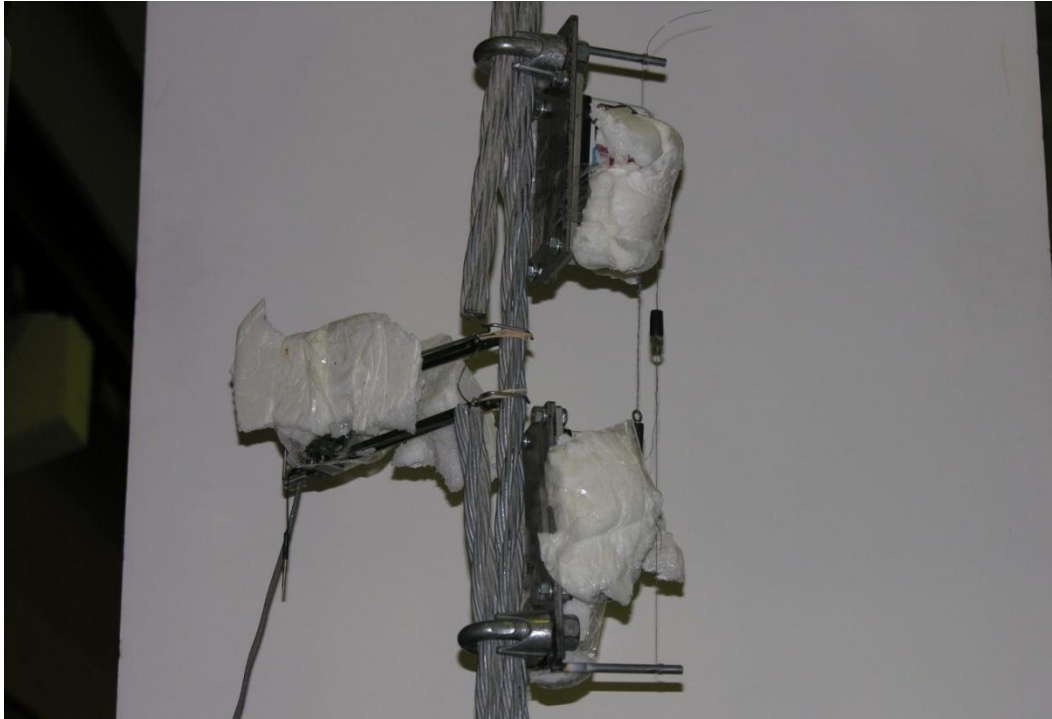


Figure 28. String Pot and Extensometer Configuration, Non-Prestretched Tensile Test

An estimate of the initial curvature of the wire rope was attempted using digital video. After attempting measurement of the wire rope, a radius of curvature of greater than 15 ft (4.6 m) was measured; however, the camera location was not perpendicular to the curve of the wire rope. Based on a radius of curvature of 15 ft (4.6 m), the difference in the length of a straight wire rope and a curved wire rope at the tested location was approximately 0.05%, which was similar to the offset displacement predicted by the string pots. Therefore, the curvature was believed to be strongly related to the variation of low-load strain data.

Nonetheless, the non-linear geometrical stretch was still present in the onset of the non-prestretched wire rope. Though the extent of the non-linearity was not known, it was believed that the non-linearity observed in the prestretched tensile test was likely indicative of the non-linearity in the non-prestretched tensile test.

It should be noted that the clamped load on the wire rope introduced a biaxial state of stress, with compression orthogonal to the axis of the wire rope and tension in the longitudinal axis. Biaxial stress in tension and compression increases strain in the tensile direction more than if the surface were loaded in uniaxial stress. Using octahedral shear stress yield criteria, the material must have yielded much sooner in the clamped region than the tested region, and larger plastic strains would have resulted at fracture [38]. This increased the measured displacement artificially. Therefore, the string pot displacements, and thus string pot strain measurements, were determined to be inaccurate for the non-prestretched tensile test.

To address concerns that the non-linear geometrical stretch would affect the unloaded wire ropes tested in dynamic component tests, a tensile force-strain curve was generated. This simulation implemented the non-prestretched wire rope modulus of elasticity, non-linear initial geometrical strain at low loads, and included an option for an unloading modulus of elasticity in the event that the wire rope unloaded along a different slope than the modulus of elasticity. Since the geometrical stretch, or non-linear change in force per change in strain, was not captured well in the non-prestretched tensile test, this region was approximated from the prestretched tensile test non-linear geometrical strain, and was believed to be representative of both types of wire rope. Extensometer strain and force at loads below 2,000 lb (8.9 kN) from the prestretched tensile test were applied to the non-prestretched tensile curve to simulate the first 2,000 lb (8.9 kN) of the non-prestretched tensile test.

Though the non-linear geometrical stretch observed in the prestretched tensile test was used as an estimate of the geometrical stretch in the non-prestretched tensile curve, this non-linear region was *not* included in the recommended load curve of a prestretched wire rope. If prestretched wire rope is used in low-initial tension applications, much of the prestretch will be

lost and the rope will again act like a non-prestretched wire rope. If the tension is above 900 lb (4.0 kN) in the prestretched wire rope, the total geometrical stretch contribution is only 0.0145%, which is very small in comparison with other numerical noise and material properties of the wire ropes. Therefore, inclusion of the non-linear geometrical stretch in the prestretched wire rope tensile curve would be superfluous and could be non-physical.

It is believed that the non-prestretched wire rope used in the tests and cable guardrail systems tested at MwRSF was initially prestretched by the manufacturer. However, "prestretch" was lost due to thermal cycling, winding on the roll, and rope vibrations all of which allowed wires to separate and develop inter-wire clearances.

To eliminate the geometrical stretch and approximate the prestretched wire rope as initially elastic, a stress-based modulus of elasticity was obtained by selecting several points in the linear region of the force-strain diagram. The variation in stress per change in strain was calculated, and the prestretched wire rope was determined to have a modulus of elasticity of approximately 16.9 Mpsi (116.5 GPa), for a force loading rate of 4,040 kip/unit strain (17,970 kN/unit strain).

Finally, it should be noted that all cable guardrail systems use a rope that is initially pretensioned. The pretension in the rope is greater than 900 lb (4.0 kN) at most temperatures, and in high-tension systems the pretension is greater than 3,000 lb (13.3 kN) at most temperatures. This pretension can cause a wire rope to become "prestretched" in service, increasing its stiffness. Though it is nearly impossible to visually determine whether a rope has been sufficiently stretched to transition from non-prestretched wire rope to a prestretched condition, engineering experience of the wire rope time in service, pretension, and number of tensioning cycles, will provide an estimate of the tensile curve that will be appropriate.

Following the conclusion of testing and evaluation of the wire rope in this study, it was observed that the non-prestretched wire rope was in fact wire rope which had previously been prestretched, but due to coiling on the roll, thermal cycling, and internal vibrations, the wire rope had lost the prestretched benefit. This result is important because even rope which is field-recommended as prestretched may not be prestretched prior to installation due to environmental factors. However, rope which is not prestretched by the manufacturer may also exhibit more of the geometrical strain observed in tensile testing.

In addition, during full-scale test validation, it was observed that the contact area of the wire rope was not accurate when the cross-sectional area was defined with the actual area of the wire rope—that is, 0.2395 in.² (154.5 mm²). The contact surface is determined by creating an equivalent pipe with a diameter determined by the cross-sectional area. Thus, in order to obtain the correct outside contact diameter, the area was increased to be equal to the area of a 3/4-in. (19-mm) diameter bar. This required adjustment to both the density and modulus of elasticity in order to maintain the same timestep and mass density. These values are shown in Chapter 4.

Since the plastic strain data for the wire rope is nearly flat after elastic loading, it may be possible to simulate a wire rope which transitions from non-prestretched to prestretched stiffness by changing the loading stiffness and matching plasticity data with the two tensile curves. However, this is generally not recommended. When wire rope is prestretched, it rebounds to the prestretched modulus of elasticity; when wire rope is non-prestretched, it has a modulus that is less stiff. Any transitional modulus not obtained from physical testing, along with the appropriate post-yielding stress-strain curve, should be held with suspicion because no intermediate moduli were observed during the prestretching process. Using untested moduli may be non-physical.

Simulations should be evaluated with both the non-prestretched and prestretched wire rope tension curves prior to creating an arbitrary intermediate curve.

Finally, it should be noted that tension-only axial response tests were conducted on the wire rope. Wire rope is rarely placed in compression and as a result, compression data are rarely provided and generally are not important for cable guardrail applications. Nonetheless, when critical compressive loads are transmitted through the wire rope birdcaging occurs, which causes the strands in the wire ropes to separate and kink outward. This condition leads to a loss of integrity in the wire rope, and it generally must be removed from service. To the author's knowledge, birdcaging has never been reported in cable guardrail systems, but if it should ever be noted compressive data on 3x7 wire rope may be necessary to predict this phenomenon.

5.6 Conclusions

Quasi-static tensile tests were conducted on non-prestretched and prestretched wire ropes in order to generate force-strain curves for the proposed wire rope model. Forces and displacements were recorded using load cells, an extensometer, and string pots. The forces and stresses were plotted against strains, and the results were analyzed. It was determined that the non-linear geometrical stretch in non-prestretched wire rope was most closely associated with the non-linear prestretch measured in the prestretched tensile test. Conversely, the non-linear geometrical stretch in the prestretched wire rope is not likely to appear in most prestretched wire rope applications, and the non-linearity was disregarded. The use of string pots was discussed and problems were noted. Rectifications were offered to improve the accuracy of the string pot results. Compressive testing may be necessary in the future if birdcaging is observed in wire rope.

The extensometer tensile curve shown in Figure 23 and the string pot tensile curve shown in Figure 25 were used to validate the simulation results of the quasi-static tension test. This will be discussed in the following section.

6 MODELING WIRE ROPE IN QUASI-STATIC TENSION

6.1 Motivation of Quasi-Static Tensile Test Simulations

The quasi-static tensile tests were simulated to consider a single beam element loaded under stress conditions similar to the tested configuration of wire rope. The quasi-static tensile tests were conducted to ensure that the tensile curves utilized in the wire rope models were reflective of the quasi-static tensile test results.

Simulation modeling of the quasi-static tensile testing was completed in three steps. First, single beam elements measuring the gauge lengths of both the prestretched and non-prestretched tensile tests were created. Material and section properties consistent with the selection of beam element were applied to the model. Then, when material properties of the wire rope were satisfactorily specified, a mesh sensitivity study was conducted to evaluate how varying mesh sizes affect the resulting predicted stress, strain, and displacement of the model. The findings were discussed, and the results tabulated.

6.2 Single Beam Element Simulations

The quasi-static tensile tests were simulated using beam elements to represent the wire rope. Stress and strain curves were used to simulate stress and strain in the type 1 Hughes-Liu beam, and force and strain curves were used to simulate axial forces and strains in the type 2 Belytshcko-Schwer beam.

6.2.1 Non-Prestretched Wire Rope

The type 1 Hughes-Liu beam element was the first model evaluated. The length of the element was set equal to the gauge length measured from the extensometer from the non-prestretched tensile test. Five relatively simple elastic-plastic material models were evaluated with the type 1 element, including piecewise linear plasticity, plastic-kinematic, and elastic

materials defined with failure. The most promising of the simple material models was the piecewise linear plasticity model, since it is widely-used in roadside safety engineering simulations and is relatively simple to implement.

Based on constitutive beam theory, the cross-sectional area of a beam element does not change with loading; therefore, engineering stress was used in the defined stress-strain curve. It was initially uncertain whether or not the engineering strain or true strain should be used with beam elements. However, strains are not intrinsically related to the cross-sectional area of the element, and most material models require true strain input. Simple simulations of the tensile tests using engineering and true strains confirmed that beam elements utilize true strains and engineering stresses.

A type 2 beam element with a length equal to the gauge length of the non-prestretched tensile test was also considered. To determine the cross-sectional properties for use in the *SECTION_BEAM card, the wire rope was assumed to be composed of 21 wires with cross-sections which were circular normal to the plane of the tensile axis. The diameter of the wires was measured with a pair of digital calipers with a sensitivity of 0.0005 in. (0.013 mm), and the nominal diameter was determined to be 0.1205 in. \pm 0.0015 in. (3.06 mm \pm 0.0038 mm). This led to an approximate cross-sectional area of 0.2395 in.² (154.5 mm²). Area moments of inertia were calculated based on three strands of 7 circular wires each, and were further approximated by assuming that plane cross-sections remain planar in bending. This traditional method for estimating the second moment of inertia provided an estimate of 0.008433 in.⁴ (3510.1 mm⁴).

Two material models were identified for possible implementation with the type 2 beam element model: a tensile force-limited perfectly-plastic material (*MAT_29), and a material model in which bulk reactions of the beam are explicitly defined (*MAT_166). The latter

material, *MAT_MOMENT_CURVATURE_BEAM, has multiple input types: (1) true strain vs. axial force curve for symmetric or asymmetric tensile curves; (2) curvature vs. moment resistance for up to 8 axial forces; (3) twist rate per unit length vs. torsional resistance for up to 8 axial forces; (4) dynamic relaxation factors; and (5) failure criteria in tension, torsion, and bending.

Linearly-elastic and elastic-perfectly-plastic material models were not selected with the type 2 beam element since the wire rope was observed to have a highly non-linear plasticity curve in the quasi-static tensile tests. Though it is relatively rare for wire ropes to be loaded plastically during impacts with cable guardrail systems, the allowance of plastic material behavior was desired for a more complete and accurate characterization of wire rope. In addition, greater flexibility with material modeling was available with material type *MAT_166.

Both the type 1 and type 2 beam element models were simulated using a displacement-controlled boundary condition on one side, and fixed boundary condition on the other. Elongation of the displacement-controlled end of the beam element was defined to be 5.000 mm for the entire simulation. The engineering strain which resulted at this displacement would be more than 0.1007 in./in., which was greater than the engineering strain observed in failure of the non-prestretched tensile test. Beam tip displacement was defined using the *DEFINE_CURVE_SMOOTH keyword to discontinuities in the displacement function.

The two models of wire rope were evaluated by comparing total elongation of the test section of the wire rope using NODOUT displacements and d3plot nodal histories; instantaneous load history using SECFORC, SPCFORC, and BNDOUT output; and derived stress and strain comparisons with the ELOUT element output. These results were compared with the displacements, strains, and loads of the non-prestretched tensile test.

It was observed and verified that the axial force curves in time were virtually identical for the SECFORC, SPCFORC, ELOUT, and BNDOUT files. Moreover, axial stress parameter in the ELOUT file actually measured axial force in both the type 1 and type 2 beam elements. When the engineering stress calculated from the non-prestretched tensile test was compared with the stresses from the type 1 beam element and the stresses calculated from the tensile force in the type 2 beam element, they were observed to be equivalent.

Displacement data output from LS-DYNA using NODOUT and LSPP Nodal History were identical. However, a plot of the force-displacement curve indicated that the axial force was not consistent between the type 1 and type 2 elements at the same end displacement. The type 1 element displayed a much larger displacement at fracture than was observed in the quasi-static tensile test and the type 2 element simulation. When the type 2 beam element results were compared with the non-prestretched tensile test the displacements were nearly identical throughout the test with a total gauge length displacement of 0.1230 in. (3.124 mm).

Force-displacement curves were generated to compare the force and displacement of the non-prestretched wire rope and the simulated forces and displacements. The simulated and measured force-displacement curves are shown in Figure 29.

Because the type 1 beam element with *MAT_024 could not simulate the initial geometrical stretch in the wire rope, the geometrical stretch was not initially included in the simulations. Strain data was examined in closer detail in order to see if there was an easily-identifiable reason why the displacement in the type 1 beam element was not similar to what was measured in the test. Engineering strain, ϵ , defined as

$$\epsilon_{instantaneous} = \frac{l_{current} - l_{reference}}{l_{current}} = \frac{\Delta l}{l} \quad [6]$$

$l = \text{gauge length}$

and true strain, ϵ , defined as

$$\epsilon = \frac{dl}{l} \quad [7]$$

$\epsilon = \text{true strain}$

were used to compare results of the simulations to the boundary-prescribed motion and material strain data. True strain is given as a function of engineering strain by

$$\epsilon = \ln(1 + \epsilon), \quad [8]$$

which assumes that volume is conserved in the tension specimen. During plastic elongation, volumetric conservation is very accurate, and the associated error during elastic loading is trivial. Since the ELOUT file calculates true plastic strain at each output time step, the plastic strain was plotted against the calculated engineering plastic strain to observe the differences. It was observed that the plastic strain output from the ELOUT file in the type 1 beam element was significantly different than the anticipated plastic strain, based on Equation 8, as shown in Figure 30.

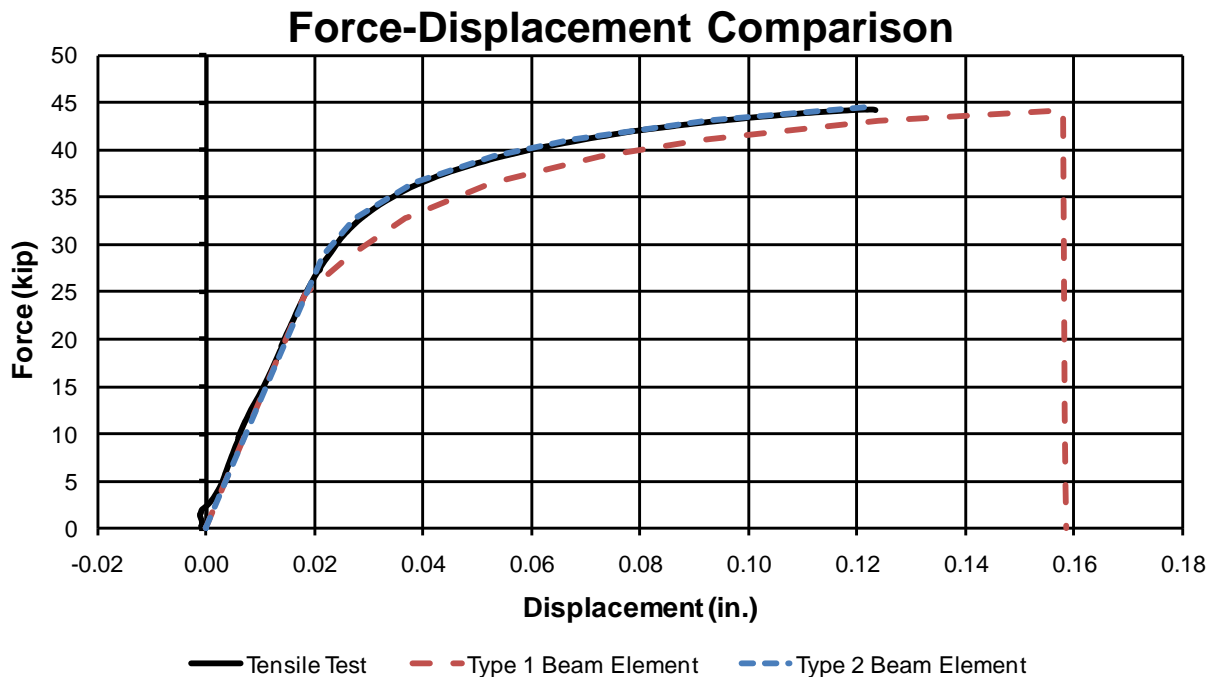


Figure 29. Force-Displacement Comparison, Type 1 and Type 2 Beam Elements

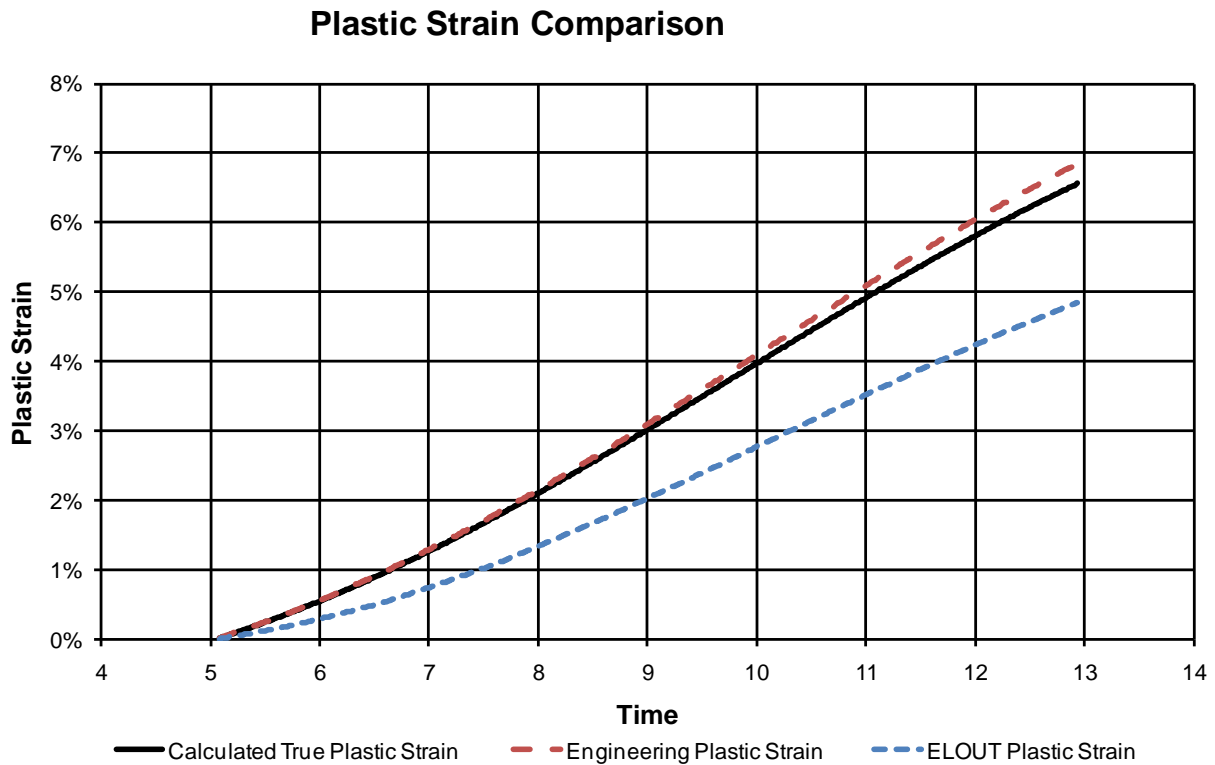


Figure 30. Plastic Strain Comparison, Type 1 Beam Element

A ratio of ELOUT plastic strain to the calculated true plastic strain was taken to see if there was a linear scale factor between ELOUT plastic strain and anticipated plastic strain. It was observed that the ratio changed with plastic strain, the ratio was approximately constant along a given increment of the 8-point stress-strain curve. This is shown in Figure 31.

No immediate relationship was determined between the ELOUT plastic strain and the anticipated plastic strain based on constitutive relations and input parameters. Further, different numbers of integration points, element lengths, and use of a plasticity curve instead of the 8-point input were attempted to reconcile the differences between the type 1 and type 2 beam elements, but were observed to have little effect. As a result, the type 1 element was not considered for further model development.

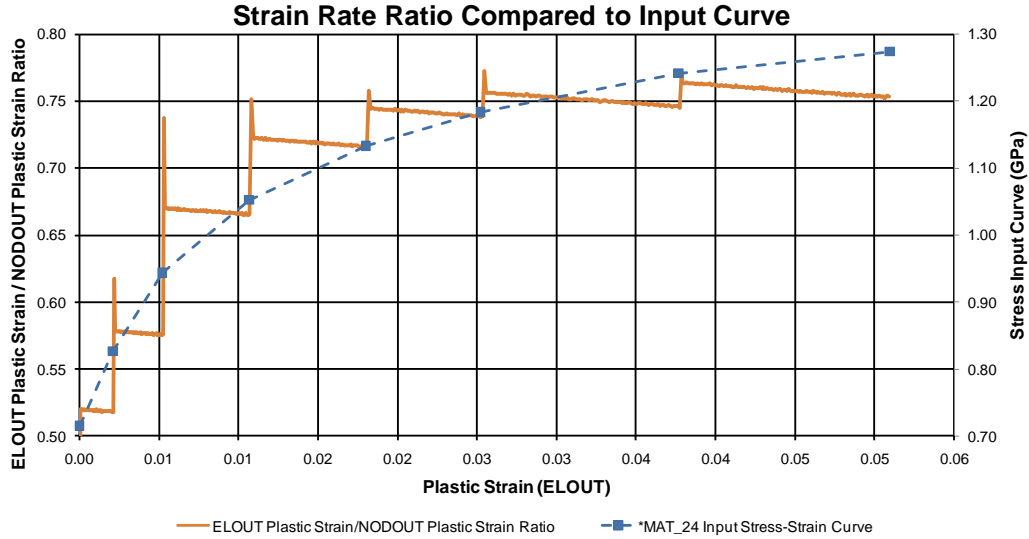


Figure 31. Ratio of ELOUT Plastic Strain to Calculated Plastic Strains

It should be reiterated that the input stress-strain curves in the type 1 (Hughes-Liu) beam element utilizing *MAT_PIECEWISE_LINEAR_PLASTICITY is of the form of engineering stress and true strain. Engineering stress is used because cross-sectional area is not reduced at any time during the simulation – thus the definition of stress, σ , given by

$$\sigma = \frac{F}{A_{initial}} \quad [9]$$

where: F = axial force acting through cross-section
 A = cross-sectional area

It should also be noted that the ELOUT plastic stress-strain curve matched exactly with the input stress-strain curve.

The engineering stresses were calculated by dividing the cross-sectional force from SECFORC by the initial area of 0.2395 in.² (154.5 mm²). Engineering strains were calculated by dividing the total displacement from the NODOUT file by the initial length 1.9545 in. (49.644 mm). The engineering stress and output stress from ELOUT were plotted against engineering strain, and are shown in Figure 32.

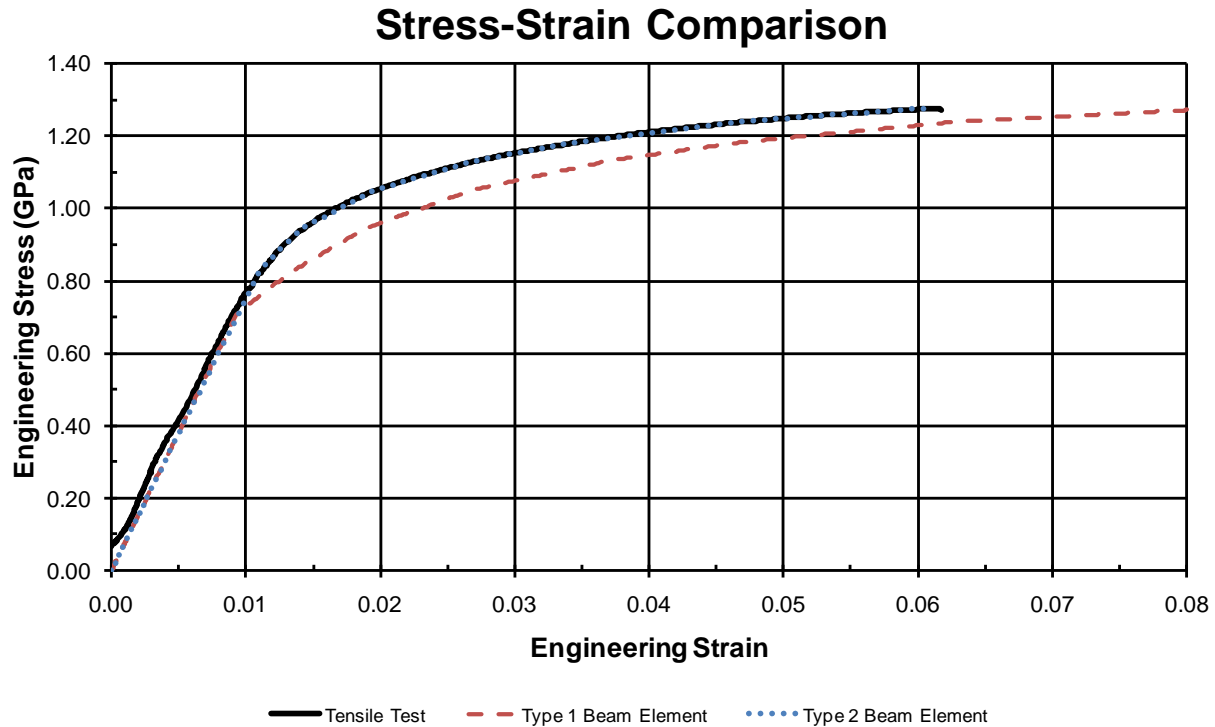


Figure 32. Calculated Engineering Stress vs. Calculated Engineering Strain

6.2.2 Prestretched Wire Rope

The type 1 element was unable to accurately capture the tensile response of the wire rope using a relatively simple and widely-used material model. Accordingly, the type 2 element was pursued for evaluation as the more logical selection. Tensile test data was tabulated, and a modulus of elasticity was calculated. Then, using data from the force-displacement curve and converting displacements to true strain, a force-strain material input curve was generated.

Since the measured gauge length of the extensometer was 1.9975 in. (50.737 mm), a beam element using the gauge length of the extensometer in the prestretched tensile test was created. Again, boundary prescribed motion was applied to one end of the beam element, and the other end was fixed with a single-point constraint (SPC) condition. The prestretched wire rope failed at a much higher strain than the non-prestretched wire rope because there was less stress

concentration in the rope than occurred with the non-prestretched wire rope. Therefore, the displacement used for the displacement boundary condition was increased by 25 percent.

The prestretched wire rope simulation very closely matched the prestretched tensile test force-engineering strain curve, as shown in Figure 33.

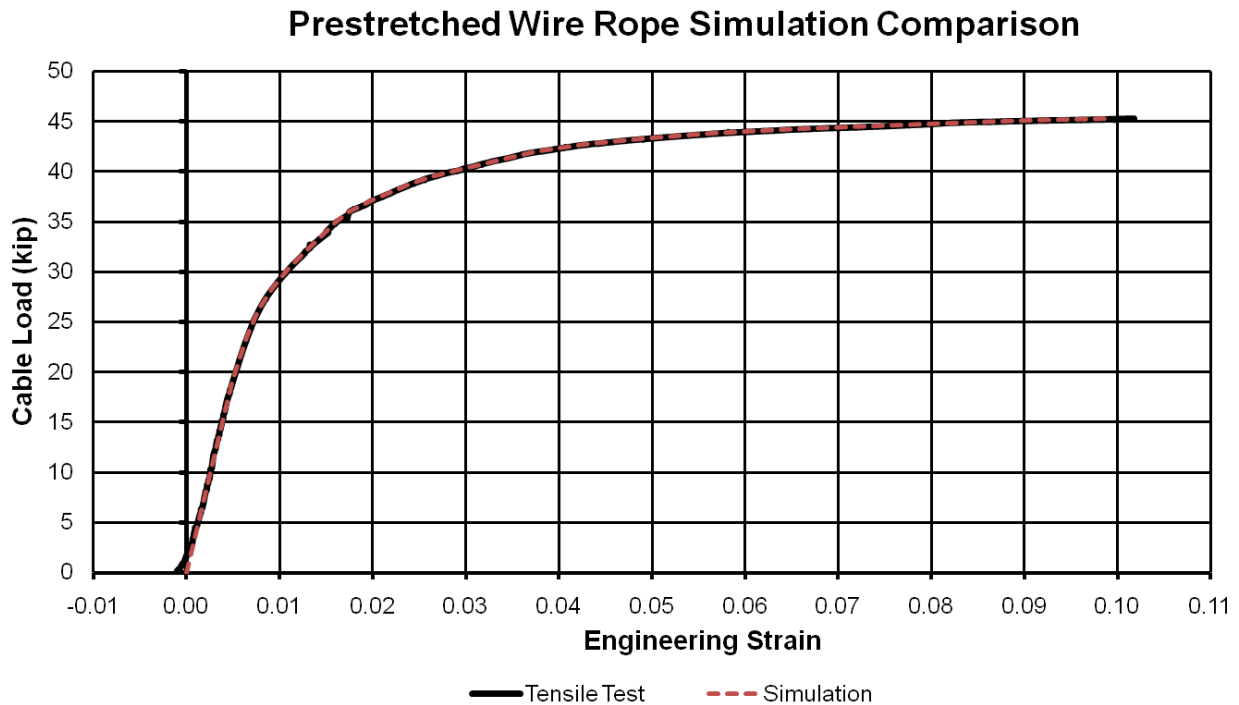


Figure 33. Prestretched Wire Rope Simulation Model and Test Results

6.3 Mesh Sensitivity Analysis

A mesh sensitivity study was conducted to see if the axial force simulated in quasi-static tensile conditions varied with element size. A 1.9545-in. (49.644-mm) long beam element, consistent with the gauge length of the non-prestretched tensile test, was partitioned into smaller elements to evaluate model evaluation time, mesh sensitivity to ramped displacement inputs, and to attempt to identify an appropriate length of beam element for further model development.

Four separate mesh densities were evaluated for the same net beam length. The element length, maximum force, and single-processor computing time are shown in Table 6. The force-

strain plots for each simulation were nearly identical. Very small differences were observed in the forces in the beams at a given time, but these were believed to be related more closely to small numerical precision errors in the data output than due to mesh size. Each model was constructed with exactly the same method as used previously; results from the SECFORC output were employed to examine axial forces and section forces were compared with ELOUT axial forces for each beam element. Engineering strain was calculated using Equation 2.

Table 6. Mesh Density Comparison, Tensile Test Simulation

No. Elements	Element Length		Computational Time Required (sec)	Relative Cost*	Axial Force at Fracture	
	in.	(mm)			kip	(kN)
1	1.9545	49.644	0.359	1	44.56	198.2
2	0.9773	24.822	0.551	1.53	44.57	198.3
4	0.4886	12.411	1.060	2.95	44.57	198.3
10	0.1955	4.964	4.683	13.04	44.57	198.3
25	0.0782	1.986	20.233	56.36	44.57	198.3

Axial strain at fracture: 0.0632

*Relative cost = Computational Time Required / Computational Time Required for 1 element

It was determined that in tension, the optimum beam element length to simulate the wire rope response was between 2 and 5 elements. The 0.50-in. (12.7-mm) element was optimal due to three reasons: (1) response time was accurate; (2) mesh can tolerate slight increases or decreases in size without substantial change in computational cost or accuracy; and (3) the relative cost is less than the gain in accuracy using additional elements—a 2.95 relative cost compared to the 4x increase in mesh density. The 2x mesh density was also a desirable and cost-effective solution.

6.4 Discussion

In both the prestretched and non-prestretched tensile tests there was an initial non-linear geometrical stretch section of loading. In both tests this loading created small variations in strain

at relatively low loads. For general non-prestretched and prestretched wire rope models in full-scale test or system modeling, the non-linear geometrical stretch observed in the quasi-static tensile tests should be disregarded. The first point on the tensile curve specified in *MAT_166 is the yield point of the rope, and the slope of the line connecting the first two points defines the loading and unloading force modulus. Here, the force modulus can be treated exactly like a Young's modulus for strain multiplied by the cross-sectional area which is used to determine the unloading and reloading rate of increase of force per unit strain.

The importance of the non-linear geometrical strain data is greater for long lengths of non-prestretched wire rope under no initial pretension. As a result, this section was added to the force-strain curve input in the simulations used to model the dynamic tensile and bending tests. It was observed in these tests that the non-linear low-load stretching of the wire rope generally had a very small effect on the outcome, but it was considered to ensure the most accurate result possible.

As discussed in the quasi-static tensile testing section, the initial non-linear geometrical stretch is unimportant for most wire rope guardrail applications. Simulations of the non-linear constructional stretch were attempted, and the results were consistent with the input curves. However, these curves are not likely to be used in most wire rope guardrail simulations. Most cable barrier installations have pretensions which range from 2,500 lb (11.1 kN) to 5,000 lb (22.2 kN). Since wire rope has viscoelastic properties when loaded in the axial direction for long amounts of time, the constructional stretch is gradually reduced by temperature cycling and vehicular impacts for wire ropes used in high-tension cable guardrail systems. In addition, the pretension loads are sufficient to load wire rope into the linear range of tensile response.

Low-tension cable guardrail systems tend to display a net inelastic stretch after impact, which may result in wire ropes drooping to the ground [39-40]. After many impacts the inelastic stretch is reduced, and the wire rope tensile response approaches that of a prestretched rope.

For low-tension cable guardrail systems undergoing relatively few vehicular impacts, and for newly-constructed systems, the non-linear geometrical stretch may be important to include in the tensile curve. If the pretension is less than 2,000 lb (8.9 kN), much of the geometrical prestretch may be present in the wire rope, requiring frequent retensionings, particularly after impacts. Furthermore, if the impact frequency on these systems is relatively low, impact prestretching may never occur in the wire rope because high temperature and low-amplitude vibrations can reduce prestretching benefits in warmer climates. The impact frequency at which the non-linear geometrical stretch of the load-strain curve is no longer necessary is unknown. Thus, if questions arise, simulations should be constructed with and without the curve modification to compare the results.

The final recommended load-strain curves for non-pretensioned and pretensioned wire ropes are shown in Table 7. These curves are recommended for use in the modeled tensile load curves under the parameter ELAF. A plot of the three curves is shown in Figure 34. The curves are shown in metric units (kg, mm, ms) to be consistent with the input to DYNA decks.

Table 7. Recommended Tensile Curves for Prestretched and Non-Prestretched Wire Ropes

Non-Prestretched Baseline		Non-Prestretched With Geometrical Stretch		Prestretched	
True Strain	Axial Force (kN)	True Strain	Axial Force (kN)	True Strain	Axial Force (kN)
0.00000000	0.00000000	0.00000000	0.00000000	0.00000000	0.00000000
0.008937121	110.398594105	0.000010000	0.145143150	0.004795620	83.619521342
0.009870041	121.813154169	0.000130000	0.774254827	0.006443918	104.867031688
0.011651737	136.049084775	0.000220000	1.085736654	0.008081977	119.626820549
0.013076832	143.858764574	0.000300000	1.459514847	0.009222070	126.604013475
0.014862910	151.164162192	0.000350000	1.646403943	0.013720171	146.756887686
0.016897369	157.585950324	0.000450000	2.198171751	0.015948646	156.684258488
0.024654681	172.995564236	0.000580000	2.910130213	0.018486490	162.384375923
0.034179644	182.817583777	0.000690000	3.595390232	0.021997547	169.210277676
0.039568289	188.164193743	0.000770000	4.267301031	0.024989359	174.358627303
0.046628261	191.823858320	0.000850000	4.859116502	0.025965115	175.822591890
0.049911007	194.385161537	0.001000000	6.118393031	0.028367689	178.541383266
0.059994686	197.000000000	0.001170000	7.689151388	0.039924366	189.274157078
		0.001290000	9.024073504	0.041177608	190.026163203
		0.009496593	110.398594105	0.047103248	192.602562887
		0.010423865	121.813154169	0.054227610	194.974274513
		0.012204576	136.049084775	0.061906827	196.860964437
		0.013628883	143.858764574	0.071521621	198.471770457
		0.015413976	151.164162192	0.093020967	201.439747295
		0.017447316	157.585950324	0.096687353	201.600000000
		0.020166744	162.477820471		
		0.027534677	175.003839659		
		0.030515308	179.667262121		
		0.039801059	188.164193743		
		0.047162102	191.823858320		
		0.060521441	197.000000000		

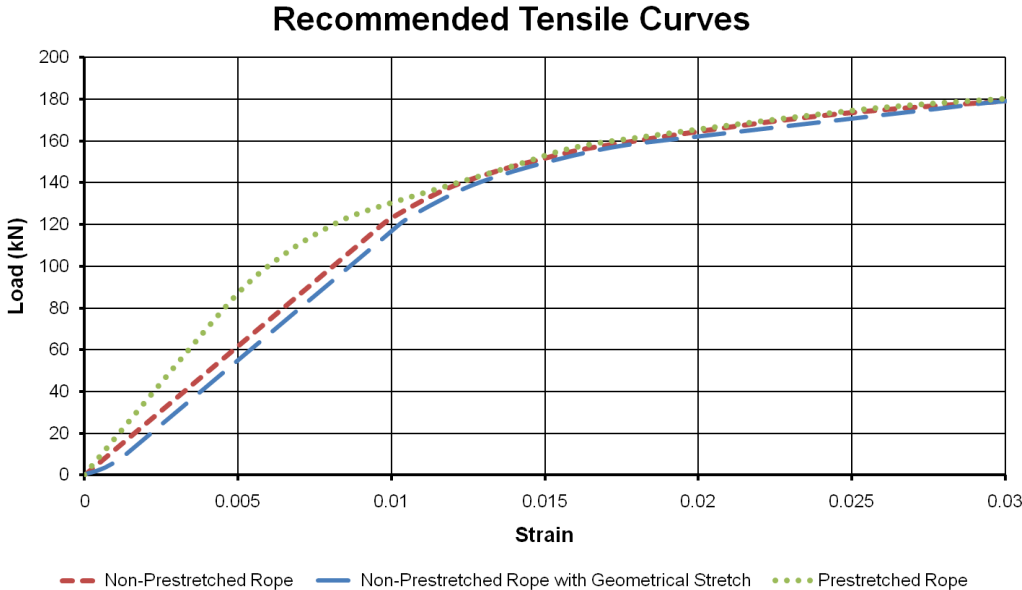


Figure 34. Recommended Tensile Curves for Wire Rope Modeling

7 DYNAMIC TENSILE TESTING

7.1 Test Methodology

Dynamic jerk testing of wire rope was conducted to evaluate the wire rope in dynamically-varying tension, determine dynamic tensile material properties for the wire rope model, and validate the simulations. Three dynamic material properties were desired: (1) the dynamic load-strain relationship, (2) the fracture load in dynamic tension, and (3) the tension dynamic amplification factor. However, during the course of the testing it became apparent that environmental effects, test temperatures, and the unloaded initial position of the wire rope affected the resulting tensile failure load. Furthermore, unintended side effects of testing increased difficulty in analyzing test results.

7.2 Test Setup

The bogie test setup consisted of a load frame assembly, a sway resistance pipe assembly, a test section of wire rope, tow cables, a heavy bogie vehicle, and a pin and shackle assembly. Test details are shown in Figures 35 through 39. Photographs of the test setup in test nos. DTC-1 through DTC-3 are shown in Figures 40 and 41.

The bogie vehicle is shown in Figure 42. The bogie vehicle consisted of frame tubes filled with concrete. Stiffeners consisting of channel sections and gussets were welded to the frame to make the bogie nearly rigid. Four 28-in. (711-mm) diameter trailer wheels were attached to the bogie using spindles. Two 16 in. x 6 in. by 48 in. long (406 mm x 152 mm by 1,219 mm) rectangular impact tubes were welded to the main frame tubes on both the front and back of the bogie vehicle, and were capped and filled with concrete.

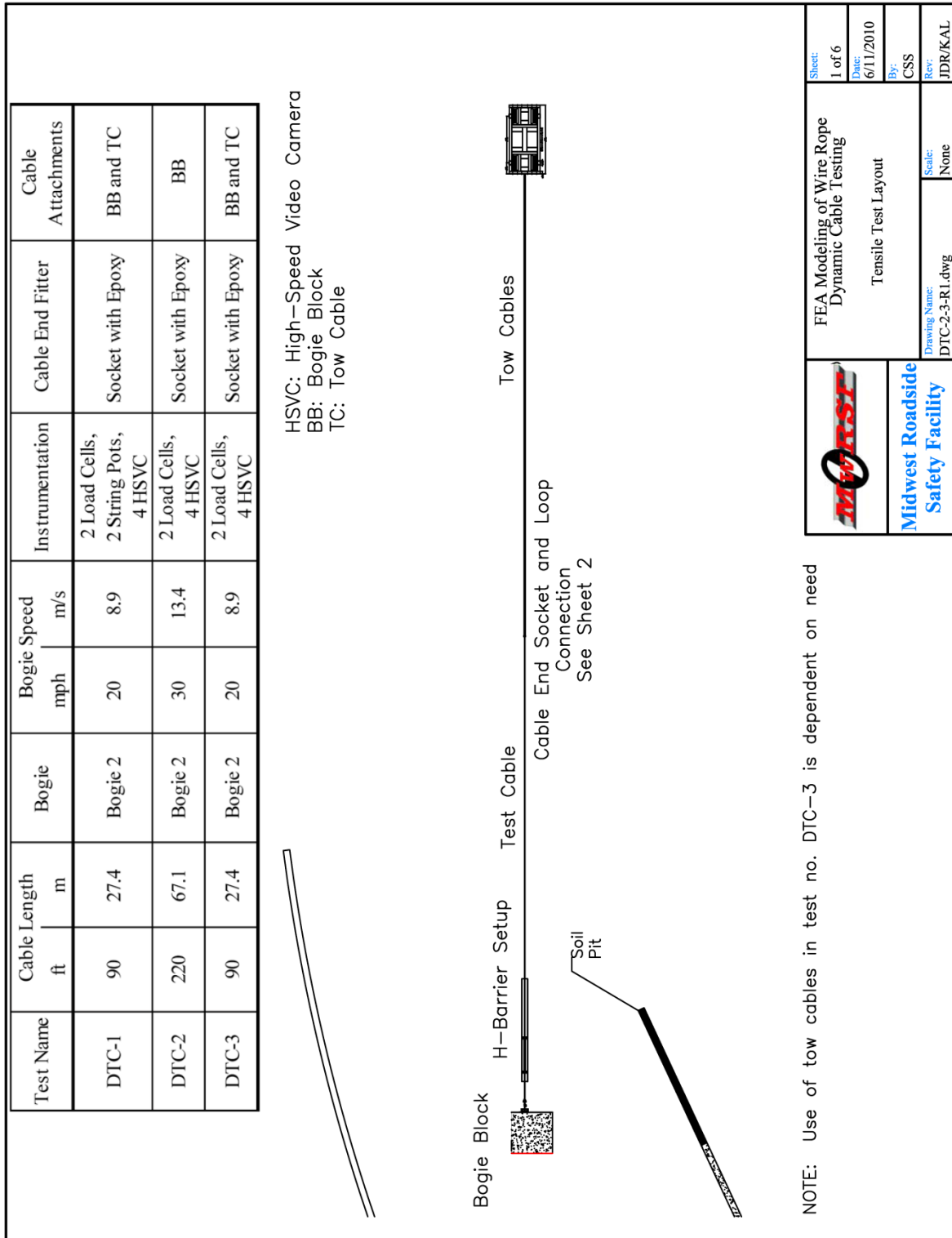


Figure 35. Test Setup, Test No. DTC-1

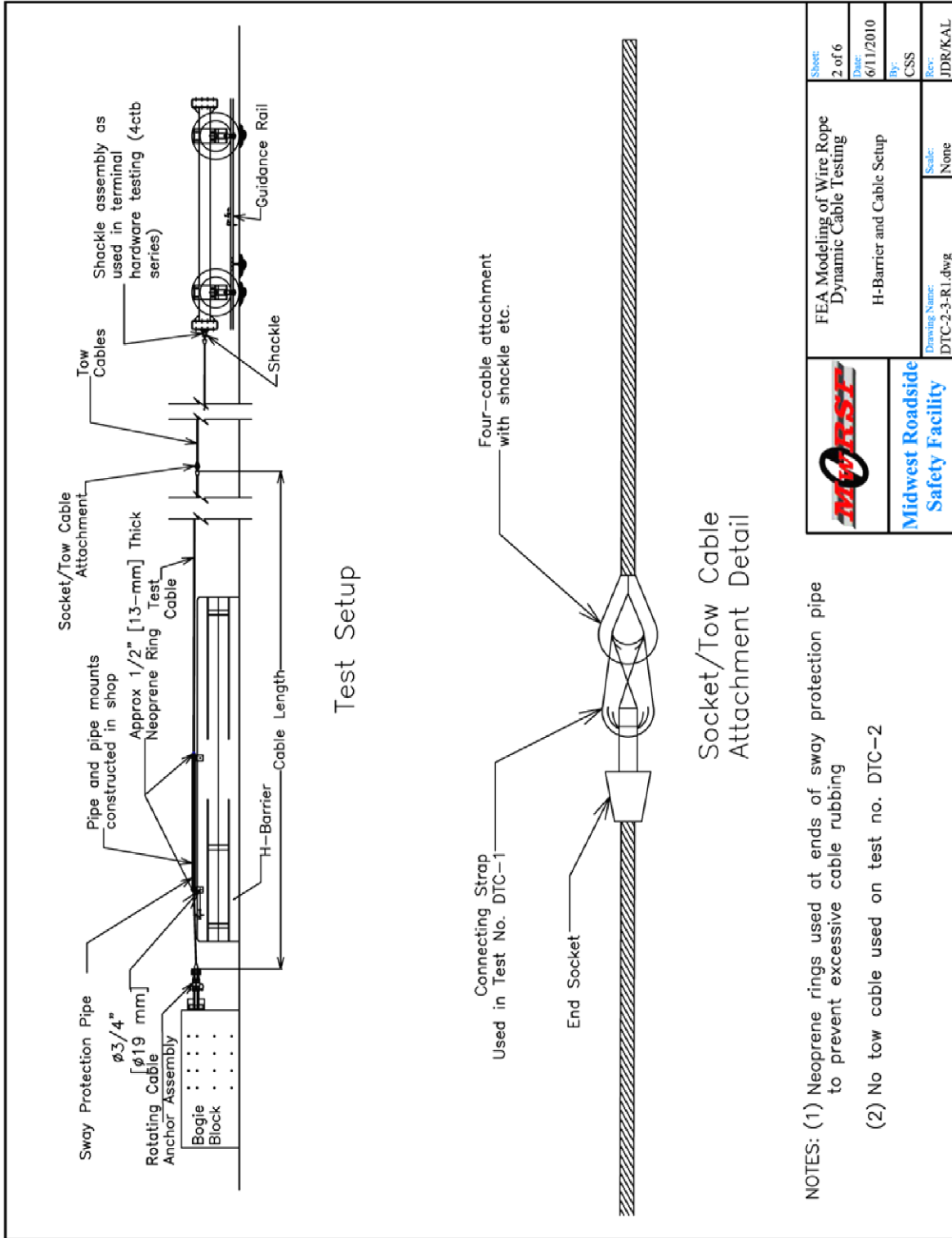
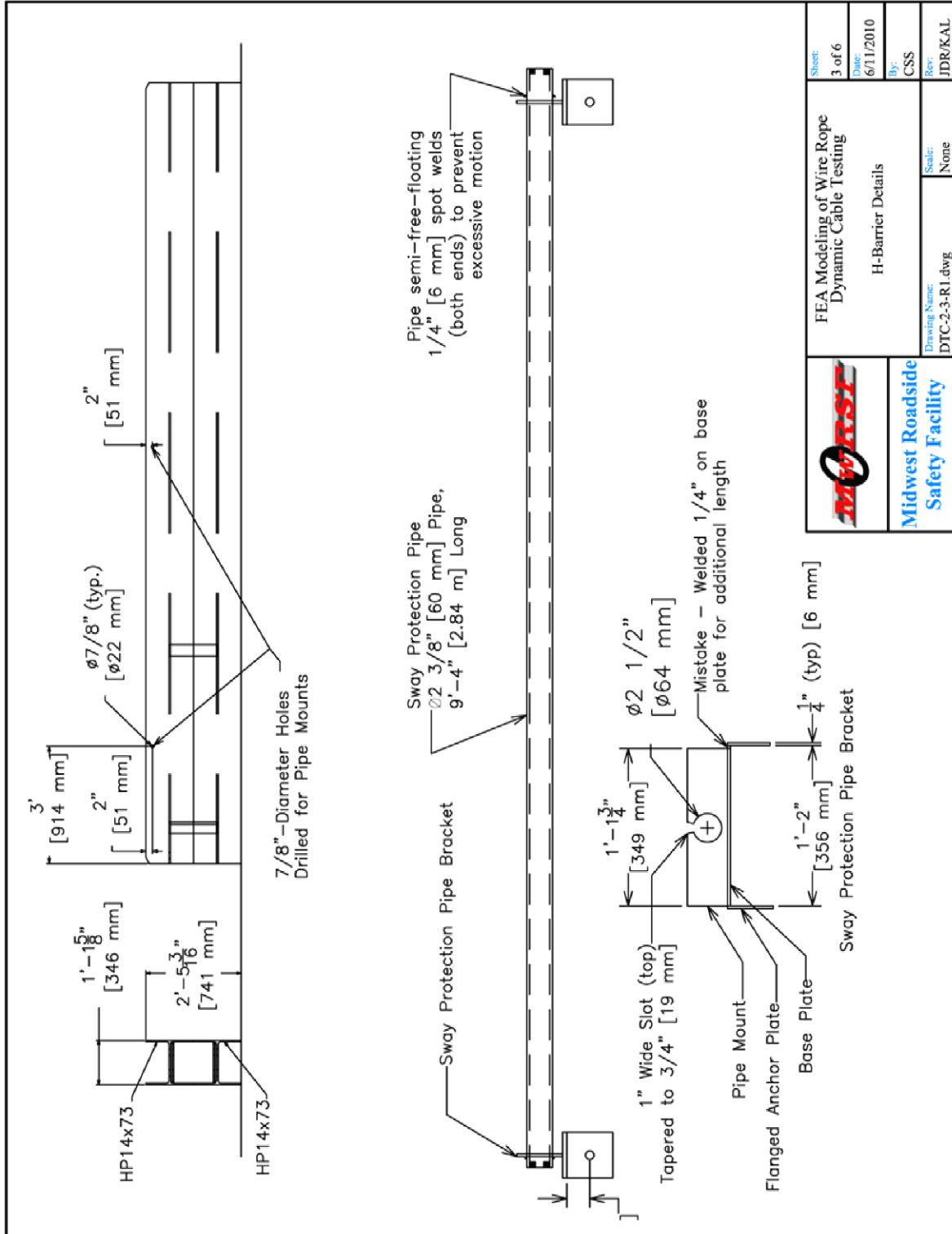
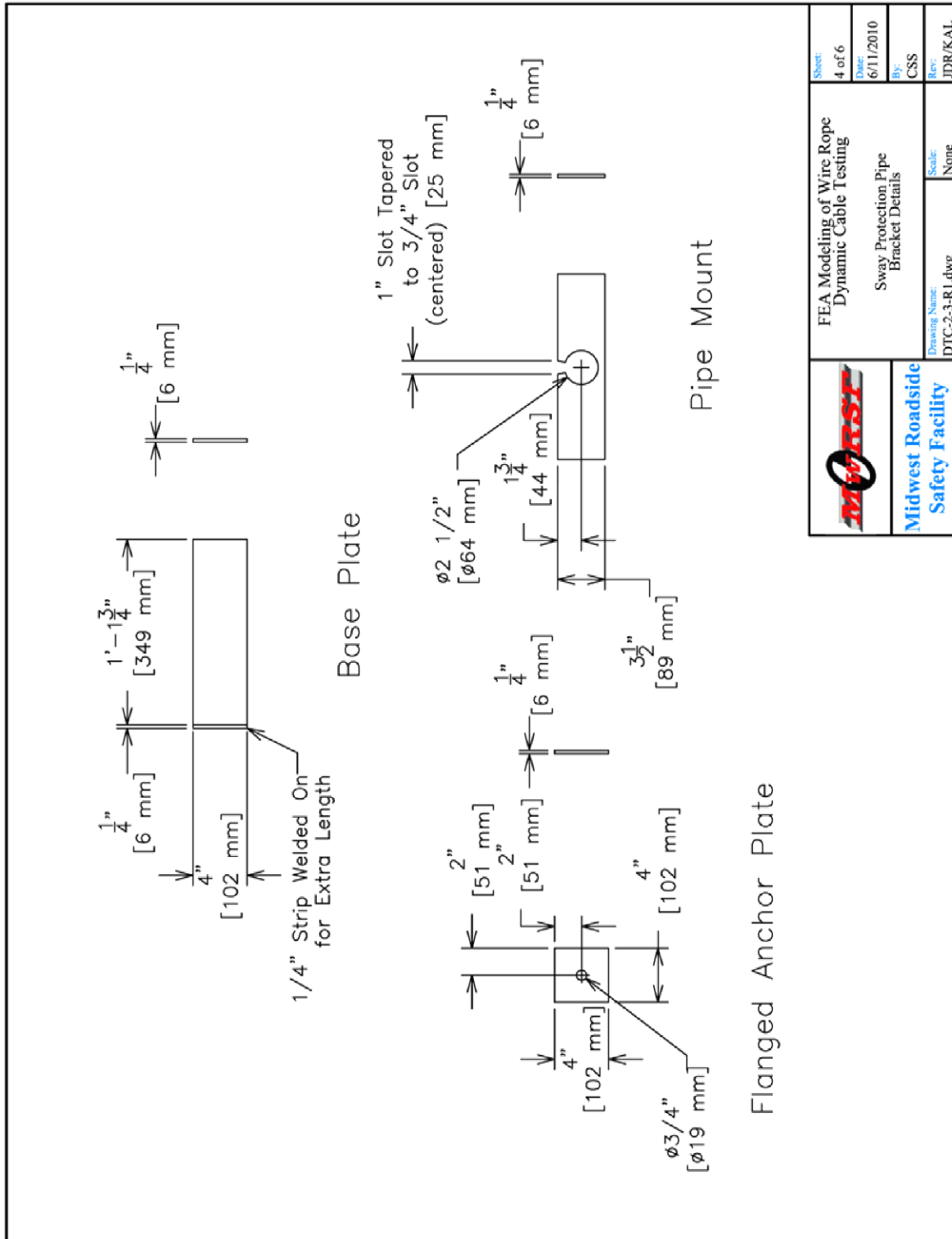


Figure 36. DTC Tow Cable Arrangement, Test Nos. DTC-1 and DTC-3



	FEA Modeling of Wire Rope Dynamic Cable Testing H-Barrier Details		Sheet: 3 of 6
	Drawing Name: DTC-2-3-R1.dwg		Date: 6/11/2010
Midwest Roadside Safety Facility		By: CSS	Rev: JDR/KAL
		Scale: None	

Figure 37. Sway Resistance Pipe Details



	FEA Modeling of Wire Rope Dynamic Cable Testing		Sheet: 4 of 6
	Sway Protection Pipe Bracket Details		Date: 6/11/2010
Midwest Roadside Safety Facility	Drawing Name: DTC-2-3-R1.dwg	By: CSS	Rev: JDR/KAL
		Scale: None	

Figure 38. Sway Resistance Pipe Part Details

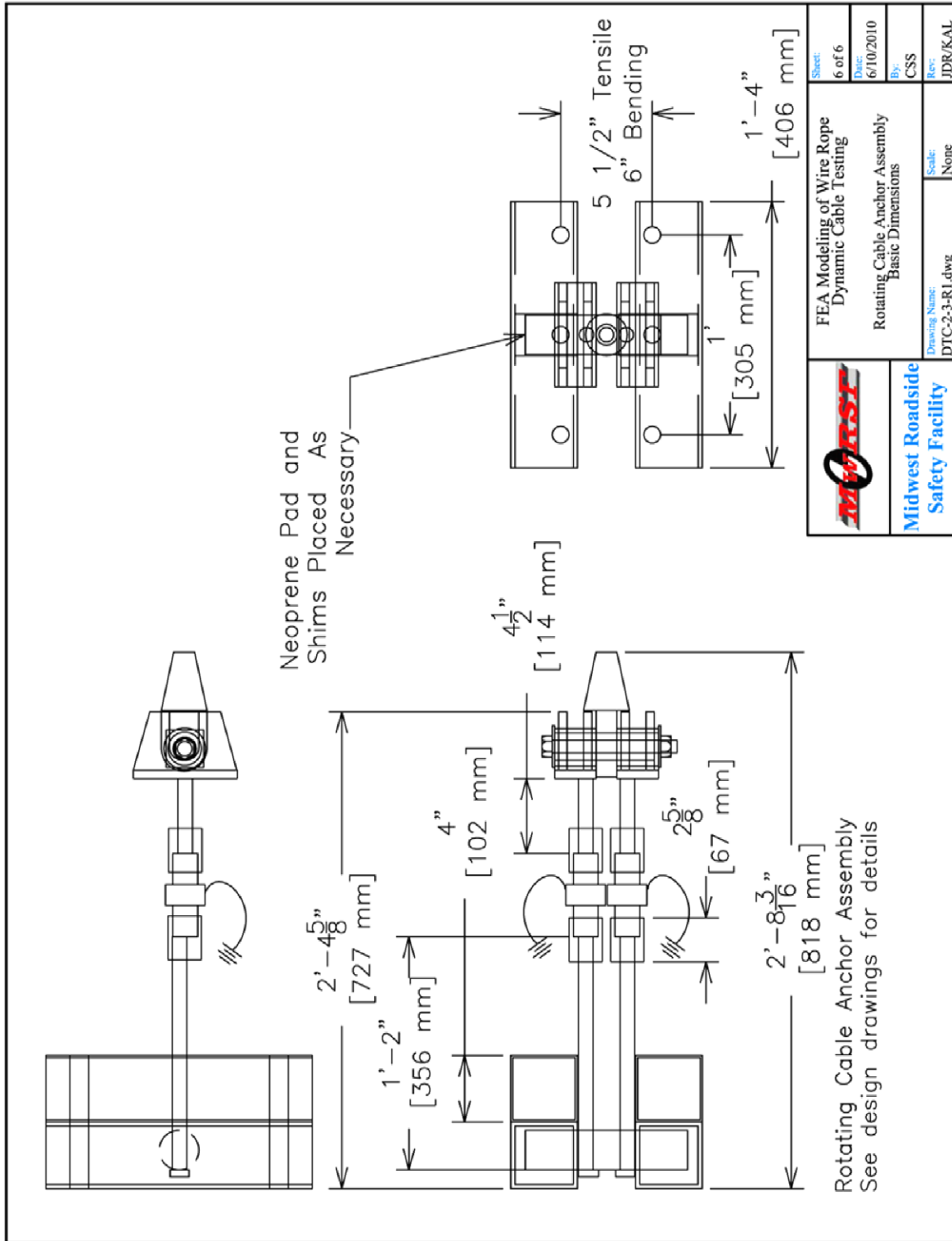


Figure 39. Load Frame Details



Figure 40. Test Setup, Test Nos. DTC-1 and DTC-3



Figure 41. Test Setup, Test No. DTC-2



Figure 42. Bogie Test Vehicle, Test Nos. DTC-1 through DTC-3

A ribbed bracket was attached to the back of the bogie vehicle, and fitted with a shackle assembly. The pin diameter was 1 in. (25 mm), and was loaded in double shear. A 4 in. x $\frac{3}{8}$ in. (102 mm x 9.5 mm) nylon strap was used to attach the tow cables to the shackle. The nylon strap was rated to a peak load of 80 kip (356 kN). Four wire ropes were used in the tow cable assembly. The ends of the wire rope tow cables were constrained using wire rope thimbles and U-bolts. Though this end fixture is not as efficient as spelter or swage sockets, the factor of safety against tow cable fracture or release from end constraints was approximately 3.5 since four wire rope were used but wire rope lengths were not identical. The tow cable length was 130 ft – 6 in. (39.78 m) long. The nylon straps were looped through the thimbles and around the shackle to form a complete loop near the bogie, and a similar loop was formed to connect the tow cables to the test cable.

The test cable length was 89 ft – 6 in. (27.28 m) long in test nos. DTC-1 and DTC-3, and 220 ft (67.1 m) in test no. DTC-2. The test wire rope was constrained with closed spelter sockets on both ends, using Socketfast epoxy resin compound. The test length of wire rope was constrained with a load pin assembly at the load frame side, and the wire rope was contained in the sway resistance assembly prior to fitting the socket with the resin.

The sway resistance assembly consisted of a sway resistance pipe, two sway constraint brackets, and a secure tie down structure. The sway resistance pipe was a 2¼-in. diameter by 9-ft 4-in. long (57-mm by 2.84-m) steel pipe. The brackets were constructed from two 14-in. x 4-in. by ¼-in. (356-mm x 102-mm by 6-mm) plow blade steel, and attached to two 4-in. x 4-in. by ¼-in. (102-mm x 102-mm by 6-mm) ear plates. Holes were drilled in the center of the ear plates to fit $\frac{5}{8}$ -in. (16-mm) diameter bolts, which connected to the flanges of a 20-ft (6.1-m) long steel H-barrier.

Load frame assembly details are shown in Figures 43 through 51. Photographs of the load frame assemblies, painted and unpainted, are shown in Figure 52. The load frame consisted of 4-in. x 4-in. x 1/4-in. by 16-in. long (102-mm x 102-mm x 6-mm by 406-mm) steel tubes for back frame tubes. The back frame tubes had two holes drilled 6 in. (152 mm) from the centerline of the tube and 1 in. (25 mm) from the bottom and top surfaces of the upper and lower tubes, respectively. A 2⁵/₈ in. (67 mm) diameter hole was drilled in the bottom of the top back frame tube and the top of the bottom back frame tube, and both holes were located 1¹¹/₁₆ in. (43 mm) from the front of the tubes. Two 4-in. x 4-in. x 1/8-in. by 16-in. (102-mm x 102-mm x 3-mm by 406-mm) tubes were placed in front of the back load frame tubes to act as stiffeners. Four 1-in. (25-mm) diameter threaded rods were used to secure the load frame tubes to an 8-ft x 8-ft x 40¹/₄-in. (2.4-m x 2.4-m by 1,022-mm) concrete block. All the frame tubes were capped and filled with concrete.

A 2³/₈-in. diameter by 9³/₄ in. (60 mm by 248 mm) pipe was used as the rotator pipe in the load frame assembly. Two 1-in. (25-mm) diameter holes were drilled through the pipe and spaced 2³/₈ in. (60 mm) apart in the center of the pipe. Two 7/8-9 UNC by 14-in. long (M22-2.8 UNC by 356 mm) Grade 5 bolts were inserted in the holes in the rotator pipes, and the heads were welded to the back. The heads were cut flush with the outside diameter of the bolt, and the cut faces were turned away from the center of the pipe. Couplers were threaded onto the bolts, and reverse-threaded onto the Transducer Techniques 50-kip (222-kN) load cells. Load cell data was captured using a wide band pass, a gain of 400 and 10 V voltage supply. Load cell data was captured at 10,000 Hz.

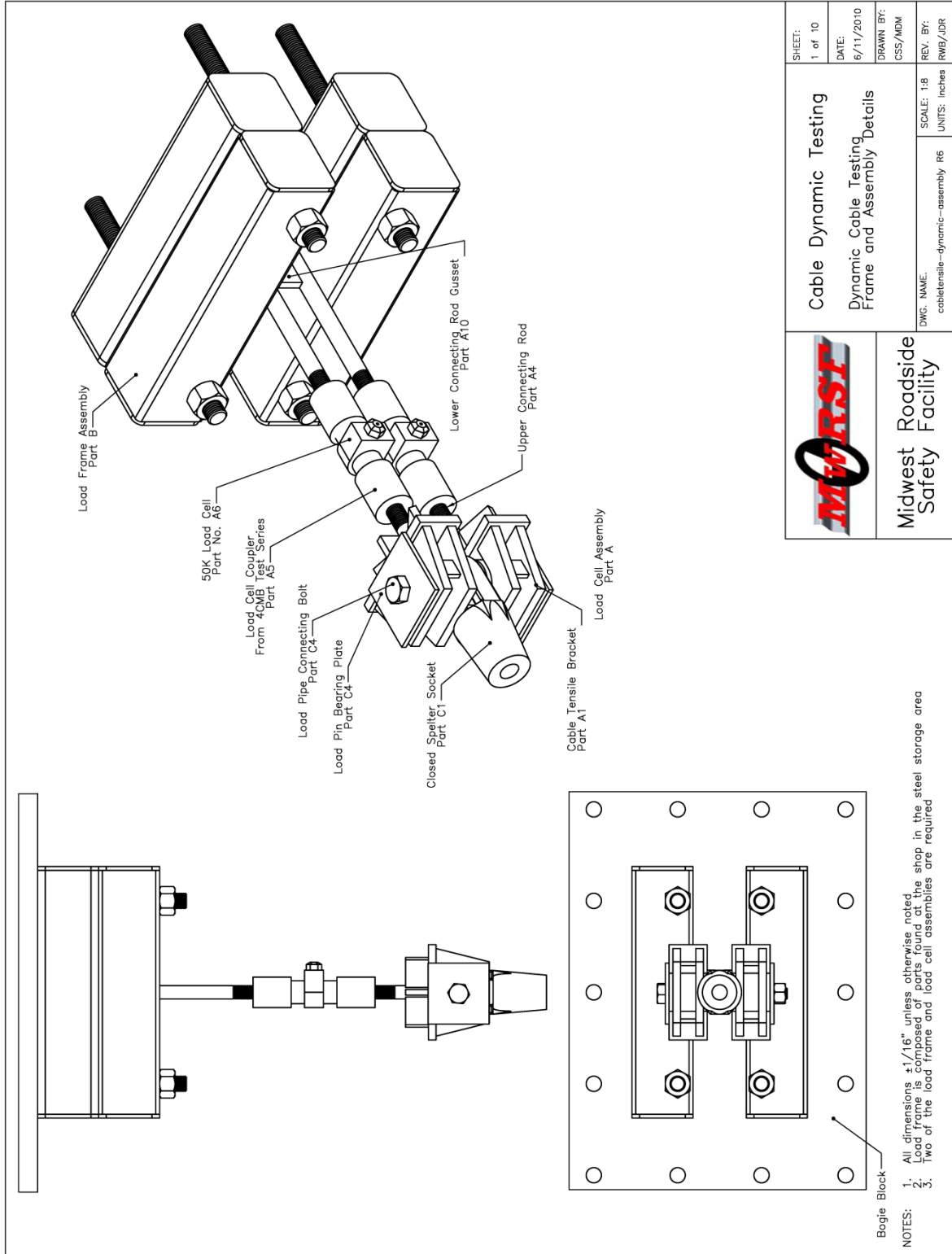
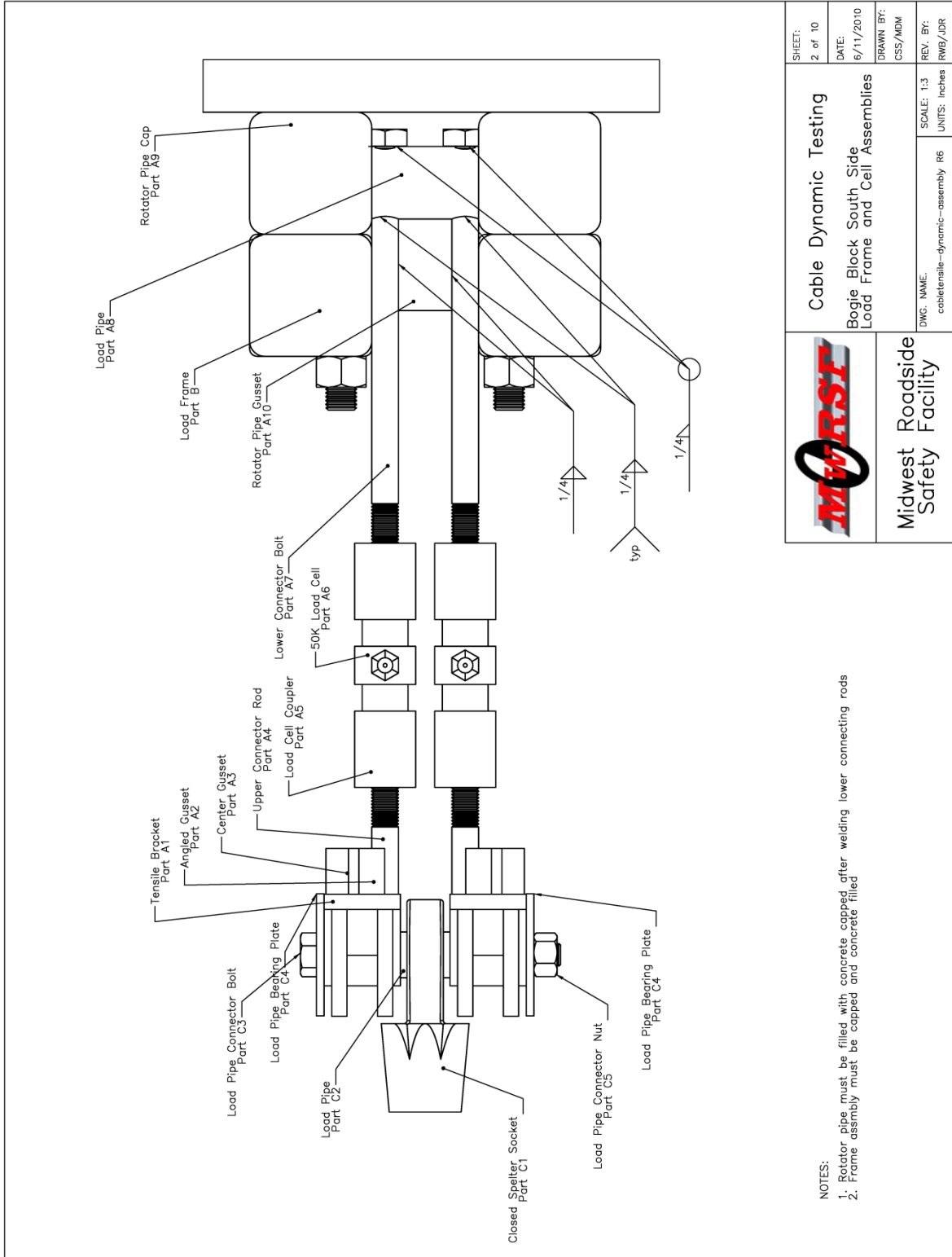



Figure 43. Load Frame Details



SHEET: 2 of 10		Cable Dynamic Testing	
DATE: 6/11/2010		Bogie Block South Side Load Frame and Cell Assemblies	
DRAWN BY: CSS/MDM		DWC: NAME: cabletensile--dynamic--assembly R6	
REV. BY: RWG/JDR		SCALE: 1:3	UNITS: inches
		Midwest Roadside Safety Facility	

NOTES:
1. Rotator pipe must be filled with concrete capped after welding lower connecting rods
2. Frame assembly must be capped and concrete filled

Figure 44. Load Frame Details

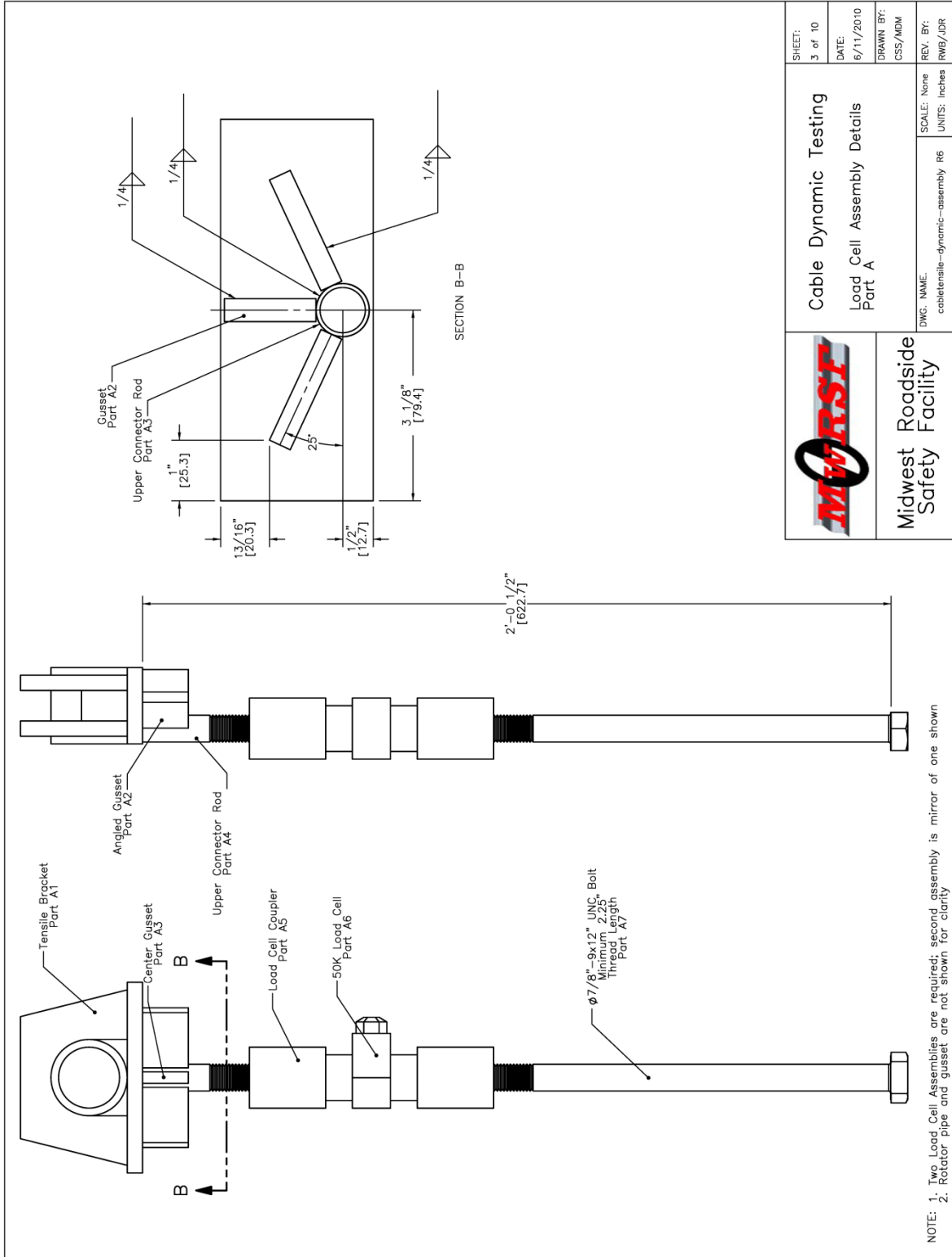


Figure 45. Load Cell Assembly Details

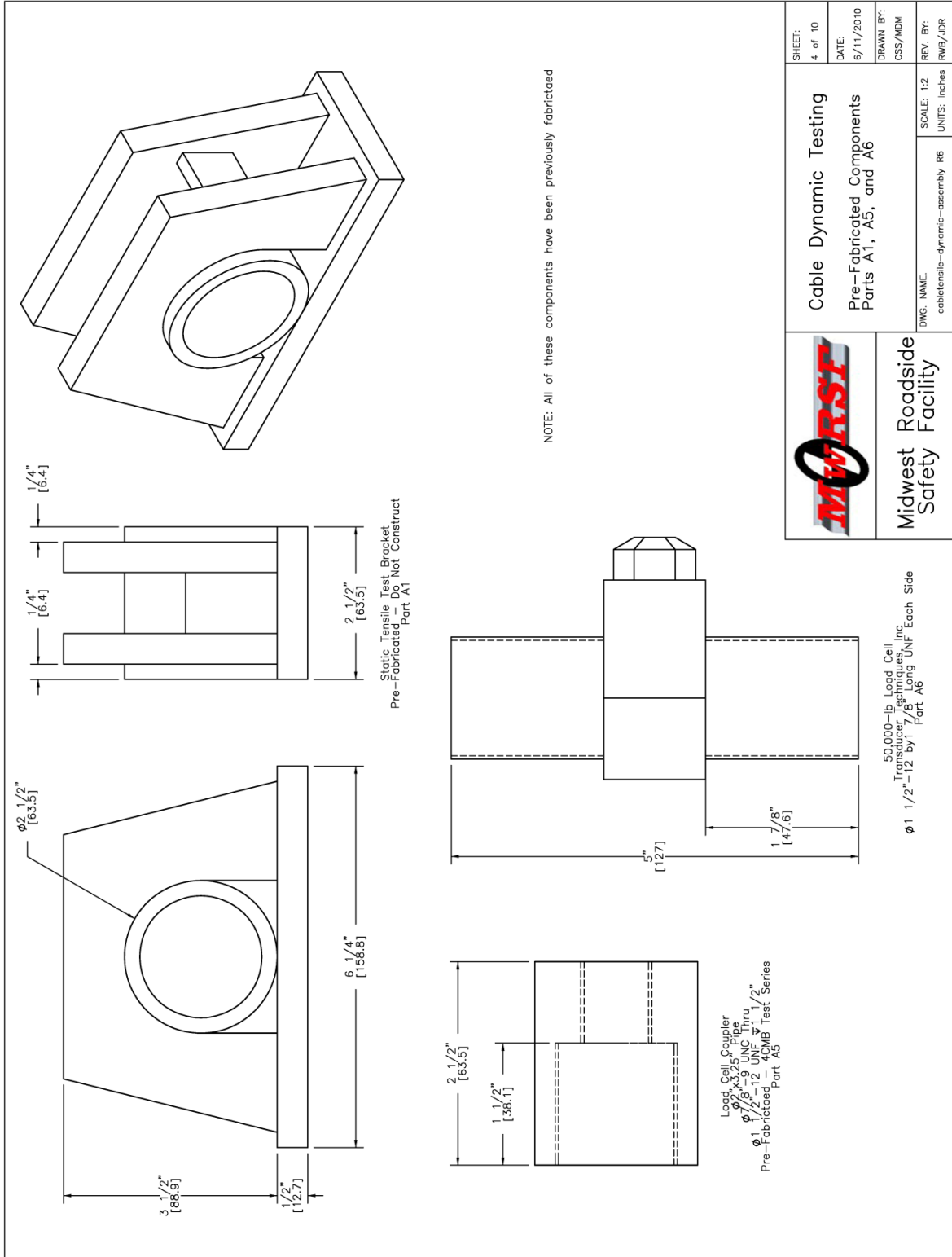


Figure 46. Load Bracket and Load Cell Details

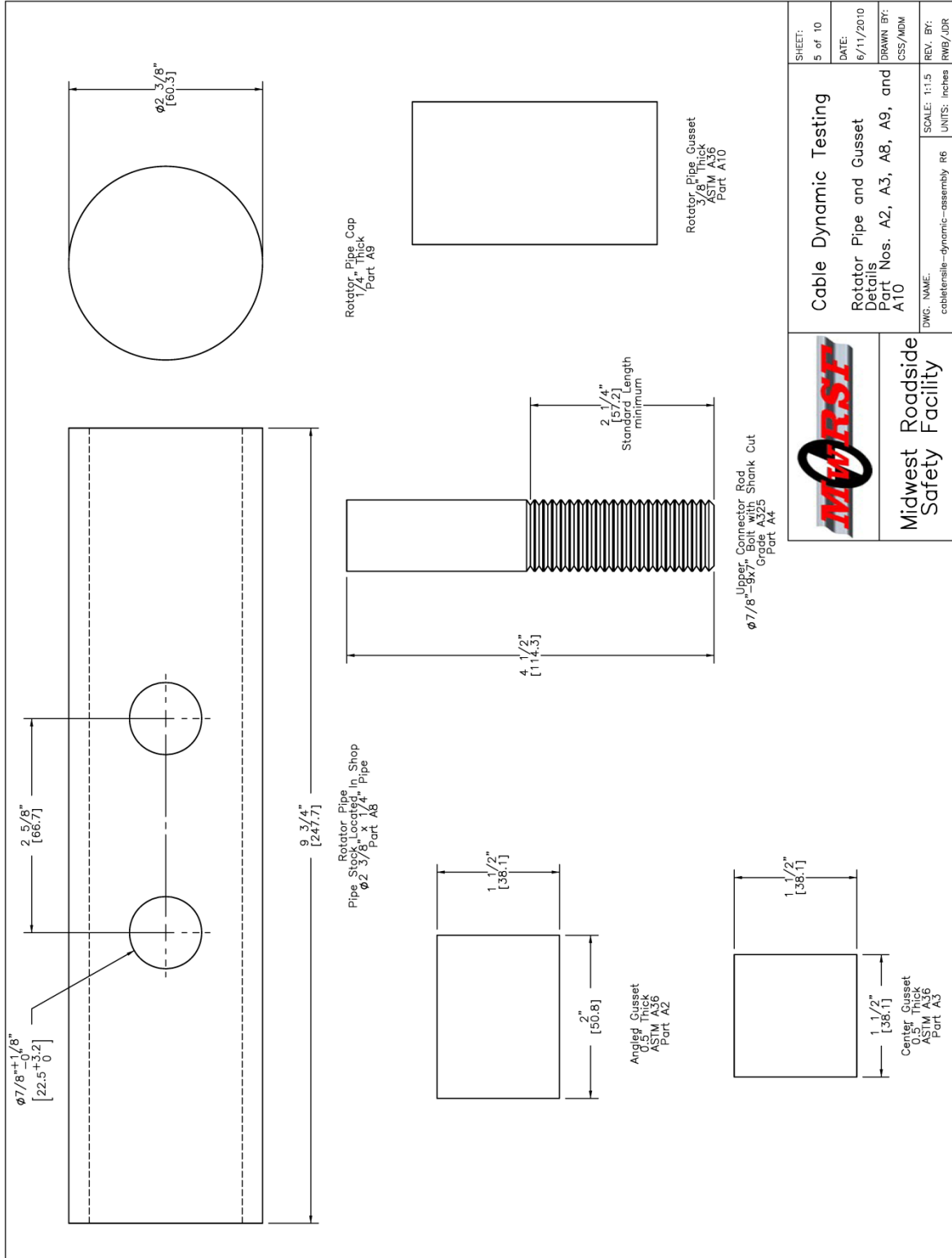


Figure 47. Rotator Pipe Assembly Part Details

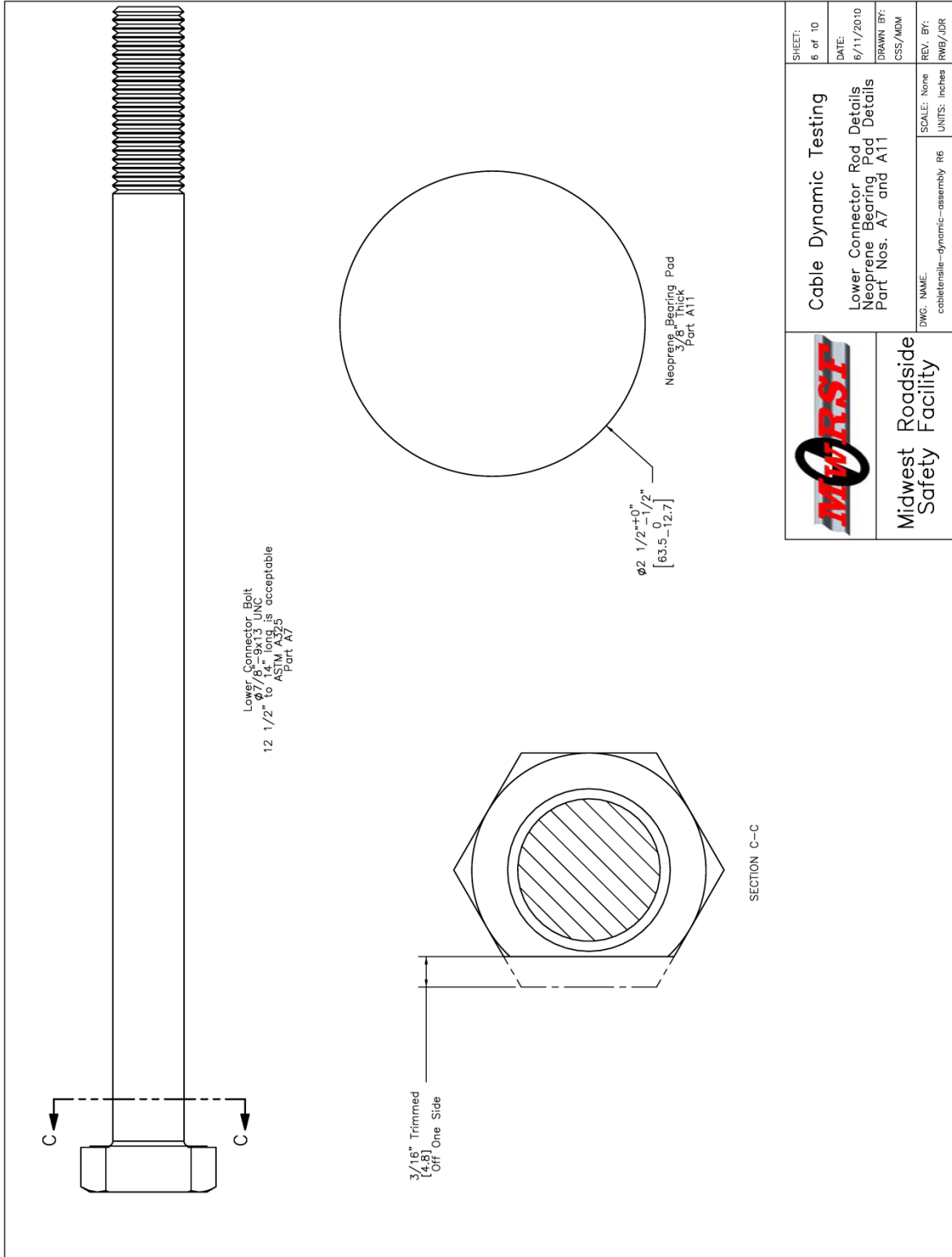


Figure 48. Lower Connector Rod and Neoprene Bearing Pad Details

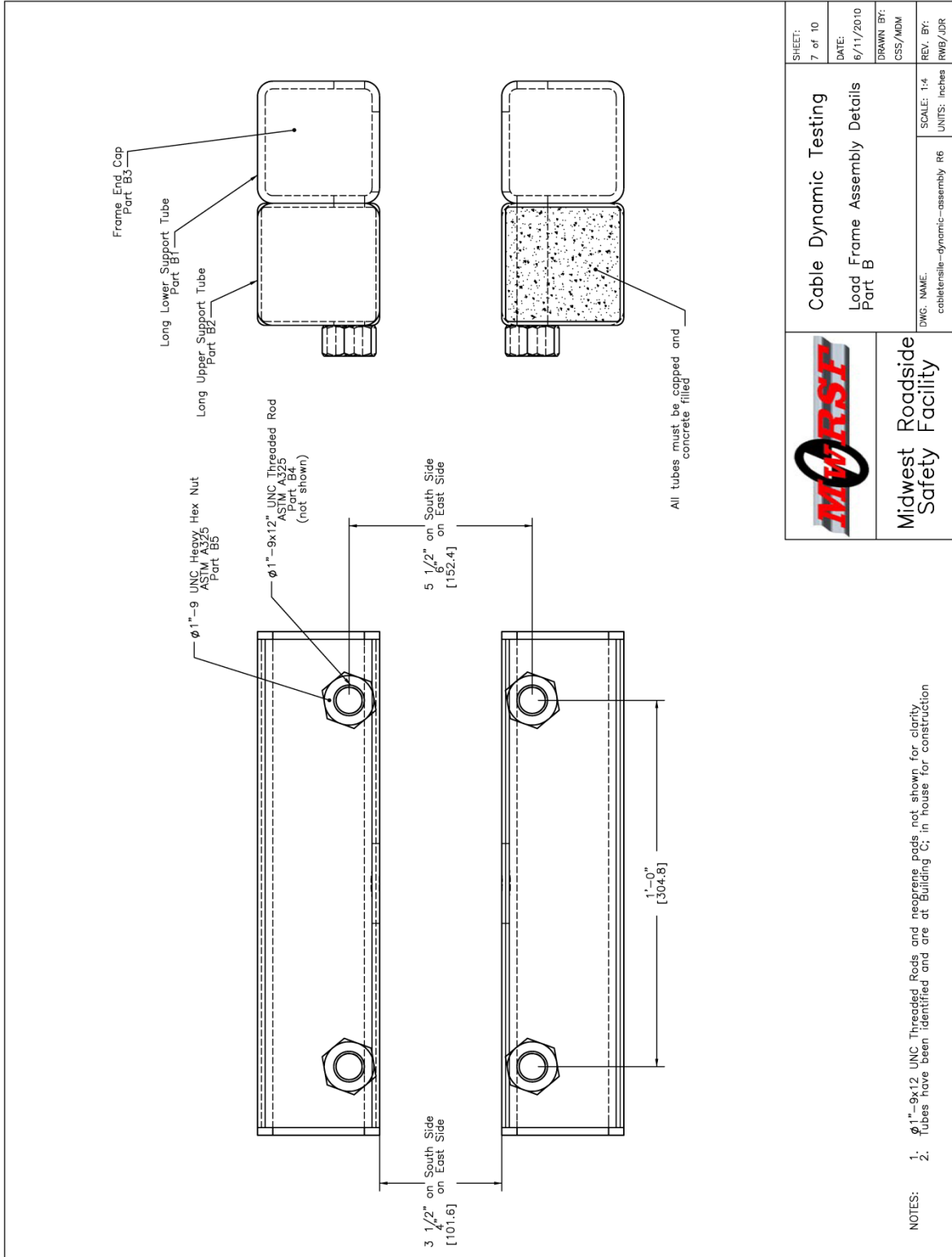


Figure 49. Load Frame Tube Details

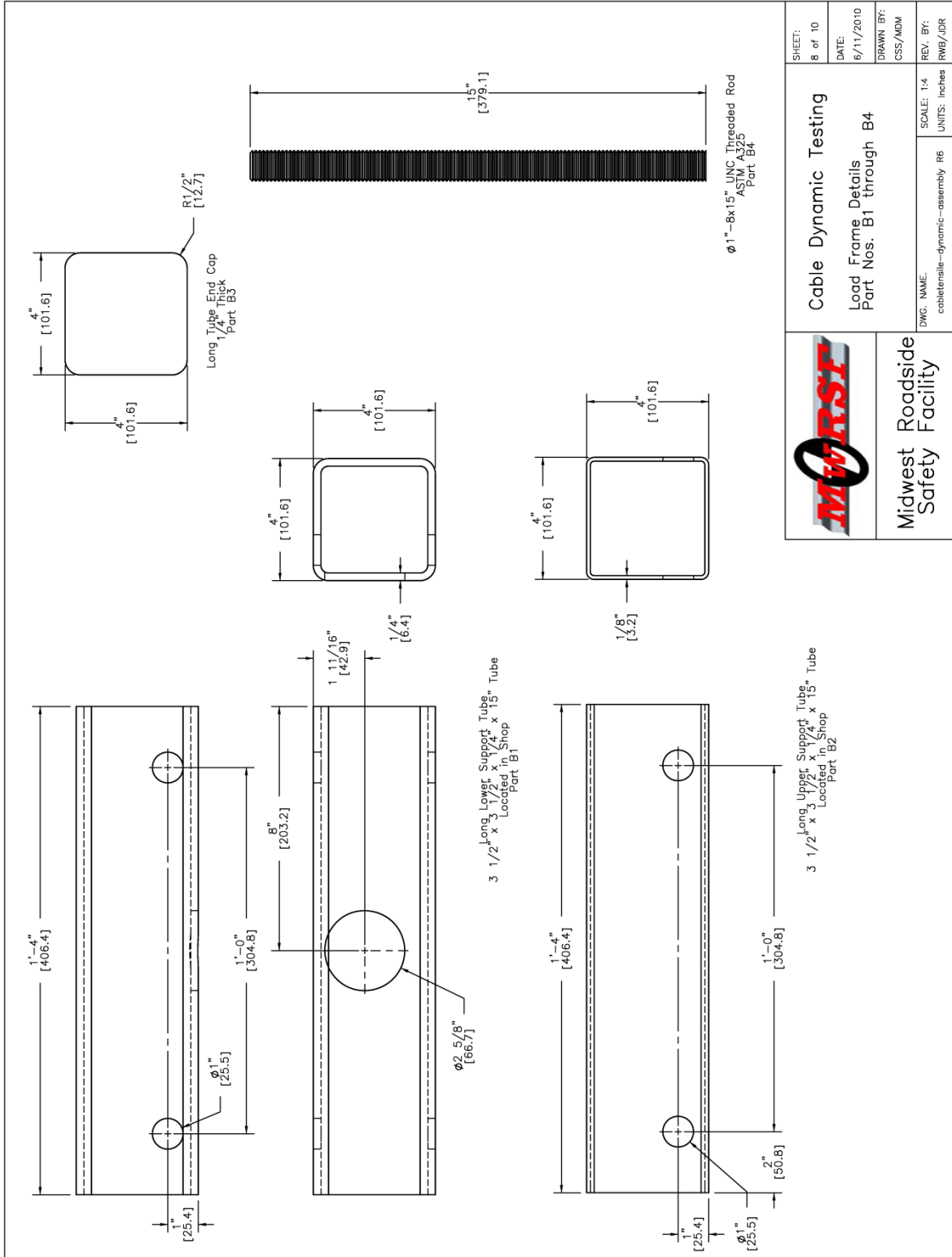


Figure 50. Load Frame Tube Details

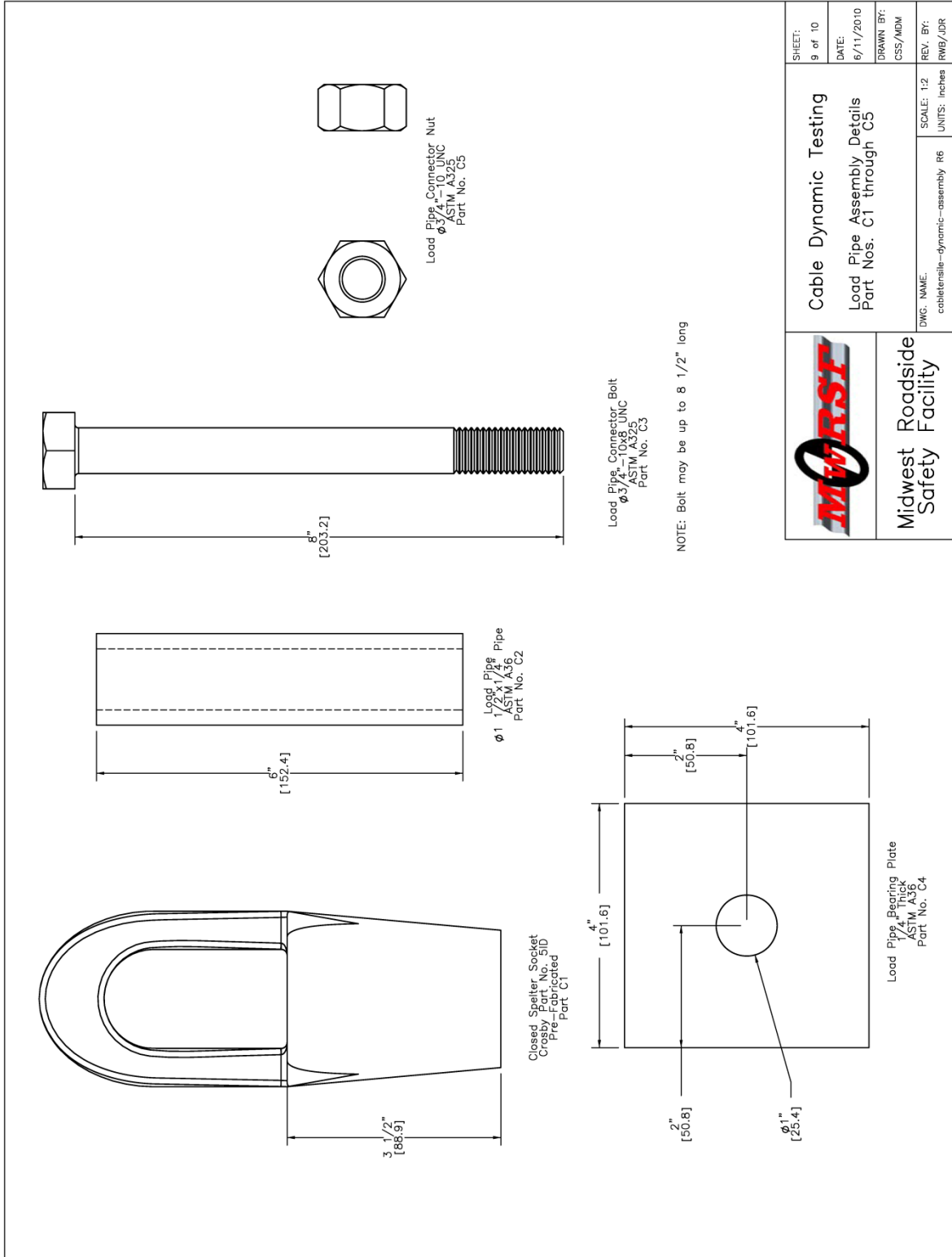


Figure 51. Load Pipe Assembly Details



Figure 52. Load Frame, Test Nos. DTC 1-3

Two string potentiometers were used to measure the dynamic strain in the wire rope during test no. DTC-1. In this test one string potentiometer was attached at a reference point on the wire rope and the second string potentiometer was wrapped pulley-style from the reference point to a measurement point and back to the reference point to create a pulley with a mechanical advantage of 2.0. String potentiometer data was also captured at 10,000 Hz using a 10 V input voltage supply and a gain of 1. String potentiometers used to measure strain in test no. DTC-1 are shown in Figure 53. The string potentiometers were UniMeasure Inc. string potentiometers with sensitivities of 12.40 and 19.45 mV/V/in. (0.488 and 0.766 mV/V/mm) and a 40-in. (1,016-mm) displacement travel.

Teflon tape was used to reduce friction at the downstream measurement point, and both string potentiometer measurement strings were routed through a static alignment notch in a guide post. The guide post was fastened to a wooden blockout bolted to the steel sway resistance pipe support frame. The two alignment notches were configured at equal heights above and below the static centerline of the wire rope, and were both routed through the reference point, so that a simple subtractive measurement of the dynamic displacements could be used to generate approximate bulk dynamic strains. Stoppers were placed in front of the guide post alignment notches to prevent the string potentiometer strings from unwinding too quickly in the event of a wire rope fracture within the sway resistance pipe. Similar stoppers were placed on the measuring side of the guide post to prevent excessive string pullout in the event of a wire rope fracture upstream of the sway resistance pipe.

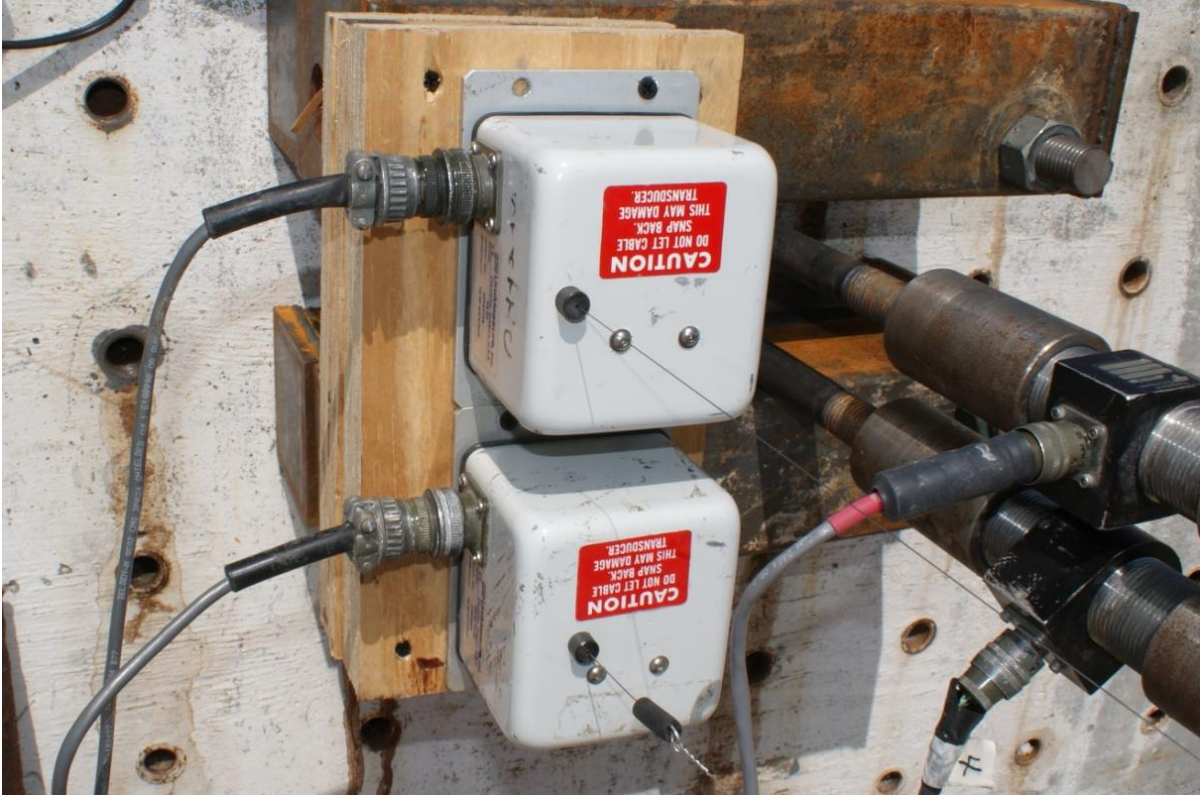


Figure 53. String Potentiometer Alignment and Configuration Details, Test No. DTC-1

Four high-speed digital video cameras, each with a frame rate of 500 frames/sec, were used in the tests. One high-speed digital video camera tracked the motion of the load frame, and was positioned overhead of the upstream load frame with a sight that included the sway resistance pipe. One high-speed digital video camera recorded the motion of the wire rope downstream of the sway resistance pipe, and one camera recorded the motion of the downstream wire rope end fitter. In test no. DTC-1 the remaining high-speed digital video camera recorded the entire dynamic jerk test event. Following this test, however, it was determined that the overall test view was not very helpful for high-speed video analysis, because the wire rope appeared too small in the frame. In test nos. DTC-2 and DTC-3, high-speed digital video camera captured the wire rope upstream and downstream of the sway resistance pipe in close-up views. In test no. DTC-2, since no tow cables were used, the downstream wire rope end fitter was coincident with the bogie position.

7.3 Test No. DTC-1

Test no. DTC-1 was conducted with a test speed of 23.89 mph (35.04 ft/s, or 10.68 m/s). The measured bogie weight was 4,987 lb (2,262 kg). The bogie track was laid such that the bogie would become free-wheeling 215 ft (65.5 m) downstream of the load frame. The selection of a time zero impact time was arbitrary as the wire rope loaded up gradually and did not become taut until the load was large on the end frame. Time zero was delineated as the time when the bogie was approximately 219 ft - 2 in. (66,802 mm) downstream of the load frame since this occurred just prior to a large increase in the wire rope tension. Sequential photographs of the test are shown in Figure 54. Photographs are shown in Figures 55 through 59.

The bogie left the guidance track and was rapidly decelerated by the wire rope. At 0.105 sec, two strands of the test length of wire rope fractured inside of the load pipe. The

fractured strands immediately began to unwind around the remaining strand. At 0.130 sec, the remaining strand was pulled through the epoxy and four of the wires fractured inside of the closed spelter socket. The freed strand struck the string potentiometer measurement string and fractured it, and was pulled along the length of the two other fractured strands. This created a circular whipping effect, which ground down the upstream and downstream openings of the sway resistance pipe. When the final strand was pulled past the fractured ends of the two other strands, the wire rope rebounded downstream.



0.000 sec



0.080 sec



0.120 sec



0.160 sec



0.000 sec



0.080 sec



0.120 sec



0.160 sec

Figure 54. Sequential Photographs, Test No. DTC-1



Figure 55. Bogie and Wire Rope Final Position, Test No. DTC-1

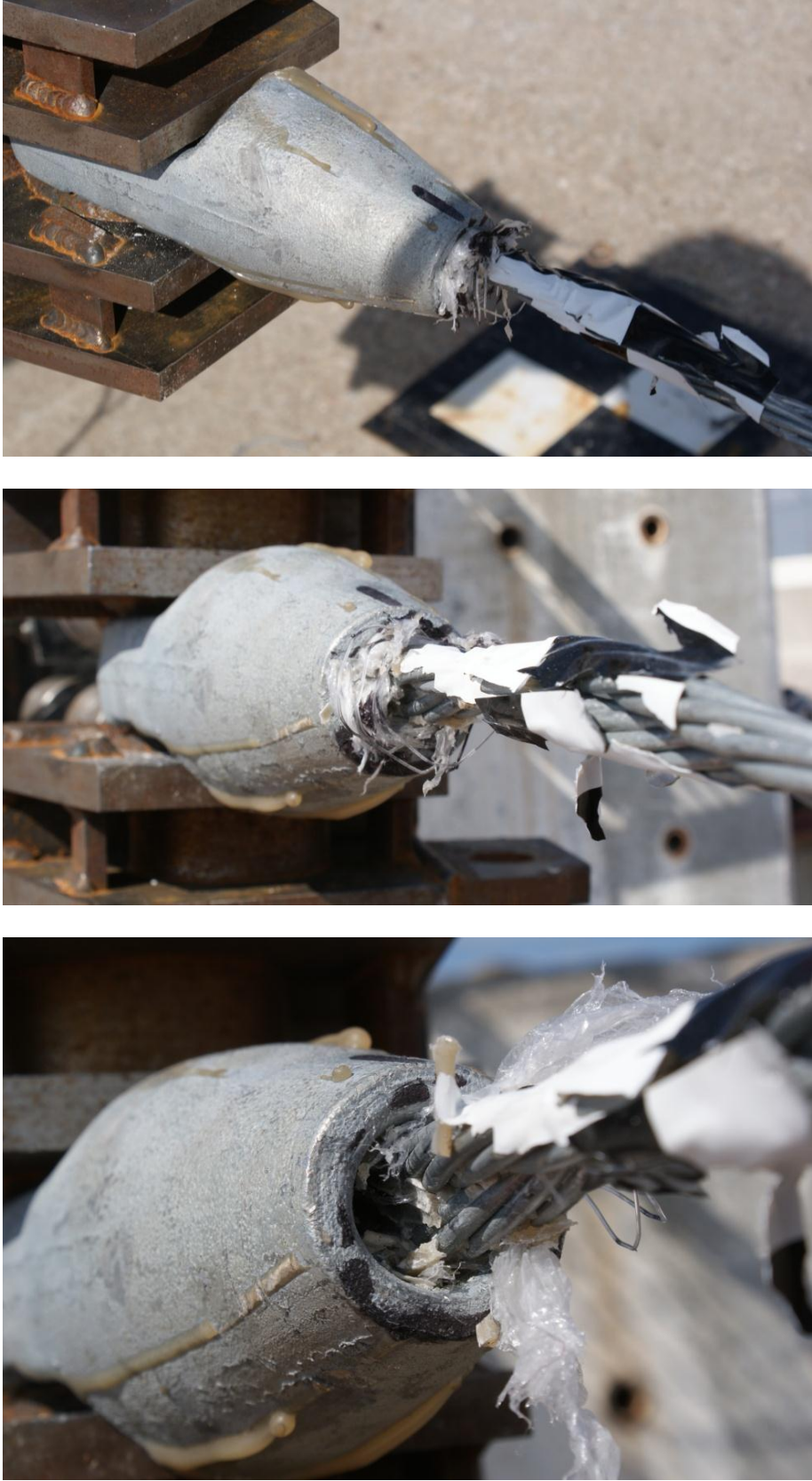


Figure 56. Upstream Wire Rope Damage at Socket, Test No. DTC-1

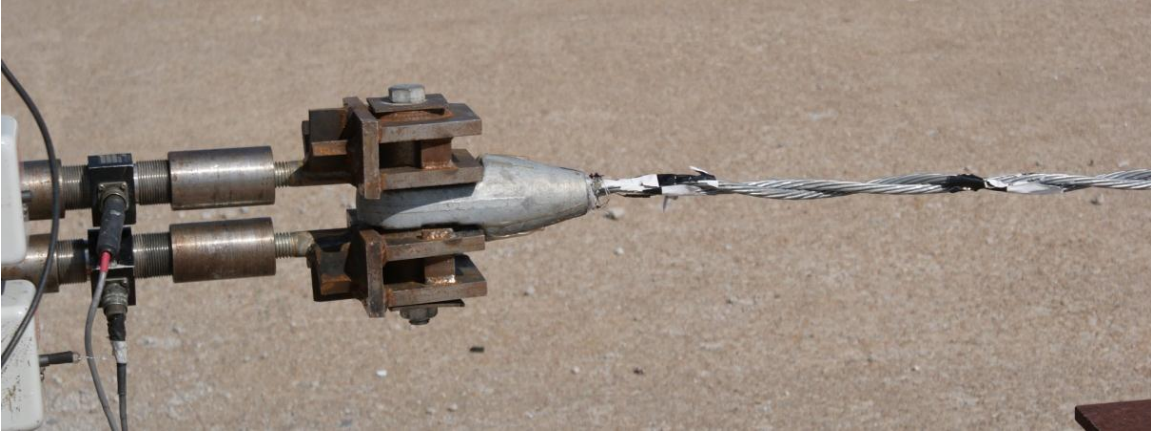


Figure 57. Upstream Wire Rope Damage, Test No. DTC-1

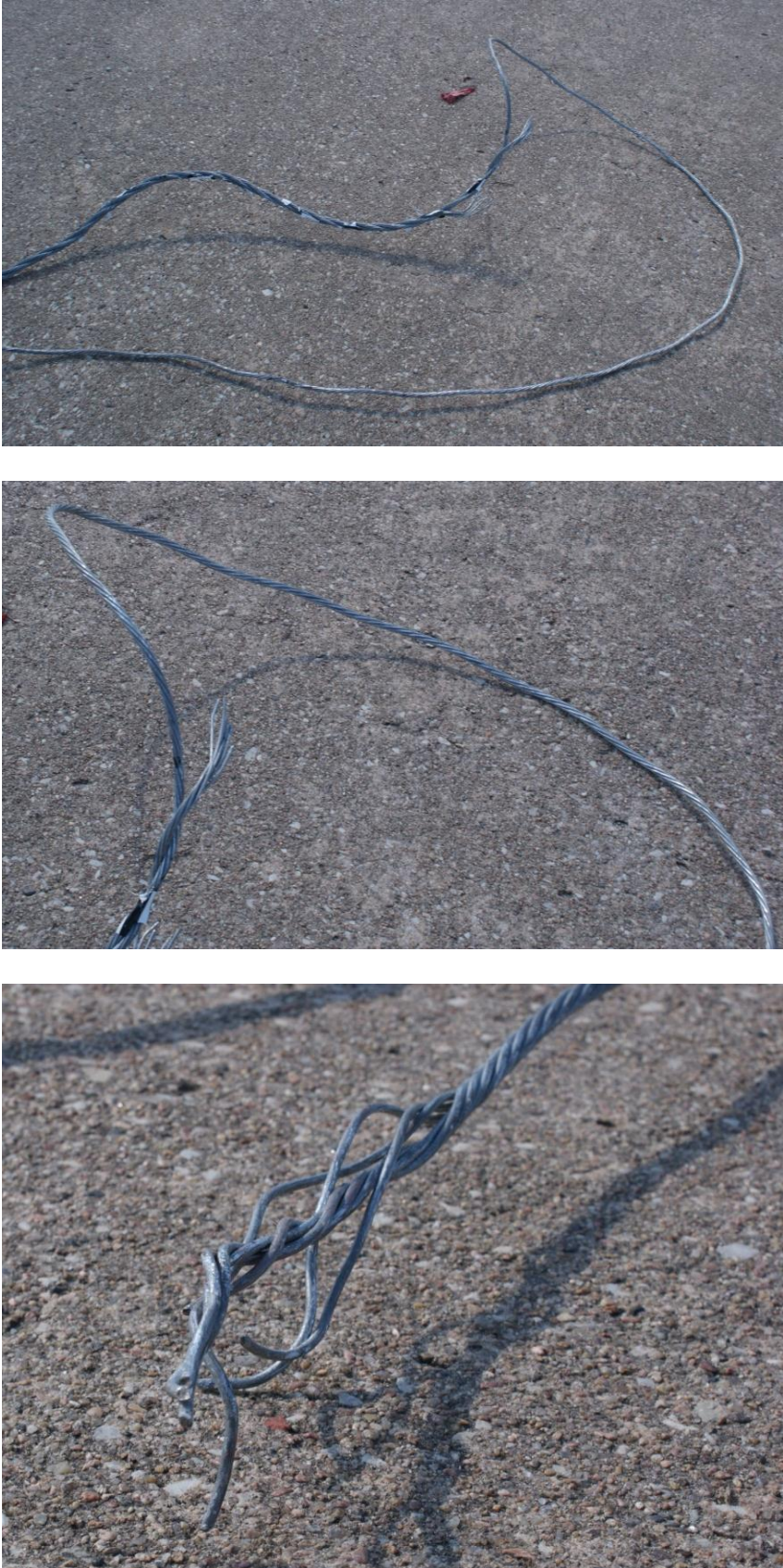


Figure 58. Downstream Wire Rope Damage, Test No. DTC-1

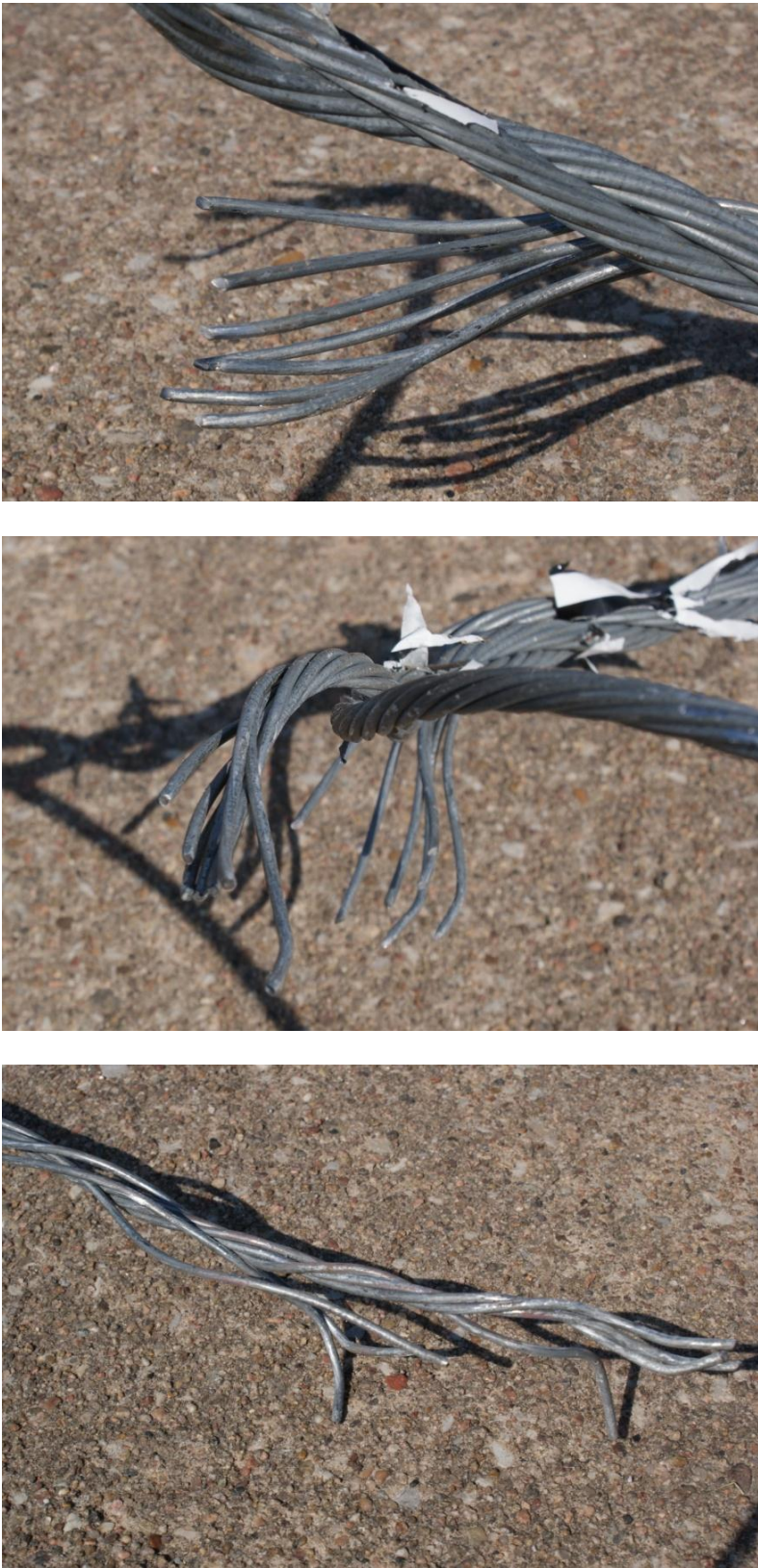


Figure 59. Downstream Wire Rope Damage, Fracture Locations, Test No. DTC-1

Load cell data from test no. DTC-1 is shown in Figure 60. The wire rope was straightened under a low load, but this was not considered a part of the actual jerk test event. Time zero in the jerk test was determined to be the time in which the wire rope was effectively fully-extended, if the rope had no resultant tensile load. A peak load of 41.07 kip (182.7 kN) was recorded at 104.8 ms, corresponding to the first two strand fractures near the downstream end of the load pipe. The second peak load occurred at 131.1 ms with a peak value of 30.57 kip (136.0 kN), which corresponded to the secondary fracture of the remaining strand at the wire rope end fitter. The load recorded by the load cell after the second fracture corresponded to the rebound of the long load cell frame members.

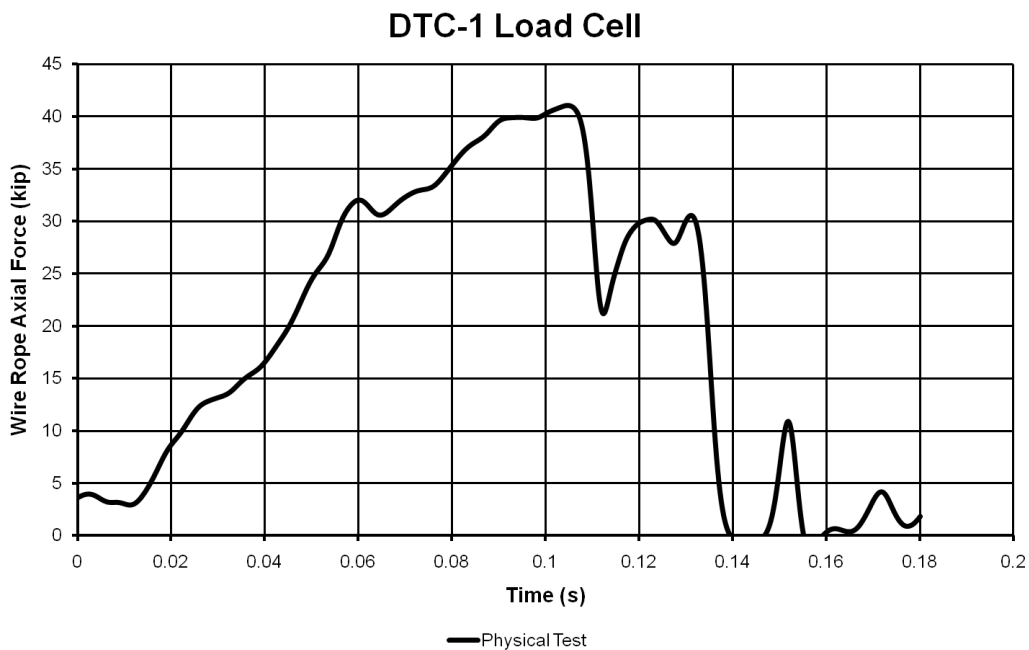


Figure 60. Load Cell Data, Test No. DTC-1

Bogie displacement in test no. DTC-1 is shown in Figure 61. The bogie was smoothly decelerated until fracture of the wire rope. Following the wire rope fracture, the bogie continued at a nearly constant velocity. The bogie displacement at the first two strand fractures was 39.3 in.

(998 mm) of total wire rope and tow cable deflection while the bogie displacement at the last remaining strand fracture was 46.9 in. (1,191 mm).

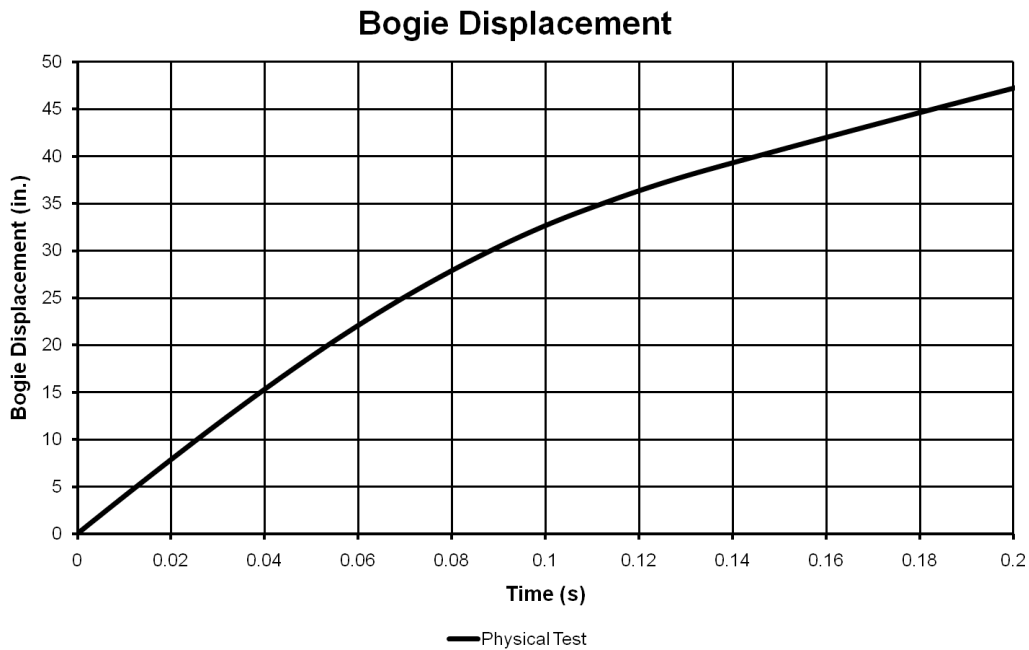


Figure 61. Bogie Displacement, Test No. DTC-1

The bogie velocity is shown in Figure 62. The bogie had a test speed of 33.3 ft/s (10.14 m/s). The wire rope initially loaded up under low-load, stretching the wire rope and pulling it off of the ground. Small bending waves were generated due to the initial geometry eccentricity of the wire rope. The bogie velocity continued to decrease until 170 ms, when all three strands of the wire rope were fractured and the separated sections of wire rope rebounded away from the fracture location.

Bogie acceleration recorded in the test is shown in Figure 63. The acceleration curve was relatively smooth, corresponding to the nearly linear load-strain relationship through 100 ms, followed by the fracture of two strands of the wire rope. The bogie acceleration plot closely mimicked the load cell data, indicating that the longitudinal tensile wave speed was very similar

to that of a solid steel bar, and tensile waves were transmitted very rapidly from one end of the wire rope installation to the other.

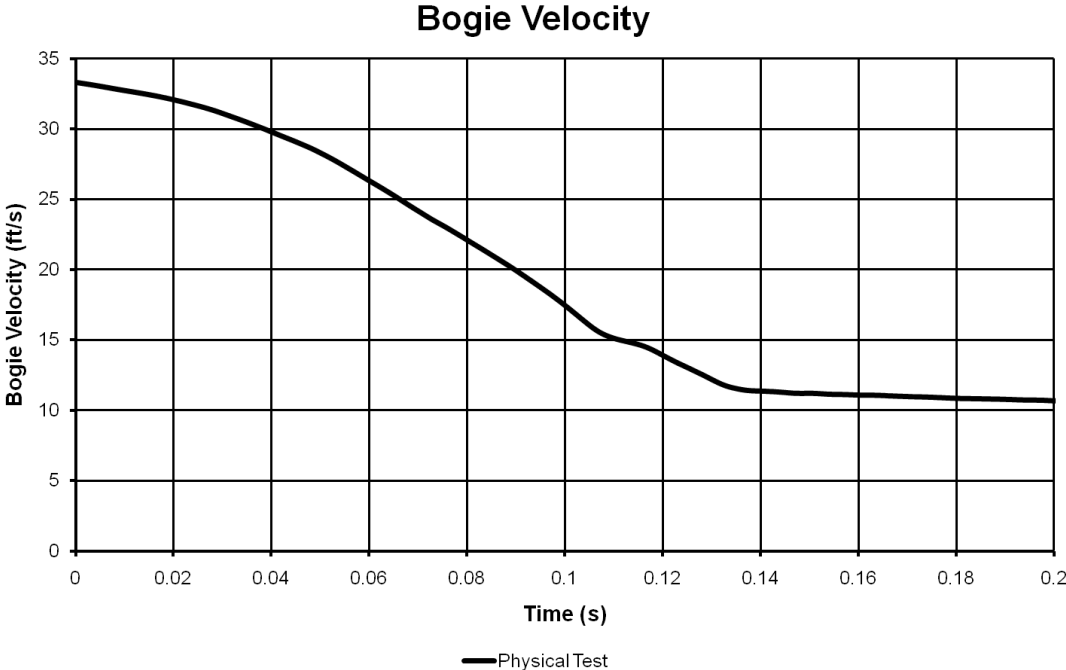


Figure 62. Bogie Velocity, Test No. DTC-1

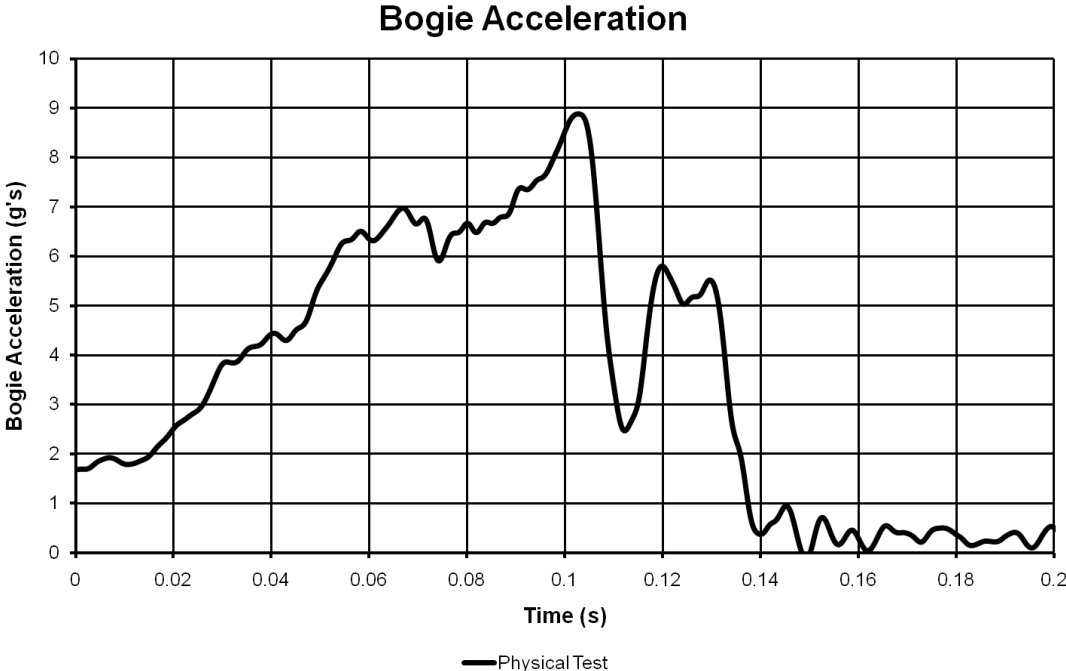


Figure 63. Bogie Acceleration, Test No. DTC-1

The bogie acceleration was non-zero at the effective time zero because the wire rope was being pulled taut, and lifted off of the ground. The acceleration slope gradually-increased over the transition period between release from the downstream chute and effective time zero.

String potentiometer data was captured and processed, as shown in Figure 64. The strain was calculated based on the total measurement length between the reference and measurement points of 84 in. (2,134 mm). The strain was calculated by dividing the net displacement between the extensometers by a factor of 2.0, then dividing by the nominal gauge length. The strain at fracture was 0.104, which is less than the strain derived from the quasi-static tensile testing curve for the same load.

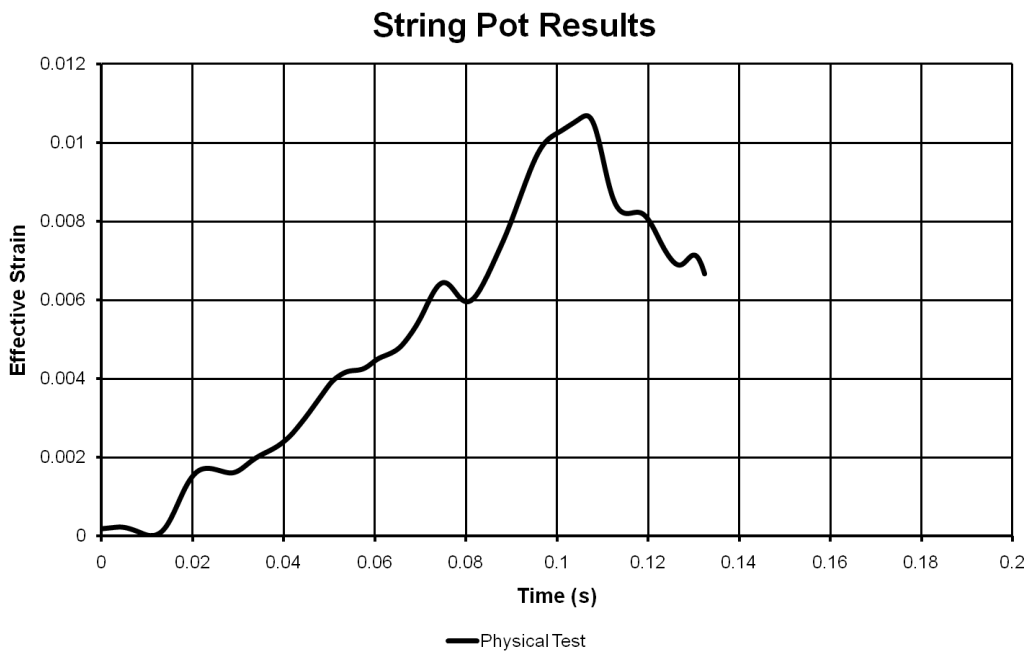


Figure 64. String Potentiometer Strain Calculation, Test No. DTC-1

The total strain and load cell results were cross-plotted and compared to the quasi-static testing load-strain plot, as shown in Figure 65. It was observed that a dynamic strain-reduction (or alternatively, an axial stiffening) factor was present in the results, though the load and strain were not recorded at the same location. The dynamic stiffening factor was approximately 2.15 at

a strain rate of 0.10. The difference in fracture strain behavior was likely caused by a combination of the following: (1) viscoelastic effects in wire rope caused by internal friction, (2) the long gauge length which allowed for intermediate bends to form, and (3) relatively low sensitivity of the string potentiometers.

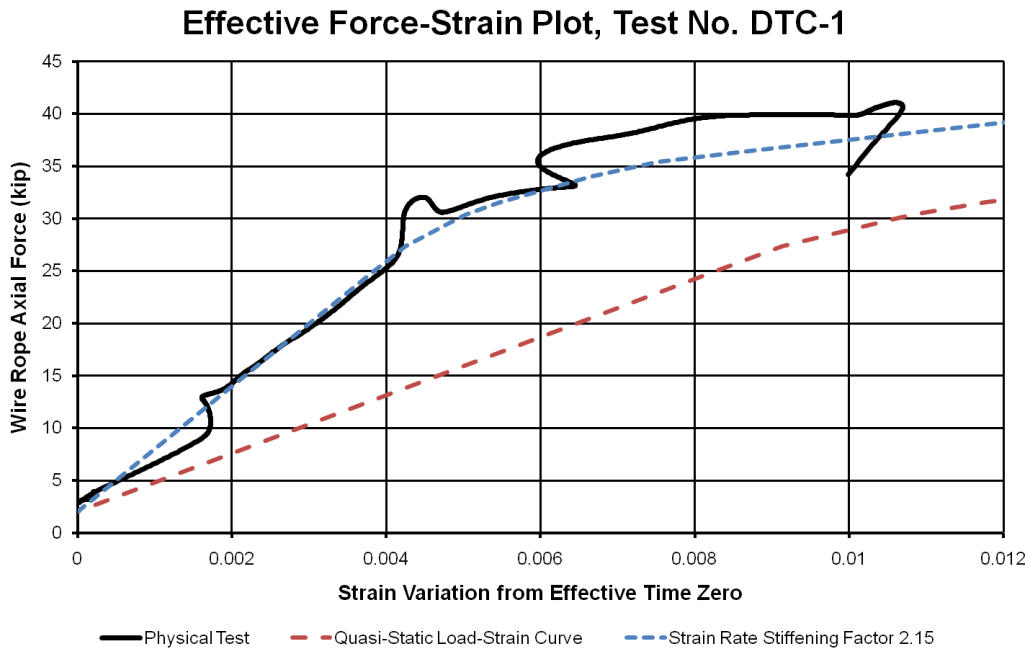


Figure 65. Force-Strain Comparison of Test No. DTC-1 and Quasi-Static Tensile Testing

The strain rate dependence factor was likely most affected by the long gauge length. When strain is measured quasi-statically, the length over which the strain is measured is assumed to be straight, and the entire section is assumed to be at the same strain at the same time. However, the long gauge length in this test led to a stiffening effect, since it cannot be assumed that the strain was everywhere uniform and that the wire rope is straight between the reference and measurement points. Small bending oscillations could have contributed to the overall actual length, and high-frequency, small amplitude bending waves were present. Therefore, the string potentiometers were not determined to be an accurate measure of the wire rope dynamic strain.

7.4 Test No. DTC-2

Test no. DTC-2 was conducted with a 220-ft (67.06-m) test length. The targeted bogie speed at the exit of the guidance track was 25 mph (11.18 m/s). Sequential photographs of test no. DTC-2 are shown in Figure 66. Photographs of the test are shown in Figures 67 through 69. Load cell results are shown in Figure 70.

The bogie was accelerated and the long test rope loaded up to a maximum of approximately $\frac{1}{3}$ of the breaking strength, or 14.29 kip (63.57 kN), prior to fracture. The wire rope disengaged from the end fitter and was pulled upstream toward the upstream end fitter, and the majority of the wire rope came to rest downstream of the sway resistance pipe.

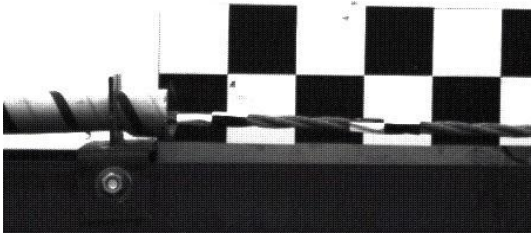
The cause of the premature pullout of the wire rope from the socket at the downstream (bogie) end of the wire rope was investigated. The poured socket was investigated, and it was observed that wire distribution within the epoxy was comparable to the distribution in the terminations used in test no. DTC-1: it was moderately uniform across the cross-section. No dirt or debris was present during pouring, and the wire rope had been degreased and had the galvanization stripped prior to setting the epoxy. Three observations were made which may have contributed to the low-load socket release:

- (1) Pouring temperatures were approximately 42-45°F at the time of the socketing, which is only barely above the minimum recommended pouring temperature of 40°F. The low pouring temperature extended the curing time by an order of magnitude, as curing occurred for three to five hours instead of the typical 30 minutes in warmer weather. The temperature remained between 35 and 50°F prior to the test, because the wire rope was tested late in the year.

(2) Prior to the test, the initial configuration of the wire rope, while lying on the ground, was a long arc. As the bogie was accelerated, the downstream-most section of the wire rope necessarily supported all of the tension in accelerating the upstream ropes, which may have led to stress concentration. The friction with the wire rope on the ground and increase in length of the accelerated wire rope artificially increased the tension in the downstream section of the wire rope with respect to the upstream end. This was not a significant factor using the tow cables, since four tow cables were used in lieu of a single test wire rope. The four tow cables would be better able to distribute the load across the four ropes instead of causing a tension build-up in a single rope. Such a setup may incur a much higher load at the downstream socket, thus facilitating failure.

(3) Epoxy penetration around the wires was reduced due to the cold pouring temperature, as the epoxy became more viscous at the low temperature. However, the portion of the socket nearest to the bottom (wire rope entrance hole) typically did not have sufficient space for the epoxy in that region to carry much load, and long pouring times allowed the viscous solution to fill most of the socket cavity. Furthermore, fracture and "blow-out" of the epoxy near the thinner orifice was evident in many of the dynamic bending tests at loads less than the nominal breaking load of wire rope. Therefore, though this may have contributed to the low-load wire rope pullout, it was not believed to have a significant effect on the load sustained by the wire rope.

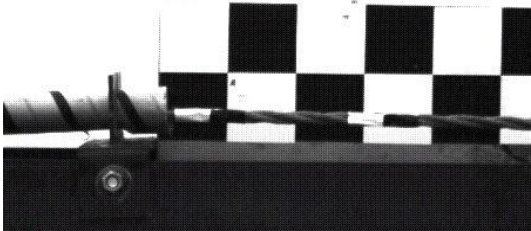
Because test no. DTC-2 was unable to sustain sufficient load the useable data from the test was limited. Therefore, this test was considered an outlier and was not analyzed further.



0.000 sec



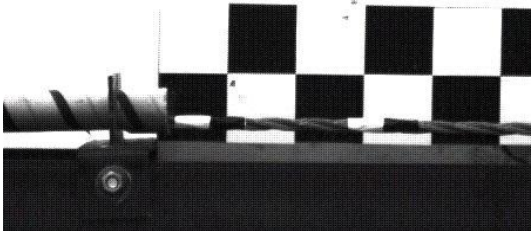
0.000 sec



0.050 sec



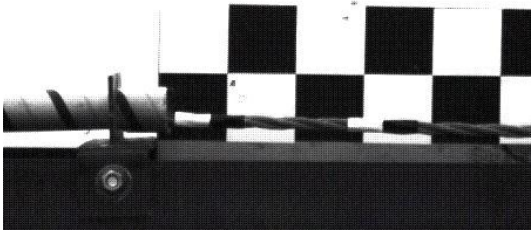
0.050 sec



0.088 sec



0.088 sec



0.110 sec



0.110 sec

Figure 66. Sequential Photographs, Test No. DTC-2



Figure 67. Final Position of Wire Rope, Test No. DTC-2

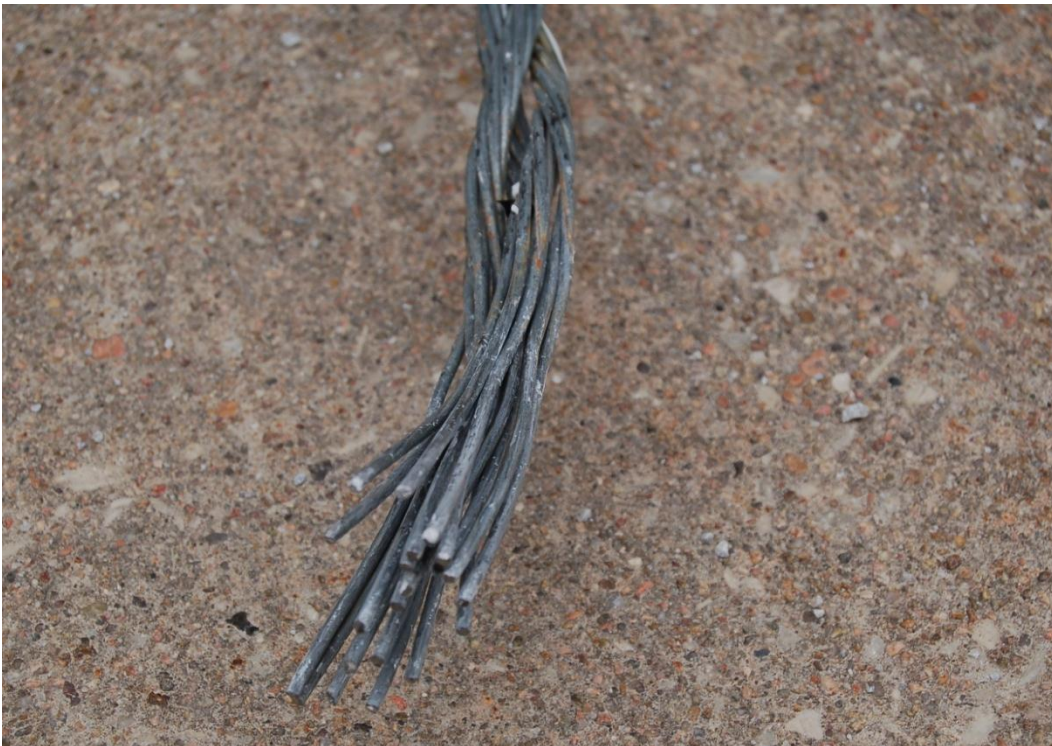


Figure 68. Downstream Wire Rope Pullout, Test No. DTC-2



Figure 69. Pullout of Downstream Wire Rope Socket, Test No. DTC-2

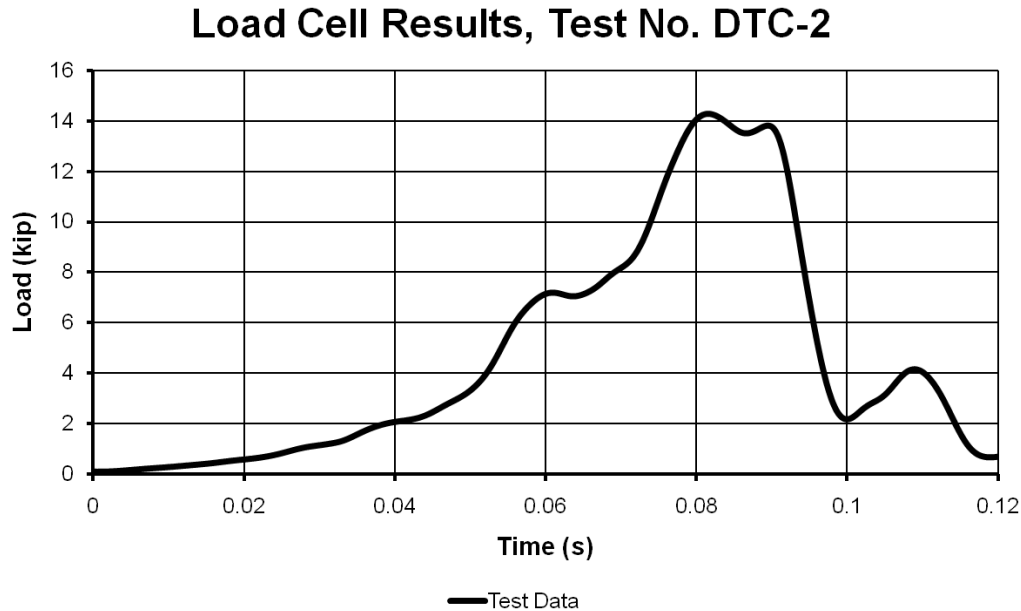
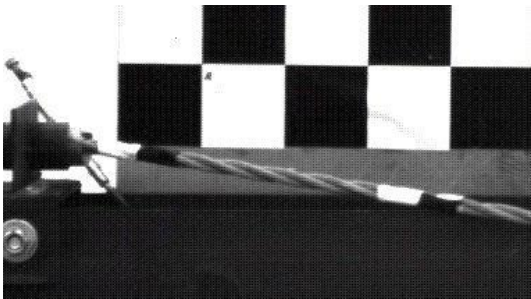


Figure 70. Load Cell Results, Test No. DTC-2

7.5 Test No. DTC-3

Test no. DTC-3 had a test length of wire rope of 90-ft (27.43 m) and a tow cable length of 130 ft (39.6 m), such that the total length of wire rope was 220 ft (67.1 m), as in previous tests. Sequential photographs of test no. DTC-3 are shown in Figure 71. Photos of the wire rope and bogie after the test are shown in Figures 72 and 73. Post-testing photographs were limited due to an impending storm approaching shortly after the conclusion of the test.

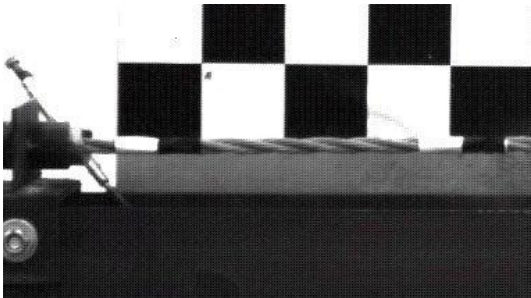
In test no. DTC-3, the bogie was accelerated to a speed of 23.98 mph (10.72 m/s) at the end of the guidance track. Load cell plot from test no. DTC-3 is shown in Figure 74. The wire rope tightened up and reached a peak load of 29.77 kip (132.4 kN) at 98.8 ms, which was sooner than the fracture load in test no. DTC-1. Furthermore, significant oscillations in the tension plot indicated the presence of many more bending waves in test no. DTC-3 than in DTC-2 or DTC-1. Though the bogie speed and the test setup were nearly identical between test nos. DTC-1 and



0.000 sec



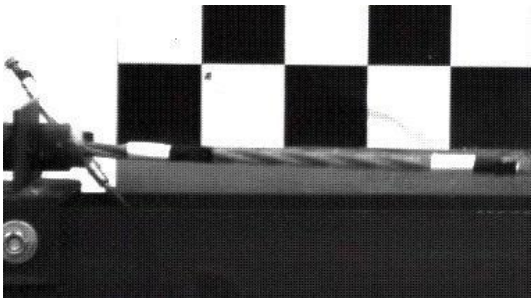
0.000 sec



0.050 sec



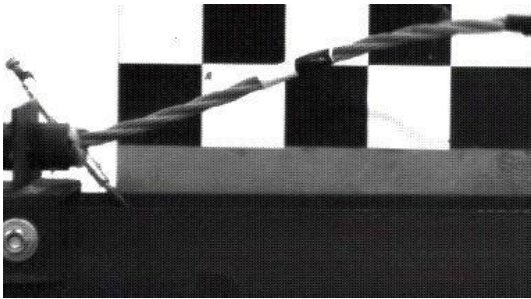
0.050 sec



0.084 sec



0.084 sec



0.120 sec



0.100 sec

Figure 71. Sequential Photographs, Test No. DTC-3



Figure 72. Wire Rope Pullout of Downstream Socket, Test No. DTC-3



Figure 73. Upstream Wire Rope Socket, Test No. DTC-3

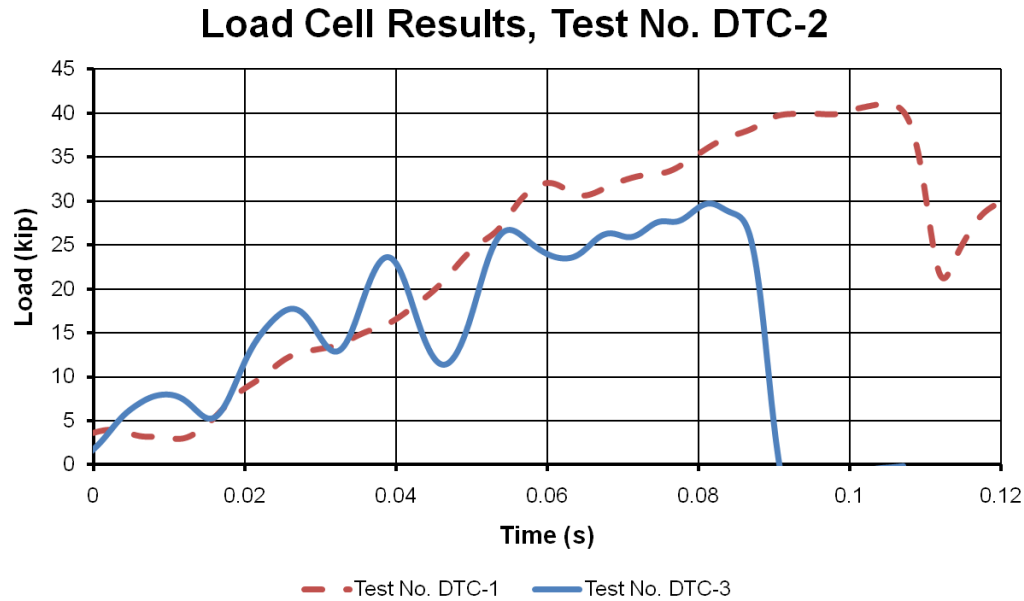


Figure 74. Load Cell Comparison, Test Nos. DTC-1 and DTC-3

DTC-3, the load cell results varied considerably. The wire rope was pulled through the epoxy on the downstream end socket, as occurred in test no. DTC-2.

Again, causes of the unexpected wire rope release from the socket were investigated. It was noted that the wire rope tested in test no. DTC-3 was socketed at the same time with the same batch of epoxy as test no. DTC-1. Preparation of the wires and socket was also virtually identical to that in test no. DTC-1. The wire rope in test no. DTC-3 had been exposed to sunlight for approximately 65 days prior to testing, and should have been fully cured. The test temperature at the time of the test was approximately 45°F, which was nearly the same as in test no. DTC-2.

Therefore, researchers came to three conclusions: (1) the coefficient of thermal expansion of the epoxy (though unknown) is different than the coefficient for wire rope, causing internal shear and axial stresses at the end fitter locations; (2) temperature effects on the bonding strength of wire rope and epoxy are not yet fully understood; and (3) the initial layout of the tow cables

may have made a significant contribution to the early wire rope release from the socket. Further research is necessary to investigate temperature and initial geometry effects.

7.6 Discussion

The temperature dependence of the wire rope end sockets is critical to the sustained performance of the system. If the epoxy bonding strength is temperature-dependent, then cable barrier systems impacted in cold temperatures may have a lower capacity than those in higher-temperature environments. In critical impact scenarios this could lead to vehicle penetration, rollover, or complete loss of tension in the wire rope due to wire rope release from end terminals. Investigation into the temperature dependence of wire rope is critical to ensuring the continued safety of passengers in errant vehicles that impact cable barriers. Namely, a recent shift toward high-tension cable barrier systems required alternative methods of terminating wire rope than the traditional mechanical wedge and, as such, will necessitate further investigation.

Dynamic tensile data showed good correlation with simulation results, but further refinement was not pursued since the dynamic tension tests are less pertinent to modeling wire rope in cable barrier systems than dynamic bending tests, which are discussed in later chapters. Though the dynamic tensile jerk response of wire rope *is* important in impact events, the strain rate of wire rope, and thus load rate, is typically very small even for sizeable cable barrier systems. Though the dynamic tension tests were important to probe the dynamic viscoelastic effects which occur due to high strain-rate loading, the results are less important in the preliminary phase of the wire rope development than the results of dynamic bending simulations.

7.7 Summary

Wire rope was tested in dynamic jerk-type tensile testing. A bogie vehicle was accelerated to a target speed of 25.0 mph (11.2 m/s) at the end of a guidance track, and was

secured to four tow cables and a test wire rope. In test no. DTC-2 the tow cables were not included. Tensile results from the load cells were compared in all three tests, and it was determined that only the results of test no. DTC-1 were applicable for comparison with simulated dynamic tensile testing simulations. The fracture load of 41.07 kip (182.7 kN) was believed to be representative of the actual tensile rupture load of wire rope since the wire rope fractured away from the end supports in test no. DTC-1. These results will be used to compare to dynamic tension simulations.

7.8 Future Work

The closed spelter sockets used in the tests to secure the wire ropes did not reach the fracture strength of the wire rope in tension, which leads to considerable concern for application in cable guardrail systems. Epoxy sockets are generally not recommended for use in dynamic-loading applications [2], but studies on the usefulness of socketed wire ropes for use in transitioning low-tension cable barrier systems to high-tension have been conducted [41]. Testing on the temperature dependence of the closed spelter sockets and epoxy compound should be conducted to ensure that cable guardrail systems maintain integrity over a wide range of temperatures. In addition, wire rope temperature dependence should be investigated to determine the effect that temperature has on the wire rope tensile properties and internal friction.

Though analytical investigations into hysteresis of wire rope in dynamically-varying tension have been conducted, no investigations have focused on the relatively simple section of 3x7 wire rope. Due to the internal friction in the wire rope, internal wire rope friction may contribute to load hysteresis. This effect may be modeled as viscoelastic damping in future wire rope models for general simplicity. The actual strain rate dependence should be investigated, and temperature effects should be included in the viscoelasticity investigation. Further information

about wire rope strain rate dependency can increase the existing knowledge base of wire rope used in cable guardrail systems, and will provide useful study parameters for future improvement of the wire rope simulation model.

8 MODELING WIRE ROPE IN DYNAMIC TENSION

8.1 Motivation

The dynamic tension tests were simulated in LS-DYNA to refine the wire rope model and generate accurate strain rate dependence. Strain rates in typical wire rope barrier impacts are much less than the strain rates induced in wire rope during the dynamic tensile testing. Nonetheless, the ability to capture wire rope response in quasi-static and high-strain impacts will instill greater confidence that the model can capture the intermediate strain rates common to cable barrier impact situations. Furthermore, this testing series clearly indicated whether or not changes were necessary to the wire rope model when it was tested under dynamically-varying tension.

8.2 General Model Description

The baseline model of test no. DTC-1 consisted of a long, straight series of 0.500-in. (12.7-mm) long beam elements with a total length of 89 ft-6 in. (27,280 mm). The wire rope extended from the simulated end socket through a sway resistance pipe. Since the bogie was located very far from the tested wire rope, the bogie dynamics did not affect cable reaction and the bogie was represented by a point mass.

The sway resistance pipe consisted of a cylinder of shell elements with a thickness of 0.25 in. (6.4 mm). The sway resistance pipe was held fixed in space 68 in. (1,727 mm) from the start of the wire rope, and was defined with a rigid material.

The modeled load frame was greatly simplified so that no components of the load frame would come into contact with the wire rope, nor separate or tear apart. The load frame was modeled with a rotator pipe, an upper and lower load cell mount, and a load pin with discrete

point masses used to simulate the components not explicitly modeled. The modeled load frame rotator pipe assembly is shown in Figure 75.

The rotator pipe was defined with shell elements with approximately 0.5-in. (13-mm) edge lengths and a diameter of 2.31 in. (59 mm). The thickness of the rotator pipe was 0.25 in. (6.4 mm). A rigid beam was defined along the axis of the rotator pipe to form the rotational axis. The rigid material was applied to the rotator pipe.

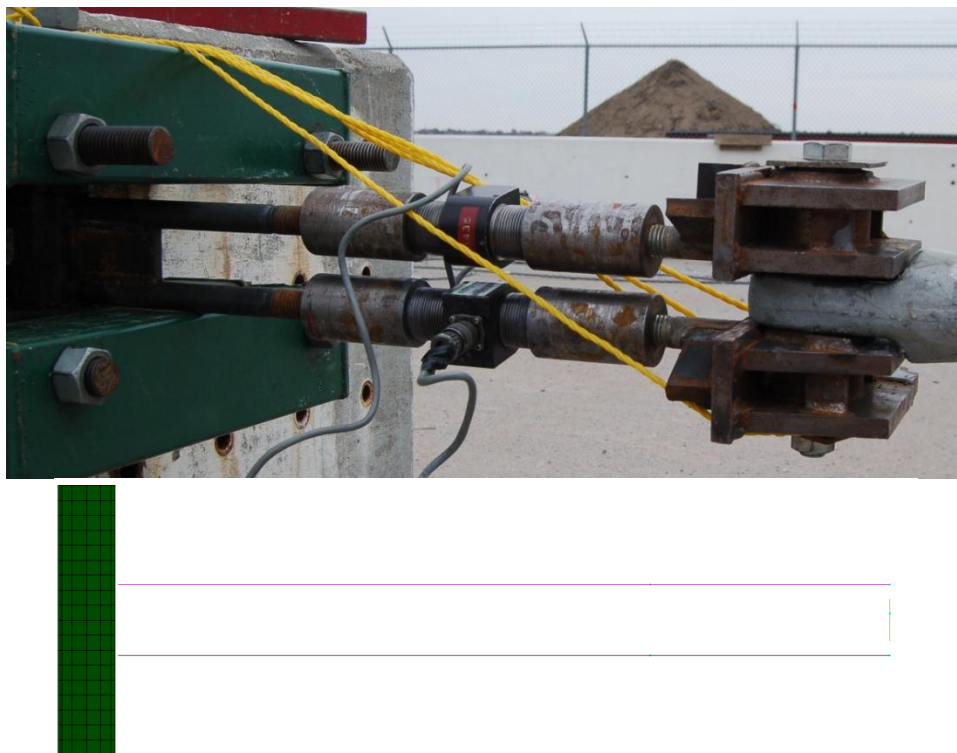


Figure 75. Rotator Pipe Assembly, Test and Modeled, Test No. DTC 1-3

The rotator pipe bolts, threaded rods, load cells, couplers, and brackets were combined into two lengths of beam elements. The beam elements were defined with a rigid material, and a section that was consistent with a $\frac{7}{8}$ -in. (22-mm) diameter bolt shank. Additional discrete masses representing the added weights of the load cell and coupler were defined in the corresponding locations on the beam elements. The masses representing the brackets were also treated as

discrete masses and the mass was added at the centroid of the bracket. Treating the bracket as rigid was justifiable since the deflection of the rotator pipe assembly was very small (less than 1%) with respect to the deflection of the wire rope. That is, there is greater uncertainty intrinsic in the wire rope response than is generated by treating the load frame as rigid. Instead, effort was taken to ensure accurate placement and values of masses in order to obtain a reasonable rotational moment of inertia.

The wire rope was attached to the rotating load frame at the load bar locations. The load bars were vertical beams extending between the upper and lower rotator pipe load cell beams, and had an additional mass defined in the center of the load bar to represent the effect of the wire rope end socket. This greatly simplified the modeling construction without adversely affecting the results because the rigid materials were a good approximation.

8.3 Baseline Model

The baseline model of wire rope consisted only of the load frame assembly, sway resistance pipe, and the modeled length of wire rope to be evaluated. The model is shown in Figure 76. The wire rope was straight and level at a height of 31 in. (787 mm). A discrete mass equal to the mass of the bogie vehicle, or 4,926.1 lb (2,234.4 kg), was attached at the last point of the wire rope, and an initial velocity of 23.89 mph (10.68 m/s) was applied to the point mass. This was consistent with the bogie speed at the end of the guidance track.

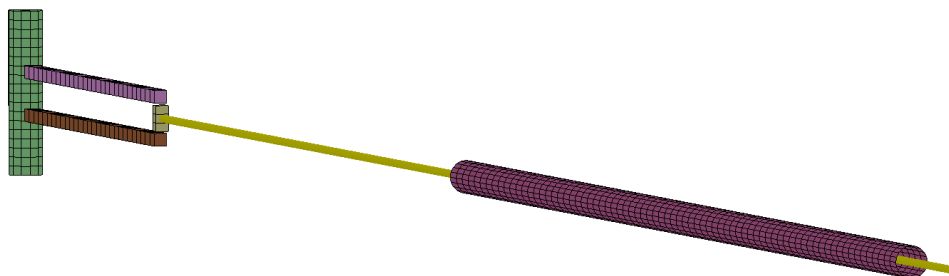


Figure 76. Baseline Model, Test No. DTC-1

Wire rope axial load data was plotted, and is shown in Figure 77. The maximum load sustained by the wire rope was 40.27 kip (179.1 kN) at 104.3 ms, as compared to a maximum load of 41.07 kip (182.7 kN) in the component test. This is a good correlation for a baseline model evaluation. Furthermore, though the loading rate was stepped and incremented, it intercrossed with the test data and had the same loading trend. The increments of increasing load corresponded to tension waves being transmitted by the simulated bogie impact.

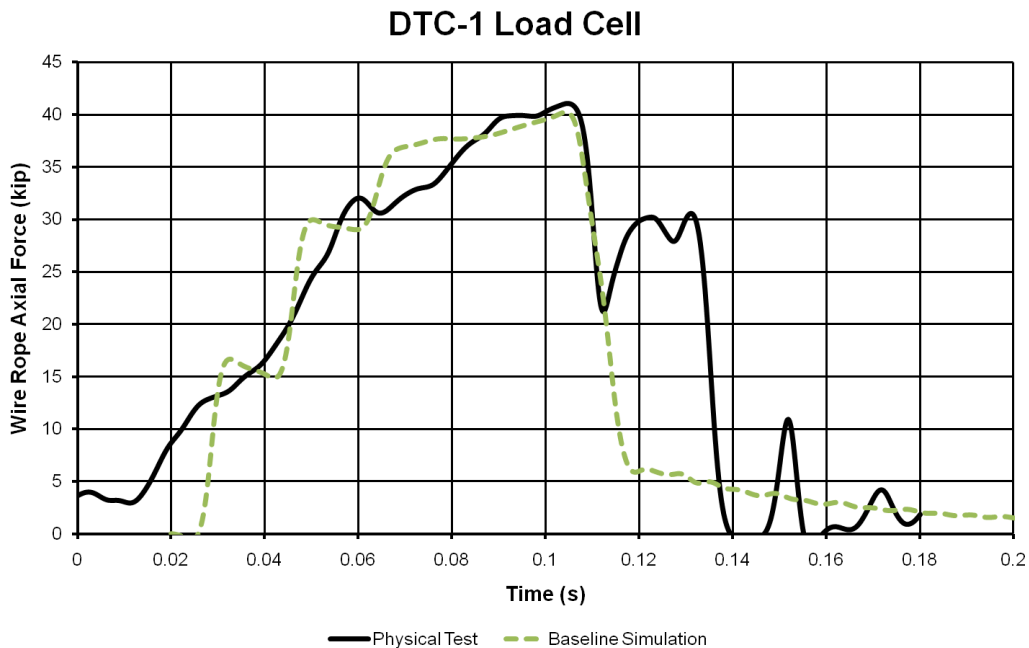


Figure 77. Wire Rope Axial Load Comparison, Test and Simulation, Test No. DTC-1

The baseline simulation time was offset by 21 ms. In the interest of preventing arbitrary results, the offset time was closely controlled. Since the baseline model did not have the gravitationally-induced deflection or slack, the baseline simulation was initialized *after* the bogie was free-wheeling at the end of the bogie track. At a bogie speed of 35.04 ft/s (10.68 m/s) traveling a distance of 10 in. (254 mm), the time offset was 23 ms; the time variable was increased by 2% to account for very low bogie deceleration due to slack take-up over the 10-in. (254-mm) displacement. However, it is nearly impossible to accurately determine the time zero

corresponding to the bogie being located 10 in. (254 mm) from the chute; thus, peaks in the acceleration data were compared to determine the correctly simulated "time zero" using this definition.

8.4 Curved Test Rope

The next evaluation conducted was to initialize the wire rope with an initial offset curvature, then conduct a similar jerk test on the end of the wire rope. The amount of curvature was varied to see what effects the curve had on the wire rope model. The applied velocity was the same in the curved wire rope model as it was in the straight baseline model.

A position-dependent velocity scale factor was applied to the nodal positions by multiplying the bogie speed by a ratio of the beam node position to the total wire rope length. The velocity distribution was modeled linearly. Though this is not the actual initial velocity distribution present in the wire rope, it was similar to the actual distribution, and analogous results were obtained in attempted models of the complete bogie acceleration.

The curved rope model was simulated, and the new velocity profiles assisted in reducing the discrete stepping in the load and acceleration curves. The wire rope loaded up slightly faster in the simulation though the load was similar throughout the event. The load results for the curved wire rope test are shown in Figure 78. The gravitationally-loaded wire rope accurately reflected the initial loading of the wire rope. However, in the component test the load rate was higher and the fracture time occurred at 140 ms with a maximum load of 41.07 kip (182.7 kN), whereas the maximum load in the simulation was 37.45 kip (166.6 kN). The wire rope did not fracture in the simulation, and the bogie was smoothly decelerated to a stop and rebounded.

As the wire rope did not fracture in the curved rope simulation, an investigation was conducted to determine what factors affected the wire rope fracture instead of sustaining the

load. The geometry of the curved wire rope was such that three circular arcs defined the wire rope. The first section was a moderately large radius of curvature of 16 ft (4.9 m), transitioning tangentially to a curve with a maximum lateral deflection of 8.5 ft (2.6 m). The long curve was again transitioned to the bogie position at the downstream end of the wire rope. The simulated geometry of the wire rope is shown in Figure 79.

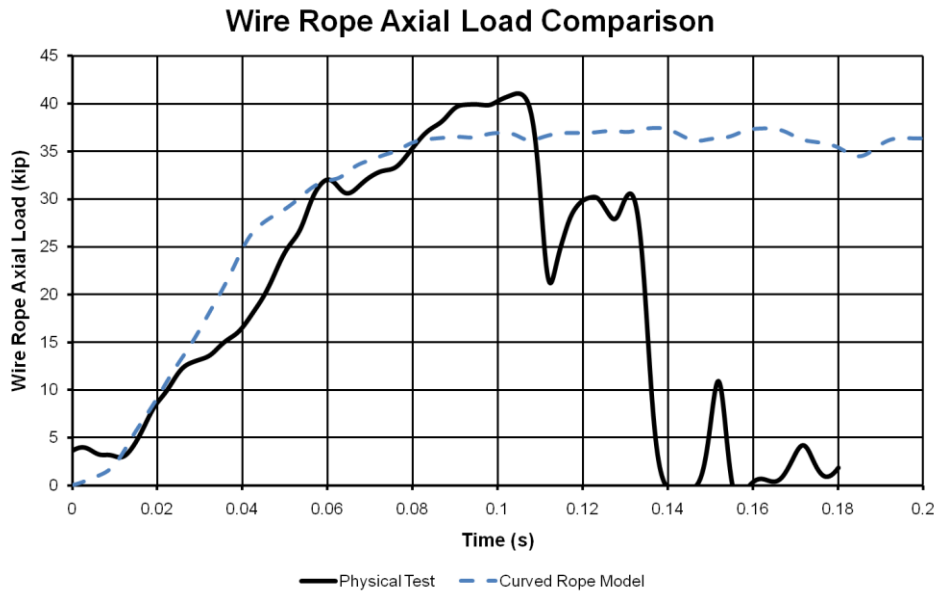


Figure 78. Wire Rope Axial Load Comparison, Test and Simulation, Test No. DTC-1



Figure 79. Curved Wire Rope Geometry, Curved Wire Rope Simulation

The use of a circular arc caused interesting side effects to occur. Tensioned bending waves, if the wave amplitudes are sufficiently small, follow harmonic overtones of the fundamental frequency. A Fourier transform can be defined such that any arbitrary function can be analyzed as an infinite series of harmonic terms with increasing harmonic frequencies. As a result, high-frequency harmonics may be represented in an arbitrary initial geometry pull test.

However, the circular curve approximation to wire rope initial geometry effectively led to only one high-energy harmonic bending wave generated, which limited the maximum amplitude and intensity of the tension peak. This allowed sufficient time for the bogie to decelerate prior to reaching its maximum displacement.

The displacement and velocity plots are very similar, though the initial velocity at the start of the event was not the same between the simulation and the test conditions. This occurred because the bogie velocity measured after exiting the guidance track was 35.04 ft/s (10.68 m/s), but the deceleration leading up to the effective "time zero" caused a reduction in speed of 1.74 ft/s (0.53 m/s). This was not accounted for in the curved wire rope model, and thus the velocity and displacement curves are offset from the actual curves. However, the rate of displacement and velocity change was nearly equal between the simulation and test, indicating good agreement.

The acceleration curves were plotted and compared, as shown in Figure 80. The acceleration behavior of the discrete mass-bogie was remarkably close to the bogie acceleration recorded in the test. Similar dynamic peak times of 66 and 110 ms in the simulation and 66 and 104 ms in the test indicated good agreement with wave propagation between the ends of the wire rope. However, the non-zero initial acceleration, which was caused by the take-up of slack prior to reaching the effective time zero point, did cause a difference at the start of the captured data.

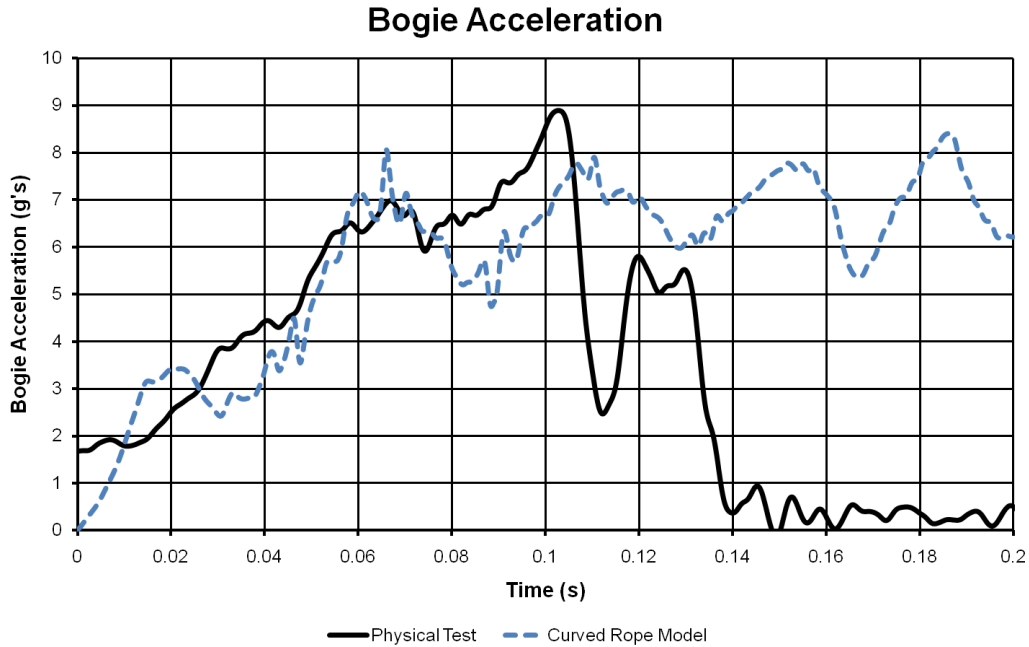


Figure 80. Bogie Acceleration Comparison, Test and Simulation, Test No. DTC-1

8.5 Curved and Gravitationally-Initialized Model

The next model evaluated was a curved and gravitationally-loaded wire rope. A small initial curve offset—this time non-symmetrically biased toward the upstream load frame—was applied to the wire rope, and it was allowed to fall under gravity. The end of the wire rope that corresponded to the bogie location was fixed at a tested wire rope tow cable attachment height of 16.25 in. (413 mm) above ground, which allowed for later updates to this model using a full bogie model.

After the gravitational run was conducted, nodal positions in the new model were updated with the gravitational and bend effects, and the simulation was conducted again. This time, the linear speed distribution was reduced to account for the bogie vehicle's initial loss of speed prior to the effective time zero. Load cell results are compared with the wire rope axial load, as shown in Figure 81. The load curve in the simulation matched the test load curve extremely well with identical force peaks at 60 ms. The maximum load predicted in the simulation was 38.95 kip

(173.3 kN), which was within 5% of the actual load. Though the secondary effect of the wire rope loading up shortly after (due to the remaining strand being tightened and fracturing) could not be simulated accurately using the model, this type of failure may not occur in full-scale vehicle impacts with cable barriers. Furthermore, wire ropes rarely fracture during vehicle impacts as impact loads are typically well below the elastic limit of the ropes.

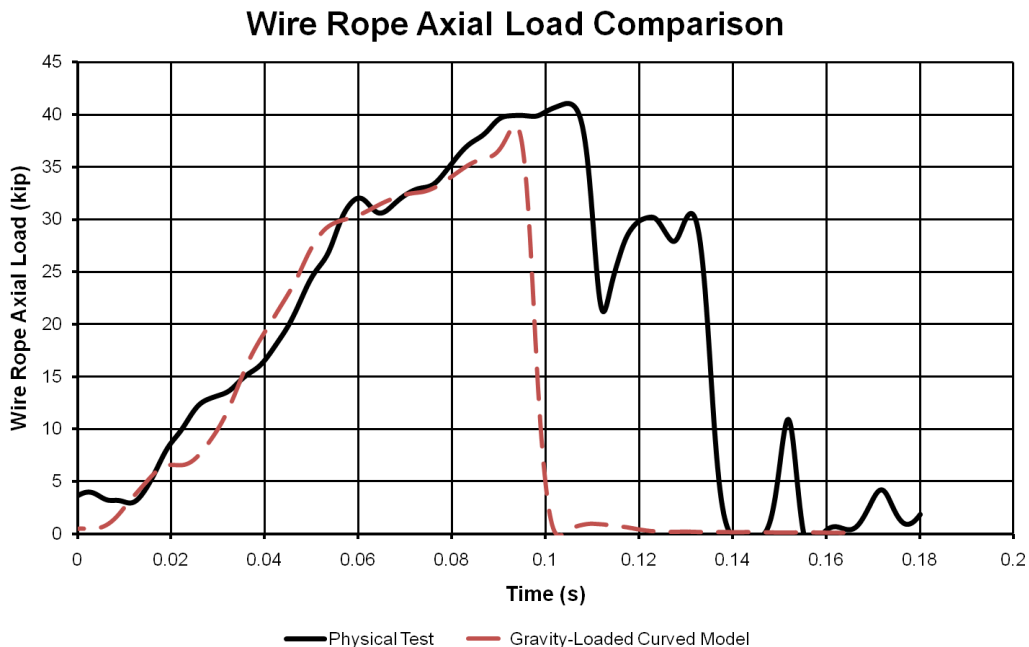


Figure 81. Wire Rope Axial Load Comparison, Test and Simulation, Test No. DTC-1

The fracture load and strain of the wire rope was iterated until a reasonable value was obtained. The total strain at fracture which was most characteristic of the wire rope fracture in test no. DTC-1 was 2.3%. However, this only represents one data point to consider for the wire rope dynamic strength.

A comparison of the bogie velocity with test results is shown in Figure 82. The simulated bogie velocity was very similar to the test bogie velocity, indicating good comparison of the results. The bogie decelerated to a speed of 10.8 ft/s (3.29 m/s), but the simulated bogie reached a constant speed of 19.8 ft/s (6.04 m/s). The bogie continued to decelerate after this time because

the remaining strand, which had not fractured, maintained tensile load and continued to slow the bogie vehicle down. This effect would require additional measures to simulate using the proposed wire rope model, which were not undertaken.

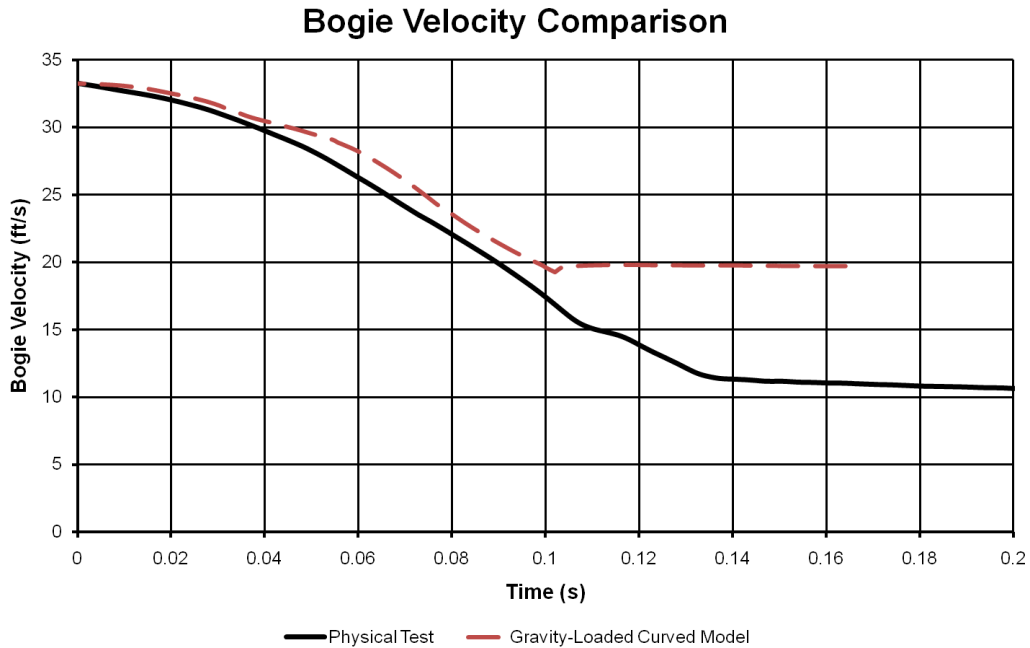


Figure 82. Bogie Velocity, Test and Simulation, Test No. DTC-1

A comparison of the tested and simulated bogie acceleration is shown in Figure 83. The simulated bogie acceleration followed the same slope as occurred in the test between 20 and 40 ms, but a tensile wave in the wire rope caused a decrease in sustained tension between 40 and 57 ms. This variation in the bogie acceleration is not likely due to differences between the wire rope and the tested wire rope, but rather to the linearized approximation of the wire rope velocity at the start of the simulation. As discussed, it was difficult to generate accurate velocity profiles of the wire rope leading up to impact since it required a simulation of more than 15 seconds. Even using double-precision LS-DYNA, the precision errors accumulated near 7-8 seconds, and the simulation required more than two days to complete. Furthermore, since the initial, static

position of the wire rope was originally unknown, it had to be estimated, which introduced additional error.

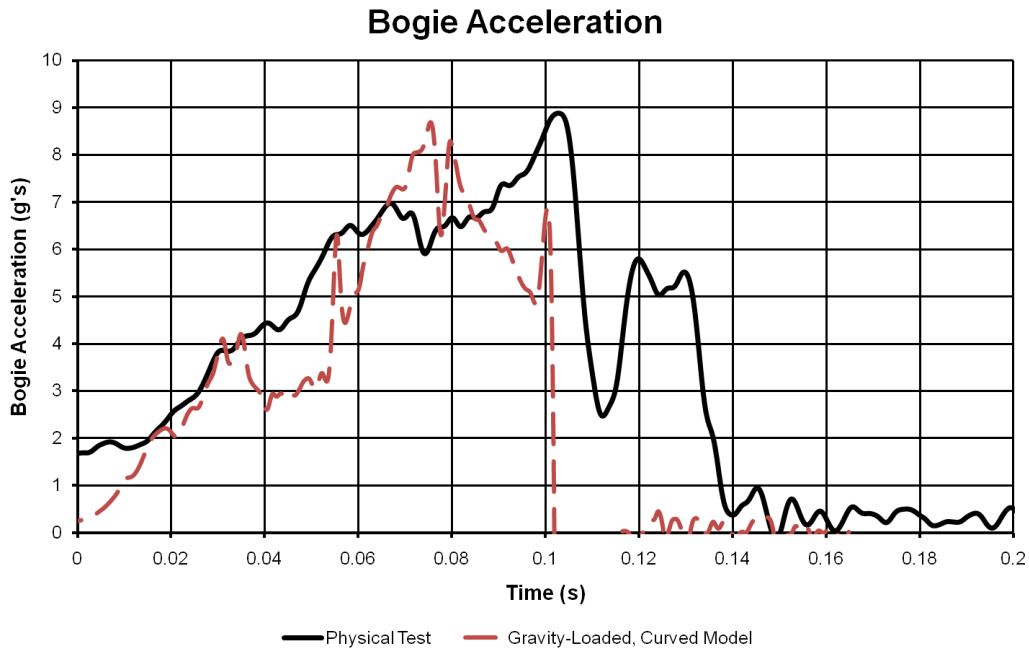


Figure 83. Bogie Acceleration, Test and Simulation, Test No. DTC-1

It is believed that if the correct velocity distribution, initial configuration, and test speed were correct, the model would be even more accurate than the gravitationally-initialized and curved wire rope model. However, the results obtained were in good agreement with the actual test data so further iteration was not attempted. Estimation of the geometrical positions of the wire rope and experimentation with different velocity profiles were attempted, but this is non-physical optimization work which is very arbitrary, and cannot be rigorously shown to be representative of the actual jerk test. Many models can, with sufficient time and effort, be made to "look" correct even if the model is not intrinsically accurate. The approach used in this simulation was defensible and realistic, and though the model did not perfectly simulate the dynamic tension test, the model demonstrated sufficient accuracy given the level of difficulty in simulating initial test configuration and was considered acceptable.

8.6 Discussion

Limited testing was conducted in dynamic tension due to (a) testing difficulties, (b) limited time frame for conducting the dynamic tests, and (c) limited overall usefulness resulting from the difficulty in accurately simulating the geometry and initial conditions of the dynamic tensile test. However, the test data was used to generate an approximation model for simulation of wire rope in dynamic impact. The approximate model was limited by the three factors that follow.

(1) Geometry of the tested wire rope was important for accurate simulation. The curved wire rope model had significant variation in the overall bogie response for different initial curvature offsets despite being compared at equivalent times. The wire rope section force and acceleration were most prone to differences. It was also observed that if the approximated initial curve was greater than 12 ft (3.7 m) laterally to the farthest-most point in the curve, the bogie would not cause the wire rope to fracture but would instead rebound after impact.

(2) Time constrained work on the simulations. A reasonable estimate of the initial geometry of the wire rope prior to the bogie being accelerated down the track was obtained since measurements were taken from photographs prior to the test. However, the long simulation times accumulated error, and this was manifested in gradually increasing tensile vibrations, inaccurate positions of the wire rope during the pull, and inaccurate velocity distributions. Iterations required extensive investment in time and analysis.

(3) Beams cannot fully capture the complexities of wire rope dynamics. Wire rope is a complex system of components that cannot be fully captured or represented by singular beam elements. Fractures of individual wires may occur in wire ropes but will not be accurately

captured using this simplified model. Even if the cross-section were complete with 21 wires, the model may still experience significant difficulty, and may be unmanageable or unstable.

However, none of these factors underscores the accuracy which was obtained using the simplified wire rope model. Despite differences in the initial geometry of the wire rope, the model accurately captured the loading slope of the bogie acceleration. Consequently, if the initial geometry and velocity distribution were more accurate in the approximation model, the results may have been even more accurate. These effects were all due to the initial approximated geometry.

Though other "tunable" parameters were present in the *MAT_166 material, a sensitivity analysis of the wire rope material model to the input parameters would have been subject to compounding error. It would have been impossible to differentiate minor differences due to a sensitivity analysis, when potentially large uncertainties were present in the results. The baseline model had a very good correlation with the physical test results, without geometrical modifications to replicate the initial conditions. These results indicated that the dynamic effects are very likely to be small, and a sensitivity study would only be required if a good correlation between the simulated and test data was obtained based on initial geometry. The sensitivity study for dynamic effects was left to the dynamic bending simulations, in which a very precisely-defined initial geometry could be obtained.

8.7 Summary

The wire rope model was simulated in a model of test no. DTC-1. The wire rope response was very accurate, despite geometrical modeling difficulties. The fracture time of 94.5 ms and fracture load of 38.95 kip (173.3 kN) was very similar to the initial fracture time of 104 ms and fracture load of 41.07 kip (182.7 kN). Though error in the initial prescribed geometry and

velocity of the wire rope was present, bogie motion was not adversely affected in the simulation, and the results were reasonable. The bogie acceleration curve was very similar between test and model between 0 and 40 ms, and the rate of change of bogie acceleration was nearly identical in the simulation as in the model. Bogie velocities were very similar through 95 ms, which led to an initial fracture speed of 19.2 ft/s (5.85 m/s). Therefore, the model of wire rope was determined to be accurate in dynamic tension.

8.8 Future Work

Though the geometry of the dynamic tension test was difficult to accurately obtain, further dynamic tension tests should use a controlled geometry with carefully-laid wire ropes and tow cables in known and documented initial conditions. The bogie acceleration and speed should be tracked from the start of the acceleration down the guidance track, and a start time should be clearly identified. With these precautions future testing of wire rope may be more accurately simulated and the results fine-tuned.

Furthermore, since the method of using string pots to measure strain was unsuccessful, future dynamic jerk test applications should consider a bulk strain gauge located on the wire rope. The difficulty of mounting a strain gauge on wire rope cannot be underestimated; however, such testing would lead to very useful and important data on the dynamic strain dependence of wire rope. Viscoelastic effects have been noted in wire rope, and analytical and testing methods to determine the viscoelastic dependence have been attempted (see references in 26). Nonetheless, physical test data would provide an opportunity for obtaining the fundamental-level response of wire rope, which can be compared with analytical models.

9 QUASI-STATIC BENDING TESTING

9.1 Introduction

Wire rope is an axially-stiff member with a low bending-to-axial stiffness ratio. As a result, the wire rope primarily reacts with changes in tension during vehicle redirection in wire rope barrier impacts. However, bending is an important aspect of the characterization of wire rope, and the elastic bending stiffness of wire rope is considerably more challenging to obtain analytically than many other stiff structural members [1]. Furthermore, the bending strength of wire rope following yield is more difficult to determine analytically since strands displace within the 3x7 wire rope, sliding friction occurs, and tension distribution within the wires of a single strand are not equal. Additionally, as wires generally have a very small diameter, compression results in a tendency for elastic buckling, so bending without sufficient axial tension reduces the effective bending stiffness.

However, if the deflection of wire rope under applied moment loading is similar to that of a prismatic beam, an equivalent model of the bending stiffness of wire rope may be generated. This method is widely-used to approximate difficult geometrical shapes in bending, but has not been successfully applied to wire rope yet. Costello proposed a method of determining bending stresses within wires of a wire rope, but the bending stresses were not extrapolated to a prismatic bending stiffness [1].

Quasi-static bending testing was used to determine equivalent prismatic beam section properties. Beam geometry and deflections were noted under applied loadings, and the moments were calculated. Equivalent prismatic beam bending strength was then determined based on the classical moment-bending resistance equations. The bend curves generated were converted to moment-curvature curves for implementation into the new wire rope model.

9.2 Beam Theory

Beam theory has been developed in many fundamental mechanics of materials textbooks [e.g., 30] and is extrapolated to beam elements in introductory texts to finite element methods [e.g. 42]. Classical beam theory applies to members that are long with respect to cross-sectional dimensions with loads and moments applied in a plane of bending. An example prismatic beam subject to an applied moment in bending is shown in Figure 84.

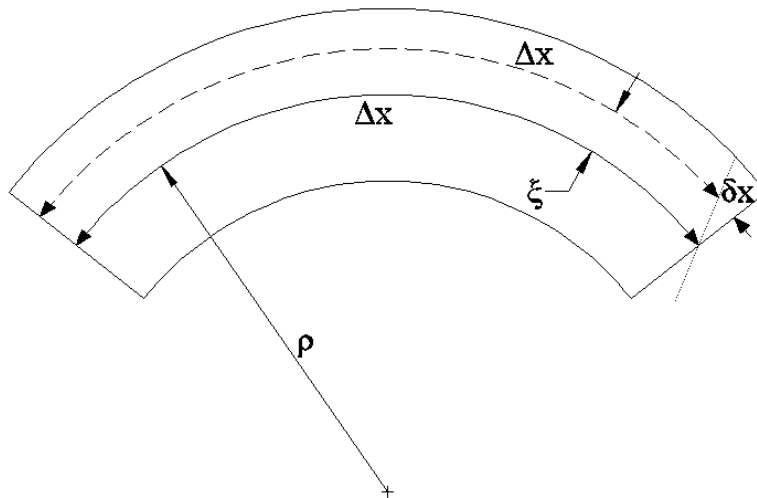


Figure 84. Prismatic Beam Subject to Applied Moment

Fundamentally, a prismatic beam subjected to a constant, uniform moment through the shear center in pure bending deforms into a circular arc, and the radius of the curvature, κ , is defined as

$$\kappa = \frac{1}{\rho} = \frac{d\theta}{ds}; \quad y = \rho - \rho_0 \quad [10]$$

where: ρ = radius of curvature
 θ = included angle of curve
 s = length of curve
 y = radial distance to longitudinal fiber in beam

Researchers observed that in pure bending, plane sections in prismatic, uniform beams remain planar when stresses and strains within the beam were within the elastic limit. This observation,

which is readily proven using geometrical arguments, and is accurate for many beams in bending [30], implies that

$$\kappa = f(y) \quad [11]$$

for y the axis extending between the geometrical center of curvature and the centroid of the beam's cross-section. Based on symmetry and geometrical arguments, it follows that for strain in the axial direction of the beam, referencing Equation 9,

$$\varepsilon = \frac{dl}{l} \quad [12]$$

then

$$\varepsilon = \frac{(\rho+d\rho)d\theta - \rho d\theta}{\rho d\theta} = -\frac{y}{\rho} = -\kappa y \quad [13]$$

for some location, y . If a material follows a Hookean linear-elastic material model, the stresses are related to the strains based only on the elastic modulus E , such that

$$\sigma_{xx} = E\varepsilon_x = -\frac{Ey}{\rho} = -E\kappa y \quad [14]$$

Stresses may then be calculated at any point in the cross-section.

Since no forces are applied to the beam in pure bending, each section of the beam must remain in static equilibrium. Summing differential forces across the cross-section requires that

$$\int_{CS} \sigma_{xx} dA = 0 = \int_{CS} -\frac{Ey}{\rho} dA \quad [15]$$

where: CS = total cross-sectional area
 dA = incremental area

Both E and ρ are constants, which requires that $y dA$ is zero and functions to define the centroid of a section. The requirement for no net axial stresses in a cross-section also indicates that the stress at the centroid of a straight prismatic beam is zero, and thus the strain at the centroid must also be zero. The stresses developed within the beam must exactly balance the applied moment,

with no net stress acting along the cross-section to satisfy conservation of linear momentum.

Achieving this balance requires that:

$$M_{applied} = \int_{CS} (-y\sigma) dA = \int_{CS} \frac{Ey^2}{\rho} dA \quad [16]$$

$M = \text{moment}$

Here again, both E and ρ are constants, and thus for

$$I = \int_{CS} y^2 dA \quad [17]$$

$I = \text{area moment of inertia}$

then

$$\frac{1}{\rho} = \frac{M}{EI} \quad [18]$$

Finally, substituting for the stress,

$$\sigma_{xx} = \frac{-My}{I} \quad [19]$$

at any point in the cross-section. Though this model was developed to address only pure curvature of prismatic beams, it may be extended to beams of varying cross-sectional shape and shear-loaded bending. Beam elements are generally accurate for beams with lengths with an order of magnitude higher than the cross-sectional dimensions which are loaded such that the elastic limits of the material are not exceeded. Furthermore, beam theory may not be applicable to non-isotropic materials. In addition, the beam must be loaded through the shear center to prevent warping. These constraints prevent localized deformations that are not accurately estimated using beam assumptions.

The most significant limitations on linear elastic beam theory are three basic assumptions: (1) that I remains constant under arbitrary loading and motions; (2) shear stresses are very small in comparison with bending stresses; and (3) end effects are minimal.

The assumption that the cross-section remains undeformed is critical since the area moment of inertia I changes with differences in geometry. To exactly treat the variation of stress in a linear elastic beam requires that I be known at each time in which the stress is to be evaluated. For relatively stiff objects with large axial dimensions with respect to transverse dimensions, the assumption of a constant I holds approximately true. Both assumptions (2) and (3) hold true if the beams are very long and are loaded far from the supports.

To determine deflection of beams, small-angle assumptions are often used. The small-angle assumption is related to the curvature of the beam. Curvature is mathematically defined as

$$\kappa = \frac{d\theta}{ds} = \frac{\frac{d^2v}{dx^2}}{\left(1 + \left(\frac{dv}{dx}\right)^2\right)^{3/2}} \quad [20]$$

x = longitudinal component of distance

With very small angles of deflection, the differential change in length ds of an arc becomes approximately equal to dx and the beam deflects according to the change in x . The angle θ is determined via

$$\tan(\theta) = \frac{dv}{dx}. \quad [21]$$

Here again, the small angle assumption permits the approximation

$$\tan(\theta) \approx \theta \quad [22]$$

and

$$\frac{dv}{dx} \ll 1 \rightarrow \left(1 + \left(\frac{dv}{dx}\right)^2\right)^{3/2} \approx 1. \quad [23]$$

Both statements of curvature lead to the generalized equation:

$$\kappa = \frac{d^2v}{dx^2}. \quad [24]$$

This applies for all small-angle beams. If the beams are linearly elastic, it follows that

$$\frac{d^2v}{dx^2} = \frac{M}{EI} \quad [25]$$

which can be inserted into the constitutive equations to find the deflection, v . Nonlinear beams require either numerical integration, piecewise approximation to the loading curve, or generalized solutions to the bending equations.

In most beams, planar sections within beams remain planar when beams are deformed in moment-loading. Using equation 13 the yield strain may be redefined in terms of the curvature, such that

$$\epsilon_y = -(y\kappa)_y = -y_o\kappa_y \quad [26]$$

for y , the nominal distance from the neutral axis. This relationship can be used to find yield surfaces as a function of y -position. When yielding occurs at the outer fibers of the beam located at $y = y_o$, setting equations 14 and 19 equal and noting that $M = PL$ for P the applied load,

$$-Ey_o\kappa_y = \frac{PLy_o}{I} \quad [27]$$

then

$$\kappa_y = \frac{PL}{EI}. \quad [28]$$

The yield location for any moment which causes plastic behavior is then

$$-y\kappa = -y_o\kappa_y = \frac{PLy_o}{EI} \quad [29]$$

so that the yield location y_y is

$$y_y = \frac{y_o\kappa_y}{\kappa} = \frac{-PLy_o}{\kappa EI}. \quad [30]$$

The stress can then be determined at any point in the cross-section, using

$$\sigma = \begin{cases} E\epsilon = -Ey\kappa, & |y| < \left| \frac{PLy_o}{\kappa EI} \right| \\ \sigma_y + F(\epsilon - \epsilon_y) = -Ey\kappa_y + F\left(-\kappa\left(y - \frac{PLy_o}{\kappa EI}\right)\right), & |y| \geq \left| \frac{PLy_o}{\kappa EI} \right| \end{cases} \quad [31]$$

For an elastic-perfectly plastic material, the function $F\left(-\kappa\left(y - \frac{PLy_0}{\kappa EI}\right)\right)$ is zero; for kinematic hardening of materials subjected to plastic deformation, the function for E_t , the kinematic tangent hardening modulus, is $F\left(-\kappa\left(y - \frac{PLy_0}{\kappa EI}\right)\right) = E_t\left(-\kappa\left(y - \frac{PLy_0}{\kappa EI}\right)\right)$. Thus, it is possible to analyze structural beams loaded beyond the elastic limit if the yield strain and plastic behavior are known.

9.3 Quasi-Static Bending Tests

Quasi-static bending tests were conducted on the wire rope in order to determine the bending stiffness as a function of curvature. Bending stiffness tests were conducted by clamping wire rope in a cantilever position, while distributing the clamping load to prevent stress concentrations. Flat steel plates were placed above and below the clamped end of the wire rope to minimize local curvature at the cantilever end. Local curvature would have affected the resulting estimates of wire rope bending.

A curved length of wire rope was selected for the bending tests. Depending on the make and construction of the wire rope, some "seating" of the wires may occur within the strands. Seating refers to the tendency of strands and wires to compact together into a no-slip condition. As a wire rope is stretched, internal stresses cause the seating to occur, after which point the wire rope acts (in linear-elastic load conditions) as a true beam. This seating effect could not be measured at the time of the test, and the extent of the seating in wire rope is unknown to the author. Nonetheless, to prevent any "seating" effects from occurring and to maximize planar stability of the wire rope tested, a curved wire rope was used in lieu of a straight rope.

Three lengths of wire rope were tested in quasi-static bending: 53½ in. 44 in., and 29¹³/₁₆ in. (1,359 mm, 1,118 mm, and 757 mm) long. Pre-determined, equally-spaced positions on each wire rope were marked before being clamped in cantilever bending to serve as reference

locations. Curvature measurements were also taken to accurately model the unloaded wire rope configuration. The initial radius of curvature of the wire rope prior to testing (measured flat without influence of gravity) was 67.26 in. (1,708.4 mm).

The wire ropes were measured in a cantilever bending configuration, as shown in Figure 85. To secure the wire rope when clamped, a ¼-in. (6-mm) thick steel plate was placed below the wire rope and fastened with screws to the wooden block supports. The wire rope was secured with U-bolt swage grips after cutting approximately ⅜-in. (10-mm) off of each side. Three clamps and three swage grips were used to secure the wire rope to the steel plate. Clamping loads were approximately 50 to 80 lb (222 to 356 N) but were not measured.



Figure 85. Clamped Configuration of Long Wire Rope Quasi-Static Bending Test

A string line was fastened at the bottom edge of the plate and extended across the range of the testing area. The string line was checked with a level and was tensioned. Pre-marked locations at the center of the wire rope in pre-determined locations on each length of wire rope

were measured from the reference line to obtain a vertical estimate of the deflection for each applied moment. The vertical estimates were then offset by $\frac{3}{8}$ in. (10 mm) to reference the initial center location of the wire rope at the cantilever end.

To measure horizontal positions of the marked locations on the wire rope, a reference board was fastened to the cantilever mount to create a flat reference surface, as shown in Figure 86. To determine the distance from the cantilever point on the wire rope to the marked locations, the width of the board was measured using a pair of digital calipers. The width of the board was added to the measured horizontal position of the marked locations on each wire rope.



Figure 86. Reference Line and Surface for Vertical and Horizontal Measurements

Discrete loads were applied to the wire rope in the marked locations using a 30-lb (133-N) high-friction thin nylon fishing line, and marked masses of precisely-measured weights. Four weighted brackets measured to within 0.0002 lb (0.1 g) were marked with locational reference letters A, B, C, and D. The loads were assigned to four measurement locations and the locations marked with the same letters. Point D was closest to the cantilever location, and point

A was closest to the end of the beam. With four weights and four positions of the wire rope to measure deflected positions, a total of 14 possible bending scenarios could be investigated for each wire rope. In each loading condition, the longitudinal and vertical position of each reference point was measured.

In practical cases, however, less than the maximum possible configurations were tested. Every time that a residual bend in wire rope was noted after a test, only loads which were greater than the last measured load were utilized in order to capitalize on increasing "plastic" bending load values. Moment loads which were greater than the plastic limit of the wire rope were likely to cause further plasticity, which does not compromise the higher-load results as unloading will occur elastically.

Loads were hung from a two-part narrow-string support, which incorporated the high-friction nylon line and a fastening clip for each measured load. Using this method, the applied loads could be accurately approximated as discrete or point loads to simplify the moment and deflection estimation. Discrete loading of the wire rope is shown in Figure 87.

Using the reference point data, the applied weights, and unloaded configurations, the bending positions of the wire rope for various moments were plotted. The bending position data were used to compare to the simulation results in order to refine the moment bending curves. Bending curves are shown in Figures 88 through 90.

9.4 Curvature Approximation

The moment resistance of a planar cross-sectional beam is linear with respect to curvature. The curvature of the beam is defined to be

$$\kappa = \frac{d\theta}{ds} = \frac{\frac{d^2v}{dx^2}}{\left(1 + \left(\frac{dv}{dx}\right)^2\right)^{3/2}} \quad [20]$$



Figure 87. Loading Configuration and Method of Applying Discrete Weights

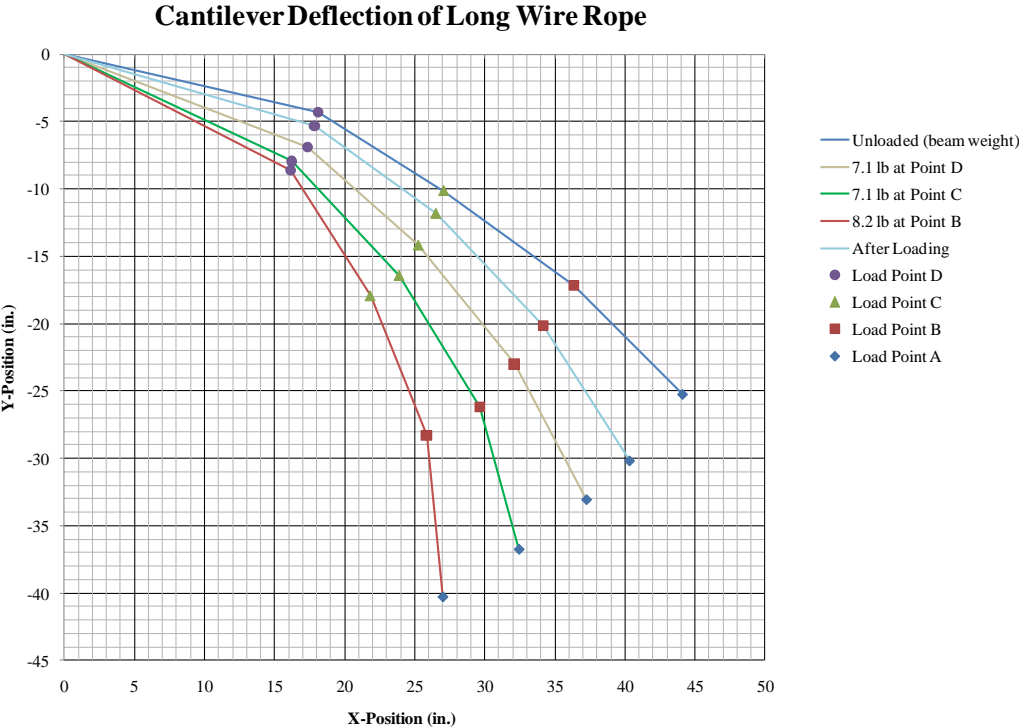


Figure 88. Long Wire Rope Deflection by Applied Moment

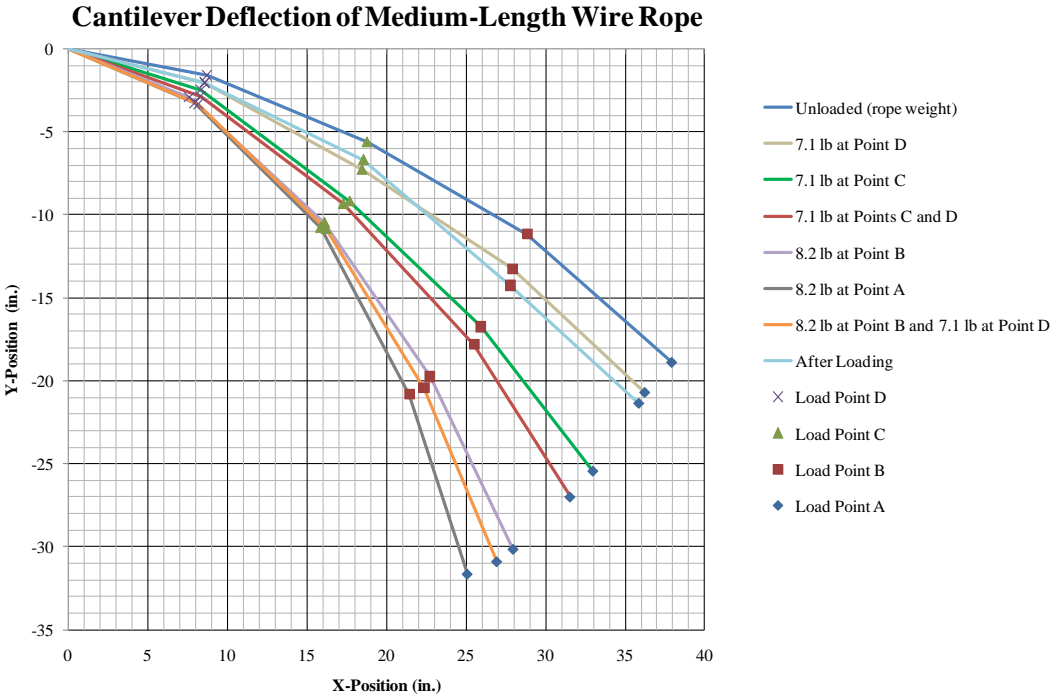


Figure 89. Medium-Length Wire Rope Deflection by Applied Moment

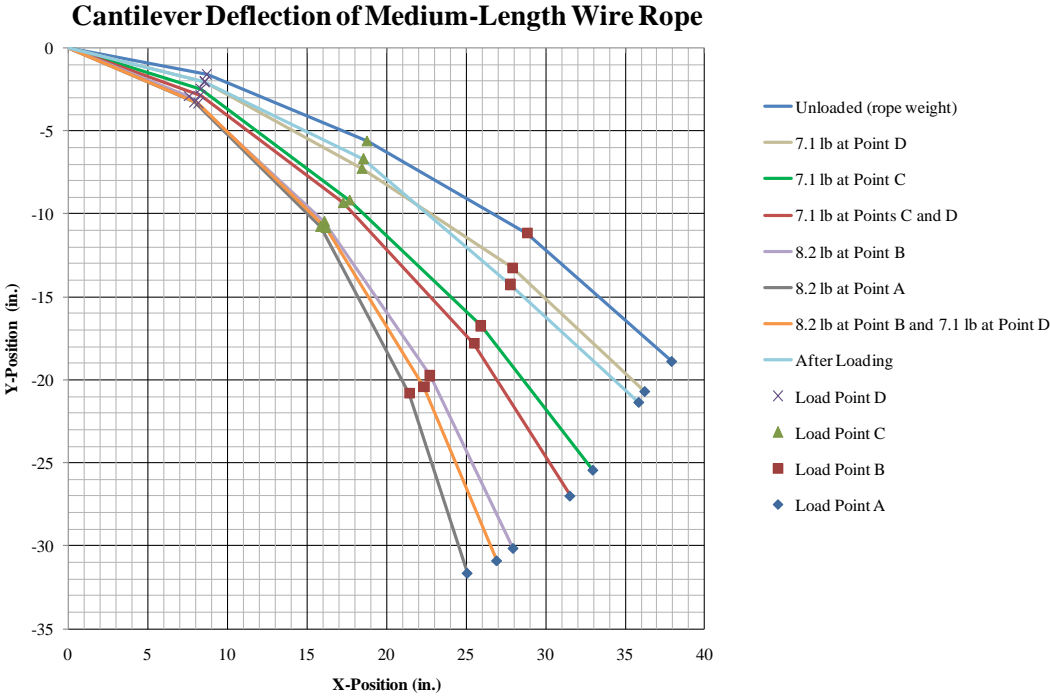


Figure 90. Short-Length Wire Rope Deflection by Applied Moment

Therefore, a fourth-order polynomial of the form

$$ax^4 + bx^3 + cx^2 + dx + e = 0 \quad [32]$$

will have a curvature equal to

$$\kappa = \frac{\frac{d^2v}{dx^2}}{\left(1 + \left(\frac{dv}{dx}\right)^2\right)^{3/2}} = \frac{12ax^2 + 3bx + 2c}{(1 + (4ax^3 + 3bx^2 + 2cx + d)^2)^{3/2}} \quad [33]$$

which, at the cantilever position ($x = 0$, no initial deflection or slope) gives a very simple curvature relation of

$$\kappa = \frac{2c}{(1 + (0)^2)^{3/2}} = 2c. \quad [34]$$

However, because of the variations in measurements and the relatively low resolution of 1/8-in. (3-mm) for each measurement, the curvature estimations were subject to significant noise using a best-fit curve fitting. Only the unloaded wire ropes subject to gravitational loading gave reasonable results for curvature using the fourth-order polynomials. This is expected since a minimum of 5 points are required to generate any fourth-order curve, and discrete loads create non-contiguous shear-based moments in the wire rope which cannot be captured using a single fourth-order curve.

Wire rope has a linear density of approximately 0.06877 lb/in. (0.001228 kg/mm) that is measured using three known lengths of wire rope measured six independent times on a gravitational scale. As a result, the gravitational moment applied at the fixed end of the wire rope was calculated by summing small discrete moments calculated over the length of the beam. Each discrete moment was calculated by summing the weight of each small segment of wire rope at its centroid, multiplied by the x-distance to the center of each segment, such that

$$M = \sum_{i=1}^N \Delta M = \sum_{i=1}^N x_i \rho_L \Delta s_i. \quad [35]$$

where: M = moment; N = number of incremental moments
 x = perpendicular distance to applied weight
 ρ_L = linear mass density
 Δs_i = incremental length of wire rope

Though the quartic curves could not accurately capture the curvature of the wire rope at the cantilever position, it *could* capture the deflected position of each wire rope very well. Therefore, incremental beam lengths were based on quartic curve incrementation. The length of each segment in the quartic curves was approximately 0.5 in. (12.7 mm).

Because the load on the wire rope in the unloaded configuration consisted only of gravity acting on the wire rope, the quartic approximation to the bending deflections were acceptable, and estimates of the curvature of the wire rope were provided. These estimates of curvature were plotted against the applied moment to observe any trends. It was observed that data was approximately scattered around a linear regression. This indicated that there was a possibility that the bending strength of the wire rope could be approximated as a prismatic beam of defined bending resistance. Estimation of the moment-curvature curve of the wire rope required interpolative evaluations using simulations.

9.5 Discussion

Though useful data was generated from the quasi-static bending tests, the data collected was incomplete. Many points should be sampled on further bending tests to ensure that adequate approximations to the curvature can be made. For many of the loading configurations, sufficient numerical noise was present to prevent the determination of the curvature of the beam.

It should also be noted that though efforts were taken to ensure that the tested wire ropes would be approximately flat at the cantilever position (i.e. no initial angular displacement), the

clamps could not be placed too close to the edge and as a result some angular offset occurred in every tested wire rope. Usually this angular offset was very small, on the order of 0.2 to 0.5 degrees. However, some of the tests had an angular displacement of up to 2.0 degrees, which is visible to the eye. Even an angular displacement of 0.5 degrees can affect the resulting offset at the end of the wire rope by as much as 2 in. (51 mm) on the long wire rope. If future bending tests are conducted on wire rope, it is recommended that the setup completely prevent initial angular offset in the wire ropes to prevent noise data from affecting the results.

One alternative method of measuring the bending strength of wire rope is to measure bending stiffness of wire rope in a "simple-beam" bending scenario on a horizontal plane. This will allow for concise, easy measurements of deflections vs. applied loads, and does not require clamping which can affect the results. However, frictional resistance of the planar surface to motion would be necessary to not skew the results.

In addition to the end conditions and data sampling on wire rope, it should be noted that the methods of measuring the wire rope, which utilized tape measures for large lengths and digital calipers for short lengths, had a relatively large margin of error. Better measurement techniques and devices may be appropriate for determination of accurate beam deflections, including photographic measurements, laser-scope measurements, or surveying equipment capable of determining vertical elevation with high precision.

The resulting linear elastic stiffness modulus, EI , based on the equation $M = (EI)\kappa$, was determined to be $EI = 11.27 \text{ kip-in./in.}^{-1}$ ($32.3 \text{ MN-mm/mm}^{-1}$).

9.6 Conclusions

Three wire rope lengths were tested in quasi-static bending, and the results were tabulated. The bending deflections were noted for later comparison with bending simulation

results. The long, medium-length, and short wire ropes were tested until residual plastic curvature was present in the wire ropes. In this way, both the elastic curvature limit of the wire ropes and the plastic curve data could be obtained for future reference. Recommendations for future quasi-static bending tests were noted, and consisted of better-constrained end conditions, use of more precise measurement techniques and devices, and sampling of many points along the wire rope length.

9.7 Future Work

The quasi-static bending tests conducted on non-prestretched wire rope had not been conducted prior to this study. The bending test data is useful in determining the nominal bending strength of the wire ropes. However, under non-zero static tension, the bending properties of wire rope may be different. Non-zero static tensions were not explored in this test series. Further testing of wire rope in bending under a variety of tensile loads will be necessary to guarantee better results from simulations.

Further, the breaking strength of wire rope under bending loads has not yet been determined. It is believed that it is not likely that wire rope will ever fail in bending. Very large bend radii have been witnessed without rupture of the wire rope. Axial stress concentrations in bending areas are more likely to cause rupture than the presence of bending stress distributions. Therefore, there is no immediate need to determine bending rupture strength determination. Any further tests conducted on wire rope should consist of more precise quasi-static bending testing, bending tests under initial axial loads, and bending comparisons of short and long lengths of wire rope.

10 MODELING WIRE ROPE IN QUASI-STATIC BENDING

10.1 Purpose

Simulations were conducted of the quasi-static bending tests to replicate the observed bending of the wire ropes and to determine the elastic bending strength. First, beam element assumptions and constitution were considered. Prior to conducting the bending analysis, a mesh sensitivity study was conducted to ensure that the adequate bending behavior of wire rope was captured. The results of the mesh sensitivity study were compared to known deflections of a very stiff beam. Then, the beam lengths of 53½ in. 44 in., and 29¹³/₁₆-in. (1,359 mm, 1,118 mm, and 757 mm) long were replicated using series of 0.500-in. (12.7-mm) long type 2 beam elements. The elastic bending strength was determined using a series of bending stiffness coefficients. Finally, the plastic loading curve was estimated and best-fit from the available data. Discussion and recommendations from the beam element study were provided.

10.2 Beam Element Constitutive Assumptions

Beam elements are fundamentally extensions of classical beam theory in three dimensions. Beam elements consist of two nodes, one on either end of the beam. The axis between the nodes is the principal axis of the beam; however, the curvature of the beam is treated mathematically at each node, based on the relative angle between adjacent beams.

At each node, beams have three linear and three rotational degrees of freedom. The degree of freedom along the axis of the beam is the axial strain degree of freedom, and is used in the determination of bulk axial stresses and forces. The degrees of freedom on the orthogonal section axes resist bending motion through shear force transmission. The axial rotational degree of freedom is the twist angle, and the rotation through the two principal section axes is the bending angles in perpendicular S-S and T-T directions. The direction of the S-S and T-T axes in

the section are defined by the user. A schematic of a sample beam, with indicated S-S and T-T axes, is shown in Figure 91.

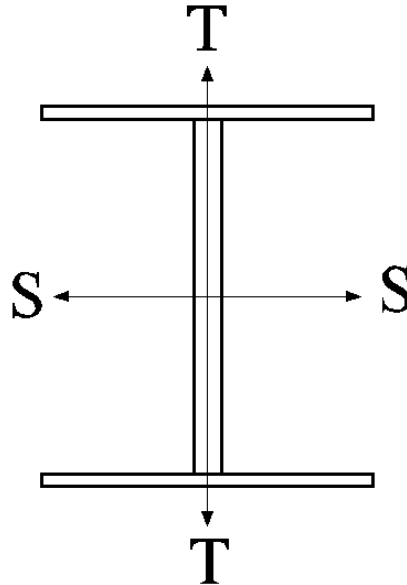


Figure 91. Example Beam Cross-Section Definition with Major S-S and T-T Axes

Type 2 beam elements utilize three coordinate systems to track element motion and deflection. The primary coordinate system is the global system, which is used to track each nodal position. Within each element there are two additional orthogonal coordinate axes, a rotational (rigid) set of axes and a deformed set of axes, as shown in Figure 92. The rigid axes are displaced only during nodal rotation. If an element undergoes deformation without rotation the rigid rotational axes do not change position.

By contrast, the deformational axes always extend the long axis of the beam through the two nodes of an element. Rotation of the deformational axis of the beam is determined by taking the relative rotational displacement of each node on the beam for an estimate of the angular difference. The difference between the rigid rotational axis coordinates of the beam and the deformational axis defines the deformation of the beam element.

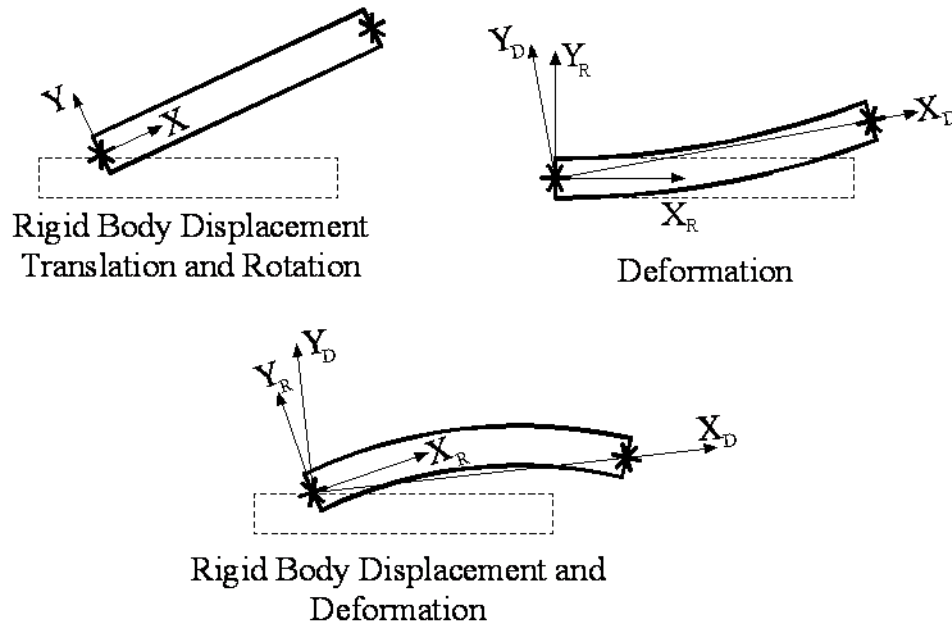


Figure 92. Possible Deformation Modes of Beams

The stresses and forces are determined using the tensile curve for the type 2 beam element. Based on the element displacement, forces are calculated that would resist the element motion, and these forces are compared to the applied force on the beam elements. The process is iterated until a solution satisfying the applied loading and displacements can be determined. Convergence of the beam element solutions is ensured using Newmark-Beta interpolation.

In all beam elements the cross-sectional area is assumed to remain constant throughout the bending and axial loading of the beam. For planar strain, stiff sections, and relatively small displacements these assumptions are accurate. However, if torsional warping or buckling occurs in a beam the types 11 or 12 beam elements may be more useful in the determination of the actual axial stress and strain of the beam elements.

Furthermore, beam elements use the small-angle theory in the same manner as classical beam theory. The small-angle assumption states that if the angle between adjacent elements is sufficiently small, the sine (and tangent) of the angle are approximately equal to the value of the

angle, so long as it is expressed in radians. Likewise, the cosine of the angle is approximately unity. For beam elements with small relative angular displacements, this leads to very small accumulated numerical error.

10.3 Modeling an I-Beam in Bending

10.3.1 Model Description

Prior to implementing a model of wire rope in bending using *MAT_166, a model of a stiff beam in bending was created to simulate a cantilever I-beam in bending. The simulated I-beam was a W14x132 (W360x196) standard structural shape. Pure kinematic hardening was assumed for material behavior. A schematic diagram of the simulated cantilever beam is shown in Figure 93.

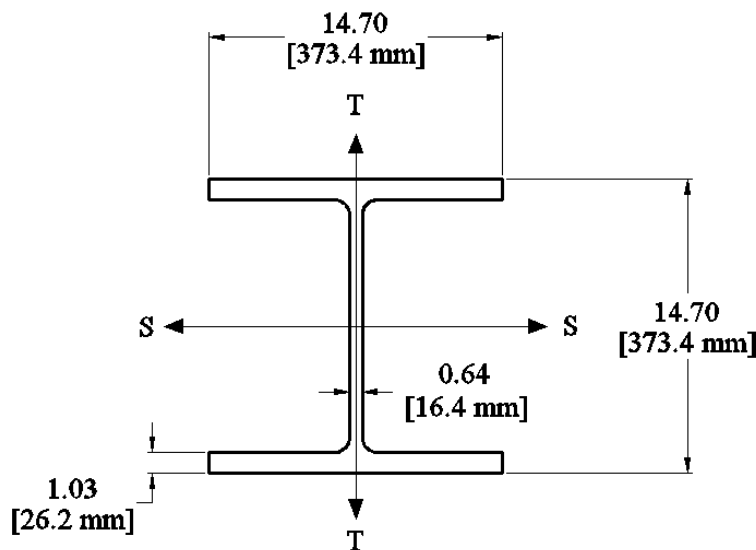


Figure 93. Modeled W14x132 (W360x196) Beam in LS-DYNA

The 19.7 ft (6.0 m) beam was modeled as a straight beam with SPC boundary constraints on the first node in the beam. A time-varying load was applied to the free end of the beam. Loads and beam-end displacements were tracked to compare the load-deflection histories of various meshes.

The load input was a triangular wave with an amplitude of 404.7 kip (1,800 kN) with a period of 40 seconds and 1.25 periods were simulated. This load history time increment is longer than the explicit calculation recommendations due to calculation of stress wave transmission, which requires very small timesteps. As a result, accuracy is lost and numerical noise is generated. Double precision was used to minimize these effects. Implicit modeling of the beams under the static loading was not pursued since the wire rope model would be used in explicit formulation declarations, and implicit and explicit models may generate differences for the same load application. The load curve is shown in Figure 94.

Mesh densities of the models were varied to evaluate sensitivity. These estimates were later used to determine the optimized length of wire rope beam elements. Mesh densities considered included 1 element, 20 elements, and 100 elements.

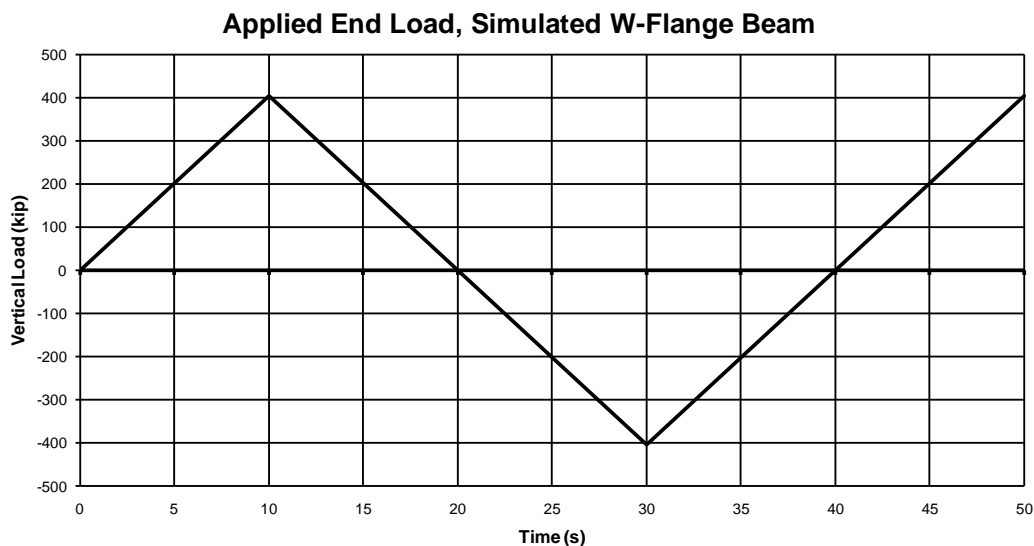


Figure 94. Applied End Load Conditions on Cantilever Beam

The load and displacement curves were linear in time. A point load was placed at the end of the beam and defined to always act vertically. The load varied between 404.7 kip and -404.7 kip (1,800 kN and -1,800 kN). Displacement constraints varied between 1.17 in. and -1.17 in.

(29.7 mm and -29.7 mm) based on the calculation of a beam with kinematic material under the applied loads.

Using a material with pure kinematic hardening, the indicated loads were applied to the cantilever beams. The moment-curvature relation for the beam was simplified significantly to reflect a kinematic-like moment curvature curve with an elastic moment-curvature modulus and tangent plastic moment-curvature modulus. The slope of the elastic moment-curvature curve was given by

$$\frac{dM}{d\kappa} = EI \quad [36]$$

which provides a slope of approximately $46.9(10^6)$ kip-in² ($134.6(10^3)$ kN-m²). The yield load curvature was defined to be $50(10^{-6})$ rad/in. (0.002 rad/m). This moment-curvature model was used both in the analytical calculations for the bending strength of the beam as well as the material model for wire rope. This curve is shown in Figure 95.

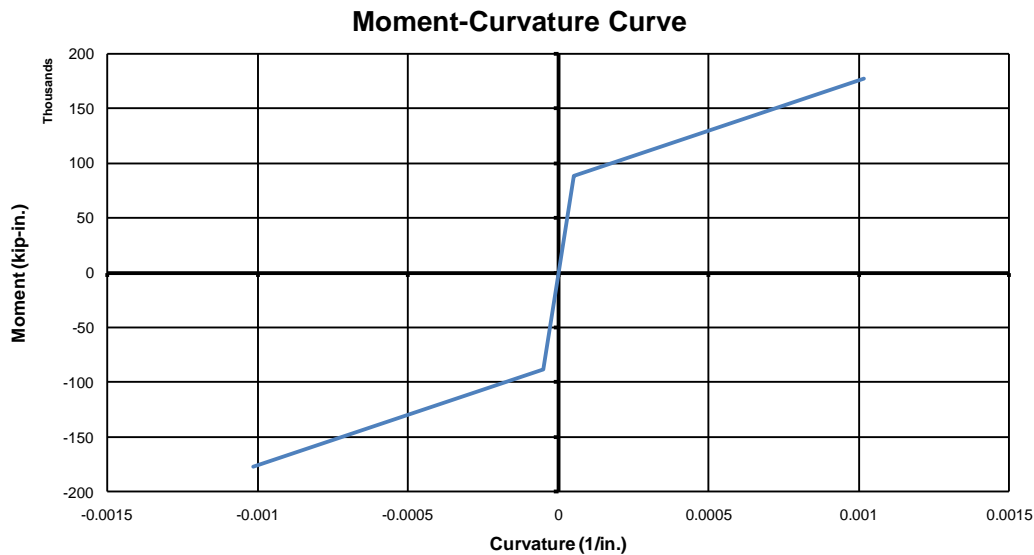


Figure 95. Moment-Curvature Input Curve for W14x132 (W360x196) Beam

10.3.2 Analytical Results

The cantilever beam was evaluated analytically to determine the maximum deflection under the applied loading. The elastic deflection was calculated and determined to be 0.9449 in. (24.00 mm). The beam yielded until a final deflection of 1.161 in. (29.48 mm). Superposition was used to determine the resulting negative yield load and deflection of 345 kip (1,535 kN) and -0.7292 in. (-18.52 mm), respectively. At a load of -404.7 kip (-1,800 kN) the beam deflection was -1.161 in. (-29.48 mm).

10.3.3 Simulation Results

The cantilever beams were simulated in LS-DYNA, and the cantilever shear forces were plotted against the beam end deflection. These results were compared to the analytical load and displacement curves. Results of the beam bending simulations are shown in Figure 96.

The single-element model failed to accurately represent the physical model. The displacement of the end of the beam was 2.41 in. (61.3 mm) which is much greater than the analytical deflection; this result is because in the moment-curvature beam material model the single element is assumed to have a constant curvature across the entire length of the beam. Because no additional elements were present to gradually step the moment down over the length of the beam, the deflection was too high.

The beam was remeshed with 20 evenly-sized elements along the length of the 19.7-ft (6.0-m) beam, and the load-controlled boundary conditions were repeated. The beam was too stiff, but much better than the single element case. The maximum deflection was 1.04 in. (26.5 mm). This matches common engineering experience that coarse meshes are generally stiffer than finer meshes.

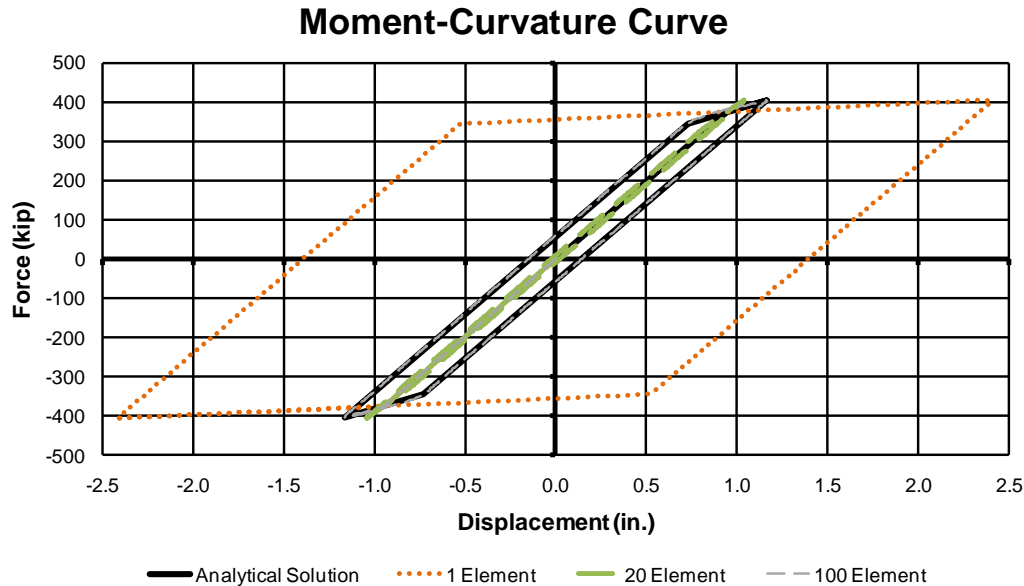


Figure 96. Analytical and Simulated Results

The mesh was further refined to 100 elements, such that each element length was 2.36 in. (60 mm) long. Though this mesh density is still relatively coarse, it was able to accurately simulate the deflection of the beam, compared with analytical calculations. The maximum deflection in the positive and negative loading directions was 1.167 and -1.169 in. (29.63 and 29.68 mm), which was within 1% of the analytical deflection.

It should be noted that in the analytical beam deflection calculations the longitudinal location of every point in the beam did not change with applied load, and therefore the effective length of the beam changed slightly as a function of deflection. This approximation is often used in estimation of the deflection of stiff beams. Furthermore, additional error using the small-angle assumption causes small differences in the resulting analytical approximate deflection. Therefore, the simulated displacements are likely more accurate, based on the applied model, than the analytical estimate since these restrictions are not present.

It was observed that the larger the element length, the longer the time required to process the model and complete the simulation. A contrast of the amount of time required to complete

the simulations and the resulting accuracy of the model, as compared to the analytical model, is shown in Table 8. The long amounts of time required to complete the simulation were due to a long applied load of 50 seconds. Most simulations will not require this much time to accurately capture the response of the beam element models; furthermore, this amount of time caused instabilities in the 400 element case, even when using double-precision. Such long-duration models are not recommended, but quasi-static load conditions were desired at every timestep in the simulation.

Table 8. Computational Time and Accuracy, Stiff I-Beam Model

Elements	Time (hr)	Maximum Deflection		Accuracy
		in.	mm	
1	0.0002778	2.411	61.234	107.7%
20	0.37	1.044	26.513	-10.1%
100	17.22	1.169	29.698	0.7%
400	> 72*	1.173	29.791	1.1%

*NOTE: 400-element simulation terminated prematurely due to numerical instability

10.4 Modeling Wire Rope in Bending

Cantilever bending of the wire ropes was modeled using type 2 Belytshcko-Schwer beam elements incorporating the *MAT_MOMENT_CURVATURE_BEAM material model as discussed in the tensile testing section.

The bending input from the *MAT_MOMENT_CURVATURE_BEAM material model is a load curve plotting applied moment against curvature of the beam. In order to generate an initial moment-curvature curve, attempts were made to approximate the curve of the wire rope under loading using fourth-order polynomials. These efforts generated a bending curve which was linear though sparse data led to significant variability. This curve is shown in Figure 97.

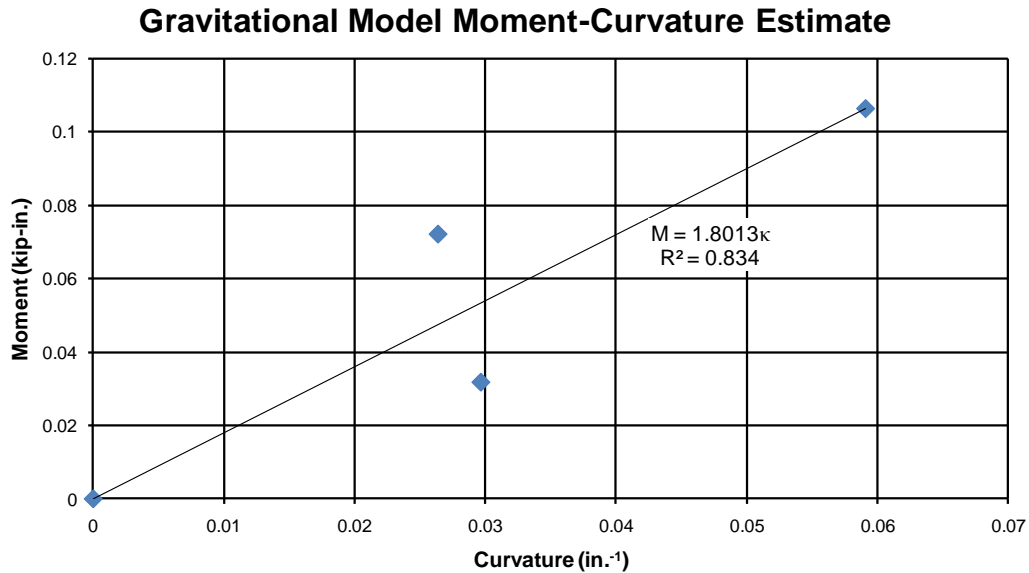


Figure 97. Moment-Curvature Curve Estimation Obtained Using Gravitational Models

10.4.1 Model Description

Three models were created to simulate the reaction of wire rope under quasi-static bending loads—one for each of the three tested lengths. Based on the results of the quasi-static tensile testing mesh-sensitivity study, a beam element length of 12.5 mm was chosen uniformly along the length of the beam. The models were defined with SPC constraints at one end of the beam, and gravity was initialized using the *LOAD_BODY_Z command.

Since the wire rope was curved in the physical test, the wire rope modeled in LS-DYNA was created with an initial circular arc. Prior to conducting the quasi-static bending tests, the curvature of the long length of wire rope was determined by attaching a string line between the ends of the wire rope. Offset displacements of eight equally-spaced increments of the wire rope were recorded. Because this length of wire rope was partitioned into the long, medium, and short wire rope tests, only one curvature value required calculation as the curvature was approximately constant throughout the length of wire rope.

It was determined that the radius of curvature of the wire rope was 67.3 in. (1,708 mm) with a margin of error of approximately 1.0 in. (25 mm). The measurements and approximate radius of curvature are shown in Figure 98.

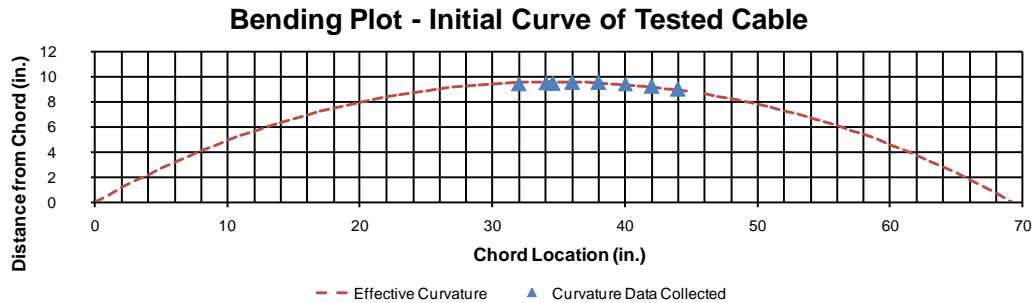


Figure 98. Measured Initial Radius of Curvature of Wire Rope

To simulate the initially-curved lengths of wire rope a circular length of wire rope was defined such that incremental element lengths were 0.500 in. (12.7 mm). To do this, formulas for the length of a line segment were used, such that:

$$ds^2 = dx^2 + dy^2 + dz^2. \quad [37]$$

Since the out-of-plane displacement of wire rope is negligible, the equation reduces to a 2-D curve. Recursive calculations were conducted to ensure each element location satisfied position constraints along the curve and incremental element lengths. The sum of element lengths was used to ensure total simulated and tested wire rope lengths were the same. The models were constructed such that angular offsets at the cantilever constraint location could be included using initial nodal locations.

Nodes were located at the measurement points used in the quasi-static bending tests along the wire rope. Each measurement point was used to compare to the deflection at each location in the wire rope bending tests. The updated density, measured in the quasi-static bending testing, was used to ensure accurate modeling of the moment loading of the wire rope.

10.4.2 Baseline Model

The moment-curvature curve was modified and refined by testing the simulated curved wire rope under gravitational and applied loads. Loads applied to the wire rope in quasi-static bending were placed in known locations on the undeformed wire rope, and the nodes corresponding to those locations on the modeled wire rope were loaded with the same magnitude of force. Then, positions of each of the measurement points A through D were tabulated from the simulation and compared with the known positions under the indicated applied moment. Physical test data from the quasi-static bending tests were then used to validate the curvature model. The initial element length was 0.5 in. (12.7 mm).

As noted in the quasi-static bending tests, an initial angular displacement was present in many of the wire ropes which could not be measured. As part of the effort to simulate the wire rope bending strength, angular offsets were simulated in the wire rope bending data based on incremental optimization efforts. An approximation to initial angular offset was accomplished by rotating the points of the simulated deflected wire rope through angular offsets until a best-fit was obtained. This calculated small angular offset was integrated into the simulation to compare the simulated geometries with the measured points on the deflected test cables. It was determined that the angular offsets were typically very small; most tested rope curves were within 0.5 degrees, and some required no modification.

The moment-bending curves were modified in parallel with the offset angular simulations. Eventually, the simulated displacements of the wire rope at the measured points were sufficiently matched to within 5% of the tested measurements. The final bending curve was validated against several of the tested configurations of wire ropes and applied loads. Samples of

the validation efforts for wire rope modeling are shown in Figures 99 through 100. The final moment-bending curvature curve is shown in Table 9.

It should be noted that the medium-length wire rope results were not simulated. As the long wire rope was loaded, plastic moments extended through much of the initial length of the wire rope. This wire rope was later partitioned and used in the medium-length wire rope tests. It was not known at the time that the moment applied to the long wire rope exceeded the elastic limit of the medium wire rope, but the yielding of the rope invalidated medium-length wire rope results and thus could not be simulated accurately.

10.4.3 Optimized Element Length

Based on the validation study of the *MAT_MOMENT_CURVATURE_BEAM, it was noted that element lengths must be within a small margin of error to prevent excessive error from accumulating in the simulations. However, the length of a beam element required to reasonably capture the bending deflection of wire rope was unknown.

An error sensitivity study was conducted to determine the percent error of bending deflection between two adjacent elements, based on relative angle. It was observed that good accuracy could be obtained for relative angles below less than 0.5 degrees. The results are shown in Table 10.

Based on a modal shape analysis of wire rope during full-scale impact, it was observed that amplitudes of 6 in. (152 mm) on a single mode shape 16 ft (4.9 m) long could be produced during impact. Element lengths smaller than 1 in. (25 mm) would be expected to accurately capture the modal vibration of wire rope.

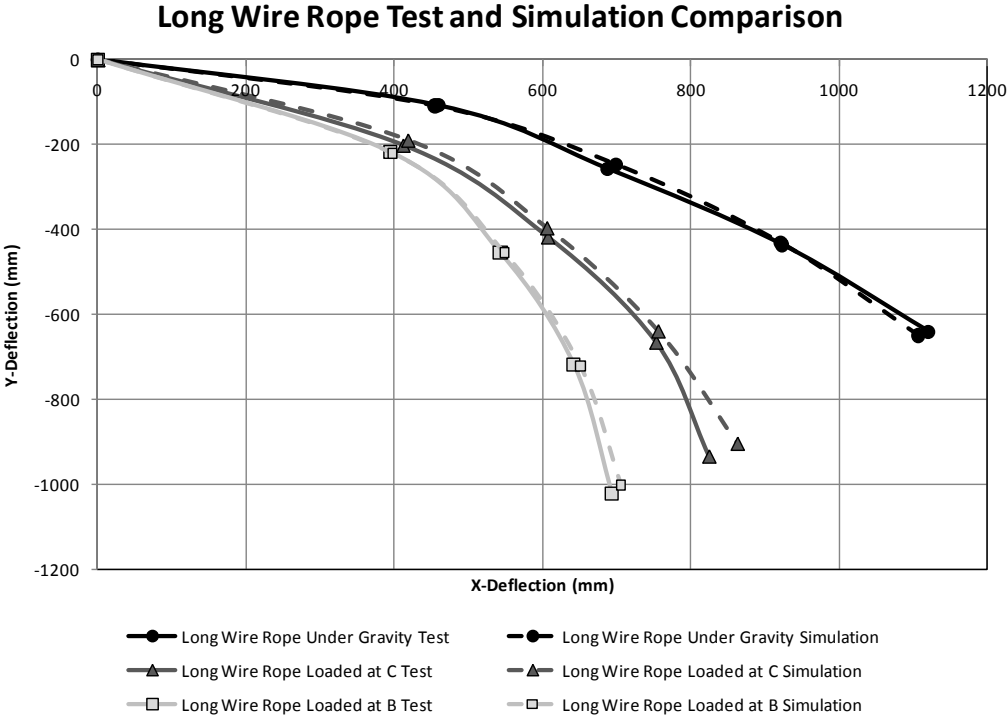


Figure 99. Long Wire Rope Test and Simulation Comparison

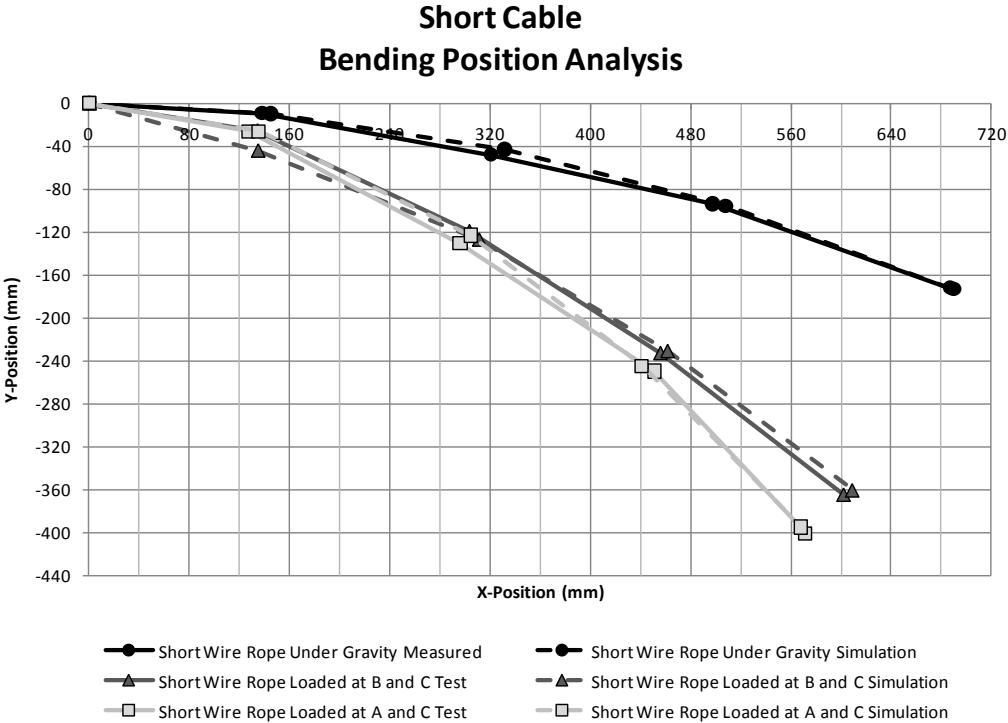


Figure 100. Short Cable Test and Simulation Comparison

Table 9. Moment-Curvature Input Curve

Curvature		Moment	
in. ⁻¹	mm ⁻¹	kip-in.	kN-mm
0.0000	0.0000	0.000	0.0
0.0076	0.0003	0.086	9.7
0.0445	0.0018	0.239	27.0
0.1270	0.0050	0.443	50.0
0.2540	0.0100	0.566	64.0
0.5080	0.0200	0.708	80.0
1.2700	0.0500	0.841	95.0

Table 10. Beam Element Percent Error in Bending

Bending Angle Between Elements (deg)	Percent Error (%)	Bending Angle Between Elements (deg)	Percent Error (%)
0.0001	5.08E-11	1.2	0.007
0.0005	1.27E-09	1.4	0.010
0.001	5.08E-09	1.6	0.013
0.005	1.27E-07	1.8	0.016
0.01	5.08E-07	2.0	0.020
0.05	1.27E-05	2.5	0.032
0.10	5.08E-05	3.0	0.046
0.20	2.03E-04	3.5	0.062
0.30	4.57E-04	4.0	0.081
0.40	8.12E-04	4.5	0.103
0.50	1.27E-03	5.0	0.127
0.60	1.83E-03	6.0	0.183
0.70	2.49E-03	7.0	0.249
0.80	3.25E-03	8.0	0.326
0.90	4.11E-03	9.0	0.412
1.00	5.08E-03	10.0	0.510

For adequate bending transverse waves to be accurately captured, the beam element timestep must be known. Timesteps are calculated using the longitudinal wave speed of wire rope, approximately given by

$$c = \sqrt{E/\rho} \quad [38]$$

which for measured wire rope density of 496.2 lb/ft^3 ($7,948 \text{ kg/m}^3$) and a measured Young's modulus of $E = 16.36 \text{ Mpsi}$ (112.8 GPa), gives a wave speed of $12,360 \text{ ft/s}$ ($3,767 \text{ m/s}$). Transverse waves were observed with amplitude of roughly 1 in. (25 mm). Using classical tensioned-string wave propagation equations, and if in 1 ms twelve beam element lengths are used to transition the wave to ensure adequate accuracy, the beam element length must be less than 1.02 in. (26.3 mm) long to transmit a bending wave with acceptable accuracy. This is consistent with previous calculations. However, since amplitudes can be much higher than 1.00 in. (25.4 mm), element lengths should be less than 1 in. (25.4 mm) long, and a recommended length is 0.50 in. (12.7 mm).

The long and short wire rope lengths were simulated using 1-in. (25.4-mm) and 0.25-in. (6.35-mm) length elements in the gravitational test, a rope loaded at B position, and rope loaded at C position. A comparison of the results of the long wire rope simulations with load applied at point C is shown in Figure 101. The differences between the mesh densities are summarized in Table 11. Because the 0.250-in. (6.35-mm) element length wire rope simulation was the finest mesh, it was used as the reference. The 1.000-in. (25.4-mm) element length beam was slightly stiffer than the other two meshes; however, the 0.500-in. (12.7-mm) element length beam was virtually identical to the mesh with 0.250-in. (6.35-mm) element length beams. Furthermore, the time required per simulation is parabolic, and the 0.500-in. (12.7-mm) element length optimized the computational expense and accuracy. Therefore, the 0.5-in. (12.7-mm) element length was chosen to be the standard length for all future wire rope simulations.

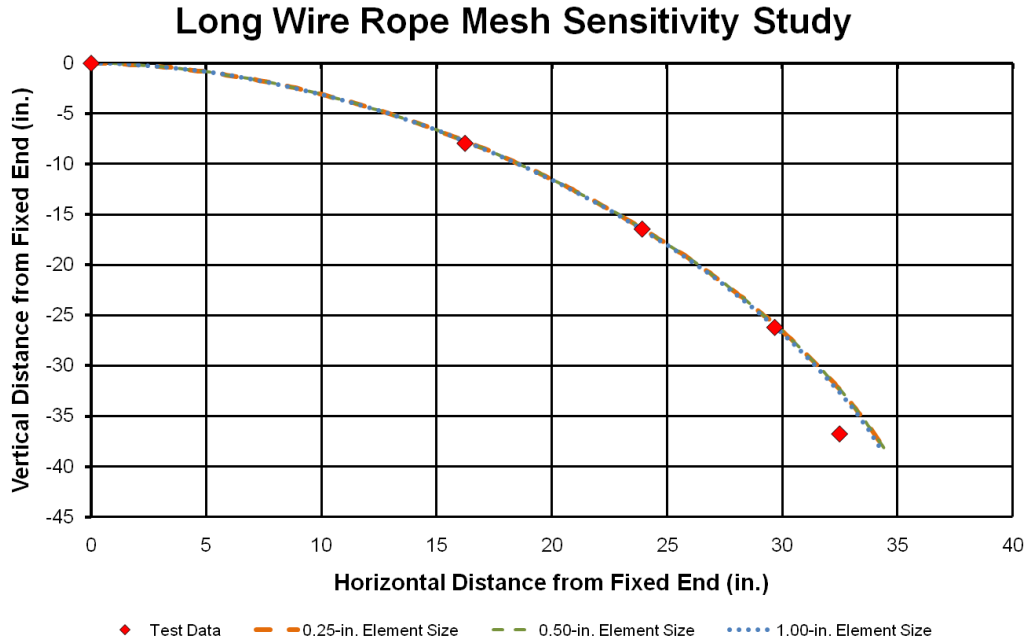


Figure 101. Mesh Sensitivity Analysis for Long Wire Rope Loaded at C Position

Table 11. Comparison of Wire Rope Mesh Density Results

Element Length (in.)	Computational Time (s)	Deflection at A (in.)	Deflection at B (in.)	Deflection at C (in.)	Deflection at D (in.)	Percent Difference from 0.25-in. Element
1.00	104	7.73	16.47	26.08	32.61	1.51%
0.50	536	7.70	16.37	25.87	32.29	0.04%
0.25	3221	7.70	16.37	25.87	32.29	-

10.5 Discussion

The wire rope bending tests were simulated based on the curvature of the wire rope as measured in the test, approximation of the initial offsets, and applied moments based on point loads and linear densities. However, it should be noted that significant effort was required at every step to ensure modeling accuracy. Each measurement step in the determination of the moment-curvature curve introduced measurement error, and every approximation and estimation increased measurement error as well. These sources of measurement error may cause variations in the moment-curvature curve.

In general, the curvature of beams and, particularly, wire rope is very difficult to estimate. One of the greatest difficulties in using the *MAT_MOMENT_CURVATURE_BEAM material model is the generation of curvature values based on moment-bending. Testing of wire rope to determine curvature is generally difficult and may require very precise and accurate measurement equipment. Analytical determination of the moment as a function of curvature can also be difficult since it requires accurate determination of stresses at each location in the cross-section of a beam.

Simulation of wire rope in quasi-static bending requires careful attention to the end conditions and angular deformation between adjacent elements. If the angular deformation between elements is observed to be relatively sharp, within the range of 3 to 5 degrees between angles, the mesh may require refinement in the area of localized high-curvature deformations.

Nonetheless, the bending strength of wire rope is relatively small. Curvature of wire rope around an impacting vehicle is generally limited and constrained to small angles, but the bending resistance is minimal in comparison to the tensile force applied by the tension of wire rope.

10.6 Conclusions

Wire rope was simulated in bending and the results tabulated. Validation of the material model was accomplished by using a known beam section and analytically determining the bending strength and deflection, and comparing simulated deflections to the actual deflections. A mesh sensitivity study on the stiff I-section beam was conducted to identify appropriate beam element lengths to accurately capture bending. Once the material use was validated and understood, the material was applied to the type 2 element in bending and the bending curves were determined through iteration of the simulated tests. Drawbacks were noted and the results

discussed. The final recommended moment bending curve for use with both the non-prestretched and prestretched wire rope models is repeated in Table 12 and Figure 102.

Table 12. Final Low Axial Load Moment-Curvature Input Curve

Curvature		Moment	
in. ⁻¹	mm ⁻¹	kip-in.	kN-mm
0.0000	0.0000	0.000	0.0
0.0076	0.0003	0.086	9.7
0.0445	0.0018	0.239	27.0
0.1270	0.0050	0.443	50.0
0.2540	0.0100	0.566	64.0
0.5080	0.0200	0.708	80.0
1.2700	0.0500	0.841	95.0

Moment-Curvature Curve

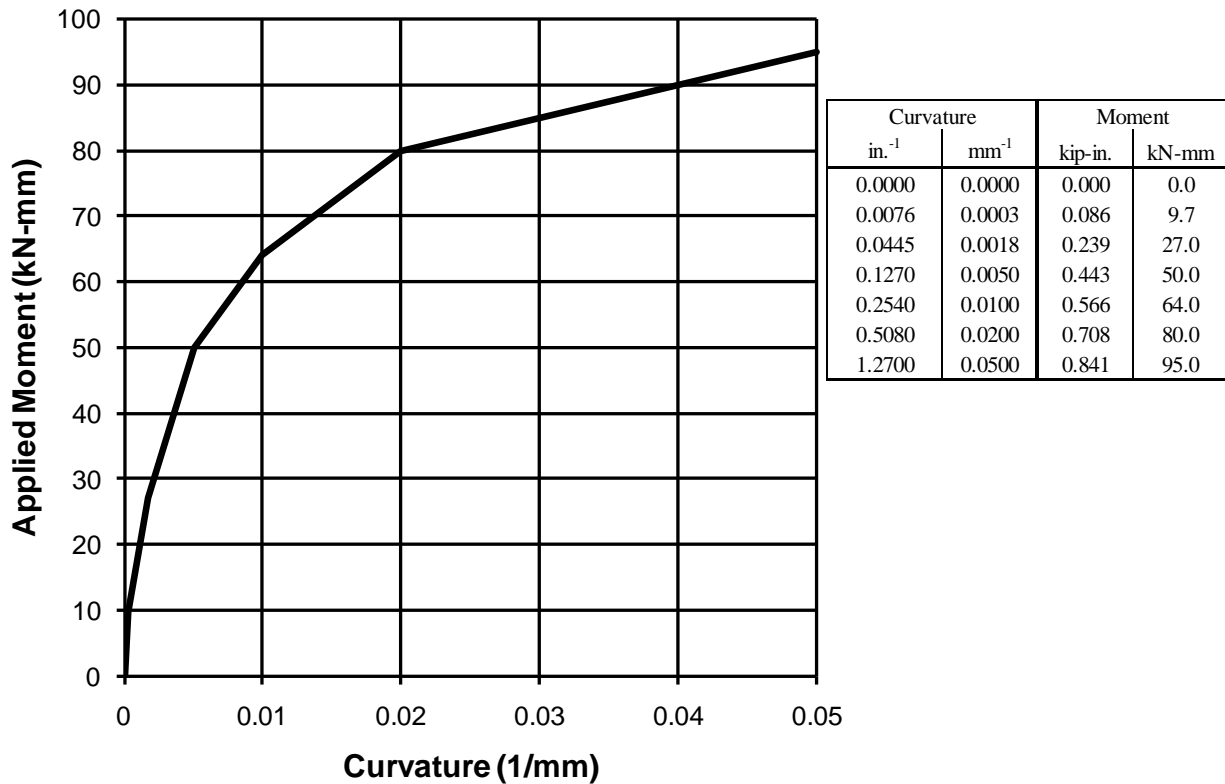


Figure 102. Moment-Curvature Input Curve for Use with Wire Rope Model

11 WIRE ROPE RESPONSE TO DYNAMIC IMPULSE

11.1 Purpose

The dynamics of wire rope impact require an understanding of bending wave transmission. Bending waves contribute to wire rope release from posts upstream and downstream of impact as well as to interlock with sheet metal and suspension components during crash testing. Fundamental understanding of bending waves, caused by tension and internal stiffness, is required to accurately capture the behavior of wire rope.

11.2 The 1-Dimensional Wave Equation for Tensioned Strings

Tensioned string theory is based on the assumption that a string has no inherent bending strength, and thus does not resist shear loads in bending [43]. If the string is initially displaced by a finite value y_0 , two waves will be generated on the string traveling in opposite directions, and each wave will have the same wave transmission speed, often referred to as the wave speed. As the disturbance propagates along the string, each location on the string undergoes a lateral displacement according to the propagating wave shape. To determine the reactionary forces and to predict the motion of the wave, the reaction of a small section of string is considered, as shown in Figure 103.

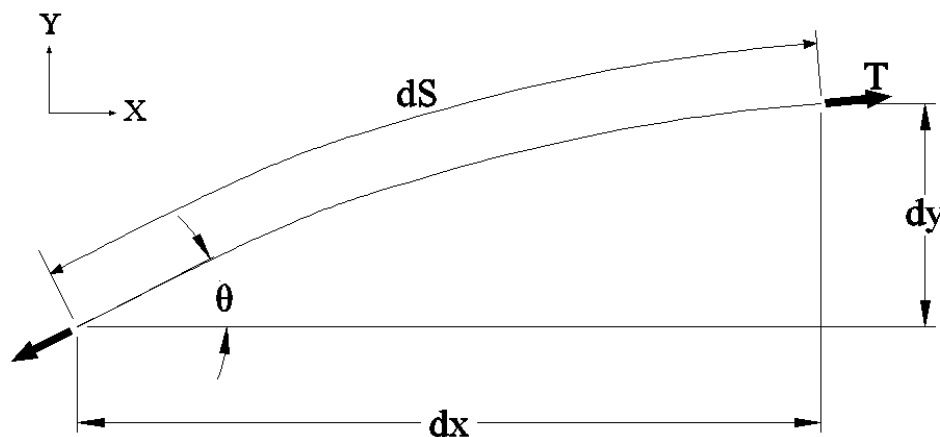


Figure 103. Tensioned String Model and Reaction Forces

A very small section of string with initial length Δx has a vertical displacement at one end measuring Δy . Since the string has no bending strength, internal string shear forces are negligible. String tension, which is assumed to be constant for small bending waves, is applied to the string on either end. As a dynamic wave propagates along a string, the tension in the string will change *direction* as a result of the string bending by Δy . The applied force perpendicular to the axis of the undeflected string, in the y -direction, is

$$df_y = (T \sin \theta)_{x+dx} - (T \sin \theta)_x. \quad [39]$$

To quantify the change in tension across the incremental length Δx , a Taylor's series expansion of the increments is performed, such that

$$f(x + dx) = f(x) + \left(\frac{\partial f}{\partial x}\right)_x dx + \frac{1}{2} \left(\frac{\partial^2 f}{\partial x^2}\right)_x dx^2 + \dots \quad [40]$$

Substituting the force equation into the Taylor's series expansion,

$$df_y = \left[(T \sin \theta)_x + \left(\frac{\partial(T \sin \theta)}{\partial x}\right)_x dx + \frac{1}{2} \left(\frac{\partial^2(T \sin \theta)}{\partial x^2}\right)_x dx^2 + \dots \right] - (T \sin \theta)_x. \quad [41]$$

Assuming that the tension is constant along the incremental length of string, and equating the sum of forces to the acceleration using Newton's second law, gives

$$\rho_m dx \left(\frac{d^2 y}{dt^2}\right) = T \left(\frac{\partial(\sin \theta)}{\partial x}\right)_x \quad [42]$$

$\rho_m = \text{linear density}$

Note that if the density varies with position the equations will become nonlinear. If the wave has a sufficiently small amplitude such that the angle formed is very small, the sine of the angle becomes

$$\sin \theta = \frac{\partial y}{\partial s} = \frac{\partial y}{\partial x} \quad [43]$$

for s the incremental length of the string. Therefore, dividing by the linear density and incremental length of the string and taking the limit as the length of the string tends to zero, the 1-dimensional wave equation can be written:

$$\frac{d^2y}{dt^2} = c^2 \frac{d^2y}{dx^2}, \quad [44]$$

The characteristic wave speed c is then a constant, and $c = \text{sqrt}(T/\rho_m)$.

11.3 The 1-Dimensional Wave Equation for Stiff Bars

Tensioned string wave propagation represents one limiting condition in the spectrum of bending wave analysis; consequently, bending waves in stiff rods are on the opposite end of the bending wave analysis spectrum. Bending response of stiff bars may be analyzed by considering that a short length of a stiff bar with cross-sectional area A and modulus of elasticity E (which is initially straight), is subjected to bending with a radius of curvature ρ , as shown in Figure 104 [43].

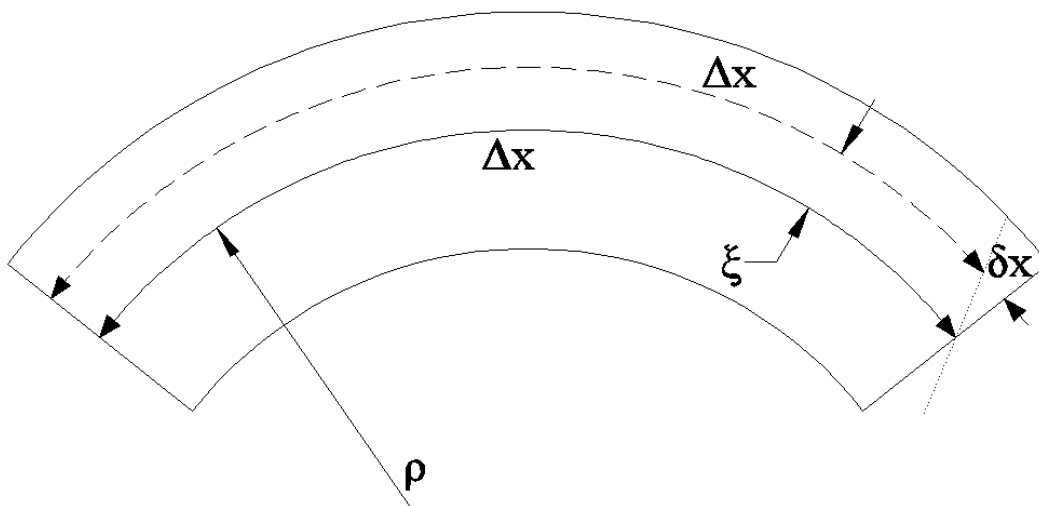


Figure 104. Stiff Rod Subjected to Bending

The increment of longitudinal force applied to an arbitrary fiber located a distance ξ from the neutral axis is given by

$$dF = -EdA \left(\frac{\delta x}{\Delta x} \right). \quad [45]$$

where: F = force
 E = Young's modulus
 dA = incremental cross-sectional area

Using geometry, it is clear that along concentric circular arcs,

$$\left(\frac{\delta x + \Delta x}{\rho + \xi} \right) = \left(\frac{\Delta x}{\rho} \right); \quad \frac{\delta x}{\Delta x} = \frac{\xi}{\rho}. \quad [46]$$

Defining a radius of gyration r_ξ , such that

$$r_\xi^2 = \frac{1}{A} \int \xi^2 dA \quad [47]$$

then the applied moment may be written as

$$M = \frac{-EA r_\xi^2}{\rho} \quad [48]$$

using classical mechanics. If the displacements of the bar in the y -direction are small, then the radius of curvature, which varies along the longitudinal axis of the bar, is given by a combination of Equations 10 and 20. Using this result, the moment may be rewritten as

$$M = -EA r_\xi^2 \frac{\partial^2 y}{\partial x^2} \quad [49]$$

Lateral forces in the beam generate bending moments. The shear force in a stiff beam may be derived from the bending moment using the relation

$$F_y = \frac{-\partial M}{\partial x} = EA r_\xi^2 \frac{\partial^3 y}{\partial x^3} \quad [50]$$

assuming that the increase in angular momentum of each fiber in the beam is small. Using a moment balance,

$$M(x) - M(x + \Delta x) = F_y(x + \Delta x) \Delta x \quad [51]$$

which can also be decomposed using a Taylor's series expansion as before. The acceleration of the fiber of the beam due to the net resultant force is given by

$$dF_y = -EA r_\xi^2 \frac{\partial^4 y}{\partial x^4}. \quad [52]$$

Assuming that the bending wave can be represented using a series of sinusoidal terms, it follows that the deflection in the y-direction can be written as

$$y(x, t) = \Psi(x) e^{j\omega t} \quad [53]$$

using a complex exponential method of representing the wave forms. The expression for the motion of the stiff bar to transverse vibrations can thus be written as

$$\frac{d^4 \Psi}{dx^4} = \omega^4 (r_\xi c)^2 \Psi = \left(\frac{\omega}{v}\right)^4 \Psi; \quad v^2 = \frac{r_\xi c}{\omega} \quad [54]$$

for $c^2 = \frac{E}{\rho_m}$ the longitudinal wave speed and ρ_m the mass density. Solving this equation for Ψ and substituting for y, the waves in longitudinally-stiff members may be described as

$$y(x, t) = \left(A e^{\left(\frac{1}{\sqrt{\omega r_\xi c}}\right)x} + B e^{\left(-\frac{1}{\sqrt{\omega r_\xi c}}\right)x} \right) e^{j\omega t}. \quad [55]$$

A bending wave propagating along a stiff, infinitely-long bar will be spatially damped. This requires that all bending waves in stiff media dissipate over time. The spatial damping coefficient $1/\sqrt{\omega r_\xi c}$ may be measured as a part-specific material property. Though this is related to the material used, elastic materials will still dissipate the bending wave over long distances. The fundamental differential equation for the wave speed is given by

$$EI \frac{\partial^4 y}{\partial x^4} = \rho_m \frac{\partial^2 y}{\partial t^2}. \quad [56]$$

Assuming a complex sinusoidal wave form, given by $y(x, t) = \exp(j(\omega t - kx))$, the resulting wave form may be expressed by

$$EI k^4 = \rho_m \omega^2. \quad [57]$$

Subject to boundary conditions, only certain frequencies will be excited in bending. If k is small relative to the driving frequency the resulting phase speed of a stiff bar subjected to bending waves is

$$c = \frac{\omega}{k} = \sqrt[4]{\frac{\omega^2 EI}{\rho_m}}. \quad [58]$$

If the stiff beam is subject to rigid boundary conditions and is impacted in the center, k can be quantized by

$$k = \frac{(2n-1)\pi}{L} \quad [59]$$

for L , the length of the beam, such that

$$c = k \sqrt{\frac{EI}{\rho_m}} = \frac{(2n-1)\pi}{L} \sqrt{\frac{EI}{\rho_m}}. \quad [60]$$

Though the wave speed is not constant for stiff beams subjected to bending but is dependent on the driving frequency and wave form, the term EI/ρ_m appears and may be measured for wire rope.

11.4 Discussion

Wire rope is intrinsically affected by the tension and stiffness bending waves. The stiffness waves, since they are spatially attenuated, i.e. have a localized effect and therefore will not propagate as far down the length of a cable barrier as the tension waves. However, both stiffness and tension bending waves are constrained by the frictional and resistive interaction of the post attachment hardware and the post flanges, which resist dynamic bending wave propagation. However, wire ropes have been known to propagate bending waves approaching a

cable barrier's natural frequency and detach from hook bolts downstream and upstream of impact away from the actual impact event.

In both bending-wave transmission theoretical analyses, many limitations were placed on the waves in order to make the problems bounded and solvable. Wire rope bending analysis is much more complicated and often is not analytically evaluated.

The tensioned-string approximation to wire rope bending analysis neglects the inherent stiffness of the wire rope in lieu of transmission of tensioned-bending waves. Though this approximation has been widely used in classical analysis of wire rope in cable guardrail systems due to the relatively low stiffness of wire rope, this approximation is not exact, and the bending stiffness of wire rope becomes significant as the amplitude of the bending waves increases. Furthermore, tensioned-string analysis is limited only to very small-amplitude vibrations, since non-linearities associated with the small-angle assumption become significant as the amplitude increases.

The bending wave transmission theory is more accurate in the consideration of low-tension bending waves in the wire rope, and the wave speed may be readily measured using a long wire rope and inducing a wave along the length of the wire rope. Both the spatial reduction coefficient $e^{(-1/\sqrt{\omega r \xi c})x}$ and the wave speed may be measured. However, this analysis is limited to elastic behavior; inelastic bending of wire rope is not considered. However, the plastic loading of wire rope is a deviation from the stiffness bending wave equations and will therefore likely be very similar to the elastic response with additional modifications on the analysis.

In both of the analyses, damping due to internal viscous resistance and static-dynamic friction was neglected. Both of these sources of friction are both present in wire rope due to sliding of the wires within strands and the lubrication required to prevent internal wear on the

rope. The effect of resistance is to decrease the actual wave speed through the wire rope and attenuate the amplitude over time; however, for short-duration impact events with wire rope, the viscous damping is the most important effect, since often the static-dynamic friction does not have time to build up and release.

Wire rope subjected to a combination of tension and bending will have characteristics of both the tensioned string bending waves and the stiff bar bending waves. In general, since the internal stiffness-related waves are spatially damped, these waves should vanish with time as they are reflected off boundaries. Spatial damping does not occur in the tensioned string analysis, so the waves are reflected at virtually the same amplitude between fixed supports. Further, the higher-frequency waveforms occur at harmonics of the fundamental frequency, so if a constant tension is applied, harmonics of the tensioned string waves may be easily observed.

Since tension-related bending waves only will become significant as the tension increases, impact events in which the entire load carried by the cable barrier is less than 30 kips (133 kN)—which is 10 kips (44.5 kN) per wire rope—may not have observable tension-related bending waves, or the tension waves may be masked by stiffness bending waves. Conversely, high-load impact events will likely be dominated by a tension bending wave response, since the stiffness bending waves are attenuated and are degenerate at higher frequencies.

The prediction of the tension and stiffness bending waves are important factors in evaluation of the new wire rope model. Bending waves in wire rope can lead to failure or successful capture of vehicles in cable barrier systems; furthermore, bending waves at the correct frequencies can be used to apply damping to the wire rope model, which is advantageous over the purely undamped model. Finally, bending wave transmission is a fundamental property of wire rope, and thus needs to be approached as a pertinent material property.

12 DYNAMIC BENDING TESTING

Dynamic bending tests were conducted on wire rope test samples in order to determine the dynamic response of wire rope to applied loading. Wire ropes were fastened to two load attachment points and a surrogate test vehicle was directed into the test setup. The test results of the dynamic bending tests were used to develop, refine, and test the wire rope material model. These tests were determined to be the most fundamental tests for evaluation of the wire rope model, since geometry, impact speed, impact conditions, and acquisition from multiple data sources was possible for evaluation and validation of simulation results.

12.1 Test Methodology

The purpose of the dynamic bending testing was to evaluate wire rope when subjected to tensioned impact laterally to the axis of tension. It was intended that two types of tests be conducted: one set to evaluate the wire rope under large plastic strains without fracturing the rope, and one to evaluate the wire rope in fracture situations. Fracture load and effective fracture strain were calculated, based on test results. The geometry and impact conditions of the bending tests would then be used to simulate the wire rope in dynamic bending using the proposed wire rope model.

12.2 Description of Tests

A total of six dynamic bending tests were conducted on non-prestretched wire rope. Dynamic bending component test nos. DBC-1 through DBC-4 were conducted on a wire rope with a nominal length of 28 ft - 3 in. (8.61 m) at speeds of 15 and 25 mph (6.7 and 11.2 m/s). Test nos. DBC-5 and DBC-6 were conducted on wire ropes with nominal lengths of 89 ft – 6 in. (27.28 m). Test details are shown in Figures 105 through 110. The load frames of the dynamic tensile tests were identical to the load frames used in the dynamic bending tests.

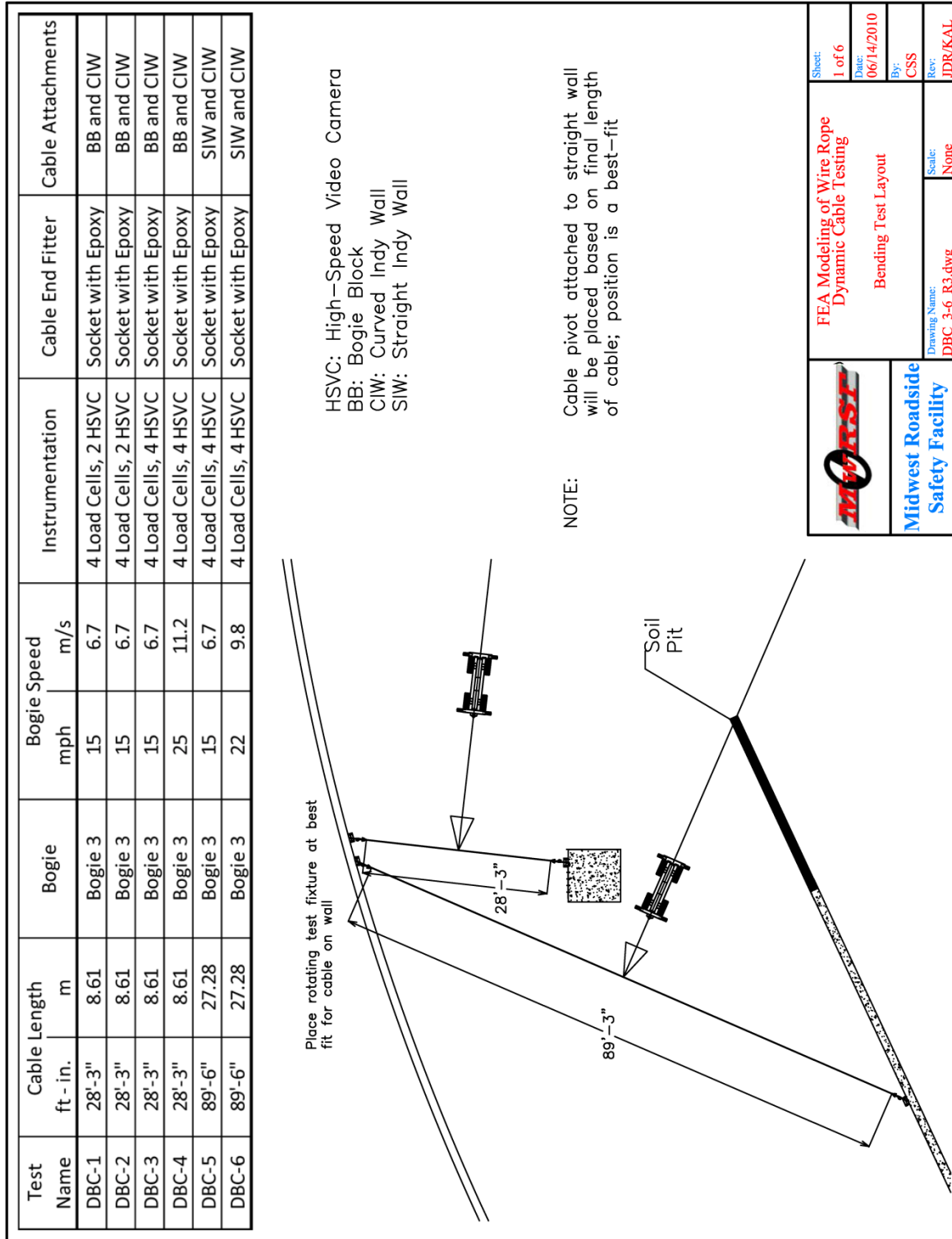


Figure 105. Bending Test Details, Test Nos. DBC-1 through DBC-6

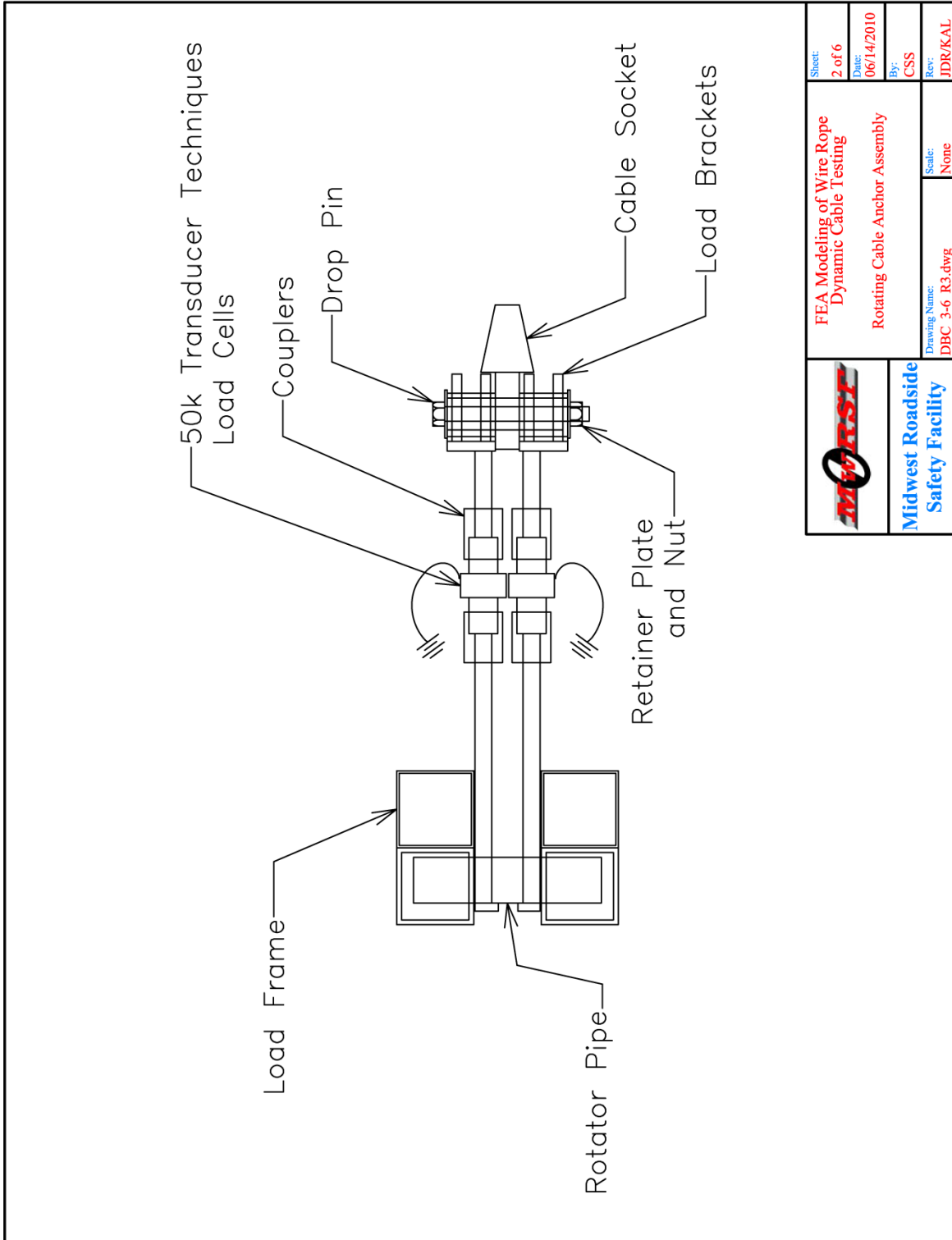


Figure 106. Load Frame and Rotator Pipe End Assembly, Test Nos. DBC-1 through DBC-6

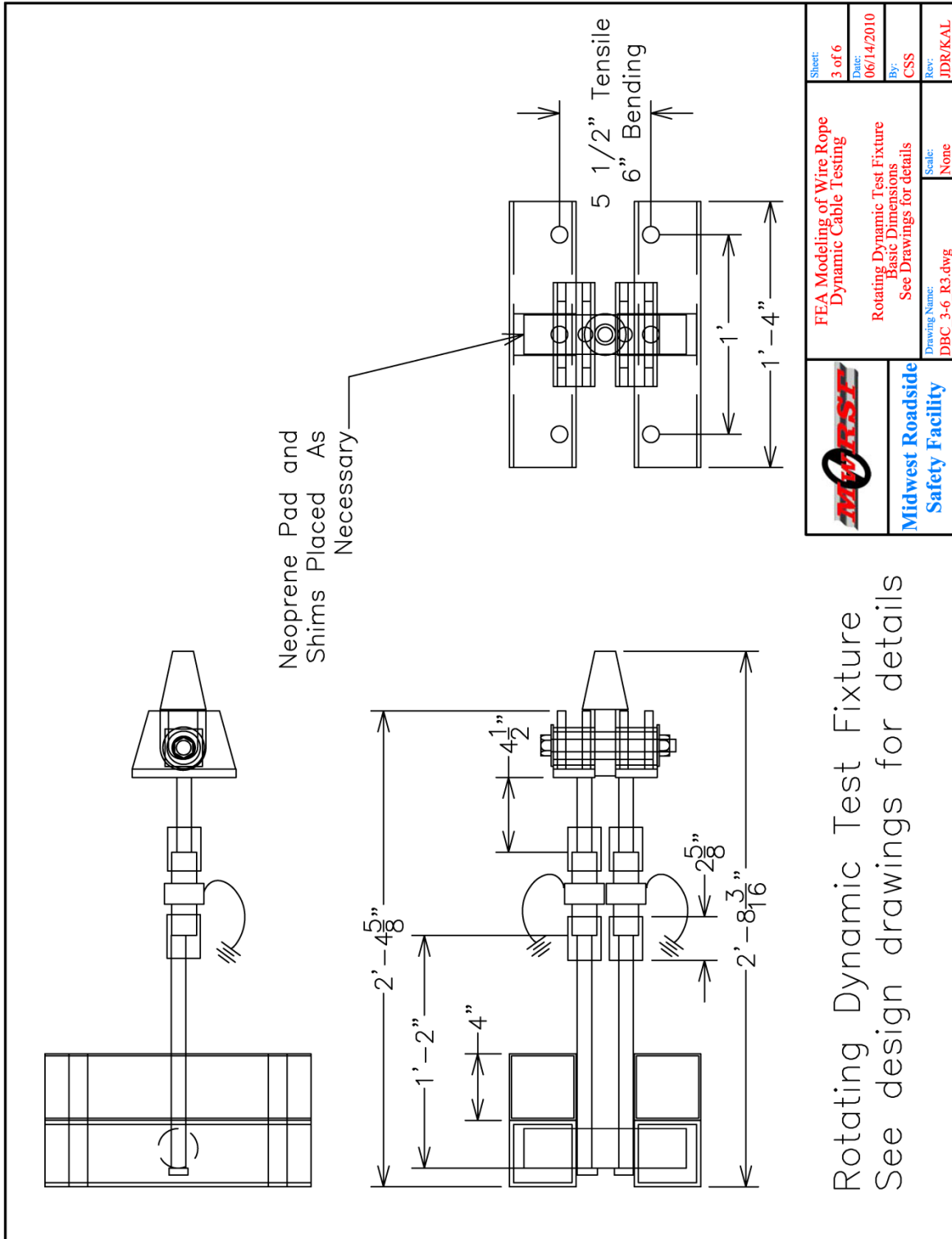


Figure 107. Load Frame and Rotator Pipe End Assembly Details, Test Nos. DBC-1 through DBC-6

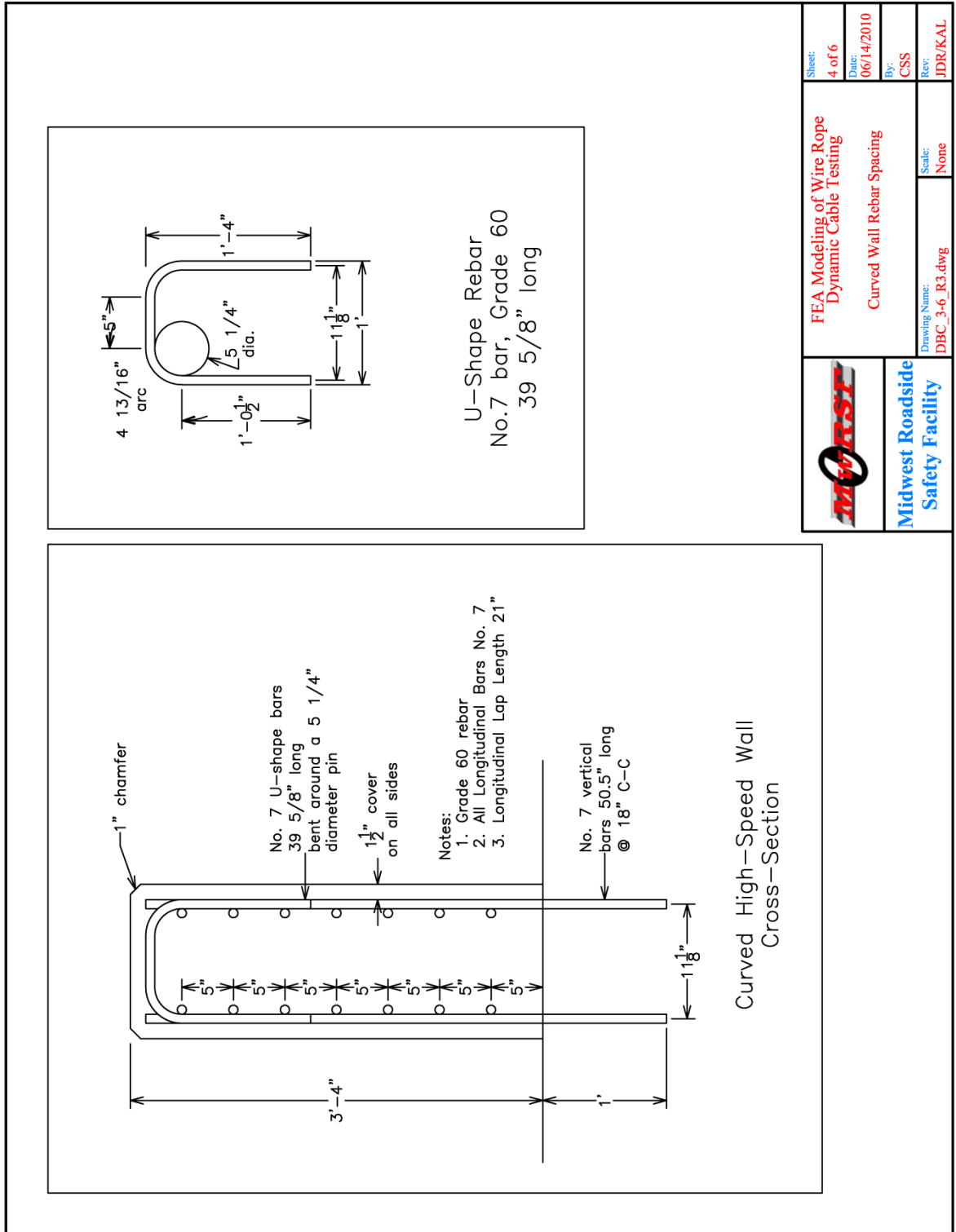


Figure 108. Concrete Wall Reinforcement Details, Test No. DBC-1 through DBC-6

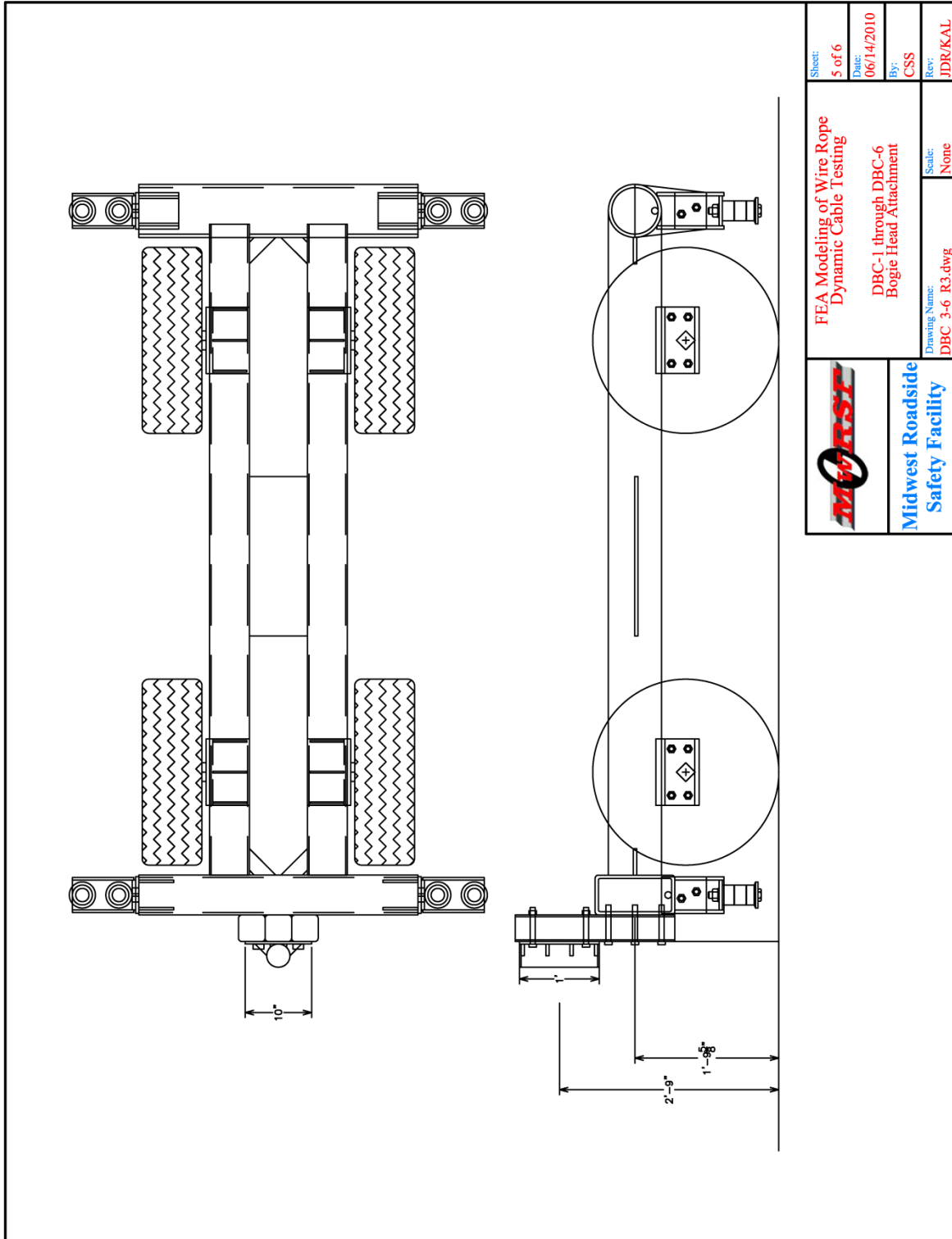


Figure 109. Bogie Head Attachment, Test Nos. DBC-1 through DBC-6

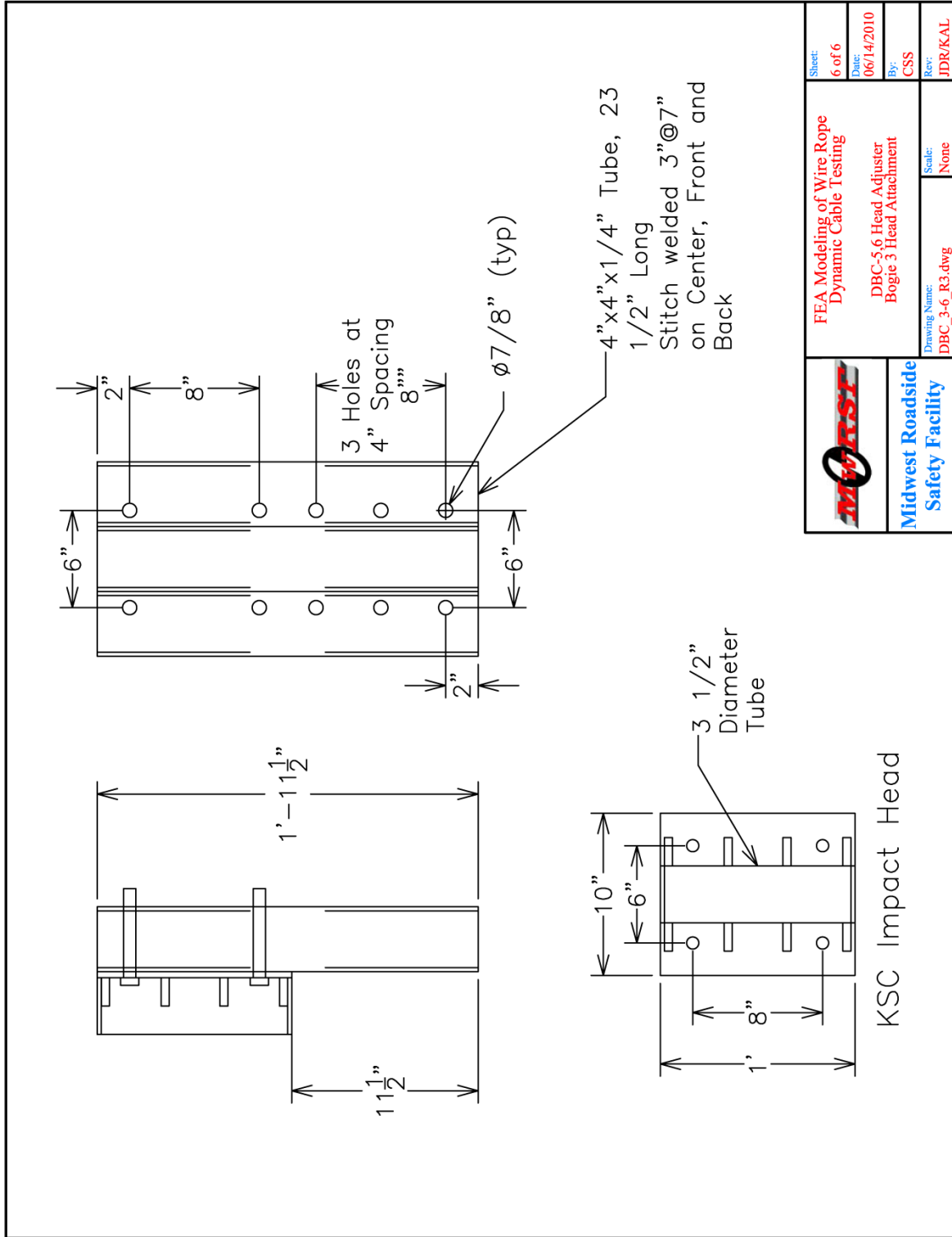


Figure 110. Impact Head Mount, Test Nos. DBC 1-6

A surrogate test vehicle, or bogie vehicle, consisted of a rigid steel-frame structure supported on four wheels, as shown in Figure 111. A rectangular tube for mounting various impact heads was located on one side of the bogie vehicle, and a cylindrical pipe was mounted on the back. A neoprene sleeve was secured to the cylindrical impact head. A braking system was installed on the bogie vehicle and consisted of a pneumatic cylinder mounted on the bogie frame which applied drum-type brakes to the bogie's wheels. The braking system was remotely-controlled.



Figure 111. Bogie Vehicle, Component Test Nos. DBC-1 through DBC-6

The weight of the bogie test vehicle was determined by placing four 2,000-lb (910-kg) scales beneath the four wheels of the vehicle. The measured bogie weight in test nos. DBC-1 and DBC-2 was 1,702 lb (772 kg). In component test nos. DBC-3 and 4, the measured bogie weight was 1696.1 lb (769.3 kg), and in component test nos. DBC-5 and 6, the measured bogie weight was 1695.7 lb (769.2 kg).

The bogie was modified with an impact head mount and impact head, as shown in Figure 112. Three 4-in. x 4-in. x 1/4-in. thick by 23 1/2 in. long (102-mm x 102-mm x 6-mm by 597 mm) square tubes were flare-V stitch welded together. An impact head was fastened to the front side of the impact head mount using four 5/8-in. (16-mm) diameter bolts. The impact head was composed of a 3 1/2-in. diameter by 1/4-in. thick (89-mm by 6-mm) pipe welded with four 2-in. x 2 1/4-in. by 0.5-in. thick (51-mm x 57-mm by 13-mm) gussets on both sides. The cylindrical pipe and gussets were welded to a 12-in. x 10-in. by 1/2-in. (305-mm x 254-mm by 13-mm) thick backup plate.



Figure 112. Impact Head and Mounting Post, Component Test Nos. DBC 1-6

A guidance track was laid down leading to the wire rope in each dynamic bending test. The guidance track was composed of a variation of W-beam guardrail sections with a wide flat valley between the two corrugations. The downstream end of each guidance tracks overlapped

the following section to minimize snag potential. The tires of the bogie vehicle located in the valley between the corrugations of W-beam and were prevented from falling off the track.

The guidance track was arranged using a survey scope and stringline. The survey scope and traffic marking cones were used to align the W-beam segments to ensure straight tracking by the bogie vehicle. The vehicle was accelerated down the track using a pickup with a padded push-bumper mounted on the front bumper. A digital tracking device located on the dashboard of the pickup monitored the pickup's velocity. Approximately 15 ft (4.6 m) of free-wheeling distance was included in the bogie track to allow some rebound distance following bogie capture by the wire rope.

In each of the dynamic bending component tests, 2-in. x 2-in. by 31 in. tall (51 mm x 51 mm by 787 mm) wooden stanchions were used to support the wire rope. In each test a small degree of slack was included in the tested length to increase ease of construction. The resulting sag of the wire rope was generally below the impact height of the bogie impact head. To ensure adequate contact, stanchions were placed between the end supports, and the impact height was measured to be approximately 30 in. (762 mm) in each of the component tests. Two stanchions were used in the 28-ft 3-in. (8.61 m) rope tests, and four were used in the 89-ft 6-in. (27.28 m) tests.

12.3 Data Collection

Since the tests were conducted with the bogie vehicle impacting perpendicular to the long axis of the wire rope, pertinent data to be collected in the test consisted of bogie accelerations, wire rope tensile load, and bogie and wire rope displacements. From these measurements, the dynamic response of the wire rope subjected to impact perpendicular to the long axis could be compared with simulation results.

The bogie vehicle was retrofitted with two accelerometers and a radio-controlled braking system. The first accelerometer, model EDR-3, was a triaxial piezoresistive accelerometer system manufactured by IST of Okemos, Michigan. The EDR-3 was configured with 256 kB of RAM memory, a range of ± 200 g's, a sample rate of 3,200 Hz, and a 1,120 Hz low-pass filter. The "DynaMax 1 (DM-1)" computer software program and a customized Microsoft Excel worksheet were used to analyzed and plot the accelerometer data.

The second accelerometer, model DTS, was a two-arm piezoresistive accelerometer system manufactured by Endevco of San Juan Capistrano, California. Three accelerometers were used to measure each of the longitudinal, lateral, and vertical accelerations independently at a sample rate of 10,000 Hz. The accelerometers were configured and controlled using a system developed and manufactured by Diversified Technical Systems, Inc. (DTS) of Seal Beach, California. More specifically, data was collected using a DTS Sensor Input Module (SIM), Model TDAS3-SIM-16M. The SIM was configured with 16 MB SRAM memory and 8 sensor input channels with 250 kB SRAM/channel. The SIM was mounted on a TDAS3-R4 module rack. The module rack was configured with isolated power/event/communications, 10BaseT Ethernet and RS232 communication, and an internal backup battery. Both the SIM and module rack were crashworthy. The "DTS TDAS Control" computer software program and a customized Microsoft Excel worksheet were used to analyze and plot the accelerometer data.

Four Transducer Techniques Inc. 50-kip (220-kN) tension load cells were located in the test setup. The load cell setup in the dynamic bending component tests was identical to the setup used in the dynamic tension test. The load cell data was sampled at 10,000 Hz, and had a gain of 400 and an input voltage of 10 V. The load cells had a sensitivity of approximately 0.1 lb (0.44 N). Output voltage from the load cells were filtered using a CFC 60 two-pass Butterworth filter.

In addition to the accelerometers and tension load cells, high-speed digital video cameras were used to record the motion of the bogie vehicle and wire rope subjected to impact. Two AOS high-speed digital video cameras with a 500 frame/sec capture rate were used in component test nos. DBC 1-2. One high-speed camera was located on a hoist, and raised 137 in. (3,480 mm) above the ground at the center of the wire rope. An additional AOS high-speed digital video camera was located with a line of sight between the wire rope end fixtures and was elevated slightly to obtain a perpendicular view of the bogie impact. Full-speed digital video cameras were also used to record the bogie test.

In test nos. DBC 3 and 4 four high-speed digital video cameras were used. Two AOS high-speed digital video cameras were mounted on a hoist and raised 223 in. (5,664 mm) above the ground at the center of the wire rope. One of the overhead video camera recorded a close-up shot of the wire rope during impact, and the second camera captured the full length of the wire rope. One AOS high-speed digital video camera was located near the west side support and was elevated to watch the reaction of the load frame during impact. One additional AOS high-speed digital video camera was located with a line of sight between the wire rope end fixtures and was elevated slightly to obtain a perpendicular view of the bogie impact. As in test nos. DBC 1 and 2, full-speed digital video cameras were used to record the test.

In test nos. DBC 5 and 6 four high-speed digital video cameras were used. The cameras were arranged identically to component test nos. DBC 3 and 4, except that the two cameras mounted on the hoist were measured to be 202 in. (5,131 mm) above the ground, and the perpendicular and end fixture cameras were located at the end of the 90-ft (27.4-m) wire ropes.

12.4 Test Results

12.4.1 Component Test Nos. DBC-1 and DBC-2

The targeted bogie impact speed in component test nos. DBC-1 and 2 was 15 mph (6.7 m/s). Actual bogie impact speed in test no. DBC-1 was 14.8 mph (6.6 m/s), and 15.1 mph (6.8 m/s) in test no. DBC-2. Sequential photographs of test nos. DBC 1 and 2 are shown in Figure 113. Impact conditions for test nos. DBC-1 and DBC-2 are shown in Figure 114. The bogie impacted the center of the wire rope in both tests and was decelerated, brought to a controlled stop, and rebounded away from the wire rope. In both tests, the wooden stanchions used to support the slack wire rope were displaced forward and were projected forward following impact. Both wooden stanchions came to rest approximately 8 ft (2.4 m) from the impact point. Photos from test nos. DBC 1 and 2 are shown in Figures 115 through 120.

The bogie impacts in test nos. DBC 1 and 2 caused kinks in the wire rope, as shown in Figures 117 and 118. The kinks had a radius of curvature of approximately $2\frac{1}{2}$ in. (64 mm), which was slightly larger than the impact head radius of $1\frac{3}{4}$ in. (44 mm). Kink depths of $1\frac{1}{2}$ in. (38 mm) and $1\frac{5}{8}$ in. (41 mm) were measured in the wire ropes analyzed in test nos. DBC-1 and DBC-2, respectively. The sag height of the wire rope following test no. DBC-1 was $11\frac{1}{4}$ in. (286 mm), and the sag height of the wire rope following test no. DBC-2 was $8\frac{1}{8}$ in. (206 mm).

The slack in each wire rope was impossible to measure while lying on the ground due to small variations along the length. The slack length of wire rope was calculated by observing the time in the high-speed video when the wire rope became visibly taut. The load in the load cells was extracted at that time and the resultant average strain displacement was subtracted from the total wire rope length. Finally, the length of the curves in the taut wire rope was estimated to determine the actual slack length of wire rope. It was determined through high-speed video



0.000 sec



0.000 sec



0.100 sec



0.100 sec



0.200 sec



0.200 sec



0.300 sec



0.300 sec



0.400 sec



0.400 sec

Figure 113. Sequential Photographs, Test Nos. DBC 1 and DBC-2



Figure 114. Bogie Impact Location, Component Test Nos. DBC 1 through DBC-4



Figure 115. Final Position of Wire Rope and Bogie Vehicle, Test No. DBC-1



Figure 116. Final Position of Wire Rope and Bogie Vehicle, Test No. DBC-2



Figure 117. Wire Rope Damage, Test No. DBC-1

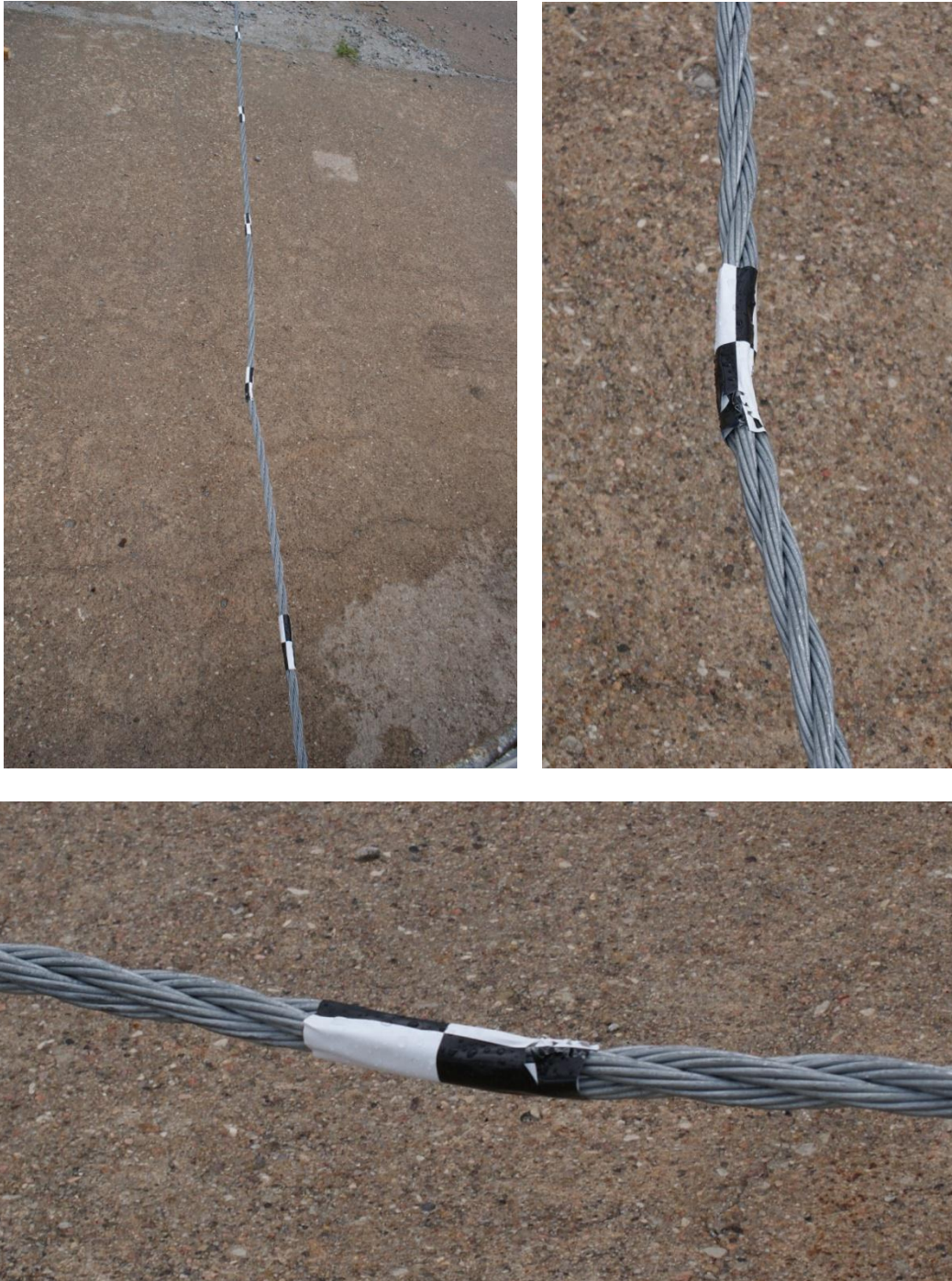


Figure 118. Wire Rope Damage, Test No. DBC-2



Figure 119. Impact Head Damage and Wire Rope Pull-Through, Test No. DBC-1



Figure 120. Wire Rope Pull-Through, Test No. DBC-2

analysis, load cell analysis, and bogie kinematics that the length of slack in component test nos. DBC-1 and DBC-2 was 0.717 in. \pm 0.118 in. (18.2 mm \pm 3.0 mm) and 1.985 in. \pm 0.125 in. (50.4 mm \pm 3.2 mm), respectively

Following test nos. DBC 1 and 2, the damage to the impact head was noted, as shown in Figure 119. The impact head sustained gouges and scratches on the front face over a total height of 2 $\frac{3}{4}$ in. (70 mm). The gouges had a depth of approximately $\frac{1}{16}$ in. (1.6 mm), and had the appearance of horizontal striations.

In test nos. DBC 1 and 2, the wire rope pulled the epoxy in the end fitters and pulled through the bottom of the socket slightly, as shown in Figures 119 and 120. Wire rope pull-through in test no. DBC-1 was estimated at $\frac{1}{16}$ in. (1.6 mm), and was measured in test no. DBC-2 at $\frac{3}{32}$ in. (2.4 mm). This pull-through was the result of debonding of the epoxy with the wires within the socket, crushing of the epoxy near the bottom of the socket, and wire extension due to axial load in each wire rope.

The wire rope tension in both tests was similar to a normal distribution, with a low-load stretching and tightening period between 50 and 100 ms. Load curves of test nos. DBC-1 and DBC-2 are shown in Figure 121. High-frequency vibrations were very low in both test nos. DBC-1 and 2, and pulses were evident which corresponded to dynamic bending wave propagation. The maximum load recorded in each test was 37.3 kip (165.8 kN) for test no. DBC-1, and 37.2 kip (165.5 kN) in test no. DBC-2. In both tests, the impact event lasted approximately 300 ms with a force peak centered near 175 ms.

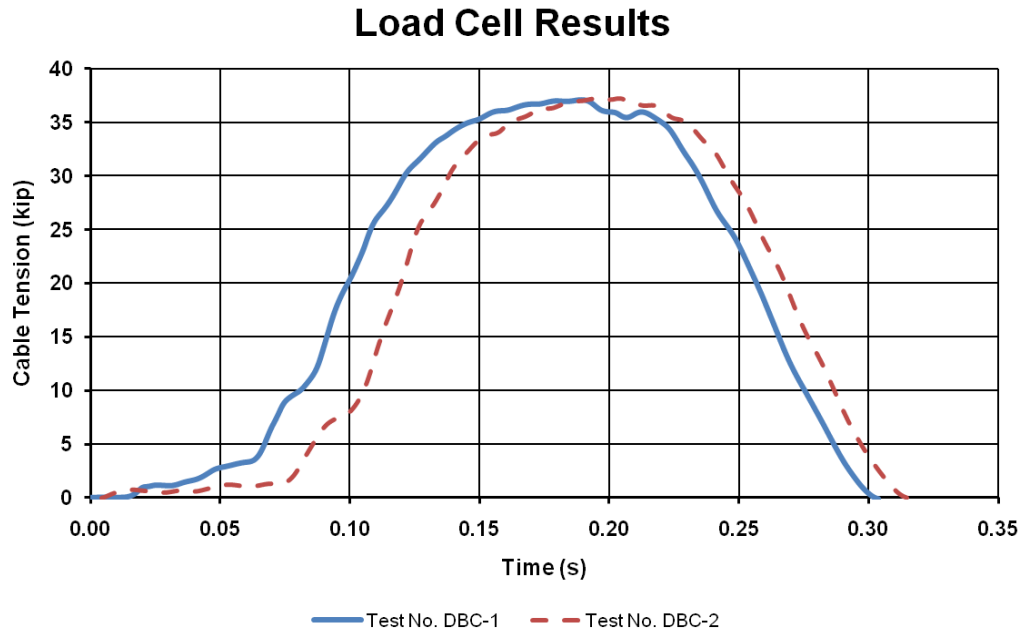


Figure 121. Load Cell Results, Component Test Nos. DBC 1-2

Following the force peak in both tests the wire rope unloaded with less elastic strain rebound than the initial loading. As the wire rope was loaded up, contact stresses between wires in each strand caused flattening of the contact region in the wires and strand compaction. As the wire rope unloaded, the wire compaction led to a difference in the load distribution within the strands and a semi-permanent stretch. The resulting compaction and tightening increased the effective modulus of elasticity during unloading. In this respect, the bogie impact was similar to the quasi-static prestretching of wire rope. If a prestretched wire rope had been used, the unloading and loading moduli of elasticity may have been the same.

The displacement of the bogie in each test was also plotted, as shown in Figure 122. The bogie vehicle caused greater deflection in test no. DBC-2. Deflection, in this instance, was related to a slightly higher impact speed and a greater length of slack in the wire rope in the second test. The maximum displacement of the bogie, as determined by high-speed video

analysis and calculated from the bogie accelerometer data, was 38.4 in. (975 mm) in test no. DBC-1, and 43.5 in. (1,104 mm) in test no. DBC-2.

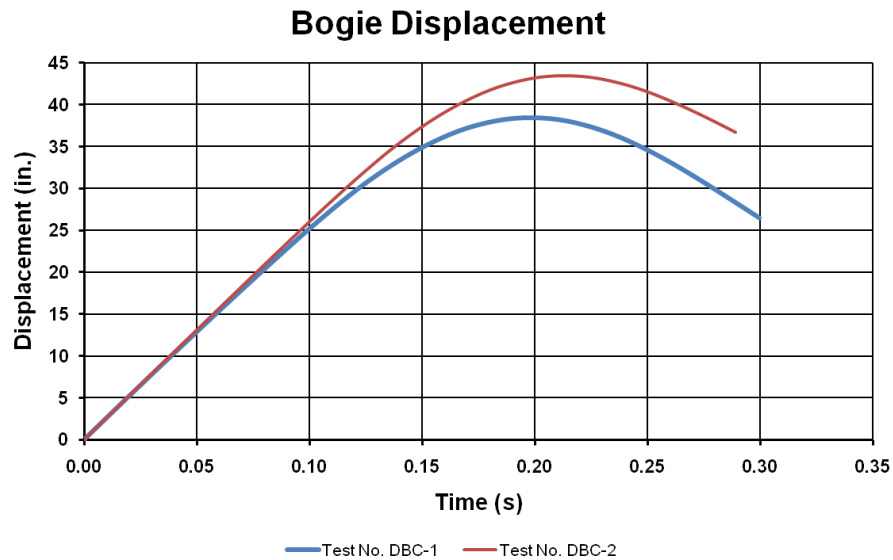


Figure 122. Bogie Displacement, Component Test Nos. DBC 1-2

Bogie velocity was also plotted for test nos. DBC-1 and DBC-2. The velocity of the bogie was smooth in both tests, as shown in Figure 123. The bogie was rebounded with a speed of 14.89 ft/s (4.54 m/s) in test no. DBC-1 and 11.6 ft/s (3.52 m/s) in test no. DBC-2. The lower rebound speed in test no. DBC-2 was related to the higher impact speed, thereby causing greater plastic deformation and more slack. The excess slack in test no. DBC-2 shortened the time over which the wire rope applied redirective force to the bogie vehicle, thus redirecting it at a lower speed.

Accelerations of the bogie were also measured and converted to non-dimensional units of g's. Accelerations of the bogie vehicles in test nos. DBC 1 and DBC-2 are shown in Figure 124. The bogie acceleration followed very similar loading and unloading paths with a longer sustained acceleration in test no. DBC-1. This outcome was expected based on the bogie's rebound velocity. The acceleration peaks were slightly higher in test no. DBC-2 with a maximum

of 9.70 g's compared to 9.49 g's for test no. DBC-1. Distinguishable peaks were evident in both tests corresponding to bending waves transmitted through the wire rope.

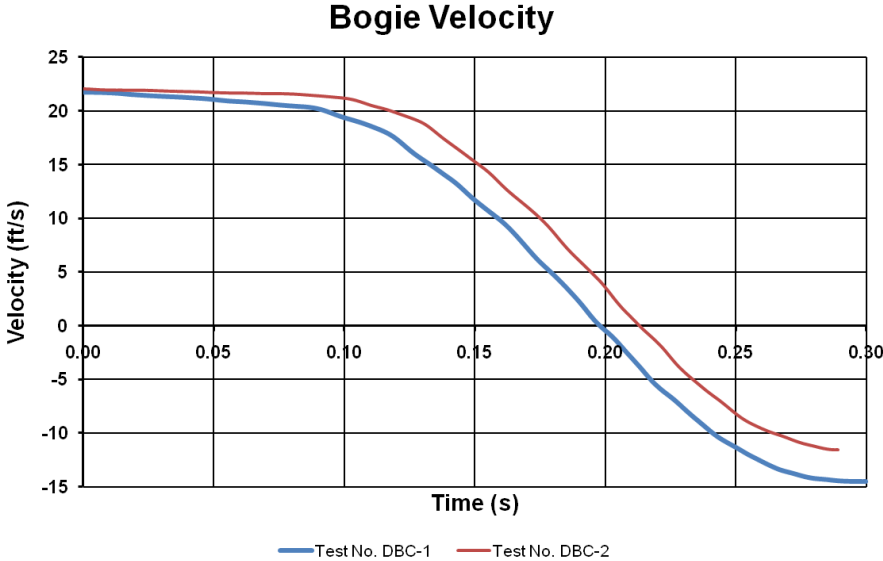


Figure 123. Bogie Velocity, Component Test Nos. DBC 1-2

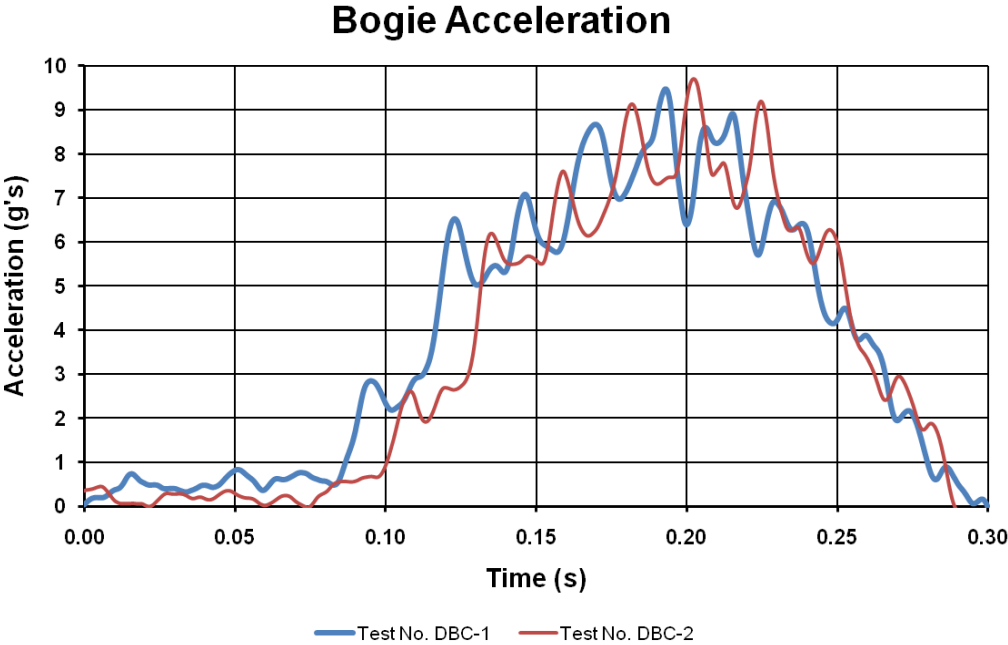


Figure 124. Bogie Acceleration, Component Test Nos. DBC 1-2

A discrete Fourier transform was performed on the accelerometer traces recorded in test nos. DBC-1 and DBC-2. Since the acceleration curves have large-amplitude peaks, corresponding to times in which waves in the wire rope passed the bogie, it was observed that the phase speed in wire rope could be experimentally determined using the wave bending frequency. The fundamental frequency of wire rope dynamic bending wave oscillations was approximately 43 Hz for both test nos. DBC-1 and DBC-2. The frequency spectrum is shown in Figure 125. This analysis assumes that the bogie vehicle is essentially rigid and internal stress waves do not contribute to the frequency spectrum, and with respect to the bending wave speed of wire rope, this is a good assumption.

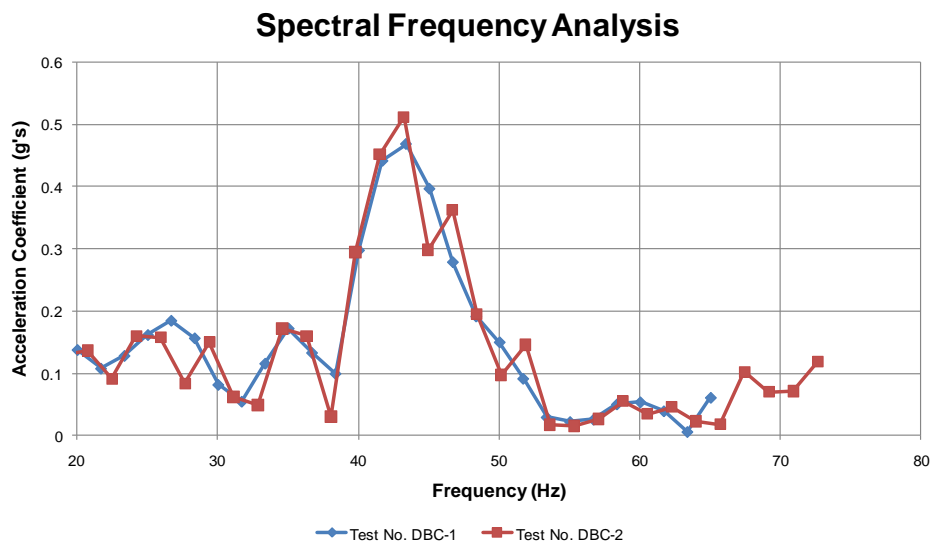


Figure 125. Spectral Frequency Analysis, Test Nos. DBC 1-2

The spectral frequency analysis was conducted using the relations found in Chapter 11. The bending frequencies of the wire rope were plotted, and based on the classical formulas for tension-bending wave propagation and stiffness-bending wave propagation, the natural frequencies of wire rope could be identified. The tension bending waves, which would vary based on wire rope tension, would not have many distinguishable peaks. However, the stiffness

bending wave speed remained relatively constant throughout the impact event, and though the tension will affect the bending properties, clearly distinguishable bending-frequency peaks should be identifiable. These bending waves were extrapolated to determine an empirical dynamic bending stiffness.

The wide array of frequencies generated in the spectral plot of the accelerometer indicated variations in stress wave transmissions in the steel frame of the bogie as well as different fundamental bending modes of the wire rope. A characteristic bending wave speed of 1,430 ft/s (435 m/s) was calculated that corresponded to wave propagation past the bogie vehicle during the test. This correlates well with the high-speed data indicating approximately 21-24 frames between wave oscillations at the bogie impact head, when the video was sampled at 500 frames per second. Though this characteristic bending wave speed is not a fundamental material property of the wire rope, it was later used to determine damping frequency ranges.

12.4.2 Component Test Nos. DBC-3 and DBC-4

The targeted impact speed in test no. DBC-3 was 15.0 mph (6.71 m/s), and the targeted impact speed for test no. DBC-4 was 25.0 mph (11.18 m/s). Actual bogie impact speed in test no. DBC-3 was 13.7 mph (6.13 m/s), and the actual speed in test no. DBC-4 was 23.65 mph (10.57 m/s). Sequential photographs of test nos. DBC-3 and DBC-4 are shown in Figure 126. Photographs from test nos. DBC-3 and DBC-4 are shown in Figures 127 through 135. The bogie impacted the center of the wire rope in both tests. Impact location for test nos. DBC 3 and DBC-4 was identical to the impact location in test nos. DBC 1 and 2. Following impact, the wooden stanchions used to support the slack wire rope were projected forward.

In test no. DBC-3 the socketing compound in the socket on the west side of the test fixture fractured near the wire rope inlet, and the wires pulled through the epoxy. The wire rope

whipped away from the end fixture and the bogie became free-wheeling at approximately 86.5 ms. Due to a malfunction in the braking system, the bogie vehicle impacted a concrete barrier used as a retaining wall to prevent the bogie from becoming a hazard to researchers or equipment, as shown in Figure 127.

The cause of the wire rope pullout through the epoxy, and the subsequent release from the socket, was unknown at the time of the test. The wire rope pullout is shown in Figures 128 and 129. The wire rope ends were examined closely to see if any defects or wire fractures contributed to the premature release from the epoxy. It was determined that the wire rope had no visible wire defects which would hinder performance of the socketed end. Furthermore, the epoxy shattered near the end of the socket with only approximately two-thirds of the length of the socket retaining the epoxy compound. This could have been the result of three factors: (1) dirt or contaminants could have been present on the wire rope or in the epoxy compound during the pouring or setting, creating stress concentration pores or reducing the bonding strength of the epoxy; (2) cold temperatures could have caused unanticipated side effects such as epoxy shrinking and fracturing in the socket; or (3) the wires may have been too closely packed within the epoxy to allow for adequate bond strength to be obtained.

The ends of the sockets were examined, and it was observed that the wires were not well-distributed in the epoxy with most of the wires located near the outside lip of the socket. Near the narrow opening of the socket, where the epoxy had shattered and disengaged from the wires and socket, wires were packed tightly together as they were in the strand. Because the size of the epoxy around the wire was insufficient to develop the shear load, the epoxy fractured and released load from the bottom third of the socket. The wire rope subsequently pulled through the epoxy by two ways: shear-peeling of the remaining galvanization and surface shear slip on the

wires. No dirt or particles were observed in the epoxy to reduce the effectiveness but bubbles were present, which were likely caused by the cold pouring temperatures of approximately 48 °F.

The loads from test nos. DBC 3 and DBC-4 were plotted, and are shown in Figure 136. In test no. DBC-3 the wire rope pulled through the epoxy at a load of 21.4 kip (95.3 kN). The wire rope load in test no. DBC-4 peaked at approximately 86 ms with a maximum tension of 38.4 kip (170.8 kN). Two strands of the wire rope in test no. DBC-4 fractured at 86 ms, which caused the initial force peak and subsequent drop-off of the load. The remaining strand unwound and lost tension as the two strands rebounded away from the site of fracture. The third strand was pulled from the epoxy on the west side of the test fixture at 105 ms, and was pulled along the strands by the bogie. The last remaining continuous strand fractured at the impact location unwound around the two fractured strands still attached to the end fixture. The bogie eventually came to a complete stop in contact with the strand that was pulled out of the epoxy from one end.

Displacements of the bogie in test nos. DBC-3 and DBC-4 are shown in Figure 137. The bogie displacement in test no. DBC-3 was derived from high-speed video analysis since significant noise in the DBC-3 accelerometer data prevented accurate determination of the start of the event. In test no. DBC-3, the bogie reached a displacement of 20½ in. (521 mm) prior to the wire rope pulling through the epoxy. In test no. DBC-4, the bogie deflected the cable to 34.2 in. (869 mm) at the fracture of the first two strands, and bogie displacement at the time of the release of the third strand from the epoxy was 40.4 in. (1,026 mm).



0.000 sec



0.000 sec



0.100 sec



0.100 sec



0.200 sec



0.200 sec



0.300 sec



0.300 sec

Figure 126. Sequential Photographs, Test Nos. DBC-3 and DBC-4



Figure 127. Final Position of Bogie Vehicle and Wire Rope, Test No. DBC-3

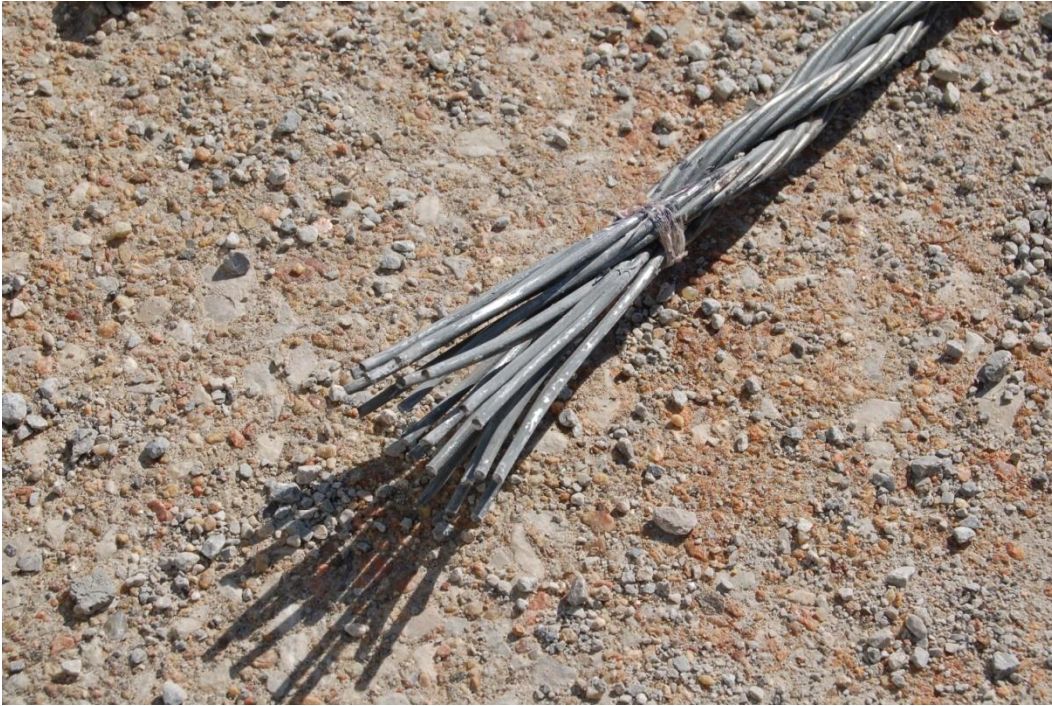


Figure 128. Wire Rope Pullout, Test No. DBC-3



Figure 129. Wire Rope Pullout Through Epoxy, Test No. DBC-3



Figure 130. Load Cell Cushion Design Modification, Test No. DBC-4



Figure 131. Final Position of Bogie and Wire Rope, Test No. DBC-4



Figure 132. Wire Rope Damage, Test No. DBC-4



Figure 133. Wire Rope Damage, Test No. DBC-4



Figure 134. Wire Rope Damage, Test No. DBC-4



Figure 135. Final Position for Load Frames, Test No. DBC-4

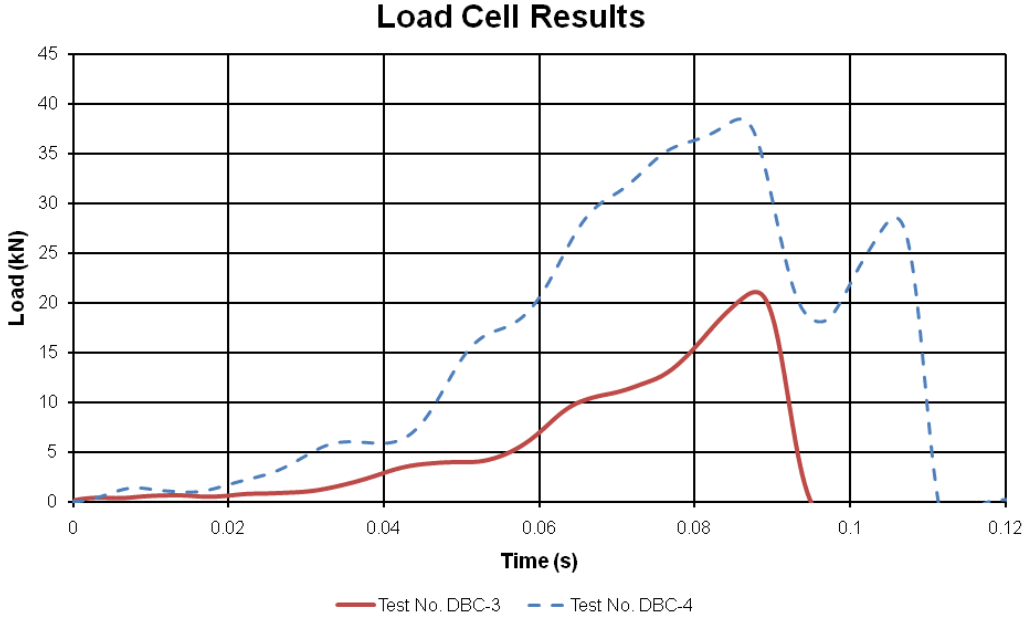


Figure 136. Load Cell Results, Test Nos. DBC-3 and DBC-4

The velocity of the bogie in test no. DBC-4 was also plotted, and is shown in Figure 138. The velocity plot from test no. DBC-3 was subject to high-frequency noise based on the high-speed digital video analysis, and therefore was not reported. The velocity plot for test no. DBC-4 was smooth until 0.100 sec, then it linearly decreased until approximately 0.600 sec.

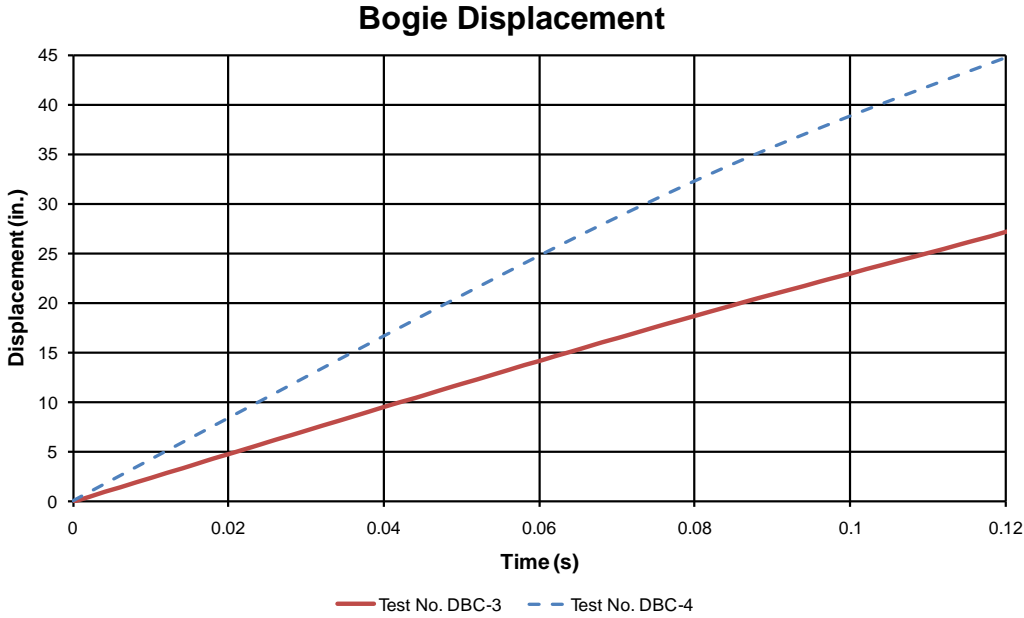


Figure 137. Bogie Displacement, Test Nos. DBC 3 and DBC-4

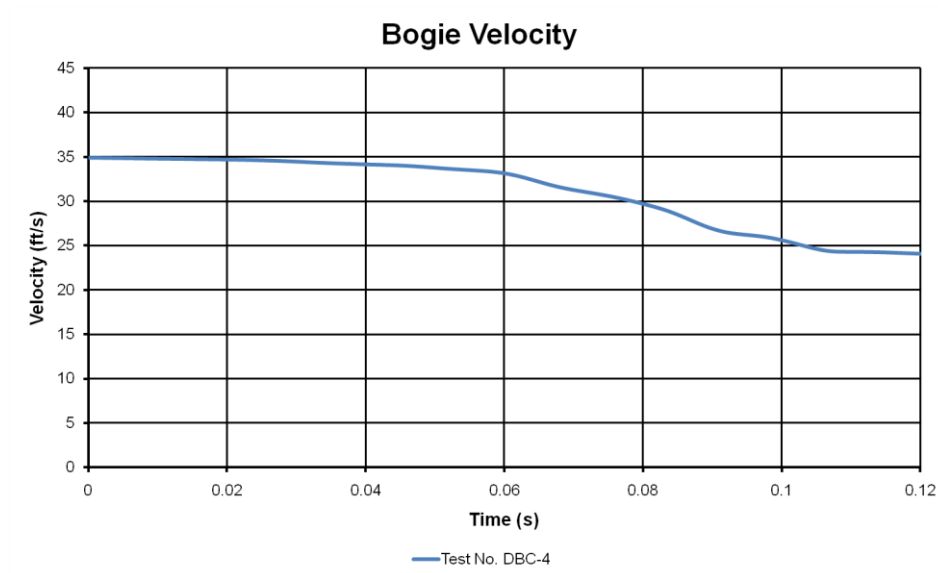


Figure 138. Bogie Velocity, Test No. DBC-4

Bogie acceleration was also plotted for test no. DBC-4. The bogie acceleration mimicked the load cell load curve with two peaks at 86 ms and 102 ms, as shown in Figure 139. A discrete Fourier transform was conducted on the acceleration trace, and it was determined that the fundamental frequency of the wire rope in test no. DBC-4 was approximately 40.5 Hz. This result was very close to the same frequency calculated in test nos. DBC-1 and DBC-2, which revealed a characteristic bending wave speed of approximately 1,347 ft/s (410 m/s). Similarity in the characteristic bending wave speeds, when loaded at different load rates and for different durations, indicated potential usefulness of this empirical parameter.

The breaking strength of wire rope in test no. DBC-4 was 38.5 kips (171.2 kN). This was slightly lower, but still consistent with the breaking strength in test no. DTC-1 of 41.1 kip (182.8 kN). Since the load in test no. DBC-4 was less than that in test no. DTC-1, and there was high-curvature bending strains present in the wire rope in the former that were not present in the latter, it was determined that the simulated breaking load of wire rope should be targeted to be approximately 38 kip (169 kN). In this way, a factor of safety can be used to determine the

strength of the wire rope under tensile load that could be sustained in a situation in which bending contributes to the failure of wire rope. It should be noted that it is very rare for wire rope installed in cable barrier systems to fracture, and thus the failure load is not likely to be reached in most simulations of full-scale impacts.

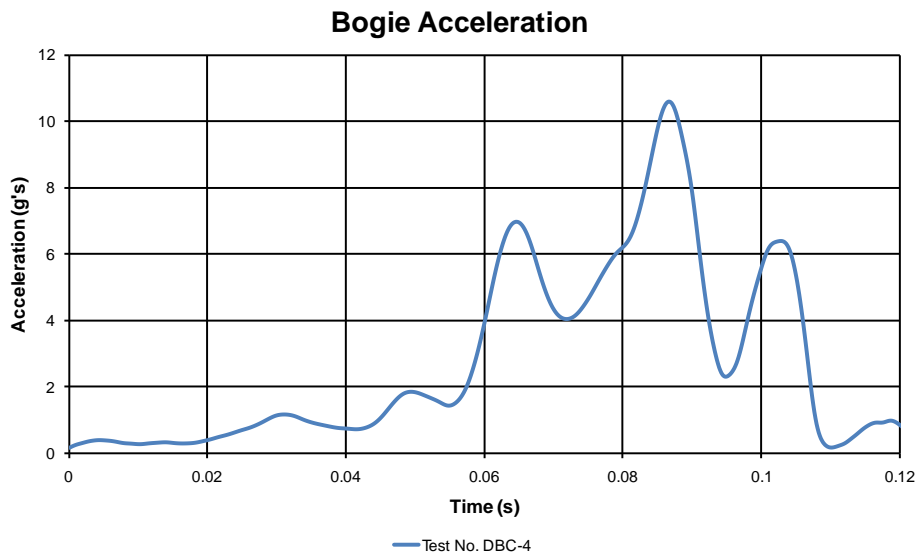


Figure 139. Bogie Acceleration, Test No. DBC-4

12.4.3 Component Test Nos. DBC-5 and DBC-6

The final two bending tests—test nos. DBC-5 and DBC-6—consisted of wire ropes with lengths of approximately 89 ft – 6 in. (1,074 in. or 27,280 mm) and impacted in the center of the rope. Sequential photographs of test nos. DBC-5 and DBC-6 are shown in Figure 140. Impact location and test setup for test nos. DBC 5 and 6 are shown in Figure 141. The targeted impact speed for test no. DBC-5 was 15 mph (6.7 m/s), and the targeted impact speed for test no. DBC-6 was 22 mph (11.2 m/s). Actual impact speeds for test nos. DBC-5 and DBC-6 were 13.68 mph (6.12 m/s) and 23.65 mph (10.57 m/s), respectively. Photographs from test nos. DBC 5 and 6 are shown in Figures 141 through 147.



0.000 sec



0.000 sec



0.150 sec



0.100 sec



0.300 sec



0.200 sec



0.450 sec



0.300 sec

Figure 140. Sequential Photographs, Test Nos. DBC-5 and DBC-6



Figure 141. Test Setup and Impact Location, Test No. DBC-5



Figure 142. Final Position of Bogie and Wire Rope, Test No. DBC-5



Figure 143. Wire Rope Damage, Test No. DBC-5



Figure 144. Wire Rope End Fitter Damage, Test No. DBC-5



Figure 145. Final Position of Bogie and Wire Rope, Test No. DBC-6



Figure 146. Wire Rope Damage, Test No. DBC-6



Figure 147. Wire Rope Damage, Test No. DBC-6

The bogie vehicle impacted the wire rope in test no. DBC-5 in the center of the 1,074-in. (27,280-mm) length. The wire rope tightened up and released from the stanchions, deflecting with the bogie vehicle until approximately 340 ms. The bogie rebounded with a speed of 8.97 mph (4.00 m/s).

In test no. DBC-6 the bogie vehicle also impacted the wire rope near the center of the installation. At 100 ms the propagating bend in the wire rope reached the load frame and pulled the rotating end support toward the impact region. An additional bending wave was transmitted by the rotating end assembly toward the bogie. The wire rope loaded up rapidly, causing five of the 21 wires in the epoxied socket to fracture and the remaining 16 wires to be debonded from the epoxy in only 88 ms after the first bending wave reached the load frame. Due to a malfunction in the brakes of the bogie vehicle, it impacted a concrete barrier used for protecting measurement equipment during the test.

Load cell data in test no. DBC-5 was lost due to data transmission problems. Only one load cell transferred data correctly from the test. In addition, a strobe malfunction caused loss of the overhead high-speed video camera views. In test no. DBC-6, all load cell channels were captured and the high-speed digital video cameras recorded the event as intended.

The load cell data from test no. DBC-6 was plotted and is shown in Figure 148. The load was very low for 100 ms before the bending wave was transmitted to the end support. The wire rope then loaded up quickly and was separated from the west-side end fixture at 186 ms at a load of 39.72 kip (176.7 kN). The load dropped off quickly after the wire rope released, but due to the spring effect of the long rotator end assembly the load assembly rebounded after the high-tensile load wave passed. This effect is evident in the secondary peak at 212 ms in the load cell data.

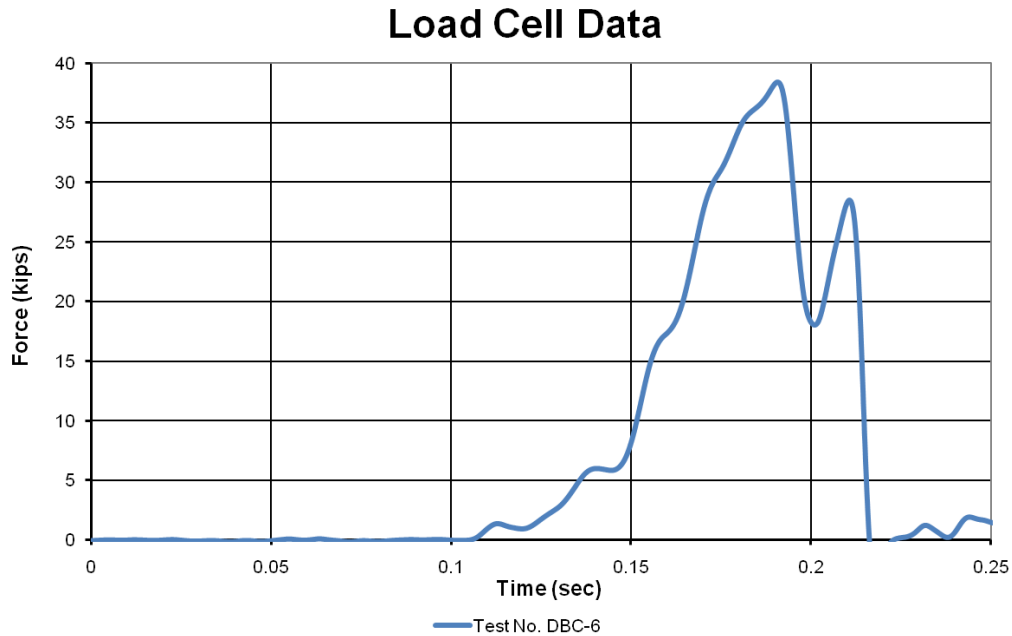


Figure 148. Load Cell Data, Test No. DBC-6

Bogie displacements from test nos. DBC-5 and DBC-6 are shown in Figure 149. In test no. DBC-5 the bogie deflected the wire rope to a maximum deflection of 59.9 in. (1,520 mm) before rebounding away from the wire rope. The maximum bogie deflection occurred at 0.340 sec. The displacement of the bogie in test no. DBC-6 increased throughout the event, and was nearly linear through 150 ms. The slope of the displacement curve was reduced near 0.200 sec, though the displacement of the bogie continued to linearly increase after 220 ms.

Bogie velocities were plotted to compare to simulation velocities. Bogie velocity in test nos. DBC-5 and DBC-6 is shown in Figure 150. In test no. DBC-5, the bogie velocity was initially corresponding linearly to very low inertial resistance of the wire rope upon impact. The bogie speed almost linearly decreased between 0.095 and 0.335 sec, and continued to linearly speed up as it rebounded until 0.430 sec. The bogie smoothly decelerated from 20.1 ft/s (6.12 m/s) to a stop before rebounding at a speed of 13.2 ft/s (4.01 m/s). The bogie velocity was initially constant near 35 ft/s (10.7 m/s), then gradually sloped down until 0.050 sec. After 0.050

sec the bogie velocity decreased nearly linearly to 24 ft/s (7.3 m/s) prior to the fracture and release of the wire rope. Subsequent bogie slowing occurred due to skidding and bouncing of the bogie after impact, and the impact with the concrete barrier at the end of the test.

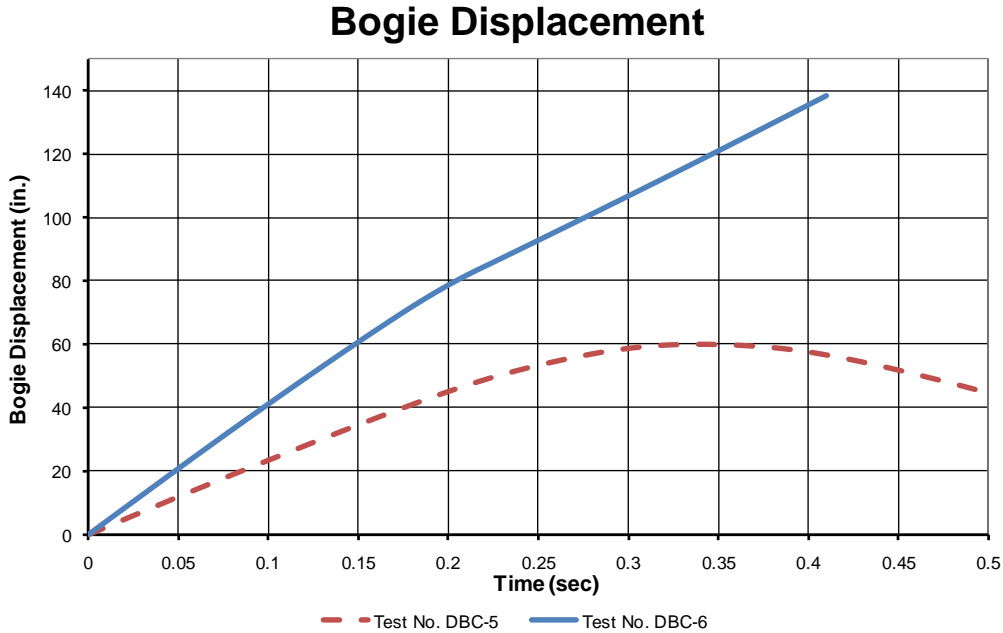


Figure 149. Bogie Displacement, Test Nos. DBC-5 and DBC-6

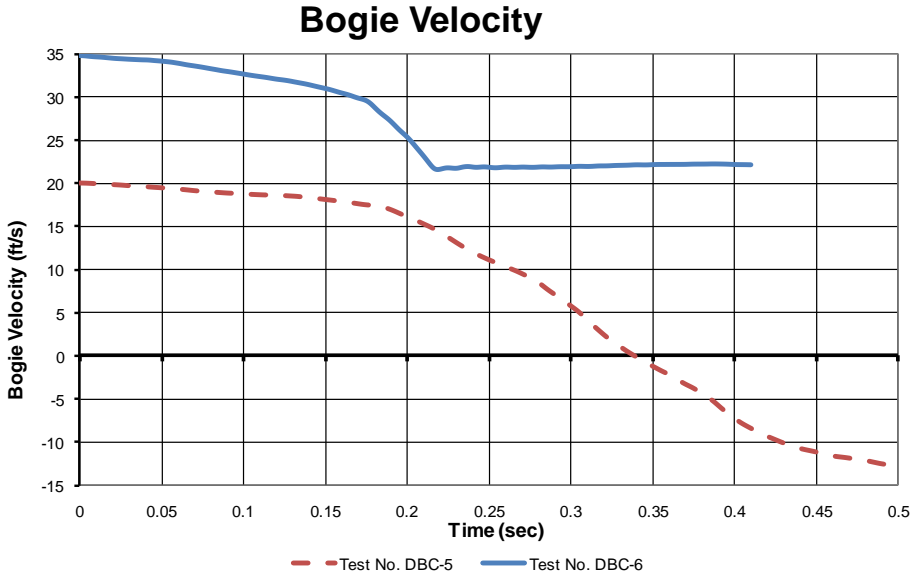


Figure 150. Bogie Velocity, Test Nos. DBC-5 and DBC-6

Bogie accelerations were also plotted and are shown in Figure 151. Bogie deceleration in test no. DBC-5 increased smoothly with nearly constant-amplitude bending waves propagating past the bogie head which resulted in oscillations in the bogie acceleration data. Wire rope inertia initially slowed the bogie motion in test no. DBC-6 until all of the slack was taken up. After the wire rope tightened, the acceleration increased by a factor of 2, and ramped up until fracture at 220 ms. Acceleration oscillations corresponding to wire rope bending waves were not as clearly observed in test no. DBC-6 as in test no. DBC-5.

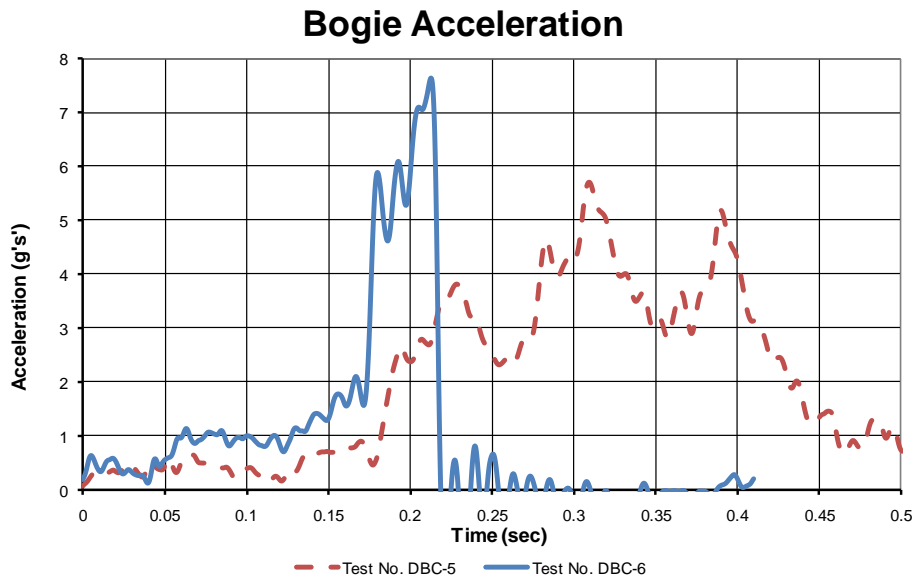


Figure 151. Bogie Acceleration, Test Nos. DBC-5 and DBC-6

A spectral frequency analysis was performed on the acceleration data from test nos. DBC 5 and 6, and is shown in Figure 152. The frequency analysis of test no. DBC-5 indicated two very clear acceleration frequency peaks, corresponding to frequencies of approximately 6.0 and 11.7 Hz with an additional small acceleration peak at 23.81 Hz. The highest-energy mode of these oscillations occurred at 11.7 Hz. The length of wire rope between the bogie and end support was 44.8 ft (13.7 m). The resulting characteristic bending wave speed with a half wavelength oscillation between the bogie and end support was 1,046 ft/s (319 m/s). Bending

wave frequencies in test no. DBC-6 were very difficult to distinguish, and were masked by the short duration of the bogie acceleration under tension.

Spectral Frequency Analysis

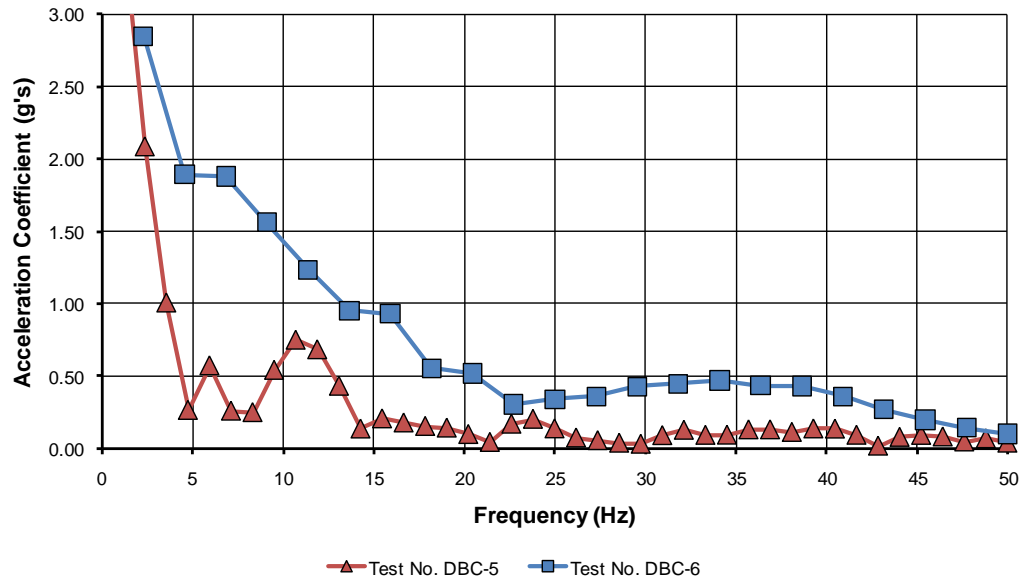


Figure 152. Spectral Acceleration Frequency Analysis for Test No. DBC 6

Though the characteristic bending wave speed in the six dynamic bending tests were not the same, all of the characteristic speeds were very similar and corresponded to the speed of wave propagation through the wire rope toward the bogie. This speed is heavily dependent on three factors: (1) length of the wire rope, (2) distance between bending constraints, and (3) tension in the rope. Despite these differences, the stiffness terms in bending equations seem to dominate bending wave behavior. Analysis of other full-scale systems indicated that the characteristic bending wave speeds for cable guardrail systems with posts spaced 16 ft (4.9 m) apart on center were all very similar to the 1,040 to 1,400 ft/s (317 to 427 m/s) range. Therefore, to accurately damp the fundamental bending mode frequencies, damping must be applied within this range.

12.5 Discussion

Six dynamic bending component tests were conducted on wire rope. Of the six tests conducted, four wire ropes retained integrity during impact and did not pull through the epoxy socketing compound. The wire rope pulled out of the socket in test no. DBC-6 after reaching the expected ultimate load of the wire rope, and pulled out of the socket in test no. DBC-3 under a very low axial load. In addition, two wire ropes were pulled through the epoxy in the tensile jerk testing.

The wire rope pull-out causes concern, since pull-out in a field-installed cable barrier system could lead to vehicle penetration and hazard to occupants of the errant vehicle. Causes of the pullout were considered, and three possibilities were determined to have the strongest effect on the likelihood of wire rope pulling through an epoxied end fitter. These possibilities include the following.

(1) The spelter-based sockets were not designed for use in dynamically-changing environments. According to the Wire Rope User's Guide, published by the Wire Rope Technical Board [2], epoxy- or spelter-based sockets are not recommended for use in environments where loads are dynamically varying. Because epoxy is very brittle, stress waves through the epoxy may cause internal cracking, leading to the ultimate loss of integrity of the socketed joint and wire rope pull-through.

(2) The epoxy used in the wire rope closed spelter sockets was designed for use with wire ropes having smaller wire diameters and more wires per strand than standard cable barrier wire rope. Standard ¾-in. (19-mm) diameter 3x7 wire rope has a total wire surface area per unit length of approximately 7.95 in.²/in. (201.9 mm²/mm). A 6x19 wire rope with the same outside diameter as a 3x7 wire rope, with all wires of equal diameter of 0.050 in. (1.27 mm), has a

surface area per unit length of 24.93 in.²/in. (633.3 mm²/mm). Since the 6x19 wire rope is standard for use with the spelter sockets, the 3x7 wire rope has approximately 62% less bonding area than the 6x19 wire rope—although the nominal breaking strength is only 16% lower. As a result, at the fracture load of the wire rope the average shear stresses in the epoxy around a 3x7 wire rope are more than twice as large when using a 3x7 wire rope in comparison with a 6x19 wire rope. The latter is more commonly used for spelter sockets with epoxy compounds. Note that due to different wire rope constructions, different makes of wire rope will have different total wire surface areas, and average stress intensities, fracture loads, and distributions of wire stresses.

(3) Temperature has a significant effect on the test results. The colder temperatures in test nos. DTC-2 and DTC-3, and the slightly higher temperatures near 55°F for test nos. DBC-5 and DBC-6 may have contributed to early release of the wire ropes from the epoxy. Test no. DBC-3 had wire rope pullout which was unrelated to temperature rather it resulted from poor wire distribution.

The temperature dependence of wire rope and epoxy bonding is not known. If the pouring temperature and the testing temperature are very different, debonding may occur between the wires and epoxy owing to a difference in the thermal coefficients of expansion. Literature and testing were not available to study the thermal effects of epoxied end treatments.

In all of the dynamic bending tests the wire ropes were initially slack for ease of construction, and to reduce the precision of length required when the ropes were initially socketed. However, since the tested ropes were not pretensioned in the component tests, it was necessary to incorporate slack in the component test models as well. It was very difficult to determine the slack length in each rope, but precise estimates were possible. By noting times on

the high-speed video when the cable became taut, reading the displacement from bogie motion analysis to estimate total wire rope length, determining the effective load from the load cells at that time and reducing the total wire rope length to zero effective strain, slack could be determined. The presence of initial pretension in the wire rope would make modeling and evaluation of future tests much easier, although test setup will become more difficult. In addition, precision is required when socketing the wire ropes to prevent excess slack or too high of a pretension load. The degree of precision required is not trivial since wire rope fractures at approximately 2.5% strain dynamically. There is a significant trade-off between ease of construction and ease of modeling in wire rope bending testing.

A good estimation of the appropriate frequency range to use when estimating for damping coefficients is based on a characteristic bending frequency. Characteristic bending frequency is defined to be the distance between bending constraints in a system (e.g., guardrail posts) divided by the characteristic bending wave speed. This characteristic bending wave speed is often witnessed in transmission of bending waves between constraining structures, such as posts, for guardrail systems with post spacings of approximately 16 ft (4.9 m). The recommended range of frequencies that should be used for damping is between 10 and 120 percent of the characteristic frequency.

Though the characteristic bending wave speed was measured and found to be relatively constant in these tests, it is not truly a physical property. Further analysis may demonstrate that alternative cable guardrail systems with post spacings smaller or larger than 16 ft (4.9 m) may have very different characteristic bending wave speeds than the ranges recommended as a result of this study.

Lastly, the primary reason for wire rope pullout of the end socket in test no. DBC-6 was due to bending wave propagation and reflection at the end condition. According to classical wave transmission principles, as waves reach rigid (or nearly rigid) boundaries, reflected waves have the same wave shape as the incident waves. By contrast, free (laterally unconstrained) boundaries will reflect waves with inverted wave properties from the incident waves. As a result, the bending wave which reached the rotating end support in test no. DBC-6 reached a resting rotating mass, and reflected part of the incident wave like a rigid boundary. This superposition at the support loaded the wire rope past the limit of the epoxy and caused failure at that location. It is possible that if the speed would have been slightly lower, the bending waves would not have superposed in such a way as to cause very rapid failure.

In addition, the pullout load in the wire rope at the failure location in test no. DBC-6 was less than the nominal breaking load of wire rope. The reduction in load acquired at the wire rope termination may have been caused by the lower temperatures around test time, which were close to 50°F (10°C). Low testing temperatures may have increased brittle characteristics of the epoxy in the wire rope and contributed to premature wire rope release.

12.6 Summary

Dynamic bending tests were conducted to observe the combination of tension and bending effects on the wire rope. The wire rope was also observed to fracture or release from the end fittings at approximately 40 kip (178 kN) in every test. Though two tests were conducted in which the socketed end failed, it was determined that the epoxy is not recommended for high-strength testing or use in demanding, dynamically-varying tension conditions. Alternative end fitter types, including zinc-poured spelter sockets, field-swaged sockets, and thimble terminations were also discussed. Further testing is necessary to determine which type of end

fitting is best suited for environments with varying temperature and ambient moisture, as well as end fitting sensitivity to operator experience.

12.7 Future Work

In the dynamic bending component tests, two of the sockets failed to maintain the wires in the epoxy when the vehicle impacted the wire rope. This was observed to be the result of close wire spacing and insufficient strand separation in test no. DBC-3, but this was not the case with test no. DBC-6. It should be noted that the sockets in this test series were evaluated primarily in October, when ambient temperatures were relatively cold.

The temperature dependence of the sockets is a critical factor in the future design of cable guardrail systems. Though it is rare for wire rope to be loaded into the plastic loading zone in cable guardrail tests [45], impacts near end terminals may cause dynamic tensions to rise much higher than normally observed in longitudinal impacts. Catastrophic release of the wire rope from the end fitter at a load below the breaking load of wire rope has the potential to cause loss of life. Therefore, further investigation into the dynamic effects of different wire rope end fitters in varying temperatures is necessary.

In addition, alternative end fittings may be affected by dynamic wave pulses generated by bending waves in the vicinity of the end terminal. The Texas Transportation Institute (TTI) conducted a study on field-applied end fittings for wire rope [41]; however, these tests were primarily conducted in tension, and the response of the sockets to bending loads is unknown.

13 MODELING WIRE ROPE IN DYNAMIC BENDING

13.1 Purpose

The dynamic bending component tests were modeled in order to capture the dynamic response of wire rope to loads applied perpendicular to the longitudinal axis of the rope. Though perpendicular impacts with cable barriers are rare, the response of wire rope to lateral loads is necessary to capture the effect of a vehicle impacting at a non-zero impact angle. The bending waves transmitted by wire rope can cause the rope to disengage from the post attachments downstream of impact, and may contribute to penetration or underride of the cable barrier system.

13.2 Modeling Test No. DBC-1

13.2.1 Baseline Model

Since test no. DBC-1 had complete data capture, did not result in cable fracture or pullout of the epoxy, and had the same basic test configuration as test nos. DBC-2 and DBC-4, it was chosen to be the baseline model for evaluation. Further refinement was possible in models of other component tests once the simulation of test no. DBC-1 was satisfactory.

A model of the baseline test is shown in Figure 153. The baseline model of test no. DBC-1 consisted of the wire rope using 0.5-in. (12.7-mm) long elements spanning between two end supports. The beam elements representing the wire rope were modeled with a type 2 Belytshcko-Schwer cross-section type, a cross-sectional area of 0.2395 in.² (154.5 mm²), and a non-prestretched modulus of elasticity of 11.6 Mpsi (79.9 GPa), which was consistent with the previous models of wire rope. For simplicity, the linearized non-prestretched wire rope curve was initially used in lieu of the curve with geometrical stretch. The baseline model of wire rope was straight and did not include any slack in the length of the wire rope.

The end supports were modeled using five parts: one rigid rotational axis, one rotator pipe, two beams to define the swiveling bolts and load cells, and one load bar. All of the frame materials were defined to be rigid in the baseline model. The rotator pipe end assembly is shown in Figure 154.

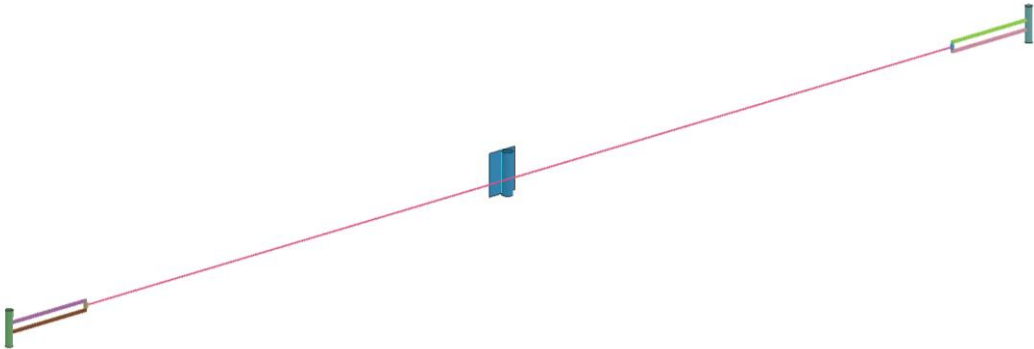


Figure 153. Baseline Model, Test No. DBC-1

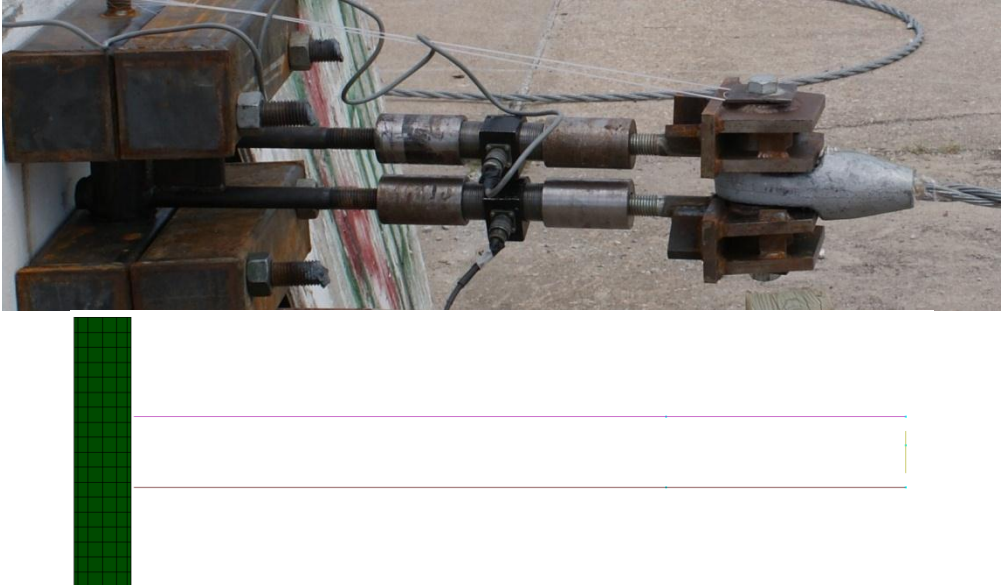


Figure 154. Rotator Pipe End Assembly, Test and Baseline Model, Test No. DBC-1

Two rigid beams were defined as corresponding to the locations of the vertical axes of the rotator pipes. The beams were defined with a cross-section that was consistent with a 1.0-in. (25-mm) diameter rod, and were fixed against translational and rotational motion.

The rotator pipes were modeled using shell elements with a thickness of 0.25-in. (6.35 mm). The model rotator pipes were given the same dimensions as the rotator pipes used in the tests, and were defined at the rotator pipe middle surfaces. The rigid material used to define the rotator pipes was a valid approximation since the pipes were filled with concrete and had a large bending and shear resistance to loading.

Two sets of beam elements with lengths equal to the distance between the center of the rotator pipe bracket and the rotator pipe were modeled to simulate the bolt, load cell, and coupler connections. Since the couplers were threaded onto the bolts over a long length of the threaded rods, and the load cells had a diameter that was more than twice the diameter of the bolts, the beams were essentially one very stiff unit with virtually no low-load compliance. Though the bolts were steel and thus did deflect elastically in the test, they were initially modeled with a rigid material for simplicity. At the maximum load in test no. DBC-1, the calculated resulting deflection of the bolts and threaded rods was 0.015 in. (0.38 mm). This value is very small in comparison with the slack length of wire rope, which was greater than 1 in. (25 mm) in all of the bending component tests; thus, the rigid beam assumption was warranted.

The load pins were also modeled with beam elements comprised of a type 2 Belytshcko-Schwer cross-section. The load pins were defined such that the area of the pins was equal to the steel area of the pipe, and additional mass was included to account for the concrete fill. The vertical beam was approximated to span between the upper and lower bolt-coupler-load cell assemblies.

Since the brackets were essentially rigid in the tests, with deflections less than 0.001 in. (0.025 mm), they were modeled as point masses located at the ends of the vertical load pins. The masses of each bracket were measured.

Load cells and couplers were modeled using point masses with equivalent masses located at the load cell locations on each beam. Sockets at the end of the wire rope, which were mostly contained within the length of the brackets, were modeled with point masses in the center of the load pins.

The impact head was modeled as one rigid part with three pieces connected at nodal locations. The modeled impact head is shown in Figure 155. A cylinder with a diameter of 3 in. (76 mm) was modeled using shell elements with a thickness of 0.25 in. (6.4 mm) and defined with a rigid material. On the back side of the cylinder a layer of shell elements was used to connect the cylindrical impact head with the mounting plate. The mounting plate was a 10-in. x 12-in. by 0.25-in. thick (254-mm x 305-mm by 6.4-mm thick) layer of shell elements. Because the impact head was defined with a rigid material, mesh density had little effect on the resulting computational cost of the model so a fine mesh was used to accurately distribute the mass. The ribs and welded wire rope catcher were neglected.

The impact head was modeled with a vertical line of distributed point masses in the center of the back of the impact head with a total mass that was equal to the mass of the tested bogie vehicle minus the simulated weight of the impact head. The applied speed of the impact head was 21.74 ft/s (6.625 m/s), which matched the impact speed in the test. The impact head was also constrained so that it could not rotate and could only translate in the direction of impact.

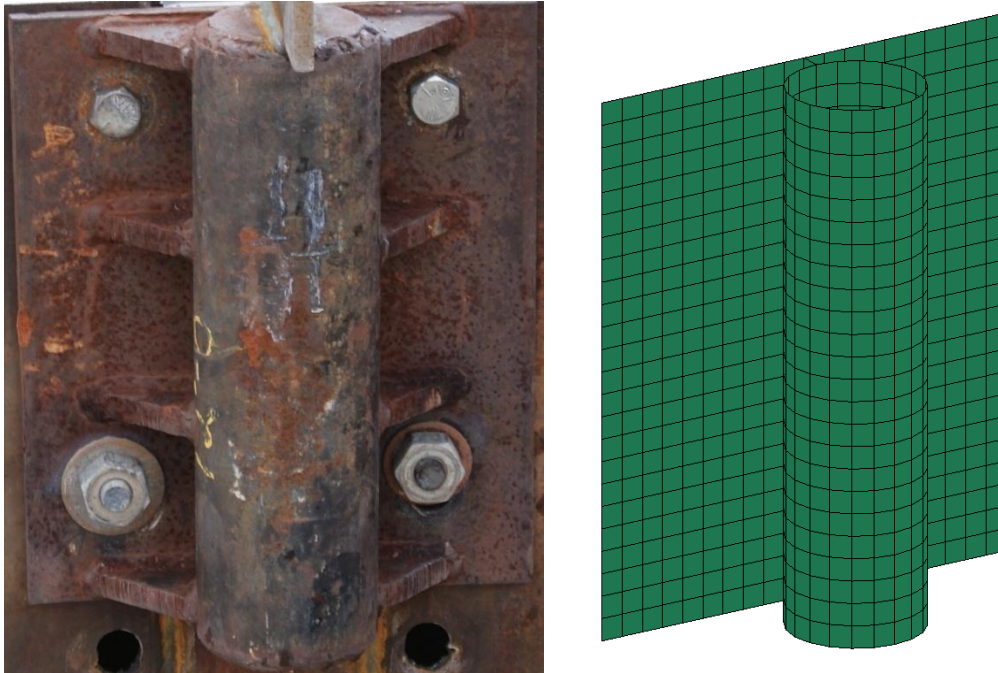


Figure 155. Impact Head, Tested and Modeled, Test No. DBC-1

The wire rope was initially defined with CONTACT_AUTOMATIC_SINGLE_SURFACE and the impact head and wire rope were included in the slave side of the contact definition. For the baseline model, this contact type was efficient and impact event was accurate.

Output for the baseline model of test no. DBC-1 included cross-sectional forces from the wire rope, motion of a fixed point on the impact head, and motion of points on the wire rope corresponding to the target locations in the physical test. The rate of output from the cross-sectional force was 10,000 Hz, which was the same as was captured in the component test. Capture of the NODOUT data was also 10,000 Hz.

The axial load of the baseline model wire rope was plotted against the load cell results from test no. DBC-1 and is shown in Figure 156. The wire rope maximum load predicted in the simulation was 38.7 kip (172.1 kN), which was 4.3% higher than the 37.1 kip (165.0 kN) load recorded in the test. Because there was no slack modeled in the simulated wire rope, it maintained tension for much longer and was loaded to a higher tension than occurred in the test;

however, loading rate and unloading times were similar. Thus, the baseline model provided encouraging results.

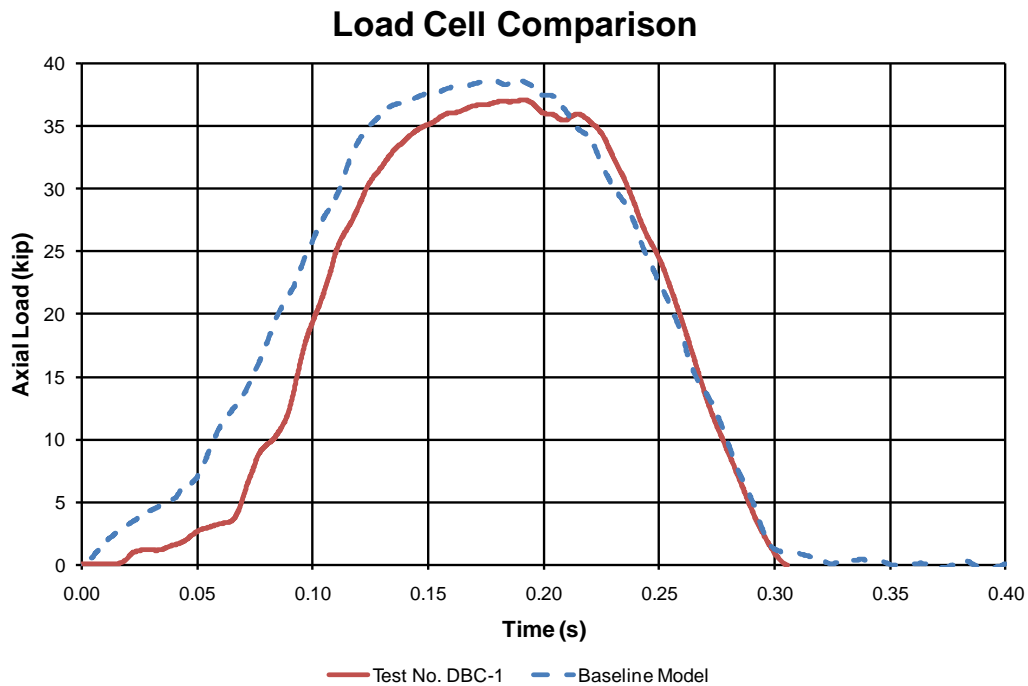


Figure 156. Wire Rope Axial Load Comparison, Test No. DBC-1 and Baseline Simulation

The displacements of the bogie in the test and the impact head in the simulation were also plotted, and are shown in Figure 157. Both displacement curves were similar with a maximum simulated displacement of 36.24 in. (920.4 mm) and a maximum displacement in the test of 38.4 in. (975 mm). The slightly lower displacement in the simulation was due to the higher axial load sustained in the baseline test model at an earlier time—leading to faster bogie rebound and less deflection.

Based on the impact head displacement and the wire rope axial load from the simulation, it was observed that the wire rope tightened up too quickly in the simulation, which was not observed in the physical test. In the physical test a bending wave was transmitted from the center of the wire rope at impact to the end supports. The wave was transmitted as the slack in the wire

rope was taken up in the bogie displacement, and the wire rope tightened at 25 ms after impact. However, in the simulation model, the wire rope tightened up immediately after impact because there was no slack and no initial non-linear geometrical stretch defined.

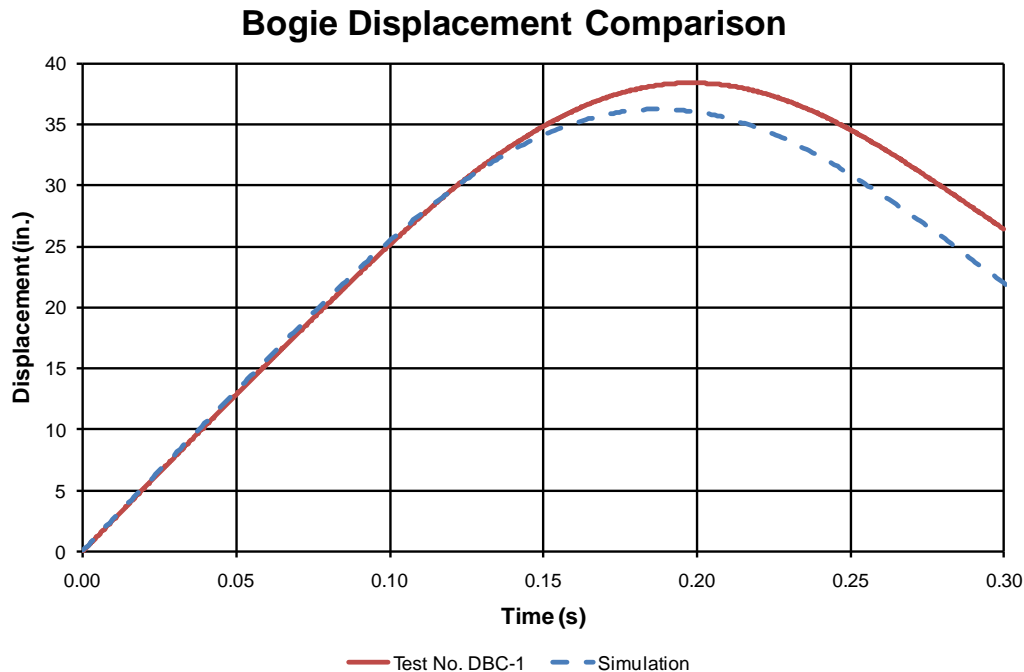


Figure 157. Bogie Displacement Comparison, Test No. DBC-1 and Baseline Model

13.2.2 Gravity and Slack in the Wire Rope

Based on results of the baseline model, it was observed that the slack present in the wire rope during the test must be accounted for in the simulation to obtain an accurate response. Furthermore, gravity was defined in the refined model to allow the wire rope to settle under gravity loading.

High-speed digital video of component test no. DBC-1 was examined to determine the amount of slack present in the wire rope prior to impact. It was observed that at 52 ms the wire rope became taut with an effective distributed load of approximately 500 lb (2.2 kN). The geometry of the taut wire rope was used to determine the effective cable length at the time that

the wire rope slack was removed. The strain in the wire rope was extracted from the tensile load curve and subtracted from the wire rope length. The method of high-speed digital video and load cell collaboration was more accurate than using a string line or a tape measure since small bends in the wire rope (when placed on the ground) gave shorter and inconsistent results. The slack length recorded using high-speed digital video, load cell and bogie acceleration data was 1.82 in. (46.2 mm), which was 0.82 in. (20.8 mm) larger than the tape measurement.

Three different methods were used to generate slack in the simulated wire rope, as shown in Figure 158. The first method consisted of defining a straight length of wire rope at the correct height, removing end constraints to the rotating end fixtures, and holding one end of the wire rope fixed while the other end was displaced by the slack length of the wire rope. This initialization was conducted slowly, and the wire rope was loaded under gravity to simulate actual test conditions.

The stanchions were modeled using the first method by including finite rigid walls measuring 1½ in. x 1½ in. (38 mm x 38 mm) that were located at the position of the stanchions in the test. It was observed that the friction defined between the wire rope and the stanchions had a significant effect on the resulting geometry. It was noted that since the type 2 elements are not stress-based elements, the stresses in each beam element in the wire rope were not transmitted between initialization and full-model simulation runs. Due to the difficulty and required time to construct and test this type of initialization, limited efforts were expended to match the wire rope slack using this method.

The second method of generating slack in the wire rope utilized the rigid stanchions from the first method, and a wire rope which was initially curved in an arc between the end supports. The radius and subtended angle of the arc were controlled to obtain a precise amount of slack in

the wire rope. Though this method was more accurate in generating the geometry of the wire rope in the region near impact, it did not accurately reflect the wire rope geometry near the end fitters and acted as a stress concentration. Nonetheless, trial runs were conducted with this method of slack introduction.

The final slack method incorporated a "gravitational bend" in the form of sinusoidal curves in the wire rope. The sinusoidal curves were defined in a spreadsheet, such that the length of each element could be independently controlled and the slack length was explicitly calculated by numerically integrating the length of the sine curve between the supports. This method was based off of the observation that the gravitationally-loaded slack curve had an approximate sinusoidal deflection between each of the supports.

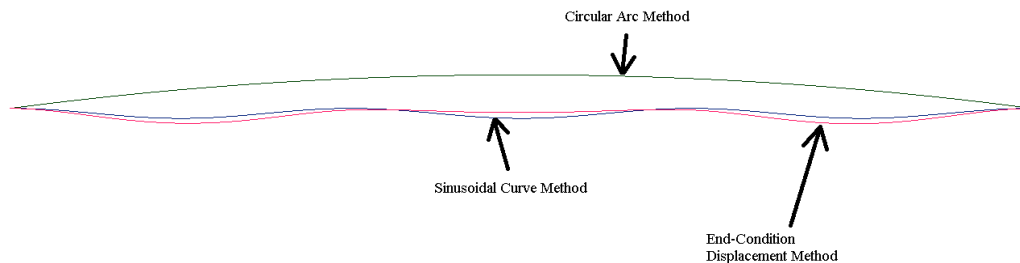


Figure 158. Methods of Generating Slack in Wire Rope, Test No. DBC-1

Though the three methods had different levels of difficulty, all three models had similar results of bogie deflection, velocity, and acceleration, as well as ultimate wire rope load. The wire rope tension comparison of the three models is shown in Figure 159.

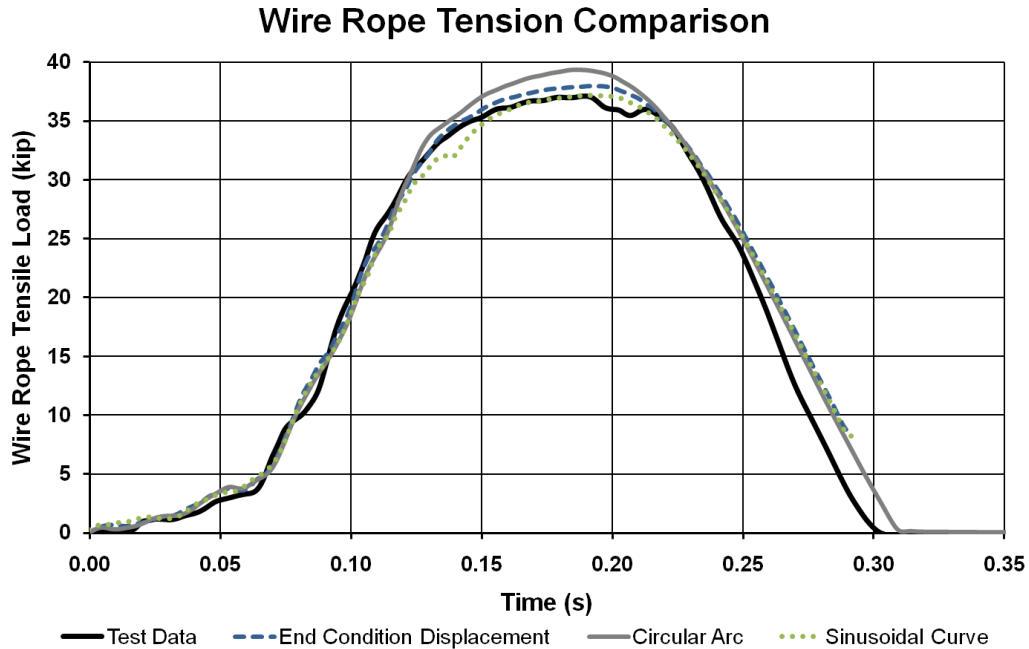


Figure 159. Wire Rope Tension Comparison, Test Data and Methods of Including Slack

The displacements and velocities of the three methods were nearly identical, with maximum displacements of the moving end condition, circular arc, and sinusoidal curve of 38.20 in., 38.12 in., and 38.44 in. (970.3 mm, 968.2 mm, and 976.4 mm), respectively. The maximum displacement determined from accelerometer data and high-speed video in test no. DBC-1 was 38.4 in. (975 mm). Likewise, the rebound velocities of the moving end condition, circular arc, and sinusoidal curve models were 16.11, 16.50, and 16.13 ft/s (4.91, 5.01, and 4.92 m/s), respectively. The rebound velocity in the test was 14.89 ft/s (4.54 m/s).

The three methods differed in bogie accelerations, as shown in Figure 160. Clear force peaks were evident in the sinusoidal curve corresponding to bending waves being transmitted around the bogie vehicle. Conversely, the acceleration of the bogie in the circular arc configuration was relatively smooth and did not have the large force peaks observed in the physical test.

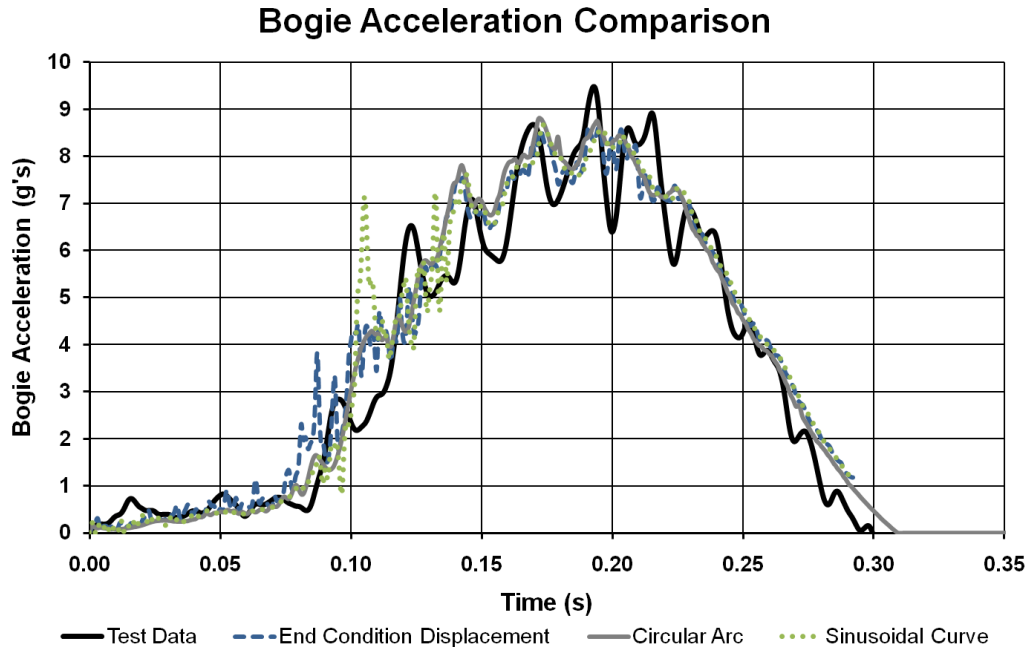


Figure 160. Bogie Acceleration Comparison, Test Data and Methods of Simulating Slack

As a result of this study, it was determined that the best method of simulating slack in the wire rope was to use the sinusoidal approximation to the gravitational curve. This method was the most convenient and controllable method of generating slack in the minimum amount of time. Because the three methods had very similar acceleration, velocity, and displacement curves, the methods were assumed to be nearly equivalent. Therefore the sinusoidal method was utilized in generating slack in all remaining dynamic bending simulations.

13.2.3 Complete Model

The final step in the refinement of the DBC-1 cable model was the substitution of a bogie vehicle model for the added mass on the impact head. The bogie vehicle model used in test no. DBC-1 and the model of the bogie vehicle are shown in Figure 161 for comparison.

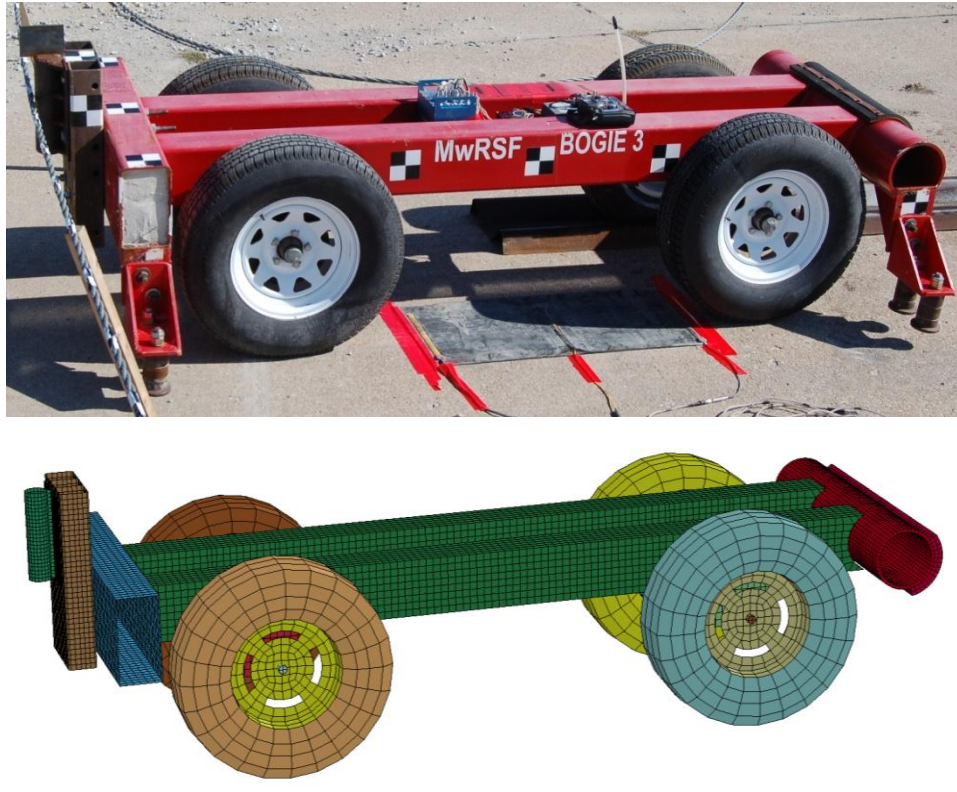


Figure 161. Bogie Vehicle Comparison, Test and Model, Test No. DBC-1

The bogie model was composed of two longitudinal tubes composed of shell elements. The longitudinal tubes were very stiff with respect to the wire rope; thus a rigid material was used to simulate the tubes to reduce computational time. The front rectangular frame tube and cylindrical post testing head were both modeled with shells and rigid material as well. The rear neoprene pad on the post testing impact head was modeled with solid elements, and was rigidly constrained to the bogie, since it did not contact the wire rope. Furthermore, the use of deformable solid elements for the neoprene pad increased computational time by a factor of 2. The frame tubes and post testing impact head were rigidly constrained to the frame tubes using *CONSTRAINED_RIGID_BODIES command.

The tires were defined with an elastic material and included an internal airbag definition to simulate tire pressure. The tire mesh was relatively coarse; however, the reaction of the tires

during the test did not affect the simulation results. The bogie only compressed the rear tires slightly during impact due to the moment load.

The adjustable impact head mount and impact head were comprised of shell elements, and were also rigidly mounted on the bogie. The height of the impact head was maintained from the baseline and gravitational slack models, while the bogie model was added to the back of the impact head and the point masses representing the bogie were removed.

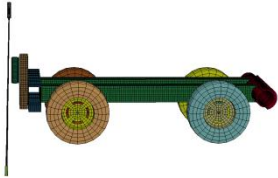
13.2.3.1 Bogie Model with Gravitationally-Loaded Wire Rope

The bogie model was placed 0.79-in. (20 mm) in front of the wire rope and projected forward with a velocity of 21.74 ft/s (6.625 m/s). The bogie model impacted the gravitationally-loaded wire rope in the center, pitched upward due to the high moment load of the wire rope, and rebounded out of the modeled system. Sequentials of the test and simulation are shown in Figure 162.

The bogie model was substantially better than the impact head model, and more accurately captured the behavior of the wire rope in tension, as shown in Figure 163. Since the wire rope was non-prestretched prior to the test, both a linearized non-prestretched tensile curve and a curve with geometrical stretch included were used to simulate the wire rope tensile loads. The curve with the non-linear geometrical prestretch was slightly more accurate in capturing the bogie tensile behavior, since the loading and unloading rates were very similar between the tests, and the time of maximum force was the same. The maximum load in the simulations were 36.90



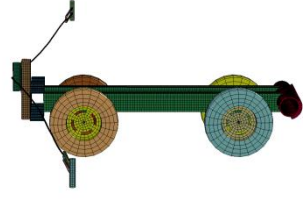
0.000 sec



0.000 sec



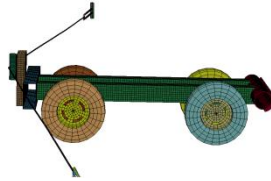
0.150 sec



0.100 sec



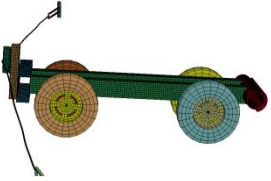
0.300 sec



0.200 sec



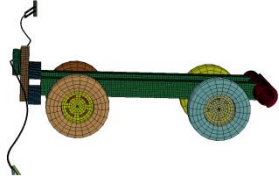
0.450 sec



0.300 sec



0.450 sec



0.300 sec

Figure 162. Sequential Photographs, Test and Simulation, Test No. DBC 1

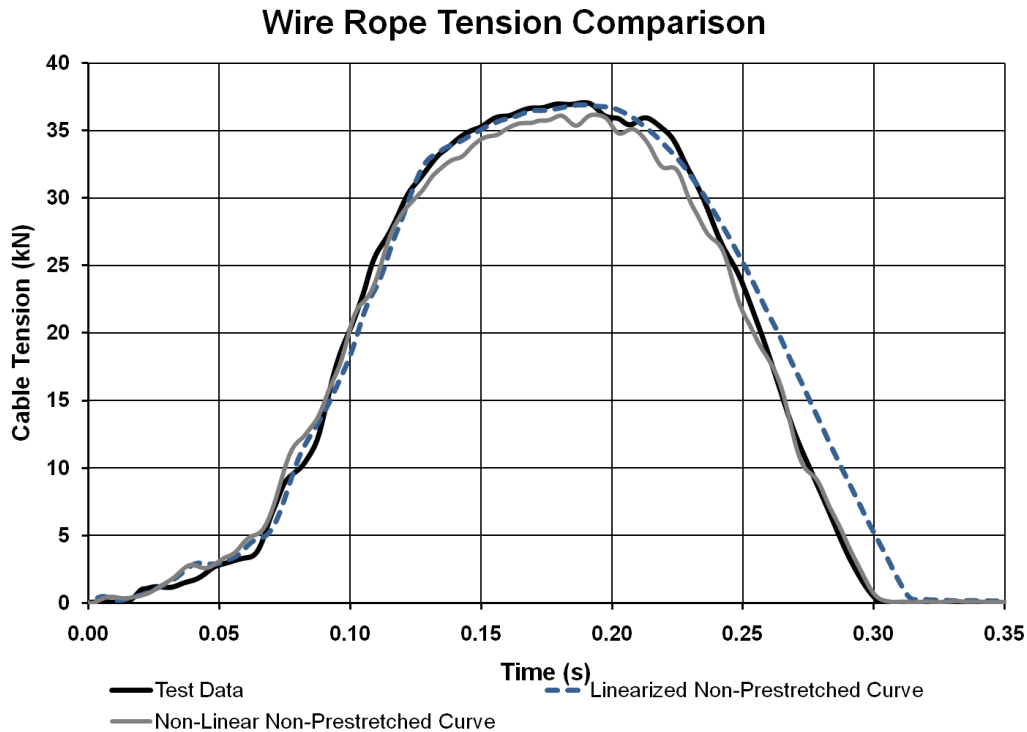


Figure 163. Wire Rope Tension Comparison, Test and Simulation, Test No. DBC-1

kip (164.1 kN) for the linearized non-prestretched wire rope tensile curve and 36.18 kip (160.9 kN) for the non-linear tensile curve including the geometrical stretch. Though the axial load was slightly lower using the non-linear geometrical prestretch curve, the correct ultimate load and unloading behavior were present using the geometrical prestretch.

Bogie displacement was plotted and compared between the linearized non-prestretched tensile test and the non-linear geometrical stretch and are shown in Figure 164. The bogie deflection in the linearized non-prestretched test was slightly higher than the displacement in the physical test and non-linear geometrical stretch curves. This was due to the fact that the slack length of the wire rope in the simulation using the non-linear geometrical stretch was slightly smaller to account for the difference in estimated strain in the wire rope at the time that the wire rope was taut, leading to a different estimate of the slack length. Maximum displacement in the test was 38.4 in. (975 mm), and in the linearized and non-linear geometrical stretch non-

prestretched wire rope simulations of test no. DBC-1 the maximum displacements were 39.36 in. and 38.41 in. (999.7 and 975.4 mm), respectively.

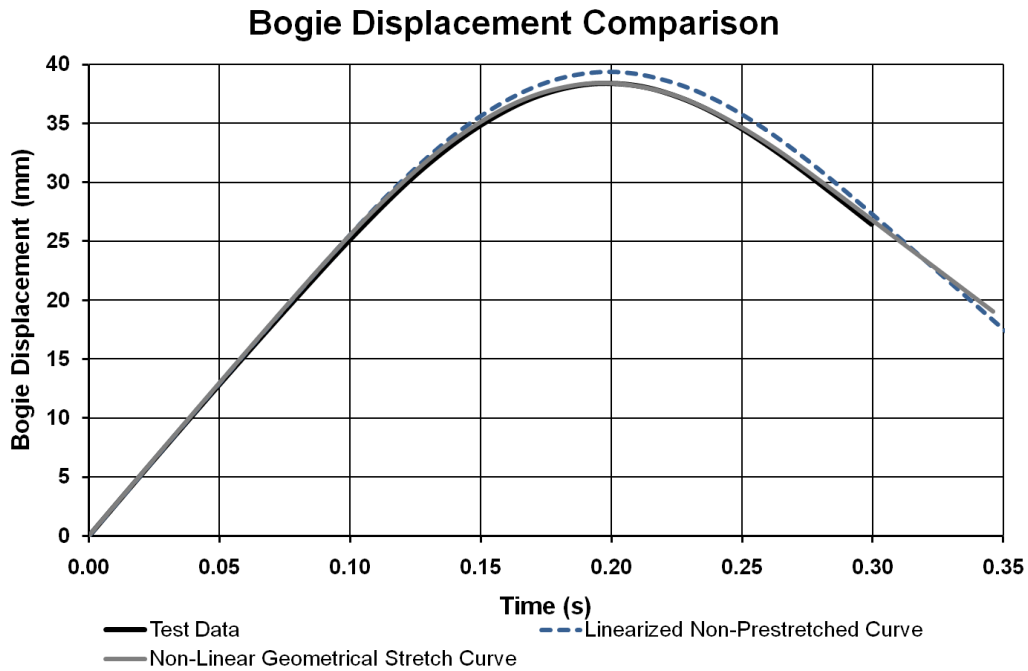


Figure 164. Bogie Displacement Comparison, Test and Simulation, Test No. DBC-1

A plot of the bogie velocity indicated a difference based on the linearized and non-linear tensile curves, as shown in Figure 165. The linearized non-prestretched tensile curve rebounded at a higher velocity of 21.11 ft/s (6.43 m/s), whereas the non-linear geometrical stretch curve had a rebound speed of 13.93 ft/s (4.24 m/s). The bogie rebounded at a speed of 14.89 ft/s (4.54 m/s) in test no. DBC-1. The increase in rebound speed using the non-prestretched linearized tensile curve was due to a higher unloading force applied to the bogie, since only one "modulus of elasticity" is defined using the linearized curve.

The test and simulation bogie acceleration curves were similar, as shown in Figure 166. Peaks and valleys occurred at nearly the same time in both the linearized and non-linear non-

prestretched tensile curve simulations. The peak frequency in test acceleration data was 50 Hz, and the frequencies in the simulations showed mixed character.

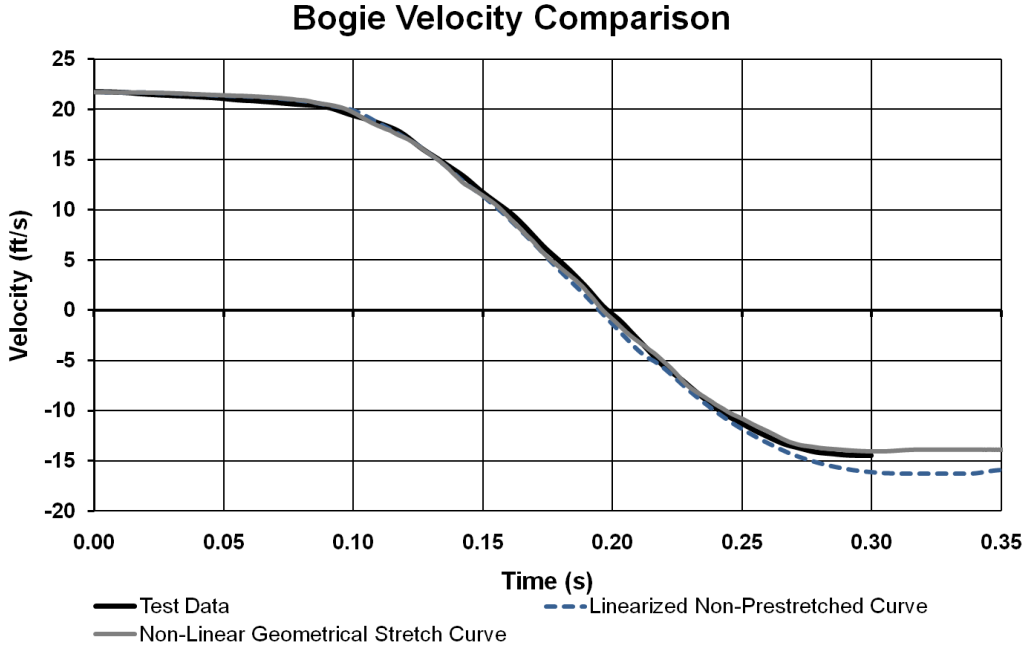


Figure 165. Bogie Velocity Comparison, Test and Simulation, Test No. DBC-1

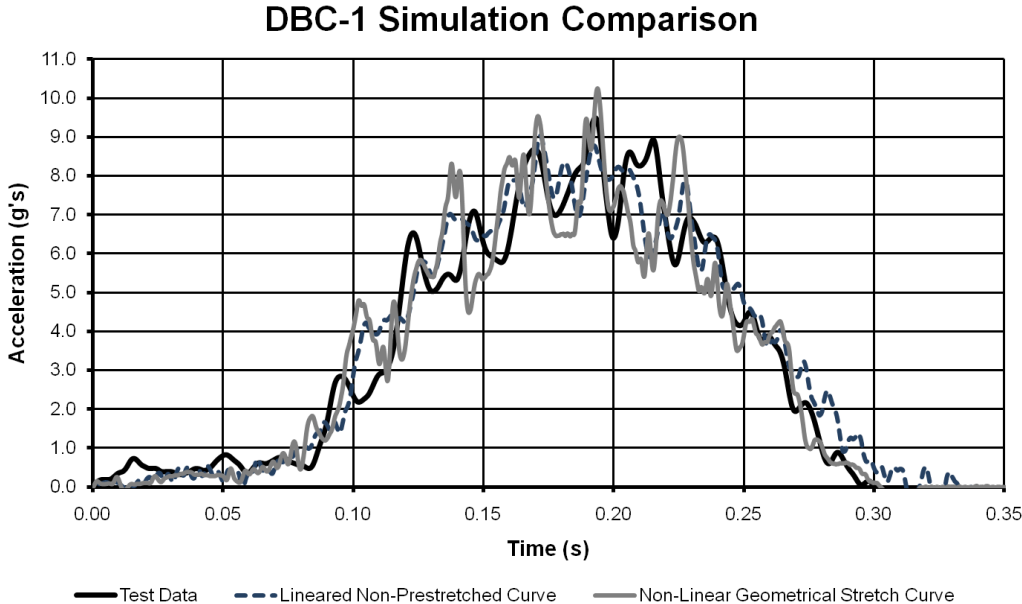


Figure 166. Bogie Acceleration Comparison, Test and Simulation, Test No. DBC-1

13.2.3.2 Effect of Other MAT_166 Parameters

In addition to the use of geometrical prestretch versus the linearized tensile curves, the effect of three other parameters were investigated in models of test no. DBC-1: bending stiffness, cfa, (axial dynamic coefficient) and cfb (bending dynamic coefficient). The results of these studies are discussed below.

Though the quasi-static bending stiffness was investigated in the quasi-static bending tests, there was still uncertainty about the dynamic bending stiffness of wire rope in impact situations. Therefore, the stiffness of the wire rope was evaluated by increasing the stiffness curve in an attempt to match the bogie acceleration peak frequency observed in the physical test. It was determined that by using spectral frequency analysis the wire rope bending frequency in the simulation was 18% lower than in the physical test for the primary bending wave forms. Thus, the bending stiffness curve was increased by 18% to determine the effect additional stiffness had on the simulation. Then, a transitioning stiffness curve was created which transitioned from the baseline stiffness to the higher stiffness curve, as shown in Figure 167.

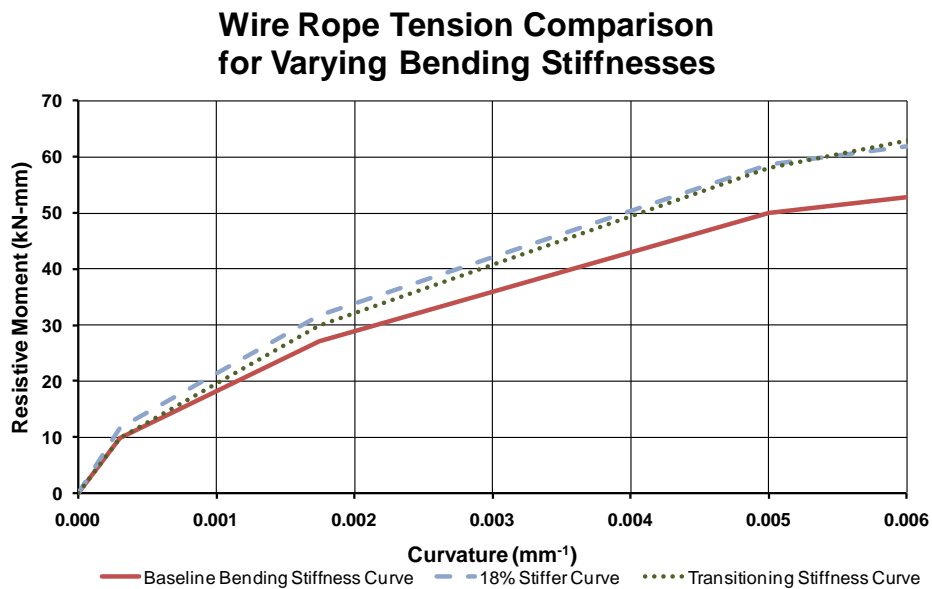


Figure 167. Bending Stiffness Curves Evaluated for Sensitivity Study

The baseline stiffness curve model was copied and the baseline stiffness curve was replaced with the new curves, and the new models were simulated. Wire rope tension curve results from the models are shown in Figure 168. The wire rope tension curve indicated no difference between the baseline and transitioning stiffness curves in terms of dynamic tension. However, the 18% stiffer curve had a higher peak load of 36.56 kip. (162.7 kN) which, despite being closer to the test load of 37.1 kip (165.0 kN), occurred out of phase with the test load and had a longer sustained wire rope tension.

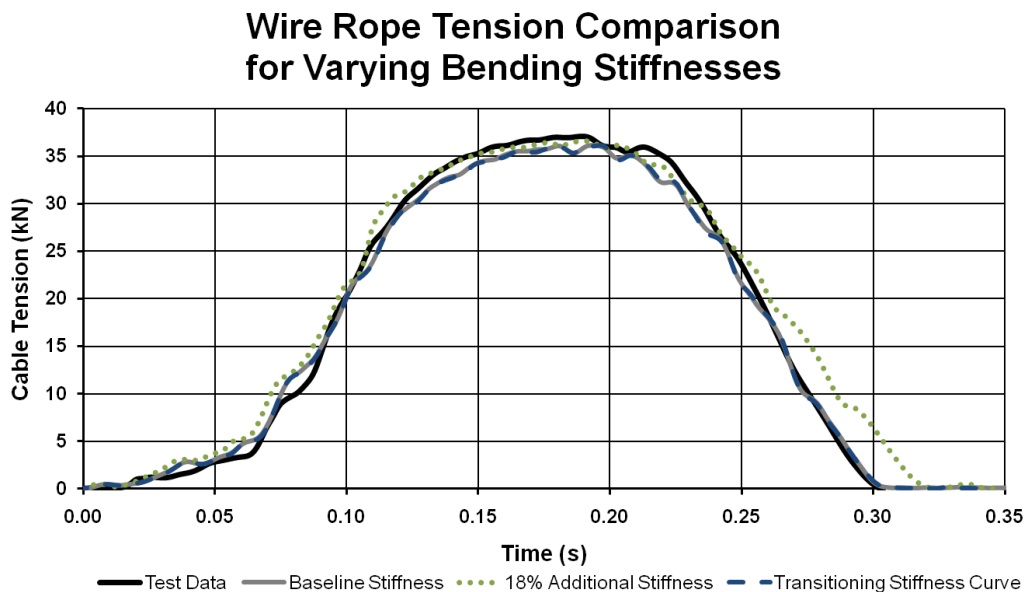


Figure 168. Wire Rope Tension Comparison, Varying Bending Stiffness Models

The longer sustained wire rope tension is non-intuitive. However, it was observed that, since the wire rope bending stiffness increased, there was less plastic bending that occurred in the wire rope, and, as a result, the wire rope was able to elastically rebound farther following impact. This indicates a condition in which the bending stiffness of the wire rope plays a significant role in the redirection of the bogie vehicle, such that the wire rope acted slightly more like a solid rod, and less like a tensioned string. Since little change was observed in the increase

between the original bending stiffness and the small increase, the lower bending stiffness in these tests indicated that the tension was the primary redirective mechanism in the lower bending-stiffness simulations.

The bogie velocity and acceleration were plotted to compare the model results, and are shown in Figures 169 and 170. The bogie rebound velocity of 16.05 ft/s (4.89 m/s) was higher than the test and baseline stiffness rebound velocity. This was due to the increase in bending stiffness elasticity and a larger portion of the bogie redirection occurring as a result of the wire rope bending stiffness. However, the bogie accelerations were not as different as the wire rope tension curves. The frequency of the peaks of the bogie acceleration occurred at a slightly higher frequency (18%) than the baseline stiffness, but the shape of the curves did not change until after the bogie reached the maximum displacement, and the shape of the acceleration curve was nearly identical to the baseline curve. The transitioning stiffness curve had nearly no difference in bogie acceleration or velocity from the baseline model. The lack of disparity indicates that most of the bending of wire rope occurred in the elastic region of the bending curves, and thus the transitioning stiffness curve acted like the baseline for most of the simulation.

The cfa parameter was varied between 0.97 and 5.0 to observe the effects of the cfa on the resulting simulation. It was observed that the cfa parameter largely affected wire rope tension, and as a result, only indirectly affected displacement, velocity, and displacement curves. The wire rope tension curve showing the differences between the values of cfa is shown in Figure 171. Using the non-linear geometrical prestretch curve, all wire rope tension curves were identical for times less than 180 ms.

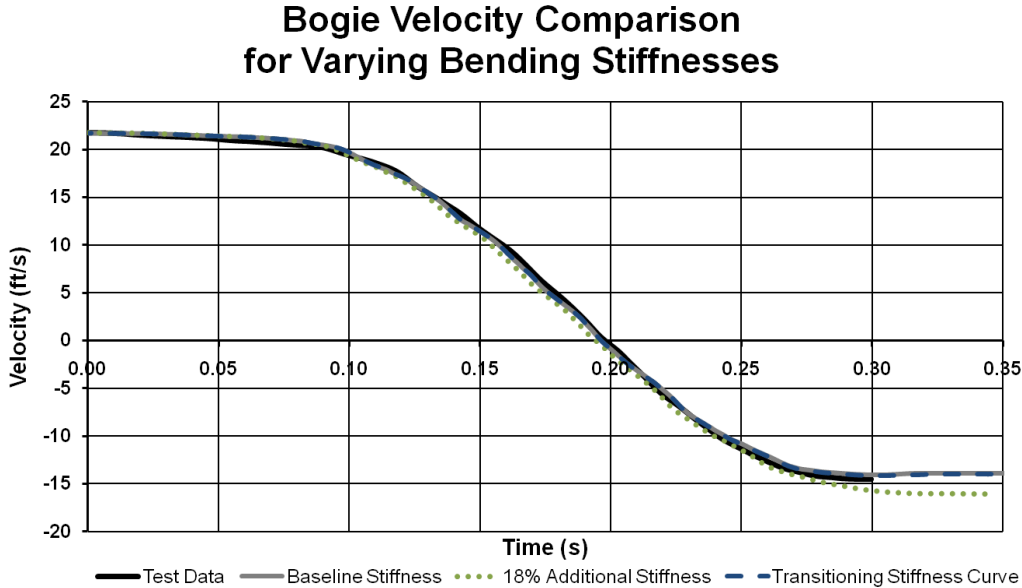


Figure 169. Bogie Velocity Comparison, Varying Bending Stiffness Models

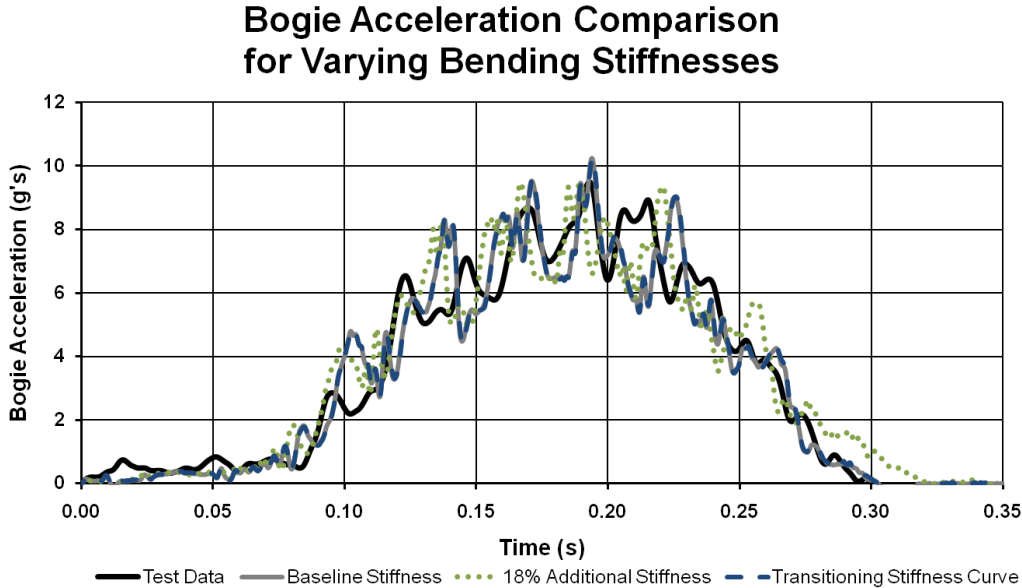


Figure 170. Bogie Acceleration Comparison, Varying Bending Stiffness Models

However, after the wire rope began to unload, the effect of cfa became evident. It was clear that the cfa parameter affected the unloading behavior of the wire rope. Since the unloading behavior is influenced by the modeled force modulus, the linear curve connecting the first two

points in the *MAT_166 tension curve, the cfa only serves to scale the elastic portion of the tensile curve by a bulk parameter. Further investigation with the cfa parameter may be required, since its behavior was unexpected. Using the linearized non-prestretched wire rope model, the amplification of the elastic force became evident, as shown in Figure 172.

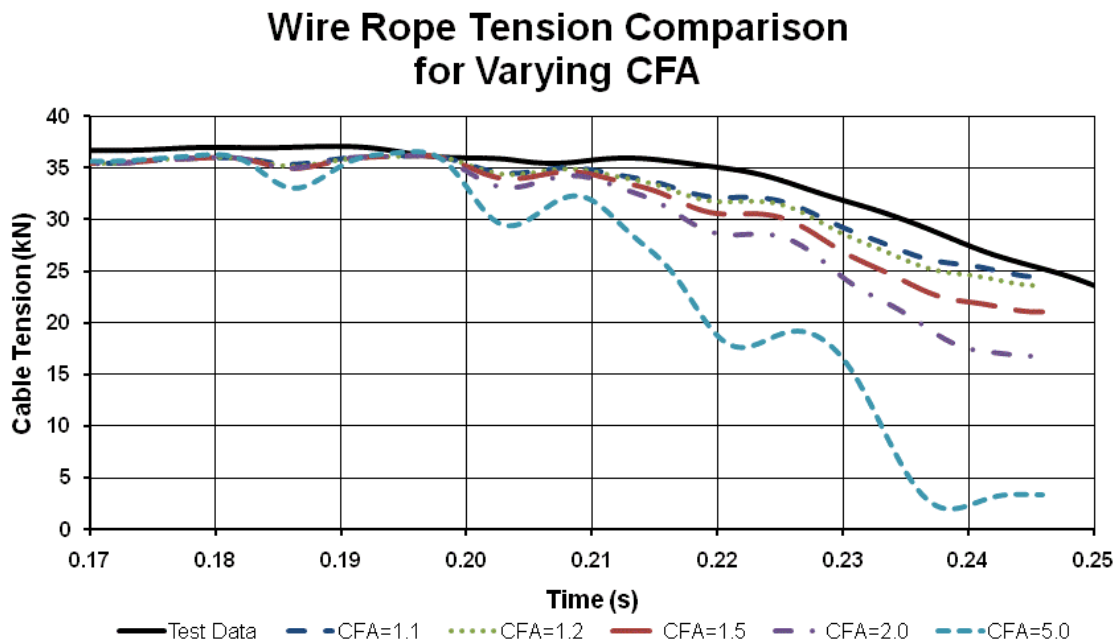


Figure 171. Effect of CFA on Non-Linear Tensile Curve Models of Test No. DBC-1

Based on the results of the cfa parameter sensitivity study, it was determined that the cfa coefficient must be similar to, but not equivalent to, the dynamic amplification factor. Dynamic amplification factors are commonly used in lieu of a viscoelastic material model analysis to estimate strain rate effects on the component being modeled. The cfa coefficient, by contrast, increases the range of linear strain as a function of strain rate. This amplifies the dynamic load and has a subtle effect on the plastic load-strain relationship. Furthermore, this parameter has very little effect, except in the unloading of the wire rope, using the non-linear geometrical

prestretch tensile curve. Only when using the linearized model will the cfa have an effect on dynamic stiffness.

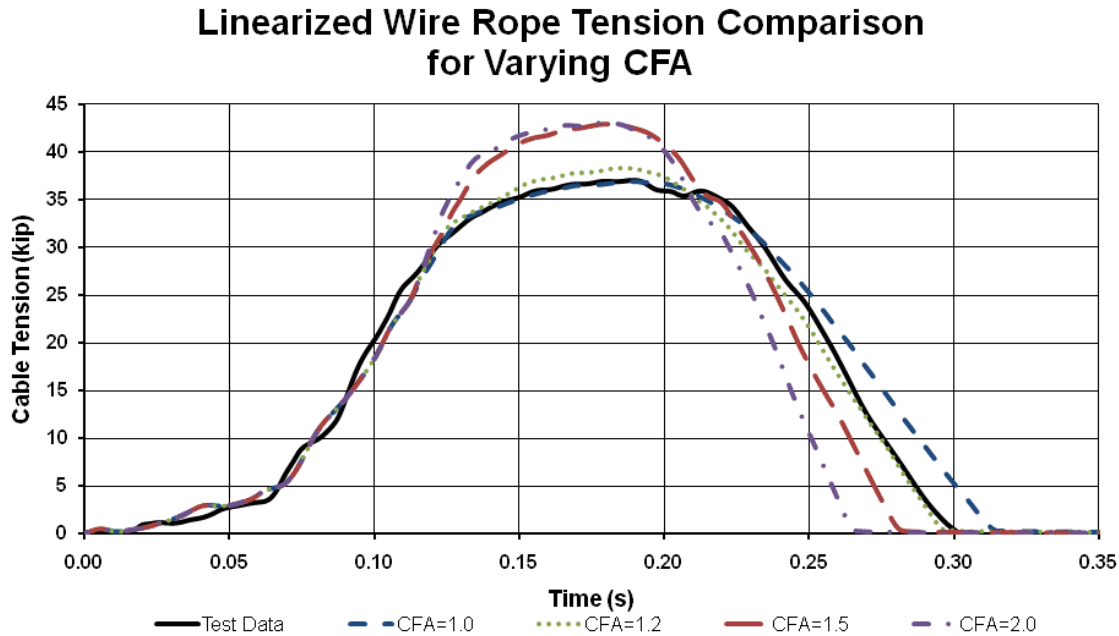


Figure 172. Effect of CFA on Linearized Tensile Curve Models of Test No. DBC-1

The cfb parameter was also investigated to determine the effect the cfb coefficient had on the wire rope model. In test no. DBC-1, very little difference was observed in any cfb coefficient. This is because the effective bending curvature rate of the wire rope was very small throughout the test. Furthermore, with the exception of an approximately 6-in. (152-mm) long section of wire rope on either side of the impact head, the remainder of the wire rope remained elastic in bending. Thus, the effect of the cfb coefficient could not be determined.

Results of the parameter sensitivity study were mixed. The bending stiffness had a relatively small effect on the resulting reaction of the wire rope for an 18% increase in stiffness. The cfa parameter was limited to scaling the elastic strain range under the constant force per strain slope. Because the non-linear force-strain curve had a small modeled elastic limit prior to becoming non-linear, the cfa parameter did not affect loading behavior of the non-linear curve,

but did affect unloading. Since there was no clear advantage to using any value but the baseline c_{fa} and c_{fb} values and the baseline bending curve, the baseline states were recommended for continued evaluation. However, because the linearized non-prestretched wire rope model demonstrated a slight improvement using $c_{fa} = 1.2$, further evaluation of c_{fa} was necessary.

13.3 Evaluation of Test No. DBC-1

The non-linear geometrical stretch curve simulation of test no. DBC-1 was considered successful in predicting the behavior of wire rope subjected to dynamic bending loads. As a next step in the analysis procedure, the wire rope response predicted by the other wire rope models previously used to model wire rope was explored. A comparison of the four models discussed in Chapter 3 used in the evaluation is shown in Figure 173. A summary of pertinent modeling information, shown in metric units as used in LS-DYNA, of the four models is shown in Table 13.

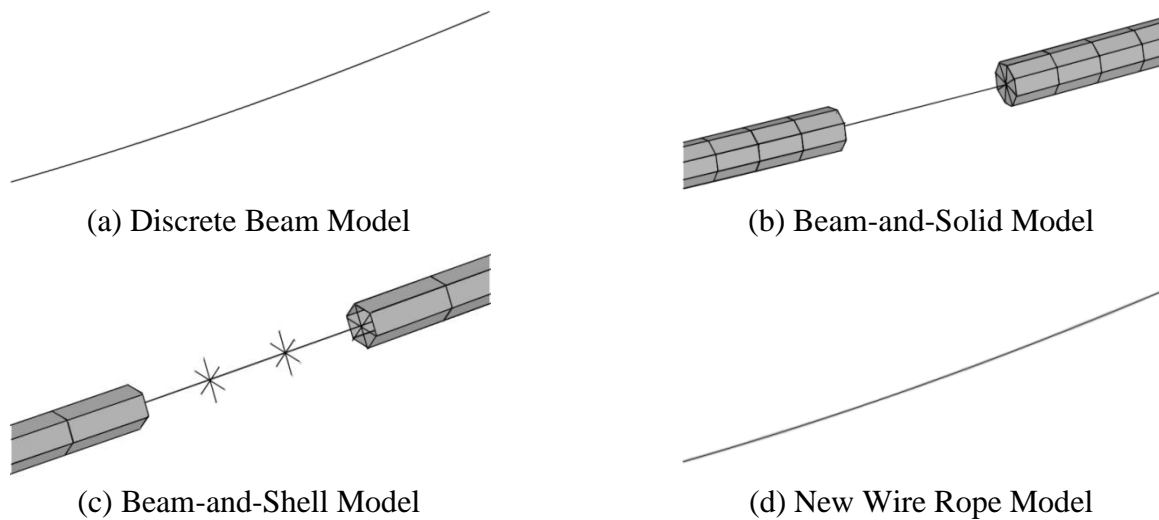


Figure 173. Wire Rope Model Comparison

Table 13. Summary of Modeling Parameters for Wire Rope Models Investigated

Model Name	Components	Materials Used	Linear Mass, ρ_L (kg/mm)	Cross-Sectional Area, A (mm ²)	Modulus of Elasticity, E (GPa)	Bending Resistance, EI (kN-mm ²)
Discrete Beam	Type 6 Discrete Beam	*MAT_CABLE_DISCRETE_BEAM (*MAT_069)	7.3301E-04	154.84	126	0
Beam-and-Solid	Type 6 Discrete Beam	*MAT_CABLE_DISCRETE_BEAM (*MAT_069)	7.3301E-04	154.84	126	0
	Type 15 Two-Point Pentahedron Solid	*MAT_PIECEWISE_LINEAR_PLASTICITY (*MAT_024)	1.3448E-03	255.27	126 / 0.02*	654,838 Fully Elastic 104 Fully Yielded
Beam-and-Shell	Type 1 Hughes-Liu Beam	*MAT_ELASTIC (*MAT_001)	1.3005E-03	283.53	85	543,755
	Type 2 Belytschko-Tsay Shell	*MAT_NULL (*MAT_009)	3.0717E-04	0**	0**	0**
New Wire Rope Model	Type 2 Belytschko-Schwer Beam	*MAT_MOMENT_CURVATURE_BEAM (*MAT_166)	1.2280E-03	154.51	79.9	32,380

* Elastic modulus 126 GPa until 7.94E-5 strain; 0.02 Gpa modulus until 0.5 strain

** Null shells did not contribute to material or section properties

The discrete beam model consisted of a series of discrete beams with a nominal diameter of ¾ in. (19 mm). The beams were defined with a discrete section and used *MAT_CABLE_DISCRETE_BEAM for the material. The modulus of elasticity was defined to be 18.3 Mpsi (126 GPa), and the cable area was 0.2395 in.² (154.51 mm²). The non-linear option for tensile loads was not used in the wire rope model since this model, as previously used in wire rope guardrail simulations, did not include a non-linear curve. All parameters were matched to existing models of the wire rope using the discrete beams.

The beam-and-solid model was identical to the discrete beam model except for the inclusion of a solid element wrap around the outside of the beam. Eight wedge-shaped solid elements were defined with termination points coincident with each node of the beam element. The solid elements were defined with the type 15 2-point pentahedron solid section and *MAT_PIECEWISE_LINEAR_PLASTICITY. Though the modulus of elasticity of the solids was also 18.3 Mpsi (126 GPa), the yield strain in the solid elements was only 7.94(10⁻⁵), which occurred at a tensile load of 0.574 kip (2.55 kN). The solids were defined with kinematic

hardening after yielding with a tangent modulus of 2.9 kpsi (0.02 GPa). This layer of solid elements aided the discrete beam model in three ways: (1) it provided a consistent and tested contact surface for full-scale impact simulations which was compatible with most element types; (2) it provided bending resistance to eliminate the high-frequency "kinking" that occurred in wire rope under dynamic oscillations; and (3) it provided compression strength to eliminate compression wave instability in the discrete beams.

The last model to be used was the beam-and-shell model, which incorporated a type 1 beam element defined with *MAT_ELASTIC and a modulus of elasticity of 12.3 Mpsi (85 GPa). Though this modulus of elasticity was more reflective of the tested modulus of elasticity of non-prestretched wire rope, the cross-sectional area of the beam was equated to a ¾-in. (19-mm) diameter steel rod, which was 84% higher than the approximated area defined in the new wire rope model. Furthermore, the elastic bending modulus, which is the product of Young's modulus times the area moment of inertia, was 16.8 times greater than the effective elastic modulus of the new wire rope model.

The three previously-developed models were simulated in the exact same configuration as was tested in the non-linear geometrical stretch model of test no. DBC-1. A summary of the test data is shown in Table 14.

Wire rope tension results are shown in Figure 174. The peak load in the wire rope varied significantly between the models even though each model had identical initial slack. The discrete beam and the beam-and-solid models were very similar, though the beam-and-solid model had a higher peak load of 68.9 kip (306 kN). By contrast, the wire rope load in the beam-and-shell model was more than twice the actual load sustained by the wire rope in the test. Furthermore,

the load in the wire rope in the beam-and-shell model continued to increase after the bogie left contact with the wire rope.

Table 14. Results Comparisons, Test and Simulation Data, Test No. DBC-1

Model Configuration	Maximum Load (kip)	Maximum Displacement (in.)	Rebound Velocity (ft/s)	Maximum Bogie Acceleration (g's)
Component Test DBC-1	37.3	38.39	14.49	9.49
New Wire Rope Model	36.2	38.40	13.93	10.25
Discrete Beam Model	68.9	33.52	21.11	13.35
Beam-and-Solid Model	60.0	33.01	20.28	14.58
Beam-and-Shell Model	80.0	28.11	26.01	18.00

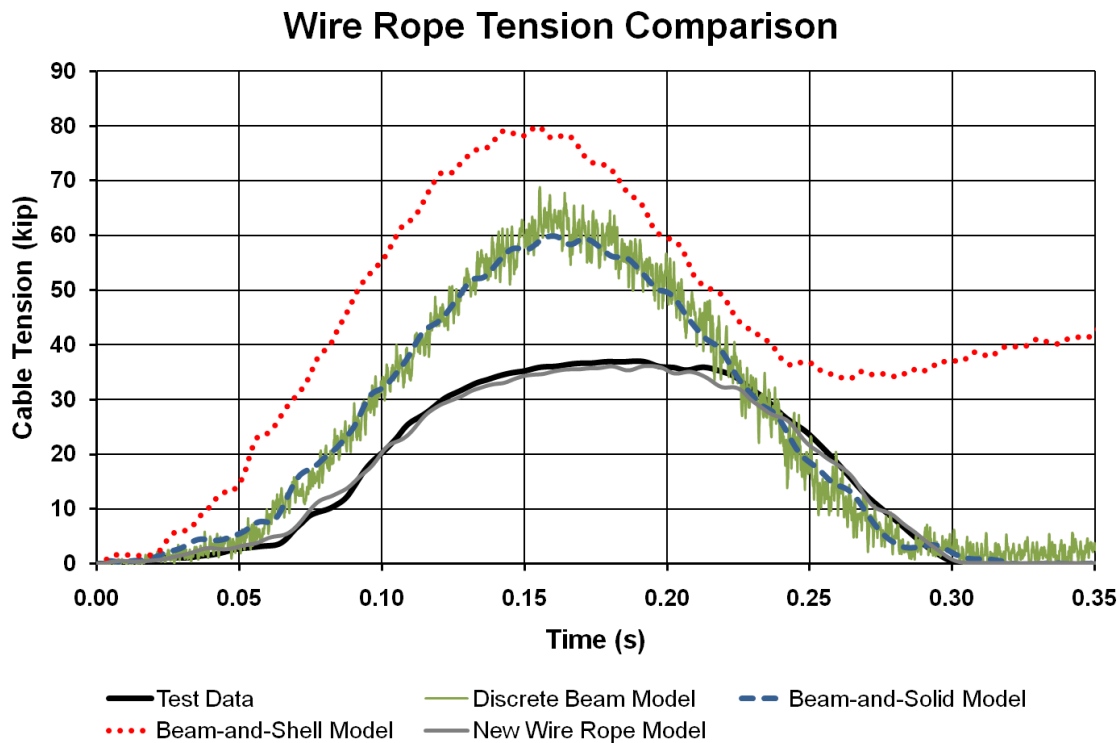


Figure 174. Wire Rope Axial Load Comparison, Test and Simulation, Test No. DBC-1

The unsettling results of the beam-and-shell model led researchers to investigate the causes of the increase in tensile force following the end of the test. Researchers examined the output states in the video and determined that the wire rope appeared to be shortening during the simulation, such that it came to a final length which was smaller than the initial length. The length of the wire rope at several increments in time were plotted and a resultant shortening of 1.0 in. (25 mm) was observed, as shown in Figure 175. This is non-physical, since the length of the wire rope in the test increased due to plastic strains in the material.

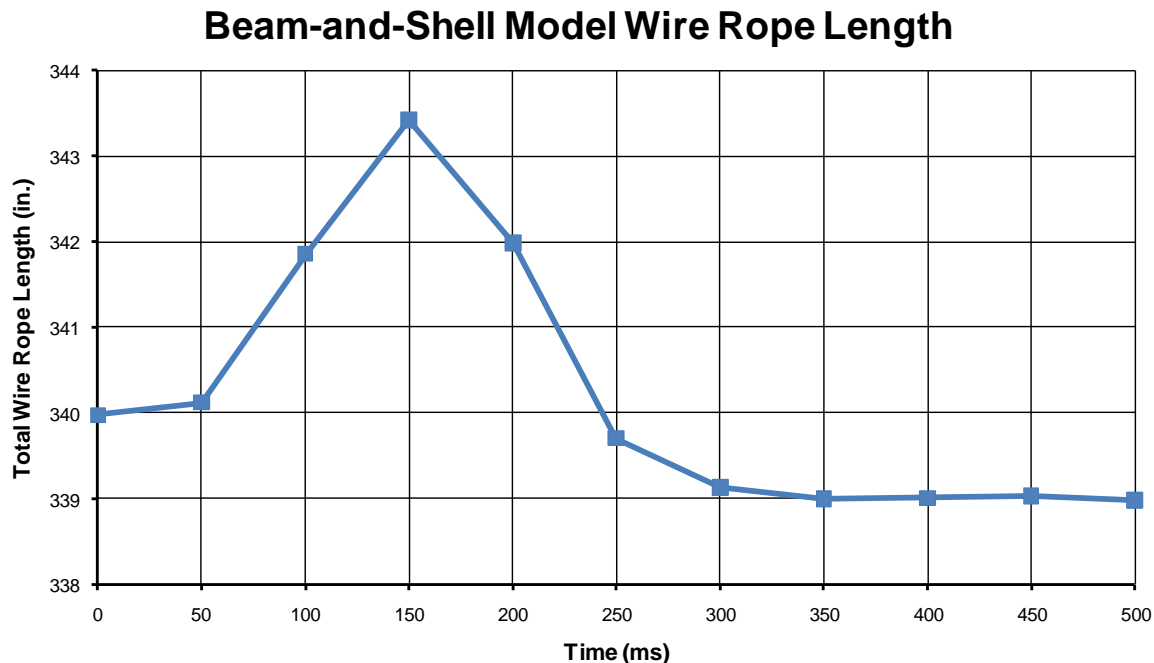


Figure 175. Wire Rope Length, Beam-and-Shell Model, Test No. DBC-1

The displacements and velocities of the previously-developed models were also compared to the new wire rope model and test results, as shown in Figures 176 and 177. The displacements of the previously-developed models were consistently below the displacements of the new wire rope model and test results. This result indicates that the new wire rope model more accurately reflects the internal compliance of wire rope than the previously-developed models.

The velocity curves likewise indicated a significant difference between the models. The rebound velocity of the test and simulation were approximately the same at 14.5 ft/s (4.4 m/s), but the rebound velocity of the bogie in the beam-and-solid and discrete beam model simulations was very close to the impact speed of 21.74 ft/s (6.625 m/s). The rebound speed of the bogie in the beam-and-shell model simulation was 26.0 ft/s (7.93 m/s). This speed is higher than the impact speed, which is not physically possible in a dissipative system.

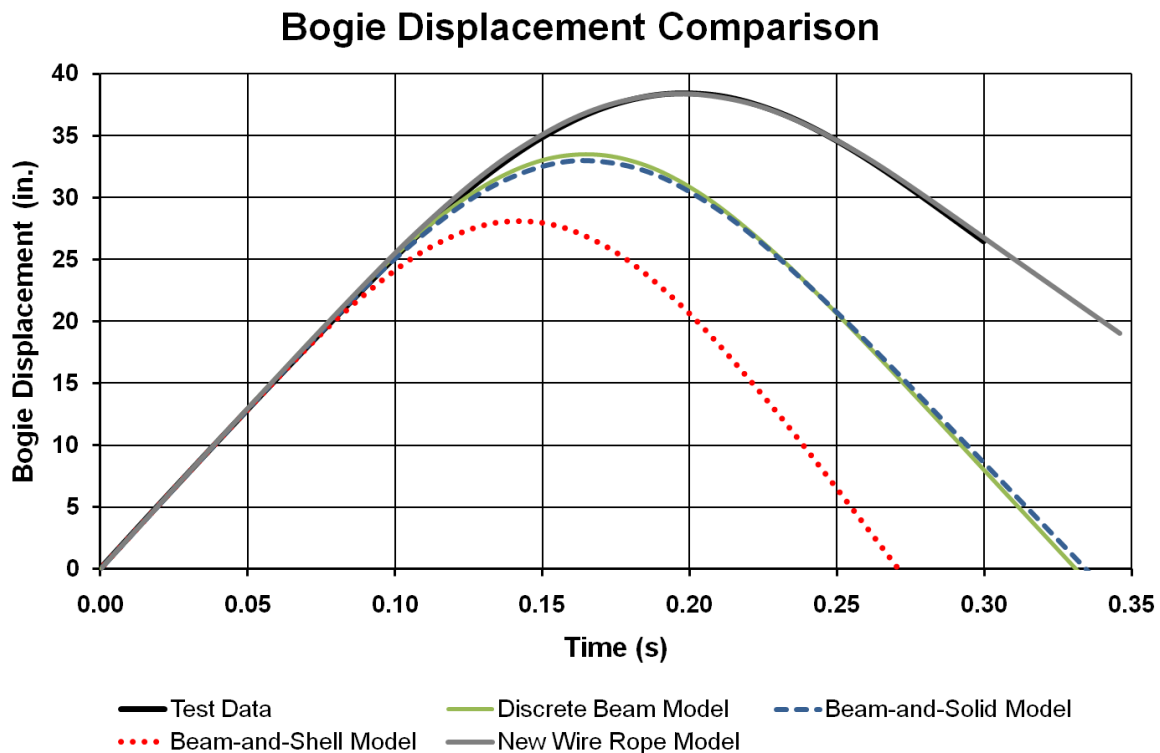


Figure 176. Bogie Displacement Comparison, Test and Simulations, Test No. DBC-1

In addition to the bogie displacement and velocity, bogie acceleration in the four simulations were plotted and compared and are shown in Figure 178. Large-amplitude dynamic peaks were present in the beam-and-shell model, and the oscillation frequencies were very large. The oscillation frequencies were less for the discrete beam model, and were further mitigated using the beam-and-solid model. However, all three models had a dynamic acceleration

oscillation frequency which was higher than witnessed in the test of 43 Hz. The new wire rope model more closely matched the acceleration frequency than the other models, and had very similar acceleration peak values. Therefore, the new wire rope model was determined to be more accurate in predicting wire rope loading than the previously-developed models for low-initial-load wire rope in direct bending.

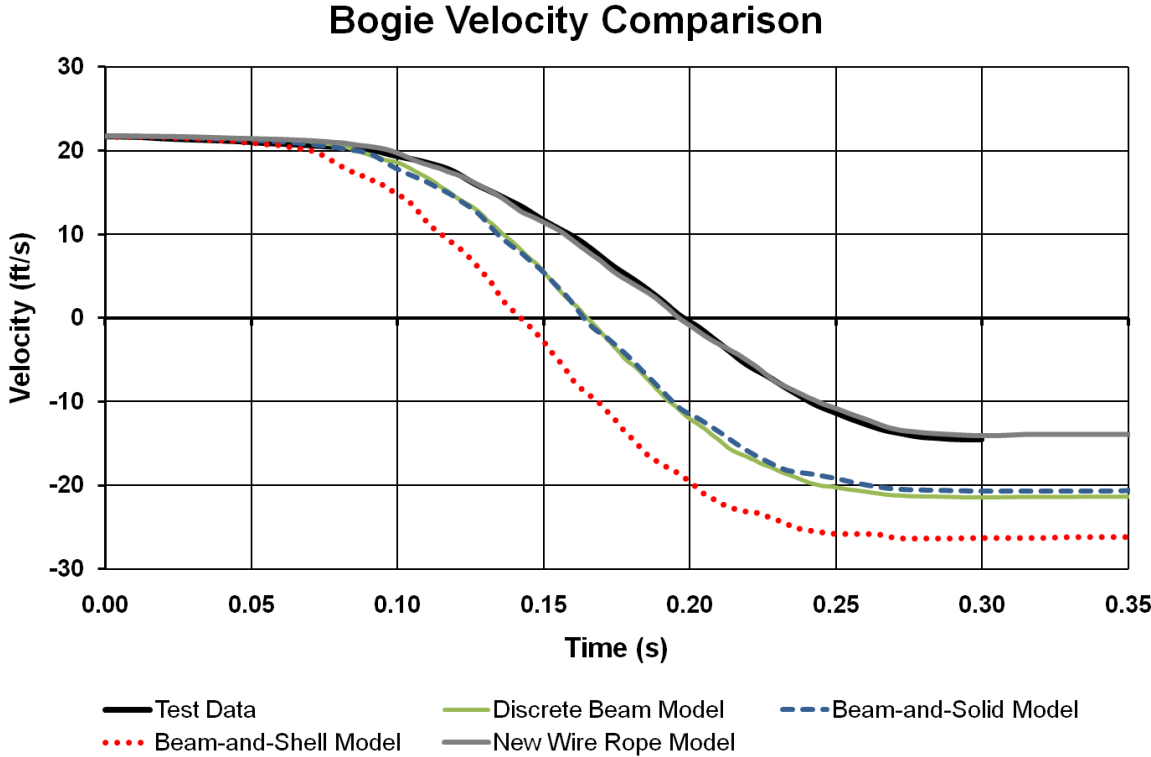


Figure 177. Bogie Velocity Comparison, Test and Simulations, Test No. DBC-1

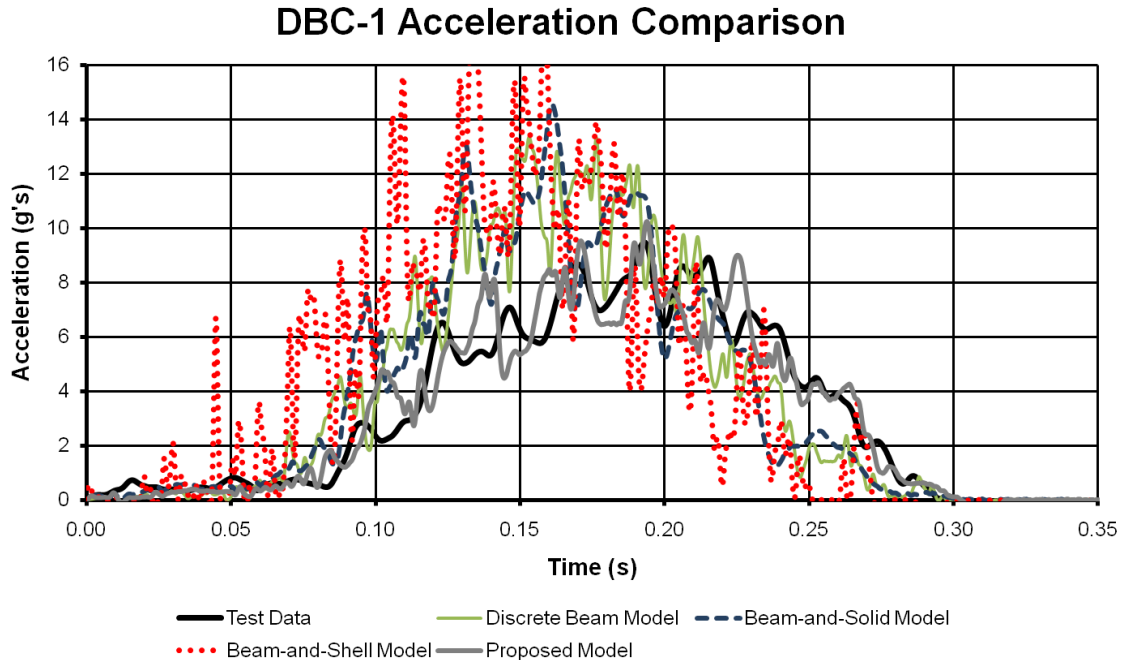


Figure 178. Bogie Acceleration Comparison, Test and Simulations, Test No. DBC-1

13.4 Modeling Test No. DBC-2

The second test of wire rope in the same bending position was also modeled and evaluated, as minor changes in the test conditions led to variations in the data. This test served as a sensitivity analysis for the accuracy of the data under minor impact variations.

The slack length in test no. DBC-2 was also measured from high-speed digital video capture, load cell results, and bogie accelerometer data. The total slack length was determined to be 1.82 in. (46.2 mm).

Wire rope tensile load is shown in Figure 179. The new wire rope model began to load up slightly earlier than the wire rope in test no. DBC-2, but the difference in load times was less than 4 ms. The maximum load in the new wire rope model was 36.16 kip (160.8 kN), and the maximum load recorded in the test was 37.2 kip (165.5 kN). It is possible that the slack length estimated was too small, which would account for the small variation in the time in which the

wire rope loaded up in the simulation; however, the increase in slack length was not quantifiable using validated methods, and the behavior of the wire rope was very similar to the test.

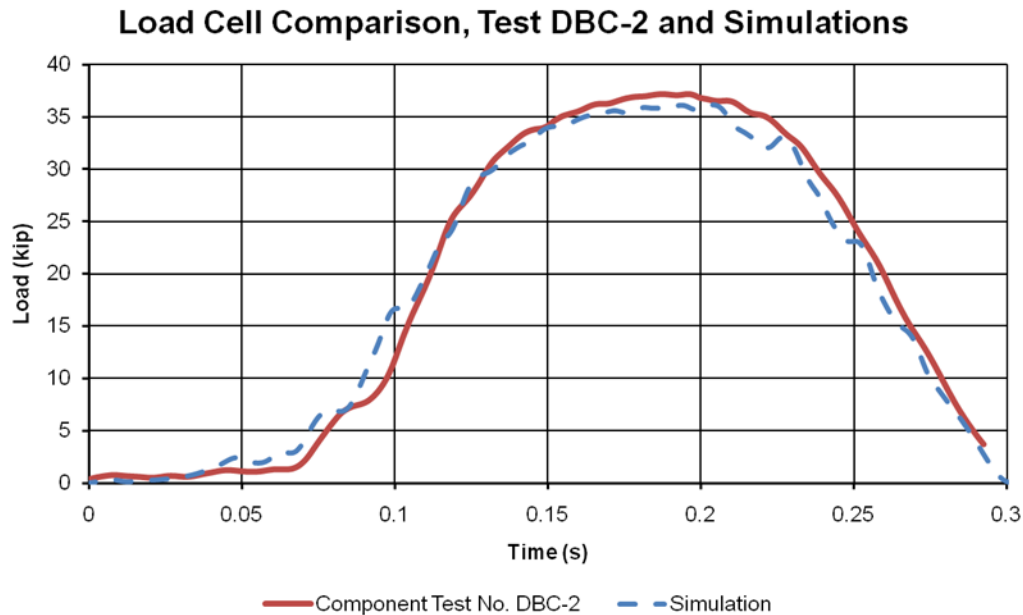


Figure 179. Wire Rope Axial Load, Test and Simulation, Test No. DBC-2

Bogie displacement is shown in Figure 180. The maximum bogie displacement simulated was 43.5 in. (1,105 mm), compared to 41.4 in. (1,051 mm) in the physical test. The displacements were very similar and also indicated that the bogie was decelerated sooner in the simulation than occurred in the physical test.

Bogie velocity in the test and simulation is shown in Figure 181. In both the test and the simulation, the bogie vehicle initially had the same velocity, and began to decelerate at 105 ms. However, the velocity curve time shift of approximately 1.2 ms occurred at 115 ms, where a small delay in the slope of the bogie velocity occurred. The test velocity was then higher than the simulated bogie velocity by a constant amount until 220 ms, when the velocities began to diverge. A close comparison of the velocities of the bogie in the test and simulation indicate good correlation between the wire rope model and the physical testing results.

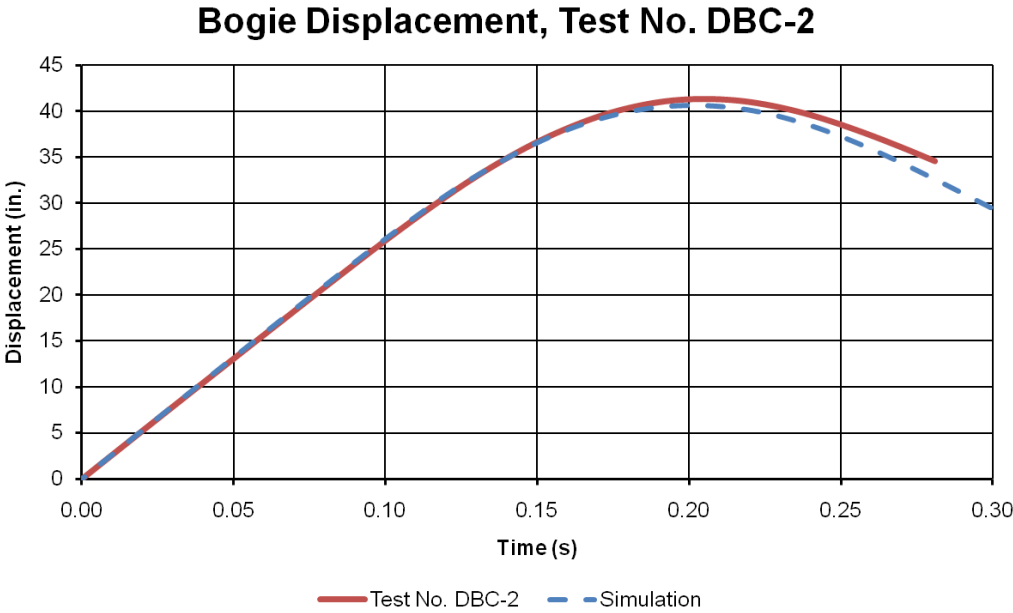


Figure 180. Bogie Displacement, Test and Simulation, Test No. DBC-2

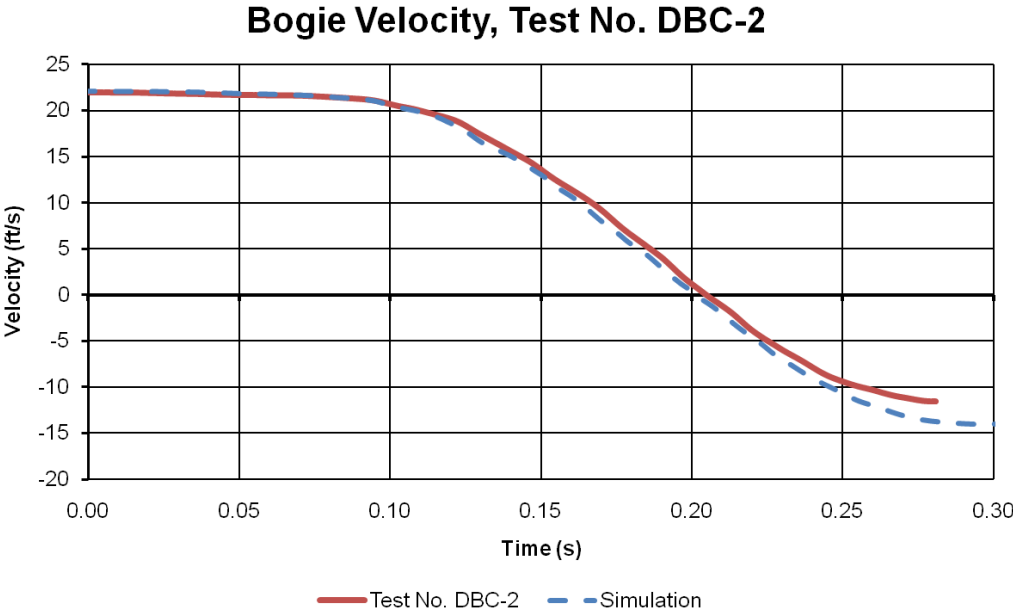


Figure 181. Bogie Velocity, Test and Simulation, Test No. DBC-2

Bogie accelerations were compared and are shown in Figure 182. Very good correlation between acceleration spikes and peaks in the test data acceleration were observed. The acceleration peaks, which are related to the bending waves being transmitted past the bogie

vehicle, are similar for the new wire rope model and the test. Both the magnitudes and the rates were very similar; thus, the new wire rope model very accurately predicted the behavior of the wire rope in component test no. DBC-2.

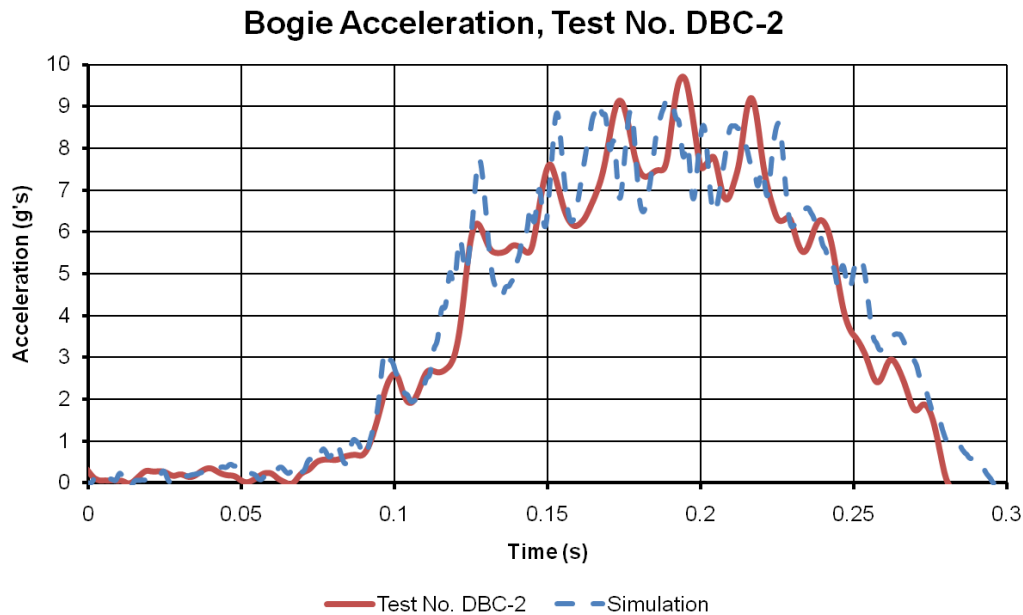


Figure 182. Bogie Acceleration, Test and Simulation, Test No. DBC-2

13.5 Modeling Test No. DBC-4

Since component test no. DBC-4 had a very similar test construction to test no. DBC-1 and DBC-2, a similar model was used with a slack length updated to the slack length calculated from high-speed video, load cell, and accelerometer analysis. The slack length of the wire rope in test no. DBC-4 was determined to be 2.00 in. (50.8 mm), which is very similar to the slack estimated in the initial construction of the socketed wire rope.

The bogie speed in test no. DBC-4 was 23.65 mph (10.57 m/s), and this speed was used to update the simulated bogie impact speed. The slack in the wire rope was approximated using a sinusoidal curve, as was done for test nos. DBC-1 and 2. The amplitude of the sinusoidal curves was 2.4 in. (61 mm) to obtain a total slack of 2.00 in. (50.8 mm).

Sequentials of the test and simulation are shown in Figure 183. Based on incremental development work, the value of cfa in the wire rope model in test no. DBC-4 was 0.97, thus corresponding to a slight dynamic softening of the wire rope. The bogie impacted the modeled wire rope in the center and caused the wire rope to deflect, sending bending waves toward the modeled load frames. The bending waves reached the load frames at approximately 40 ms. At this time, all of the slack in the wire rope had been completely taken up, and the wire rope became taut very quickly. The wire rope fractured in the test at 85 ms, after a nearly linearly-elastic load ramp. The simulated wire rope tensile load reached the plastic load and the load rate per time flattened as it turned plastic. The modeled wire rope fractured at 104 ms at a load of 38.06 kip (169.3 kN). A comparison of modeled and tested wire rope tensions are shown in Figure 184.

Because the simulated wire rope tension curve diverged from the physical test at approximately 65 ms, corresponding to the onset of plastic loading, an additional simulation was run in which the rotating end supports were held fixed (i.e. not allowed to rotate) during the simulation. The fixed end support simulation had a wire rope fracture at a load of 38.21 kip (170.0 kN) at 96 ms. The initial simulations did not model resistance in the rotating end support at all. Therefore, in the absence of testing data indicating the resistance of the rotating pipe, the two extremes were simulated to see if the actual load was bounded between the solutions.

The breaking load of the wire rope was closely matched between the free- and fixed-end simulations. The basic behavior of the wire rope tension curve was the same between simulations and the component test. However, at 65 ms, the wire rope tension diverged from the no-resistance end support simulations and rose above the simulated loads of the fixed-end and free-end simulations. The cause of this spike, which occurred through the plastic loading zone in



0.000 sec



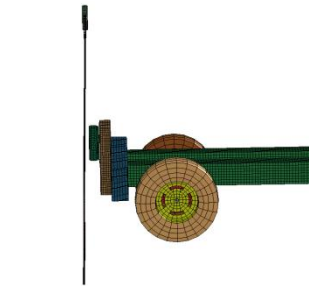
0.050 sec



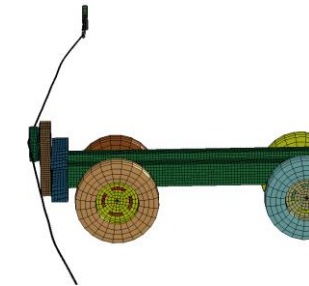
0.100 sec



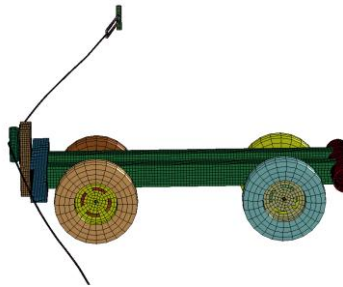
0.150 sec



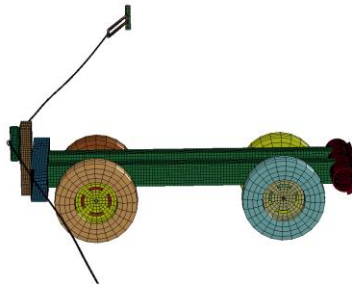
0.000 sec



0.050 sec



0.100 sec



0.110 sec

Figure 183. Sequential Photographs, Test and Simulation, Test No. DBC 4

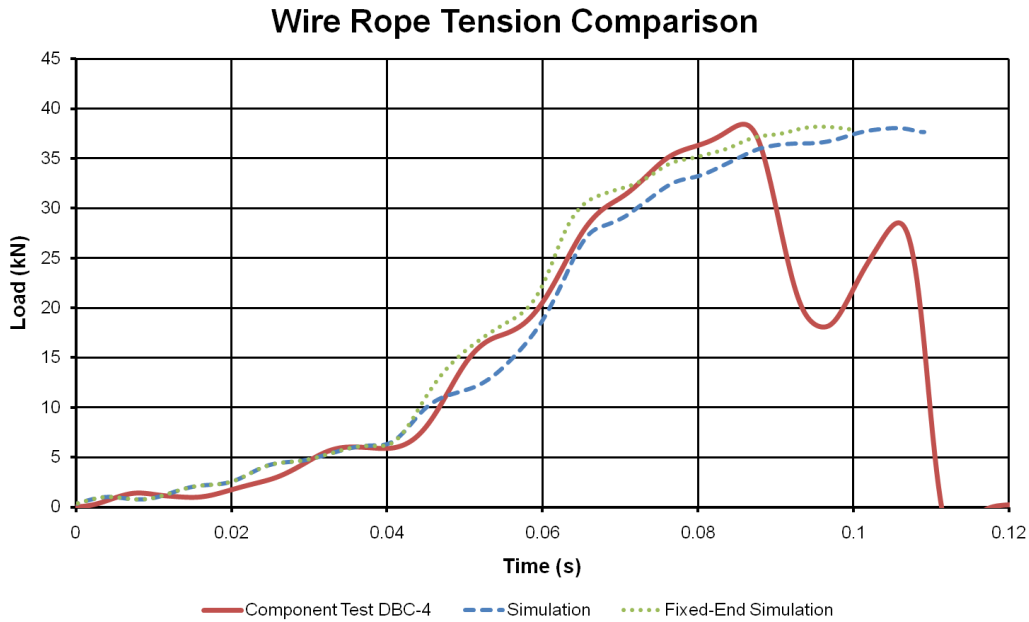


Figure 184. Wire Rope Tension, Test and Simulations, Test No. DBC-4

the wire rope, was due to a viscoelastic load effect at very high strain rates in tension. When the wire rope is plastically loaded, the wires are incapable of distributing load between each wire quasi-statically, so the outside wires temporarily carry a greater portion of the total tensile load than occurs quasi-statically. This allows the rope to act much stiffer during high-strain impacts. This effect was not witnessed in the lower-speed tests, and does not occur in long wire ropes with long load durations.

Returning to the results of test no. DBC-1, it was observed that the *cfa* parameter in the linearized non-prestretched wire rope model caused the load rate to remain elastic for a longer amount of time for higher values of *cfa*. Based on observation of the *cfa* coefficients in simulated test no. DBC-1, values of *cfa* less than 1.2 were acceptable with results in the simulations remaining very similar to the results of the test. Therefore, the non-linear geometrical prestretch tensile curve was replaced with the linearized tensile curve, and a parameter study was again conducted to consider the axial coefficient using the refined model.

The new models were run and compared, and the results indicated that values of cfa greater than 1.0 in the wire rope model were not able to predict the tensile loads in wire rope. The wire rope tension curves are shown in Figure 185. Though the same bending, tension, and torsion curves were used, all three values of cfa led to the wire rope fracturing at nearly the same time and load, with minor jumps near fracture.

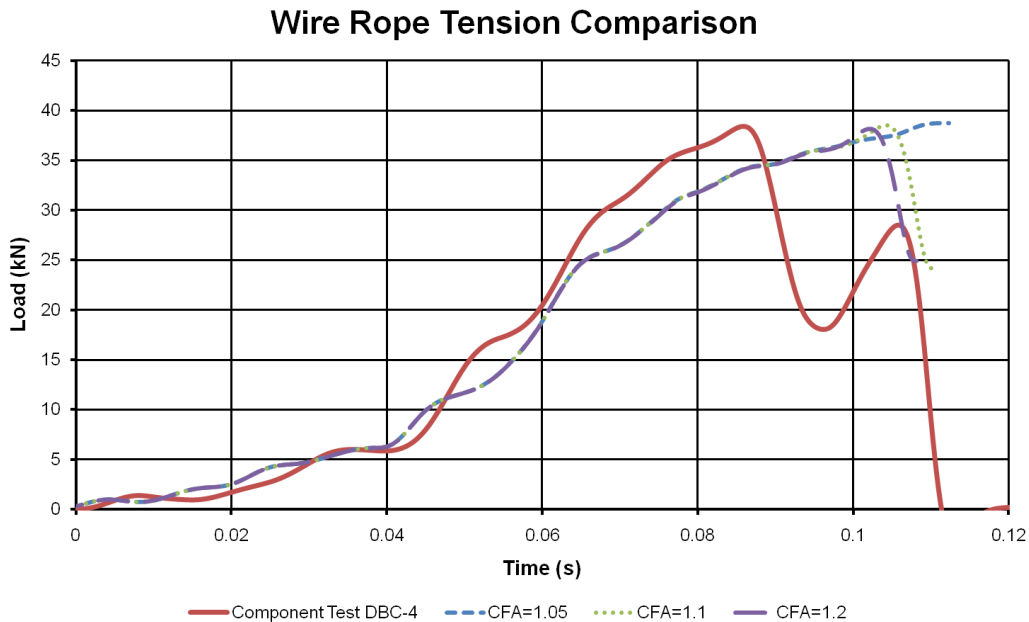


Figure 185. Simulated Wire Rope Tension, CFA Greater than 1.0, Test No. DBC-4

By including dynamic softening of the wire rope and setting the cfa to 0.97, the resistive force on the bogie decreased slightly during the dynamic process, and the bogie penetrated further in the wire rope system at a higher speed. The additional deflection led to a higher wire rope strain hence increasing the tensile force. This led to slightly more accurate wire rope tensile behavior in tension, as shown in Figure 184. As a result, the cfa parameter was set to 0.97, however it is possible that the increase in load and deflection prior to impact in the simulation of test no. DBC-4 resulted from the use of the non-prestretched wire rope tensile curve with inclusion of the non-linear geometrical strain.

Bogie displacements are shown in Figure 186. The bogie displaced the wire rope in both tests and the wire rope fractured at a displacement of 40.09 in. (1,018 mm) and a time of 105 ms. By comparison, the bogie displacement at fracture in test no. DBC-4 was 34.2 in. (871 mm). The displacement was very smooth.

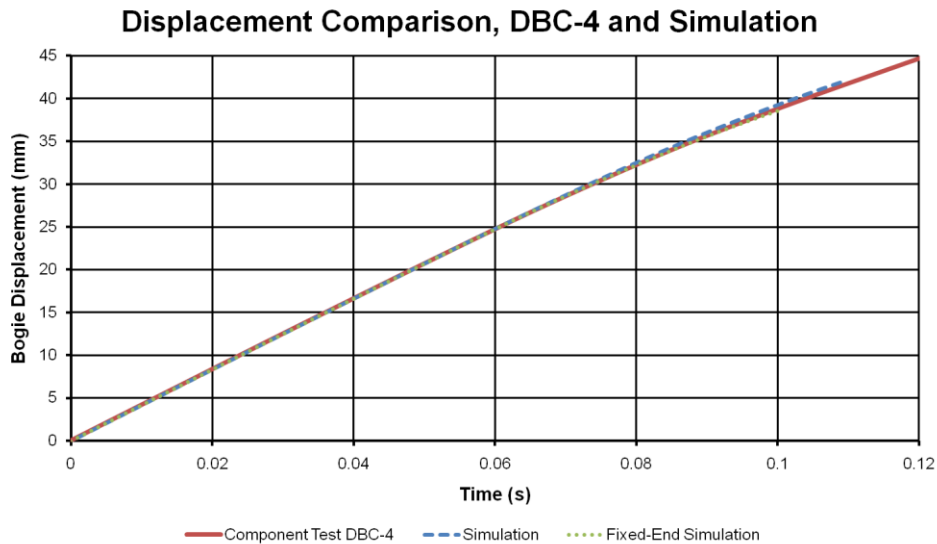


Figure 186. Bogie Displacement, Test and Simulation, Test No. DBC-4

Bogie velocity is shown in Figure 187. The bogie velocity curves were very similar through 60 ms, and the bogie velocity was always bounded by the fixed-end and free-end rotation curves. This result indicated that the resistance of the load pipes in test no. DBC-4 was not trivial, but had a significant effect on the end conditions. Furthermore, it also showed that the wire rope is a good, but not perfect, estimate of the load and bogie motion characteristics of the wire rope. The bogie velocity at the time of fracture was 24.30 ft/s (7.41 m/s).

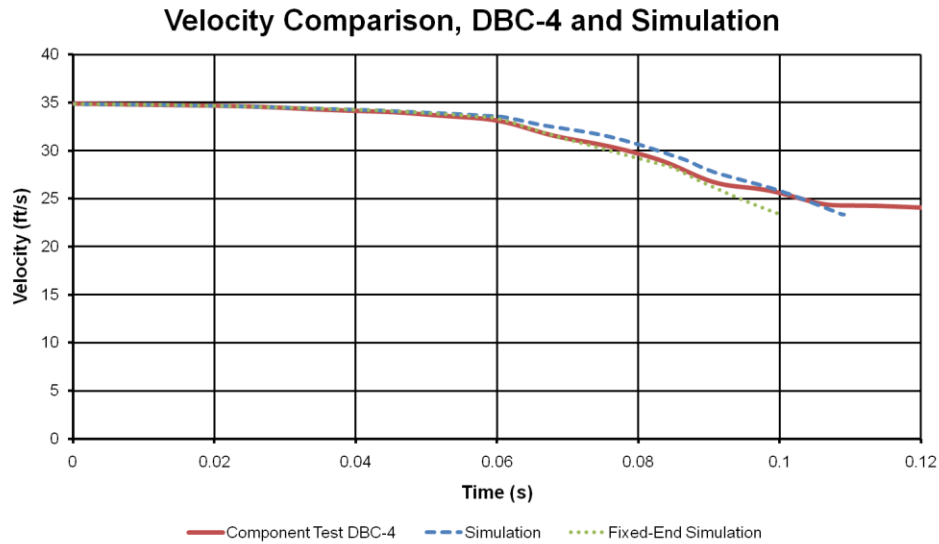


Figure 187. Bogie Velocity, Test and Simulations, Test No. DBC-4

The simulation was unable to capture the fracture of two strands in the wire rope without the third failing. This kind of fracture is impossible for beam-type elements to predict, since damage and fracture of individual wires cannot be tracked. Furthermore, this type of failure is extremely uncommon and limited to fractures near end supports. Wire rope failures in cable guardrail systems are extremely rare; the author has not witnessed nor has information about wire ropes fracturing in field operation. Furthermore, any time two strands fracture in a wire rope, the entire wire rope may be assumed to have lost all of the structural integrity. The fracture of two strands is the limit of the applicability of this wire rope model.

Bogie accelerations for the first 120 ms are shown in Figure 188. The bogie acceleration profiles were similar with force peaks occurring at nearly the same time. Only three peaks were witnessed in the simulation and the full-scale test data. The fracture of two strands of wire rope at 86 ms was witnessed by the drop in effective time-averaged acceleration of the bogie thereafter. As mentioned, this behavior was not pursued, and thus the new wire rope model was determined to be acceptable for prediction of the wire rope loads.

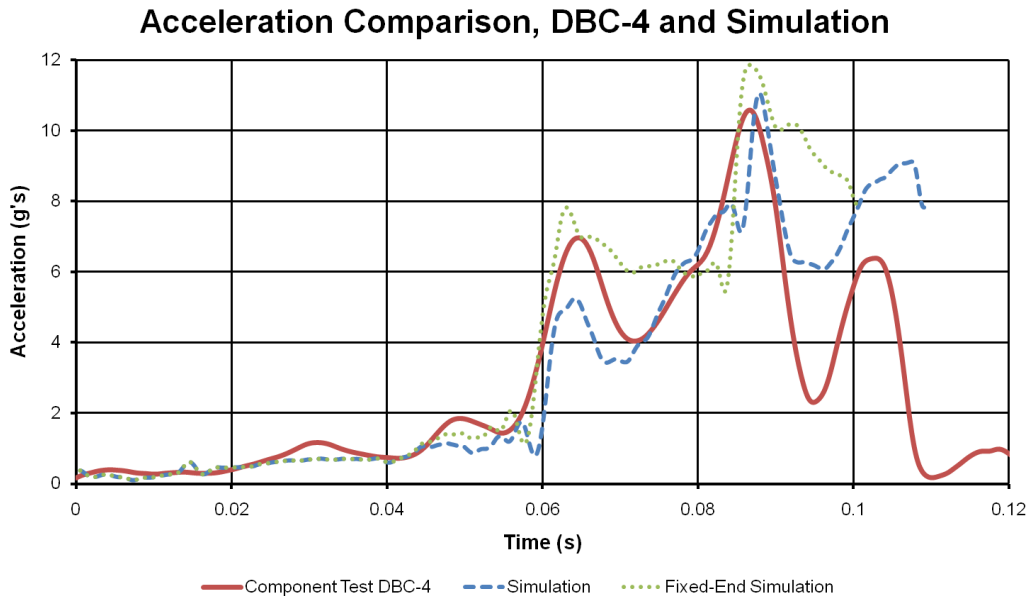


Figure 188. Bogie Acceleration, Test and Simulations, Test No. DBC-4

13.6 Modeling Test No. DBC-6

The final dynamic bending test to be modeled was test no. DBC-6. The distance between the fixed-rotating end supports was increased to 339 in. (8,611 mm), and the wire rope length was increased as well. Based on high-speed video, accelerometer, and load cell analysis, the slack length in the wire rope was determined to be approximately 2.05 in. (52.1 mm), which was consistent with measurements taken before the test. Sequential photographs of the test and simulation are shown in Figure 189.

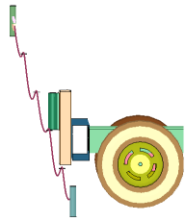
The simulation did not match the physical test very well. The bogie deflection was similar until approximately 120 ms but diverged thereafter. Furthermore, the wire rope was jerked free from the socket at 212 ms, corresponding to the transmission of a large-amplitude bending wave. The bogie was redirected by the wire rope in the simulation, and rebounded after 320 ms. An investigation was conducted to determine why test results and simulations varied in wire rope response.

A comparison of measured and simulated wire rope tension is shown in Figure 190. The test and simulated curves vary significantly over the first 100 ms. The tension recorded in the test was nearly zero, indicating that the tensile load transfer from the bogie impact with the wire rope was not transmitted to the end fitters for a long amount of time. By contrast, the simulation had a very rapid transfer of load across the wire rope to the end supports. The tensile reaction in the simulation, using the indicated slack length, reduced the bogie speed more quickly than in the test, and when the slack was taken up by bogie displacement, the bogie did not load the wire rope quickly enough as occurred in the test.

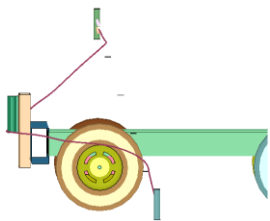
The difference in tensile response was troubling since the wire rope model had performed very well in the dynamic tensile and other dynamic bending tests. However, several differences were noted between test conditions in test no. DBC-6 and test nos. DBC-1 through DBC-4. First, the tension in the wire rope was not independent of the deflected configuration of the wire rope in test no. DBC-6. As the bogie impacted the wire rope, a bending wave was created and transmitted from the bogie position to the load frame at each end of the test setup. The load frame recorded no change in load until 106 ms, despite the obvious stretching of the wire rope after bogie impact. This corresponded to the first bending wave reaching the load frame. At 150 ms, two more waves cascaded on the load frame; one wave was related to tension, which was high but unknown in the area of the bogie. The other bending wave was a stiffness bending wave. The combination of these waves caused the tension in the rotating end assembly to rise rapidly, and rotate quickly toward the bogie.



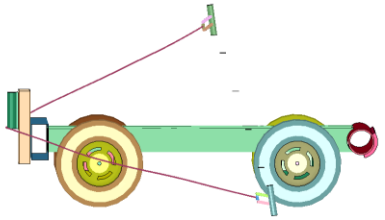
0.000 sec



0.100 sec



0.200 sec



0.300 sec

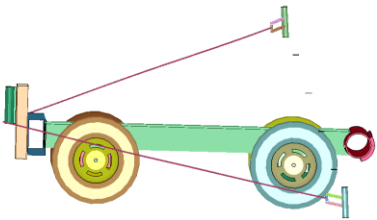


Figure 189. Sequential Photographs, Test and Simulation, Test No. DBC-6

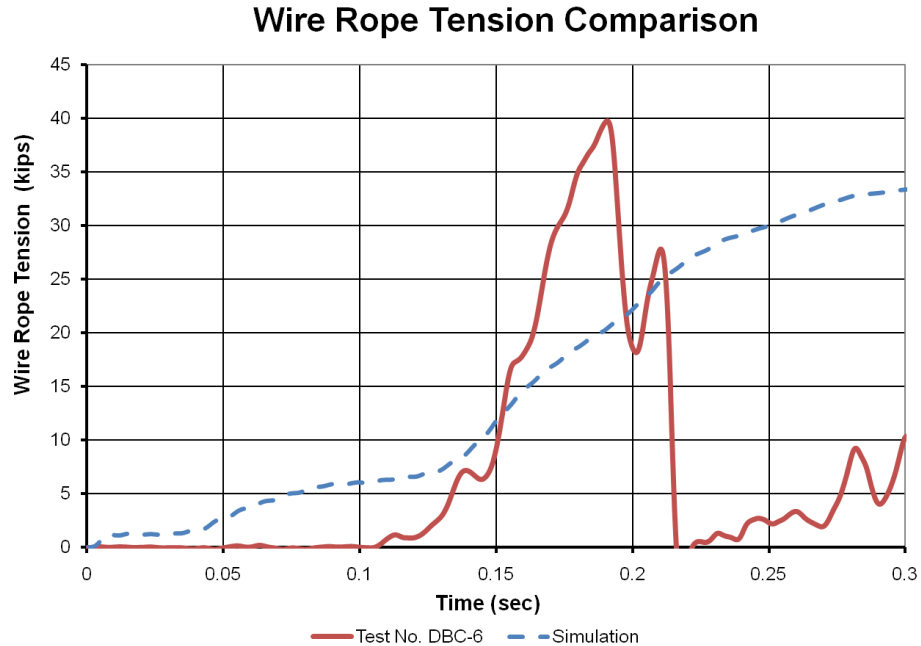


Figure 190. Wire Rope Tension, Test and Simulation, Test No. DBC-6

However, in the simulation the tension rose only 4 ms after impact, corresponding to the reception of a longitudinal tension wave within the beam elements. As the slack was taken up by the bogie vehicle, the tension gradually increased until 0.145 sec, when the slack was completely taken up. Following this time, the wire rope was loaded up to the maximum tension of 33.8 kip (150.3 kN) before the bogie was redirected.

Upon further investigation of the test results, it was noted that the tension was transmitted from the bogie to the load frame through the transmission of the bending wave. This was initially surprising, but it was noted that the increase in tension due to the take-up of slack in the wire rope tended to "drive" the bending wave instead of transmit through the wave. Increasing tension along a deflected length of wire rope causes a larger amplitude of bending wave to be transmitted, as shown in Figure 191. The unbalanced y-direction force is responsible for driving the wave down the wire rope.

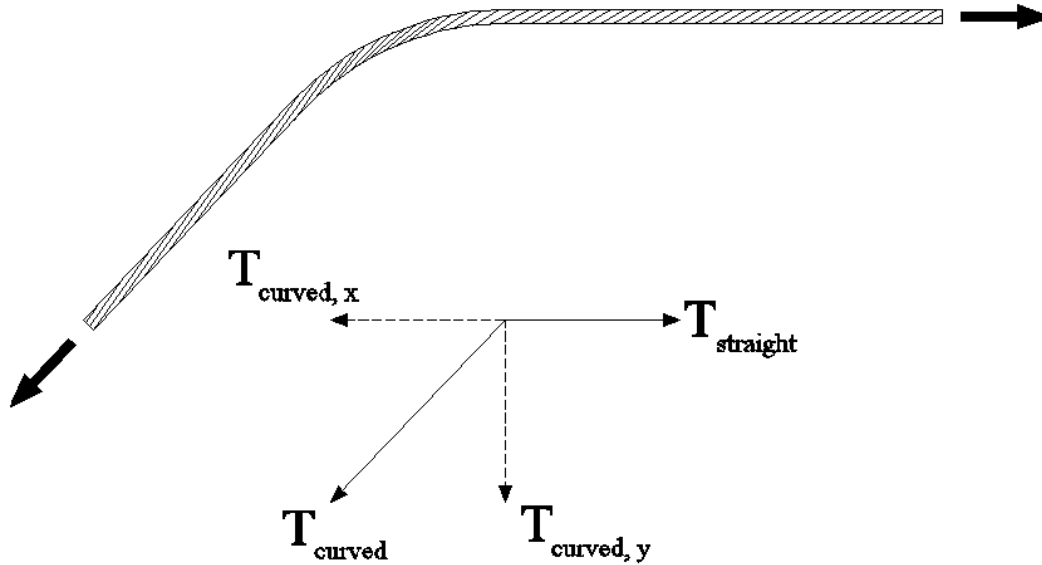


Figure 191. Wire Rope Bend and Tension Transmission

The longitudinal wave speed in small-diameter bar steel is approximately 16,570 ft/s (5,050 m/s), and in plane strain conditions the speed increases to 20,000 ft/s (6,100 m/s). However, the bending wave speed noted in the wire rope was 1,040 ft/s (317 m/s). Since the bogie impacted the center of the 89-ft 6-in. (27,280-mm) wire rope, two 45-ft 2.5-in. (13,627-mm) sections propagated the bending wave. The time required for a bending wave to reach the load frame is thus 43.5 ms from the time that the wire rope becomes taut. Not surprisingly, the time in which the high-speed video and accelerometer analysis indicated that the slack had been taken up was 80.3 ms. Simple addition between the bending wave transmission time and the slack take-up time gives 117.5 ms, which is very close to the time in which the tension began to rapidly increase, as shown in Figure 190. This substantiates the analysis conducted on the propagation of wire rope tension driving the bending wave; however, this finding also indicates that the slack in the wire rope had unintended consequences.

The bogie displacement was compared between test and simulation, as shown in Figure 192. Both tested and simulated displacements were nearly identical through 180 ms, but diverged

due to the difference in total wire rope tension. This was expected based on the results of the tension comparison.

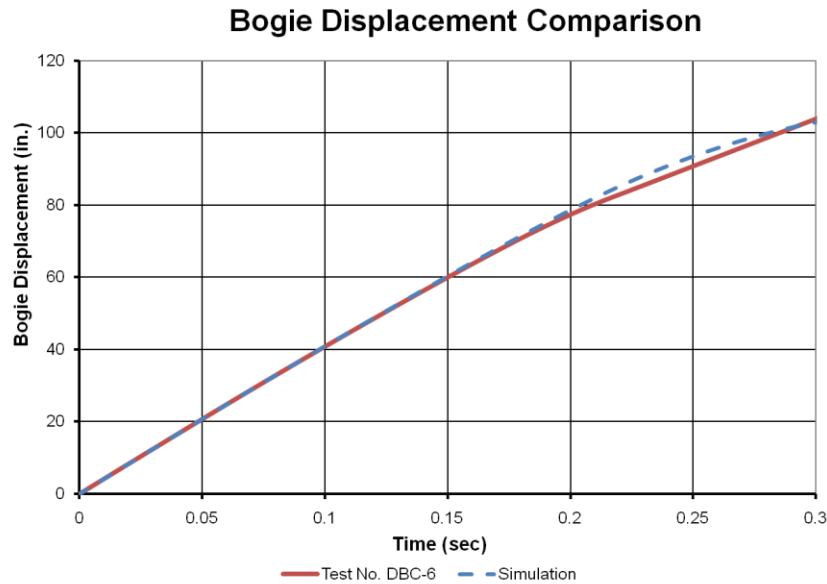


Figure 192. Bogie Displacement Comparison, Test and Simulation, Test No. DBC-6

Bogie velocities were also plotted and are shown in Figure 193. The bogie velocities were very similar between test and simulation through 130 ms, but it should be noted that though the load frame experienced no resulting load prior to 106 ms, the bogie velocity from the test decreased almost identically with the simulation velocity change. This indicates that the tension in the wire rope adjacent to and in contact with the bogie was likely much higher than the tension recorded at the load cell and load frame.

The acceleration calculated from the bogie acceleration data in the simulation was compared with the recorded acceleration in the test, and is shown in Figure 194. The simulated bogie acceleration was very similar to the actual bogie acceleration through 170 ms. After this time, the bogie acceleration jumped rapidly, corresponding to the sudden tightening of the wire rope as the bending wave reached the end support. The very rapid increase in bogie tension is a result of the viscoelastic stretching of the wire rope. Since the wire rope was under tension

between the outward-propagating bending waves, once the waves reached the end supports the tension became nearly uniform throughout the wire rope. However, the sudden transition to high tension and the relatively high bogie speed of 30 ft/s (9.1 m/s) rapidly increased the strain and thus activated the high-strain-rate viscoelastic resistance of the wire rope. This effect cannot be simulated using the current wire rope model.

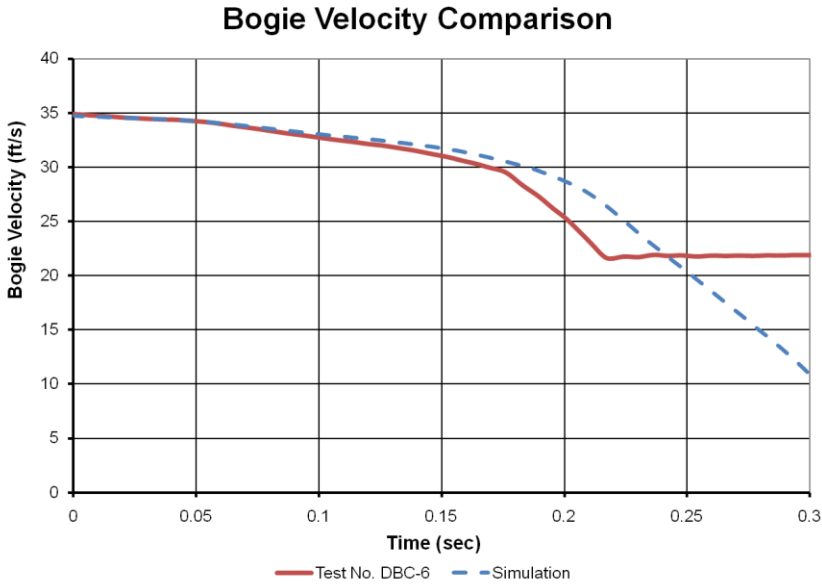


Figure 193. Bogie Velocity Comparison, Test and Simulation, Test No. DBC-6

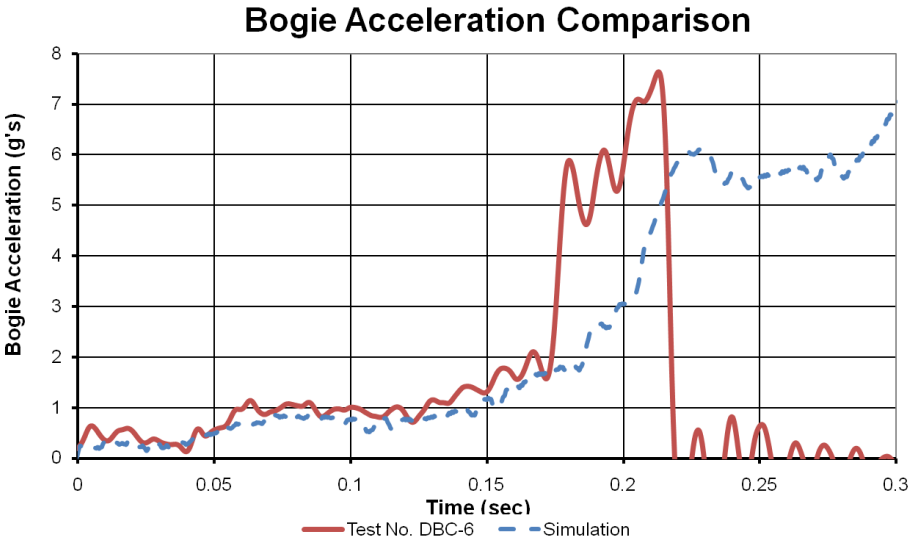


Figure 194. Bogie Acceleration, Test and Simulation, Test No. DBC-6

13.7 Discussion

The bending test simulations were very complex with many variables, initial conditions, and parameters to check. The wire rope reaction to loads required vigilant attention to detail in order to physically model the most important phenomena occurring in the test. Even still, correlation between wire rope response and the test results was not perfect.

One of the biggest obstacles to overcome in simulating wire rope bending behavior was the end conditions. Though the end conditions did act as solid, rigid pieces during the test, some compliance was present between the rotating load pipe and the holes drilled in the load frame. Furthermore, very slight misalignment of the load frame in test no. DBC-4 added to the resistance of the rotating end pipe, which led to differences in rotator pipe positions in the test and simulations.

Another source of difficulty in the wire rope tests was the viscoelastic strain rate dependence of the wire rope tensile load curve. Though the elastic load curves of all of the tests were similar, the plastic tensile loads of the high-speed test nos. DBC-4 and DBC-6 activated the strain rate dependence witnessed in the wire rope axial load curves recorded by the tensile load cells. These effects cannot currently be accurately modeled with *MAT_166 for any arbitrary load and configuration dependence. However, it should be noted that the wire rope loads rarely exceed 25 kips (111 kN) during physical full-scale testing, and these results are consistent with motion of end supports and soil displacement for installations constructed near roadways. Because the loads are low with respect to the breaking load of ¾-in. (19-mm) diameter 3x7 wire rope, and the load is ramped up over long durations of time in full-scale impacts, viscoelastic dependency of wire ropes is minimized and the wire ropes remain elastic. Further, the long wire

ropes used in cable guardrail installations allow for a relatively low effective strain rate. Therefore, no attempt was made to model this occurrence in the bending tests.

In test no. DBC-6, the bending waves effectively acted as moving tension boundary conditions, which locally constrained the length of wire rope under dynamically-varying tension. However, when the bending wave reached the end supports, the loaded wire rope was already at a very high tension between the bends. The sudden nearly-fixed end condition on the wire rope, restricting further bend motion, induced a reflected bending wave which transmitted very rapidly under the high tension. The lack of initial pretension may have aggravated the constrained-tension bending wave effect.

Though the difference in simulated and tested wire rope tension and wave properties were noted and considered important, this phenomenon will not affect pretensioned wire rope guardrail systems. Dynamically, the unbalanced shear force on the wire rope causes moment bending and curvature in the wire rope. Larger unbalanced tensile moments cause greater curvatures; in effect, the perpendicular tension to the straight length of wire rope remains nearly constant as a large-curvature bending moment is propagated. This multiplication occurs since changes in tension upstream of the bend result in changes in the propagating curvature of the bend. In cable barrier systems, however, shear forces are sustained by the posts and wire rope attachments to the posts, so the forces are unbalanced only over a small length, leading to an analysis of wire rope which appears much more like an incrementally-varying statics problem. This leads to relatively small bending waves being transmitted along the wire rope, and this allows the tension to increase nearly independently of the bending wave transmission. Further research is necessary to determine the effect of pretension and post spacing on constraining tensile waves, and whether or not the new wire rope model is capable of predicting the response

of tensioned wire rope to large-amplitude bending motions such as may be found in systems with large post spacings.

It should be noted that a value of cfa was set to 0.97 for simulations of test nos. DBC-4 and 6 for test results. This value violates normal conventions that the dynamic stiffening coefficient should be greater than 1.0, corresponding to a dynamic hardening of the material. However, the dynamic softening implied using a cfa of 0.97 has physical correlation with actual wire rope dynamic response. Stresses in wire rope are non-linear across the cross-section, and vary based on the wire and the position within a wire. In dynamic tension, the stresses are not able to redistribute as quickly between the wires leading to greater plastic deformation in some of the wires than occurs in quasi-static tension. This can be manifested in a slightly lower stiffness during dynamic plastic loading. However, the differences in simulation results using a value of 1.0 in lieu of a value of 0.97 for the cfa parameter are generally very small.

During simulation validation against full-scale crash testing results, it became apparent that the contact surface of the wire rope was too small, as already discussed. As a result, the cross-sectional properties of the modeled wire rope were adjusted. Investigation into differences using the new cross-sectional defined geometry indicated that, with exception of contact distance, the simulation results were otherwise very similar when contact surface was not a critical performance factor. The contact surface was not critical in any of the dynamic bending or tension tests; therefore the results are not expected to differ sufficiently to cause acceptable results to become unacceptable.

Furthermore, updating the material model during full-scale testing had little effect on model reaction, with exception of updating the contact surface. In order to maintain the same mass density, the density was scaled down by the same factor that the cross-sectional area was

scaled up. The modulus of elasticity term E in the material parameter—which is not the actual loading/unloading modulus of elasticity but instead affects only timestep—was then scaled by the same factor as the density to ensure that the timestep of the wire rope remained identically the same. Therefore, updates to the model were critical only to the performance of the wire rope in regards to hook bolt and post interaction and did not have a significant effect on dynamic bending or dynamic tensile tests.

13.8 Summary

Wire rope bending component tests were simulated using a full bogie vehicle and a rigid impact head. Test results for low-speed test nos. DBC-1 and DBC-2 were very similar to the tested wire rope load and bogie displacement, velocity, and acceleration. Wire rope load results in test no. DBC-4 was also very similar, though viscoelastic response at high strain rates was evident. The simulation of test no. DBC-6 was less accurate, caused by the culmination of bending waves which bounded and constrained tension, causing large force spikes near the load frames. This effect was isolated and was not witnessed in low-speed test no. DBC-5 nor in many applications of full-scale testing. Comparisons of the new wire rope model with previous wire rope models indicated a substantially better reaction of the new wire rope model than other models. Thus, the new wire rope model is a beneficial advancement in wire rope modeling of cable guardrail systems.

13.9 Future Work

Though the effects of the high strain rate and tension-bounded bending waves was difficult to model using the new wire rope model, these effects may be important for more intrinsically-difficult wire rope modeling situations in the future.

Incorporation of viscous effects in *MAT_166 may be necessary to create a robust, accurate, universally applicable model of wire rope. Using viscoelastic time-marching algorithms, the frictional effect within wire rope may be modeled without the use of computationally-expensive and occasionally less stable solid elements for wire rope cross-sections. Further experimentation with the viscoelastic material properties of wire rope may be necessary.

Further testing to evaluate the tension-bound bending wave phenomena is highly recommended, but is not required for further model development yet. Though the conjecture of tension-binding related to the unbalanced forces in wire rope was substantiated by physical test data, this claim is not analytically derived in literature. The bending and tensile reactions of a complicated specimen such as wire rope are inherently difficult to analytically derive. Further research related to the binding of tension within bending waves is necessary to understand or debunk this apparent phenomena.

14 FULL-SCALE TEST SIMULATION

14.1 Motivation

Though the new wire rope model was successful in replicating the dynamic impact behavior of wire rope, full-scale impact modeling of the new wire rope model had not yet been created. One full-scale test model was proposed to evaluate the wire rope model, which consisted of a cable barrier installed adjacent to a steep slope. A model of a cable barrier located 1 ft - 6 in. (457 mm) from the center of the posts to the slope break point of a 1.5H:1V slope was created, consistent with full-scale test no. CS-1 [44]. Good correlation of the wire rope model with the full-scale test would indicate good performance of the new wire rope model.

14.2 Test Description

14.2.1 System Description

A cable barrier system was constructed 12 in. (305 mm) in front of the break point of a 1.5H:1V slope. System details are shown in Figures 195 through 199. Test photos are shown in Figures 200 and 201. The cable barrier system was composed of four important components: posts, wire ropes, hook bolts, and soil conditions. Additional test information may be obtained from the test report in reference no. [44].

A 1.5H:1V slope was constructed 13½ in. (343 mm) back from the center of the post, as intended. The slope was cut using a grader to obtain a representative and controlled slope surface for testing. The soil was a compacted coarse fill aggregate.

The cable barrier system consisted of S3x5.7 (S76x8.5) steel posts embedded 30 in. (762 mm) below ground. A total of 34 posts were used in the system, which included two anchor posts and two slip-base "cable router" posts. The posts supported three ¾-in. (19-mm) diameter wire ropes with an approximate pretension force of 950 lb (4.2 kN). Wire rope

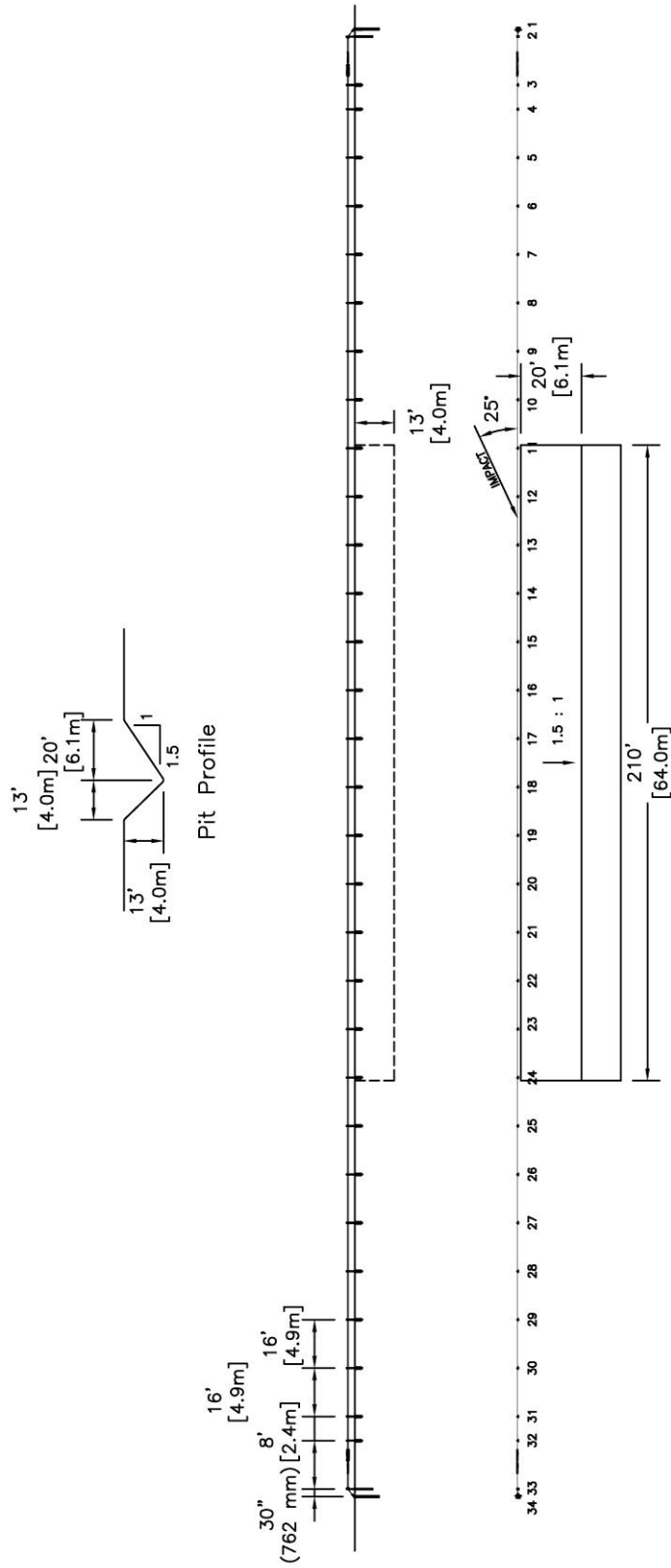


Figure 195. Cable Guardrail System Details, Test No. CS-1 [44]

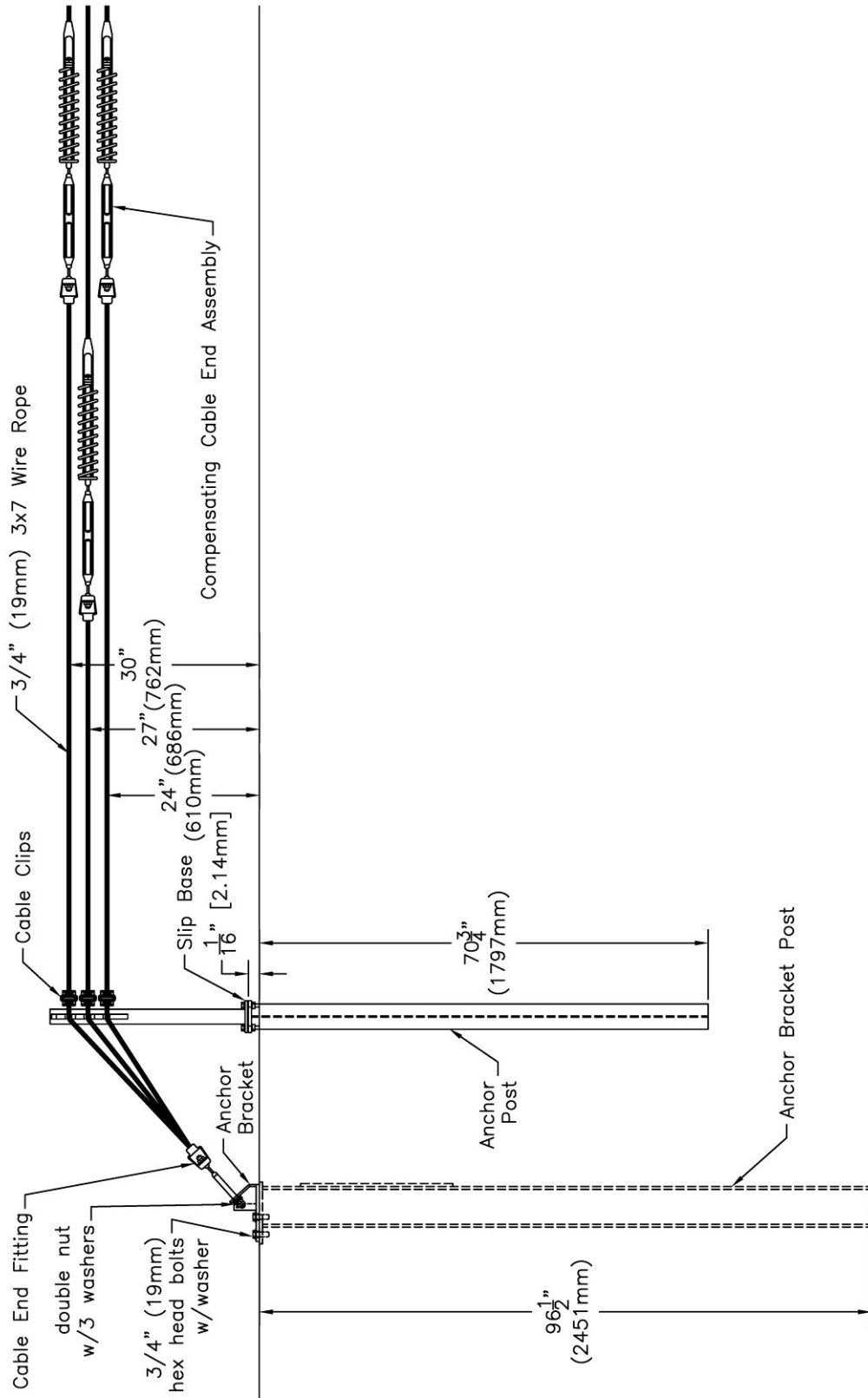


Figure 196. End Post and Compensator Assembly Details, Test No. CS-1 [44]

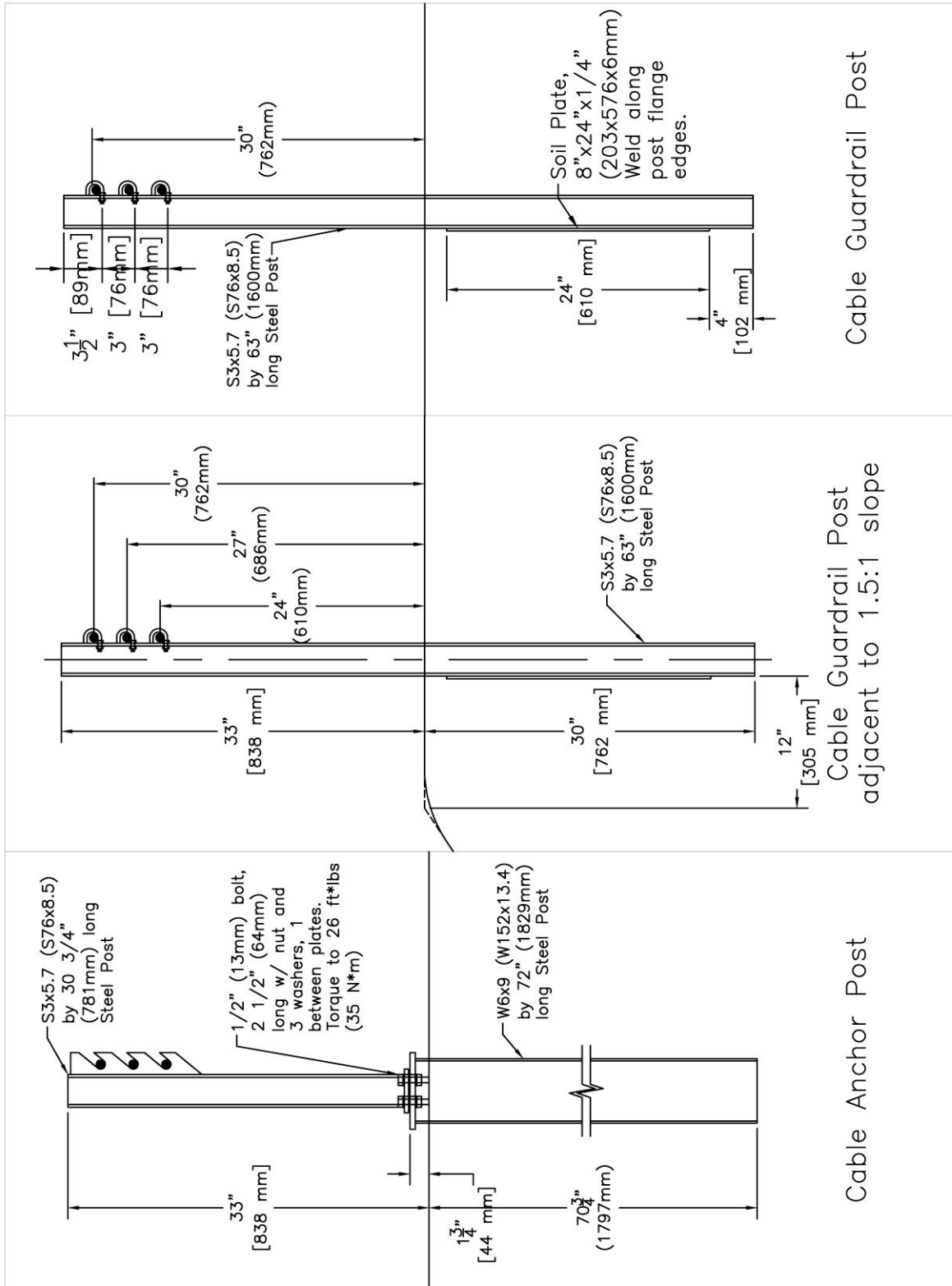


Figure 197. Anchor Post Details, Test No. CS-1 [44]

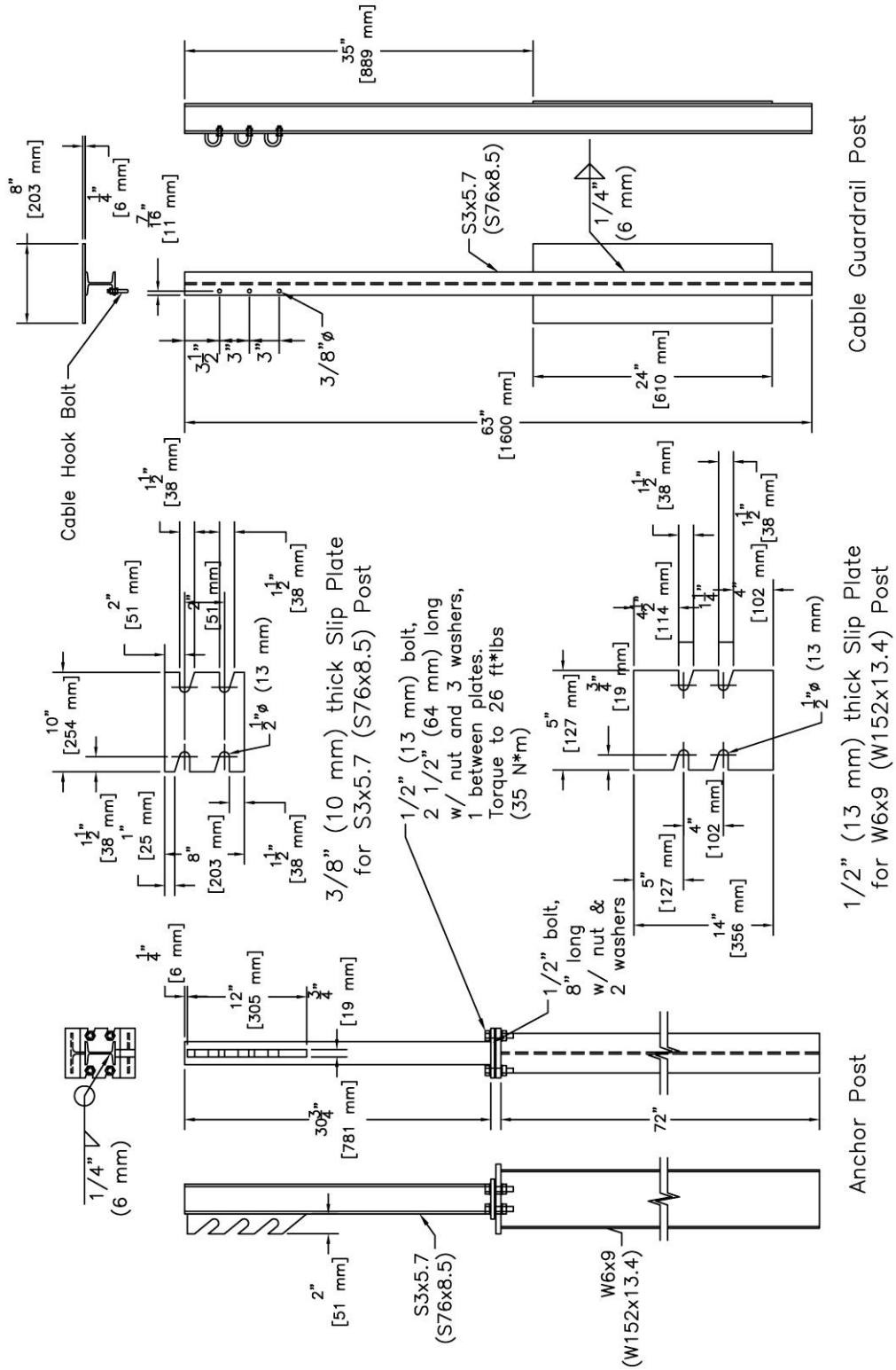
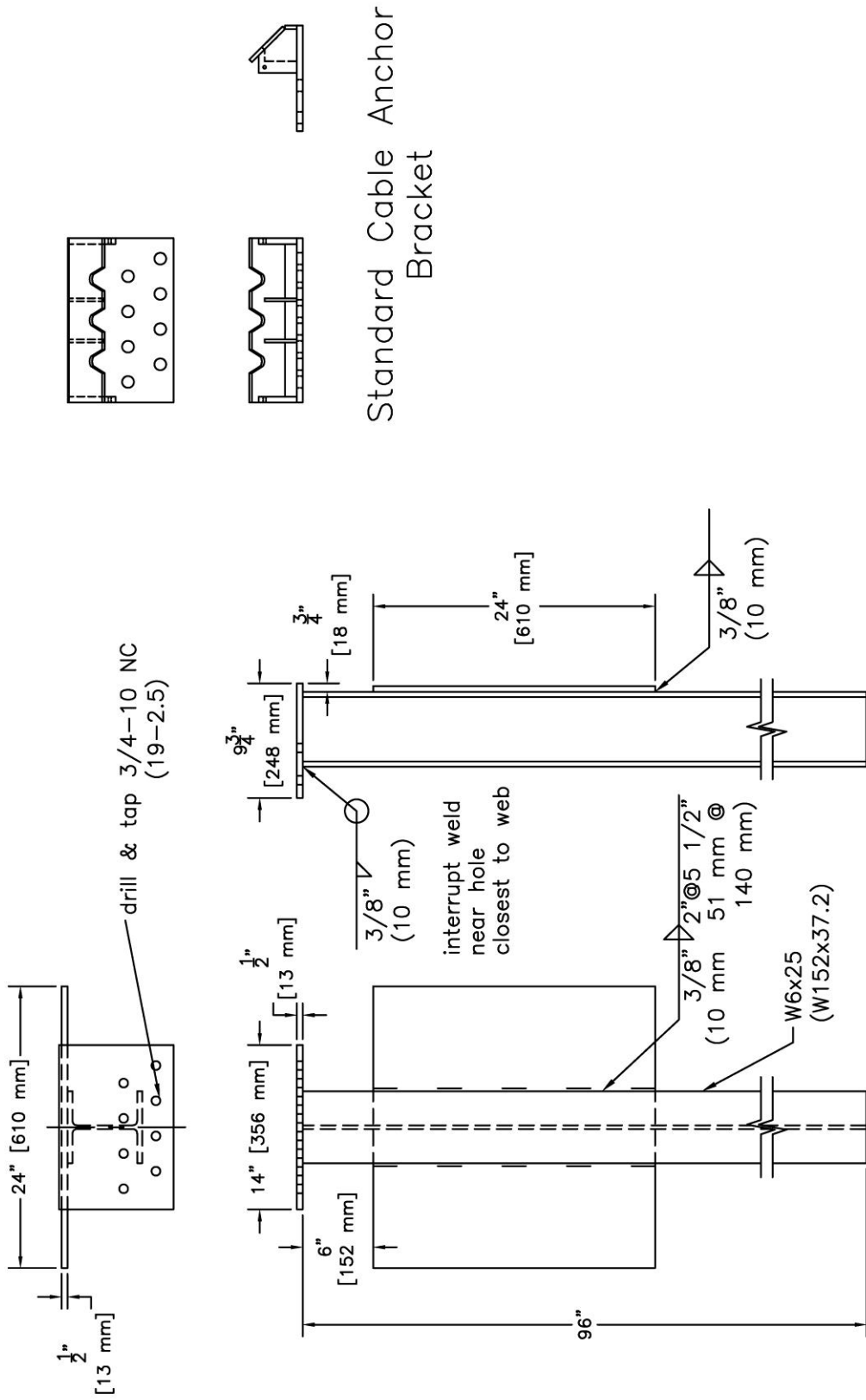


Figure 198. Line Post Details, Test No. CS-1 [44]



Standard Cable Anchor Bracket

Anchor Bracket Post

Figure 199. Slip Base Post Details, Test No. CS-1 [44]



Figure 200. System Details and Impact Location, Test No. CS-1



Figure 201. Line Posts and Cable Compensator, Test No. CS-1

mounting heights were 30, 27, and 24 in. (762, 686, and 610 mm). The wire ropes were mounted on the posts using $\frac{5}{16}$ -in. (8-mm) diameter hook bolts.

A compensator assembly was used at the upstream end of the wire rope barrier system to maintain tension in varying temperature and to be consistent with real-world low-tension barrier applications. The cable compensators were secured to the wire ropes using wedge sockets and threaded rods, and were located 16 ft (4.88 m) downstream of the upstream anchor.

14.2.2 Instrumentation

The wire rope was instrumented with two kinds of transducers: load cells and string pots. The load cells were Transducer Techniques TLL-50K load cells with a load range up to 222.4 kN (50,000 lbs). During the test, output voltage signals from the string potentiometers were sent to a Keithly Metrabyte DAS-1802HC data acquisition board, acquired with “Test Point,” and stored permanently on the computer. The sample rate of the load cells was 10,000 samples per second (10,000 Hz).

A string potentiometer (linear variable displacement transducer) was installed on the end terminal anchor to monitor longitudinal displacement of the anchor. The string potentiometer used was a UniMeasure PA-50 string potentiometer with a range of 1.27 m (50 in.). A Measurements Group Vishay Model 2310 signal conditioning amplifier was used to condition and amplify the low-level signals to high-level outputs for multichannel, simultaneous dynamic recording on “Test Point” software. After each signal was amplified, it was sent to a Keithly Metrabyte DAS-1802HC data acquisition board, and then stored permanently on the computer. The sample rate of the string potentiometers was 10,000 samples per second (10,000 Hz).

The vehicle was equipped with two accelerometers. The environmental shock and vibration sensor/recorder systems, Models EDR-3 and EDR-4, were developed by Instrumental

Sensor Technology (IST) of Okemos, Michigan. Test data for the EDR-3 and EDR-4 data recorders was captured at 3,200 Hz and 10,000 Hz, respectively. Both EDR units were equipped with an on-board low-pass filter. The EDR-3 data recorder was placed on the vehicle as a backup, in the event that the primary data recorder EDR-4 failed.

14.3 Test Results

The 4,484-lb (2,034-kg) pickup truck impacted the three-cable guardrail system at a speed of 61.0 mph (98.1 km/h) and at an angle of 26.2 degrees. Sequential photographs of the test are shown in Figures 202 through 204. Post-testing photographs are shown in Figures 205 and 206.

The first post downstream of impact deflected downstream at 0.056 sec. The second post downstream of impact deflected at 0.084 sec. The wire ropes released from the hook bolts on the first post downstream of impact and the left-front tire projected over the slope at 0.110 sec. At 0.176 sec the right-front wheel of the pickup reached the slope break point. At 0.172 sec, the wire ropes slid up the bumper of the vehicle and engaged the left-front quarter panel and headlight casing. At 0.180 sec, the third post downstream of impact began to rotate backward in the soil. At 0.200 sec, the wire ropes disengaged from the second post downstream of impact, the left-rear tire rode over the slope break point, and the pickup began to visibly redirect. The second post downstream of impact rotated backward and out of the soil at 0.232 sec, and made secondary contact with the pickup at 0.300 sec. The fourth post downstream of impact deflected at 0.256 sec. At 0.362 sec the bottom cable disengaged from the quarter panel and headlight casing and began to slide down the bumper, and the wire ropes disengaged from the third post downstream of impact. The wire ropes disengaged from the third post downstream of impact at 0.376 sec. At 0.452 sec, the bottom wire rope had slid completely under the bumper

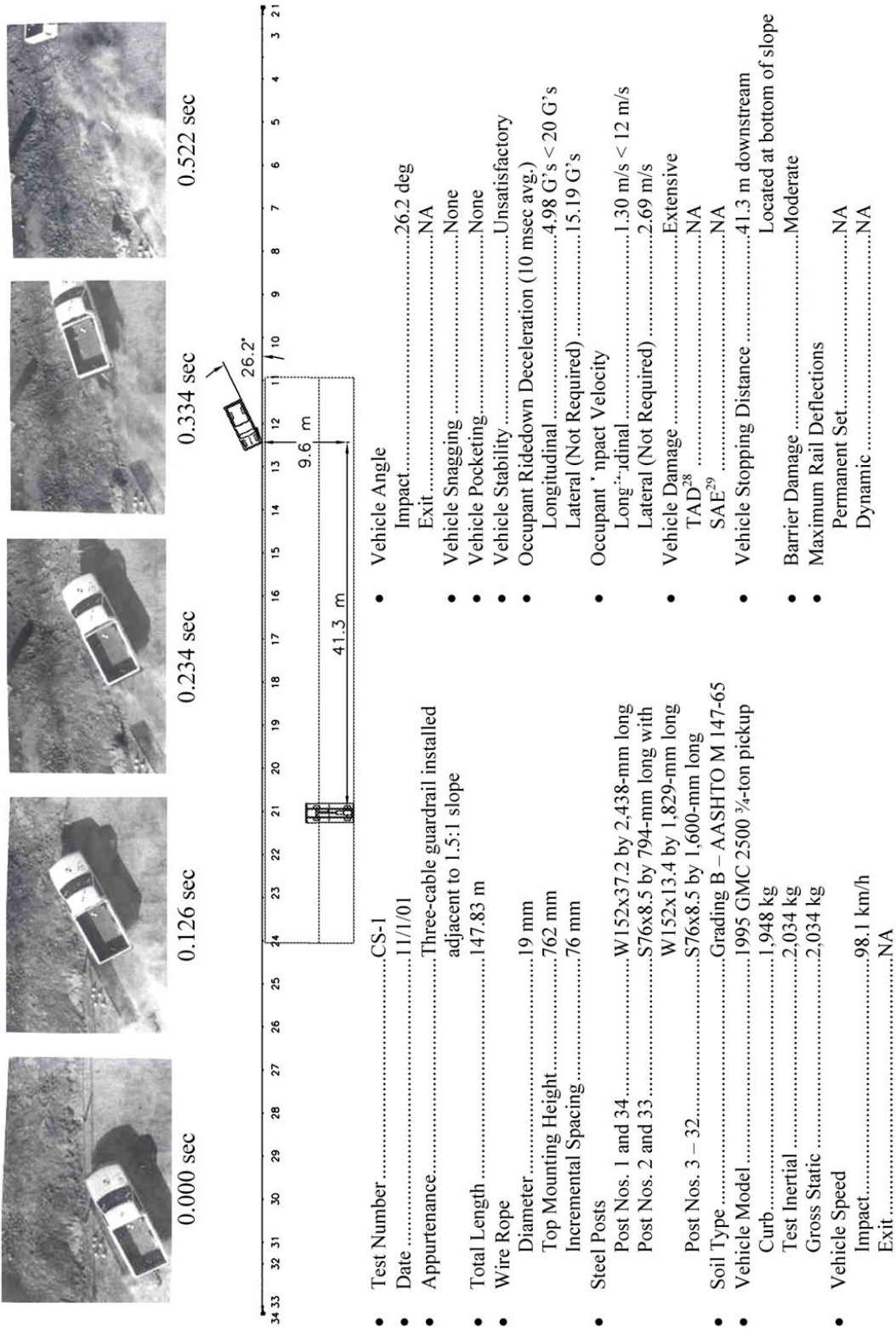


Figure 202. Test Summary and Sequential Photographs, Test No. CS-1 [44]



0.000 sec



0.122 sec



0.218 sec



0.334 sec



0.418 sec



0.458 sec



0.532 sec



0.650 sec

Figure 203. Sequential Photographs, Test No. CS-1



0.000 sec



0.300 sec



0.467 sec



0.734 sec



0.934 sec



1.335 sec

Figure 204. Sequential Photographs, Test No. CS-1



Figure 205. Vehicle Damage, Test No. CS-1



Figure 206. System Damage, Test No. CS-1

and made contact with the vehicle's left-front tire. At 0.478 sec, the left-rear tire overran the three cables as the pickup yawed and pitched forward. The left-front tire of the vehicle made contact with the slope at 0.614 sec, causing the pickup to rebound and roll over as it traveled down the embankment. The top wire rope released from the fourth post downstream of impact at 0.610 sec, and the bottom two cables released at 0.750 sec. The vehicle came to rest at the bottom of the ditch.

14.4 New Wire Rope Model

A model of CS-1 was created to analyze the new wire rope model in a full-scale crash test simulation. The model consisted of: (1) an impacting pickup truck, (2) cable barrier posts, (3) a wire rope model, and (4) a soil model. The model used to simulate test no. CS-1 is shown in Figure 207.

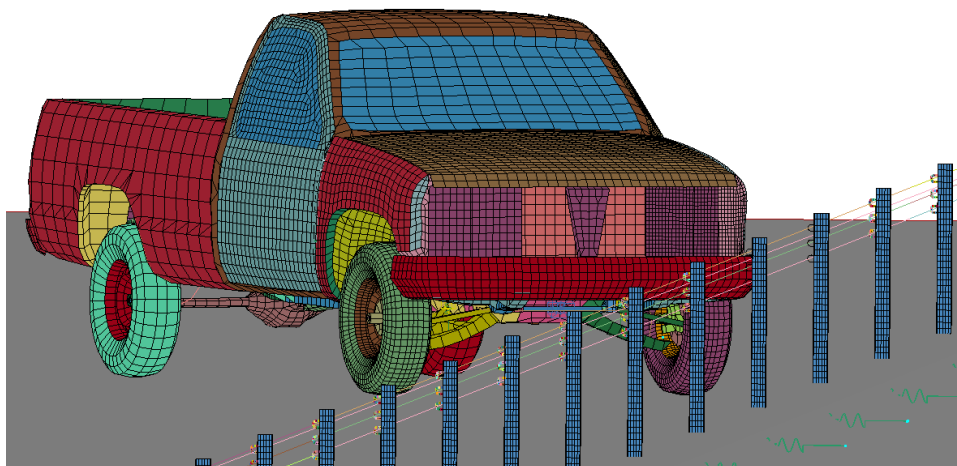


Figure 207. Modeled System, Test No. CS-1

The pickup model used in the simulation was a C2500 model, which was a common full-scale crash-testing vehicle prior to 2007, and is still used in some crash tests currently. The C2500 model is comprised mostly of shell elements. When contact with a line-based element (beam elements) occurs, snagging may result from the capture of the beam elements along the

free edge of a shell element part. To reduce the snagging which was observed in early models, wheel well cover pieces were added to the wheel well, and were excluded from contact definitions with the remainder of the truck. Only the cable was slave to the wheel well cover contact. This allowed the wire rope to wrap around the front and rear edges of the front fender without snagging. The modeled C2500 vehicle is shown in Figure 208.

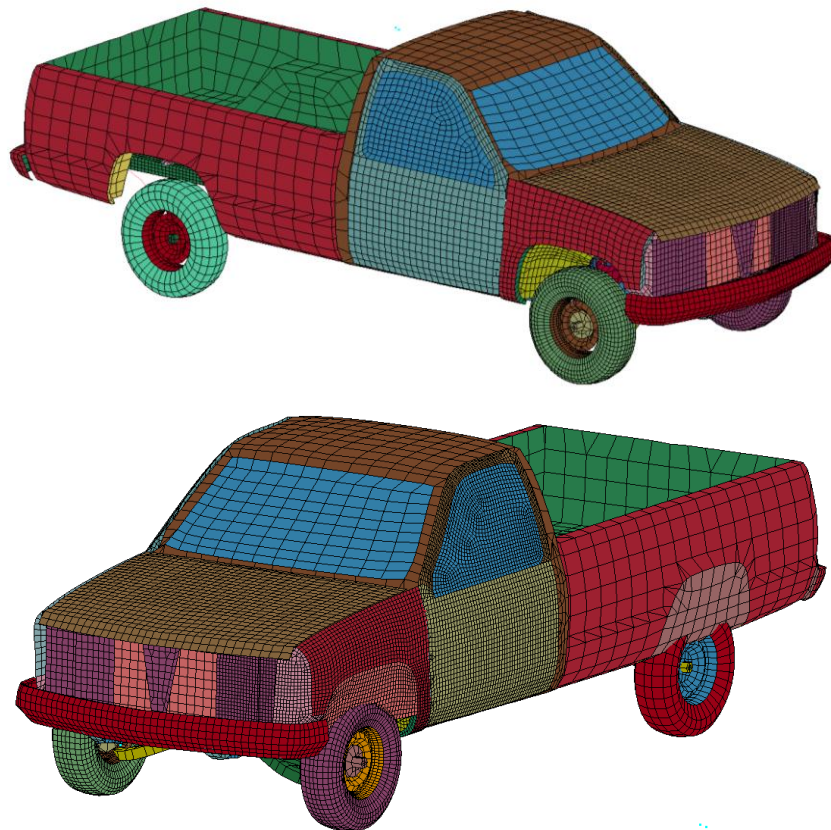


Figure 208. C2500 Pickup Model with Wheel Well Covers, Left Side

Post modeling required greater effort. The post models were a relatively coarse mesh which had been independently tested and was used in several cable barrier models. The post model was composed of shell elements with incremental widths approximately equal to 1-in. (25.4 mm) wide. The post model is shown in Figure 209. Though the post was defined with a plastic-kinematic material, the flange section at the hook bolt location was made rigid.

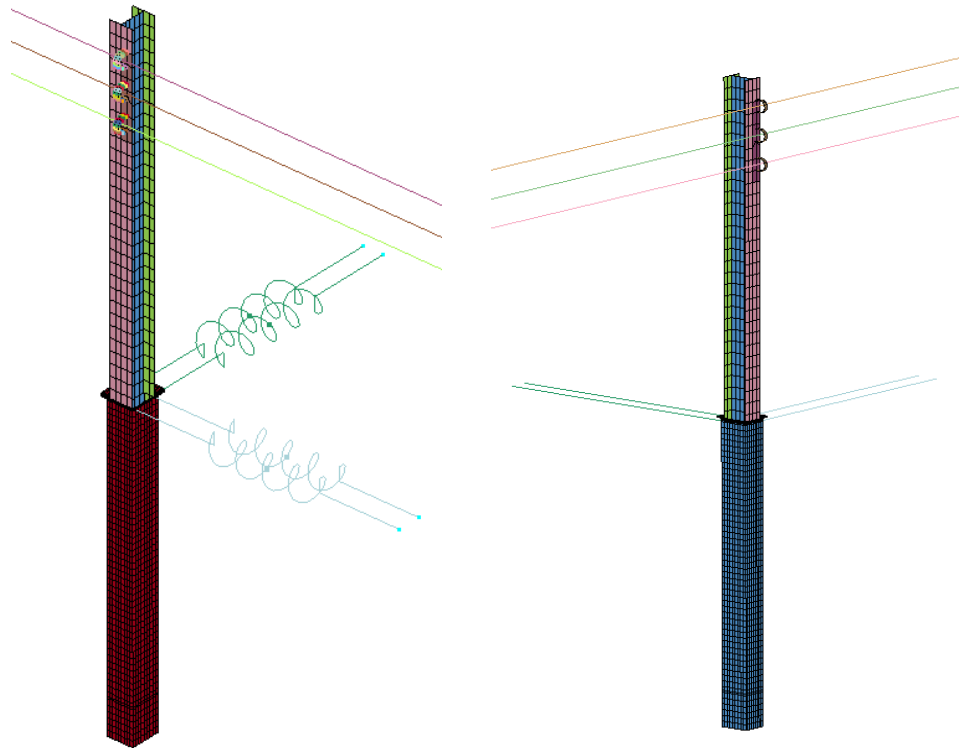


Figure 209. Post Model and Hook Bolts

The posts were modeled in rigid soil tubes to simulate the effects of soil and were constrained 2 in. (51 mm) below ground with two springs in the strong and weak axis directions. Strong and weak axis load curves were defined independently of unloading curves for maximum control of soil reaction forces. The same soil resistance curve was applied to the post in the weak- and strong-axis directions, since the S3x5.7 (S76x8.5) posts have nearly the same flange width in the weak- and strong-axis directions. However, since the posts are weaker in weak-axis bending than in strong-axis bending, very little weak axis rotation is sustained before the posts collapse via buckling.

Hook bolts were modeled using beam elements to simulate the $\frac{5}{16}$ -in. (8-mm) diameter J-bolts commonly used in cable guardrail systems, as shown in Figure 210. The end nodes of the hook bolts were coincident with nodes on the rigid flange piece to generate an effective rigid

boundary condition. Null shell elements were modeled coincident with the hook bolts to assist in contact definitions with the wire rope, and were constrained along the width of the elements.

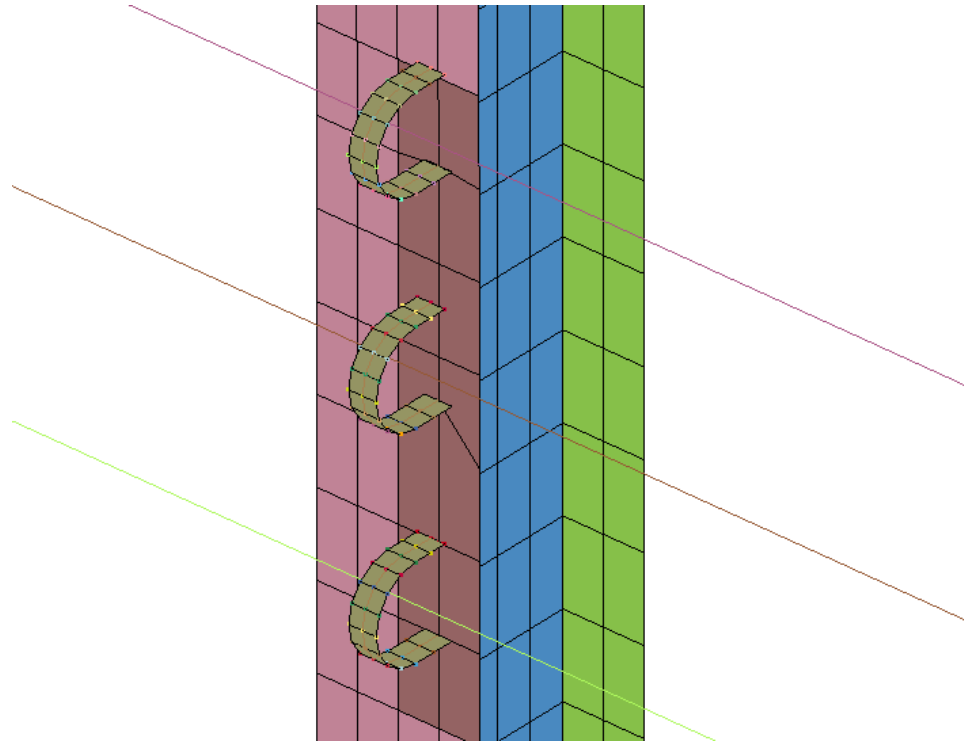


Figure 210. Hook Bolt Modeling

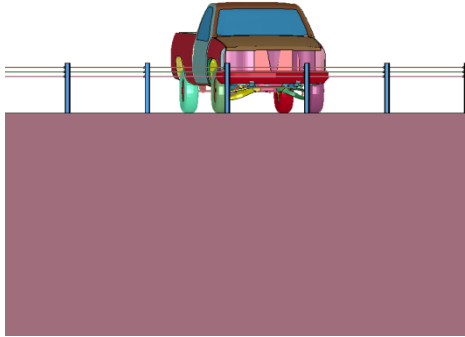
The wire rope in the simulation was matched to be the same length as the straight length of wire rope in the test. Eighteen of the posts which did not contribute to vehicle capture in the full-scale test (i.e., undeflected posts) were neglected in the model while the other sixteen posts—five upstream and eleven downstream of impact—were included.

14.5 Simulation Results

Test no. CS-1 was simulated in a full-scale impact using the Chevrolet C2500 model. Sequential photographs of the simulation, compared to the full-scale test, are shown in Figures 211 through 213.



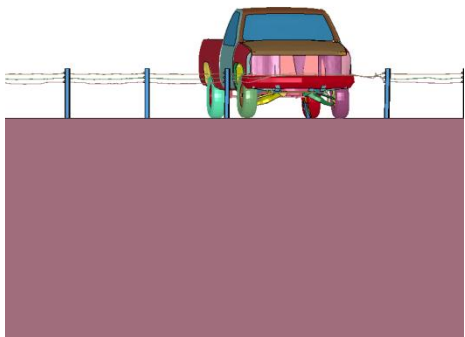
0.000 sec



0.000 sec



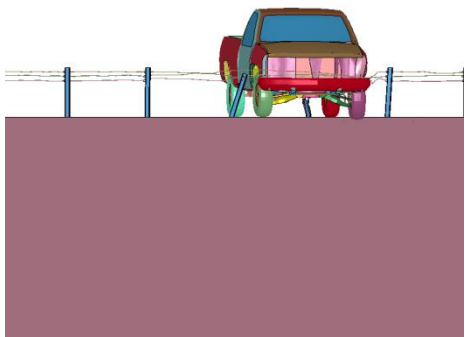
0.110 sec



0.110 sec



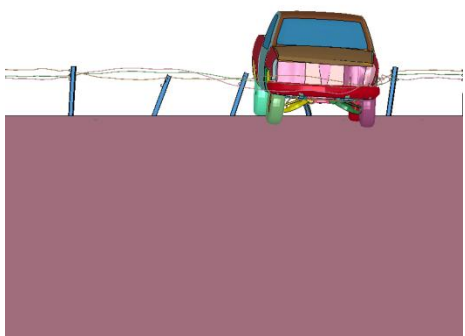
0.190 sec



0.190 sec



0.300 sec

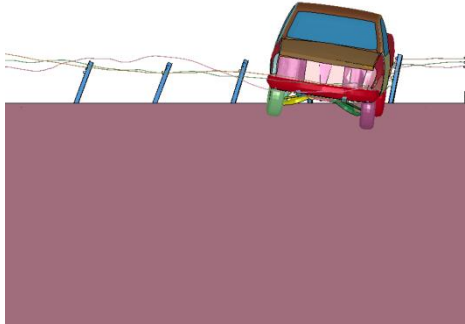


0.300 sec

Figure 211. Sequential Photographs, Test and Simulation, Test No. CS-1



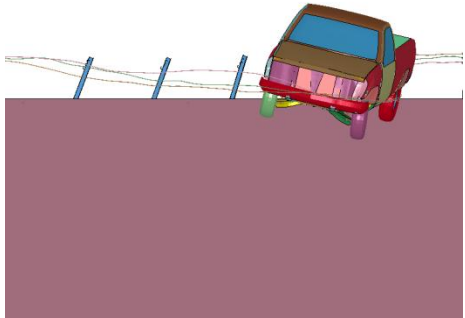
0.390 sec



0.390 sec



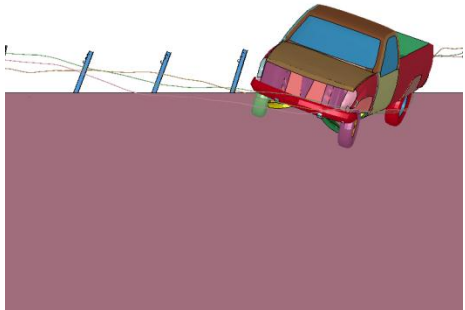
0.460 sec



0.460 sec



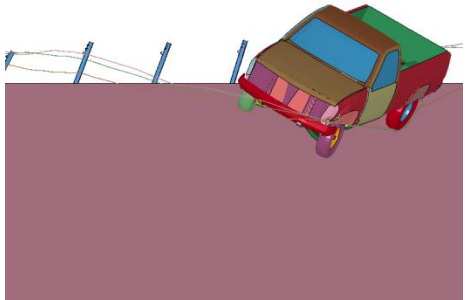
0.520 sec



0.520 sec



0.590 sec

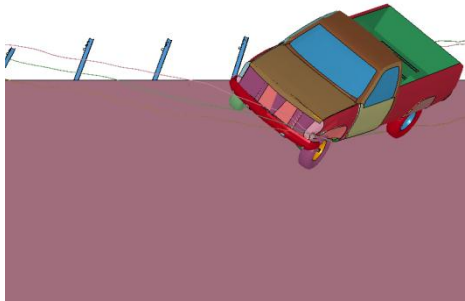


0.590 sec

Figure 211 (cont). Sequential Photographs, Test and Simulation, Test No. CS-1



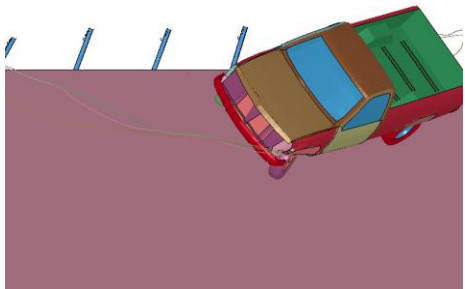
0.640 sec



0.640 sec



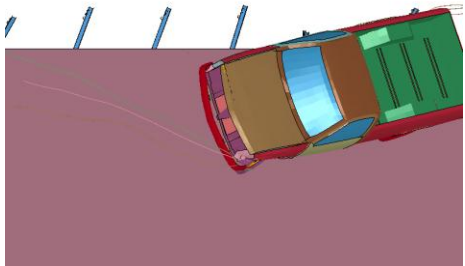
0.720 sec



0.720 sec



0.800 sec

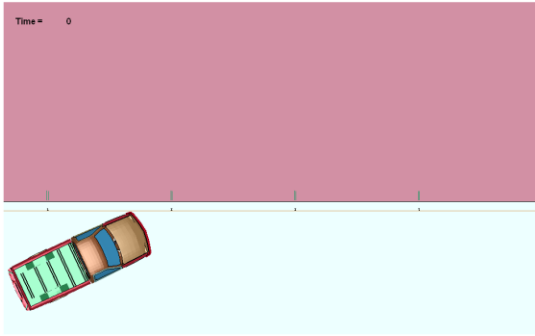


0.800 sec

Figure 211 (cont). Sequential Photographs, Test and Simulation, Test No. CS-1



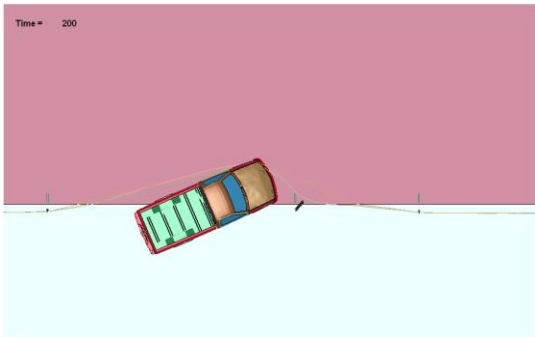
0.000 sec



0.000 sec



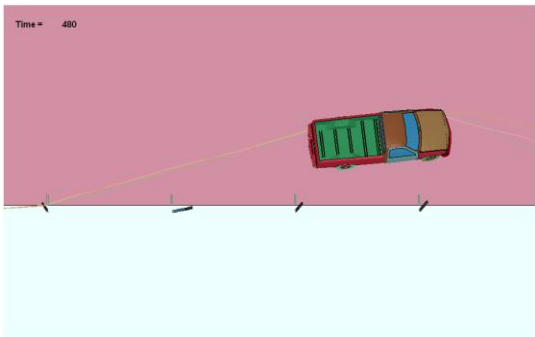
0.204 sec



0.204 sec



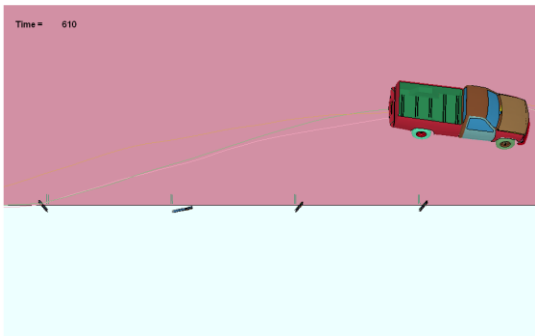
0.478 sec



0.480 sec



0.614 sec

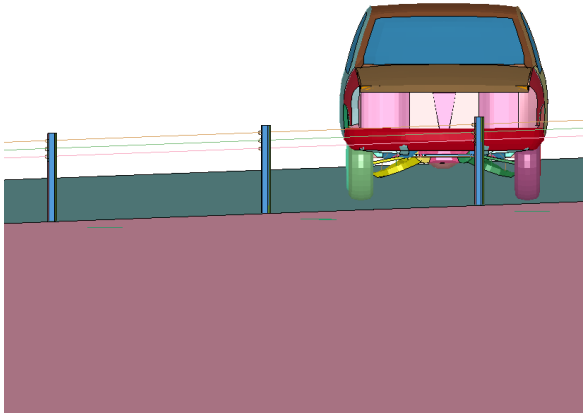


0.610 sec

Figure 212. Sequential Photographs, Test and Simulation, Test No. CS-1



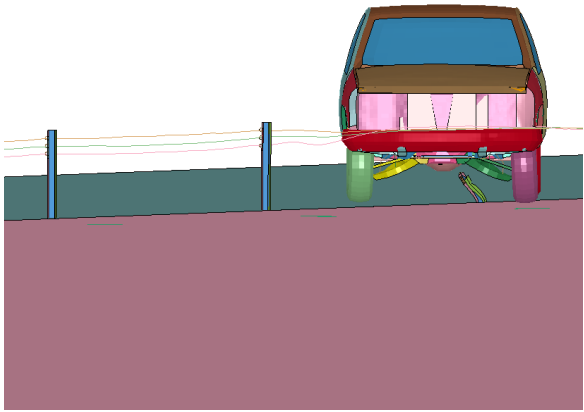
0.000 sec



0.000 sec



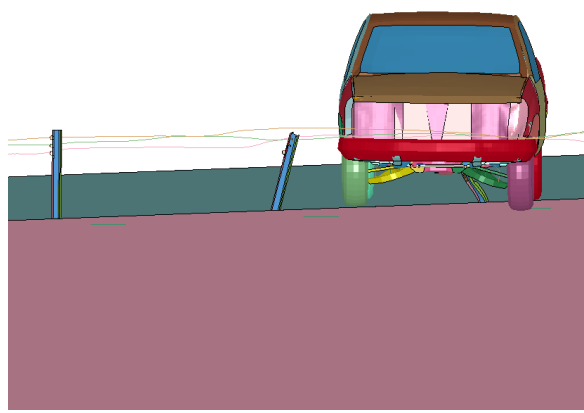
0.110 sec



0.110 sec



0.190 sec

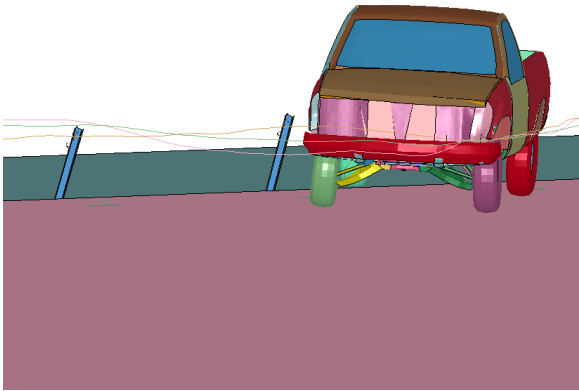


0.190 sec

Figure 213. Sequential Photographs, Test and Simulation, Test No. CS-1



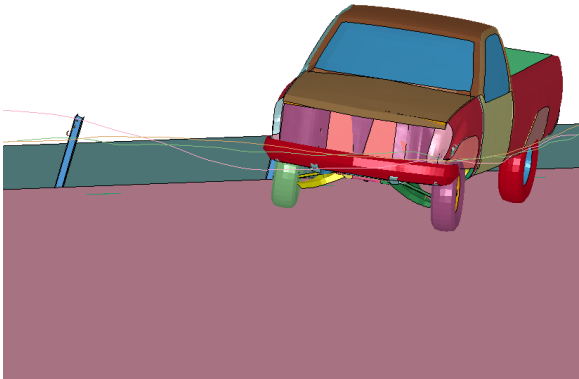
0.300 sec



0.300 sec



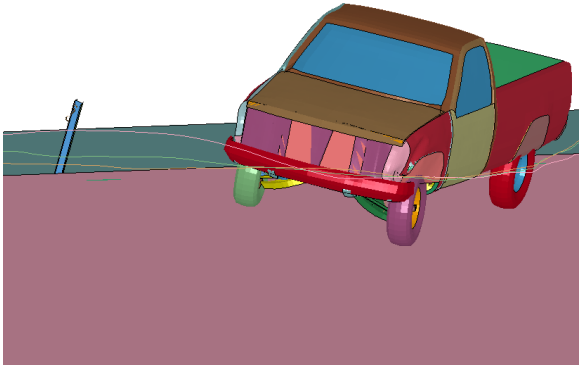
0.390 sec



0.390 sec

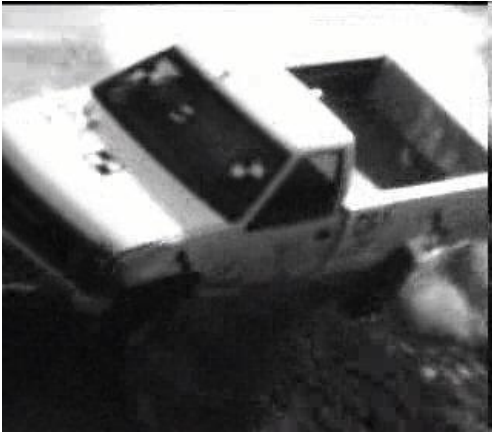


0.460 sec

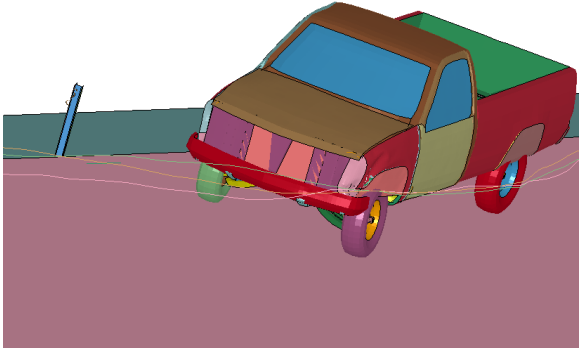


0.460 sec

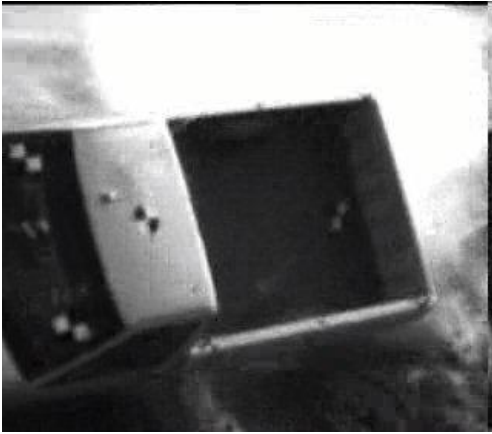
Figure 213 (cont). Sequential Photographs, Test and Simulation, Test No. CS-1



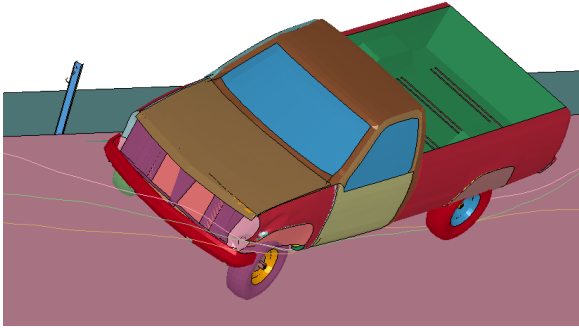
0.520 sec



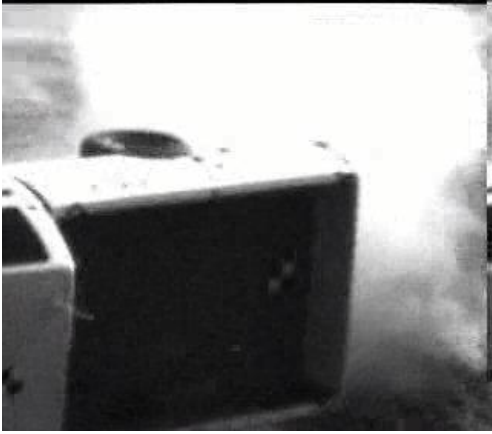
0.520 sec



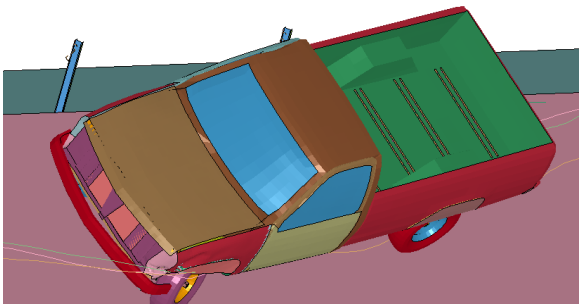
0.640 sec



0.640 sec



0.720 sec



0.720 sec

Figure 213 (cont). Sequential Photographs, Test and Simulation, Test No. CS-1

14.5.1 Simulation Event Timeline

The pickup truck impacted the barrier system and caused the first post downstream of impact to deflect backward at approximately 0.040 sec, and the second post deflected at 0.110 sec. The wire rope disengaged from the first post downstream of impact after impact at 0.060 sec, and the second post at 0.190 sec. At 0.200 sec the right-front wheel of the pickup rolled over the slope break point, and the third post downstream of impact deflected. The wire rope released from the third post at 0.240 sec, and at 0.270 sec the fourth post downstream of impact began to deflect. At 0.295 sec, the wire rope released from the fourth post downstream of impact. The fifth post downstream of impact deflected at 0.350 sec. At 0.390 sec the top wire rope pulled out of the top hook bolt of the fifth post downstream of impact. At 0.460 sec the bottom and middle wire ropes pulled out of the bottom two hook bolts on the fifth post downstream of impact, and at 0.480 sec, the top wire rope pulled out of the sixth post downstream of impact. At 0.560 sec the fifth post downstream of impact bent over due to the wire rope loads, and the bottom two wire ropes pulled out from the bottom two hook bolts of the sixth post. The top wire rope continued to pull away from the top hook bolts as the wave propagated downstream. At 0.570 sec the left rear tire overran the wire ropes. The bottom wire rope was pulled below the front bumper at 0.620 sec. The right-front tire and right-front bumper corner contacted the slope at 0.850 sec, and the pickup subsequently rolled over.

14.5.2 Simulation Analysis

The simulation and full-scale test share very similar characteristics. In both simulations the wire ropes wrapped around the right-front bumper corner and engaged the right-front quarter panel. The pickup knocked the first post downstream of impact down, and the instant in when the pickup began to pitch was nearly the same. In the simulation and full-scale test, the wire rope

disengaged from the hook bolts of the downstream posts due to bending wave propagation along the wire rope. In addition, the post deformation in the simulation, which typically consisted of bending backward in the soil and torsional bending downstream, also occurred in the test.

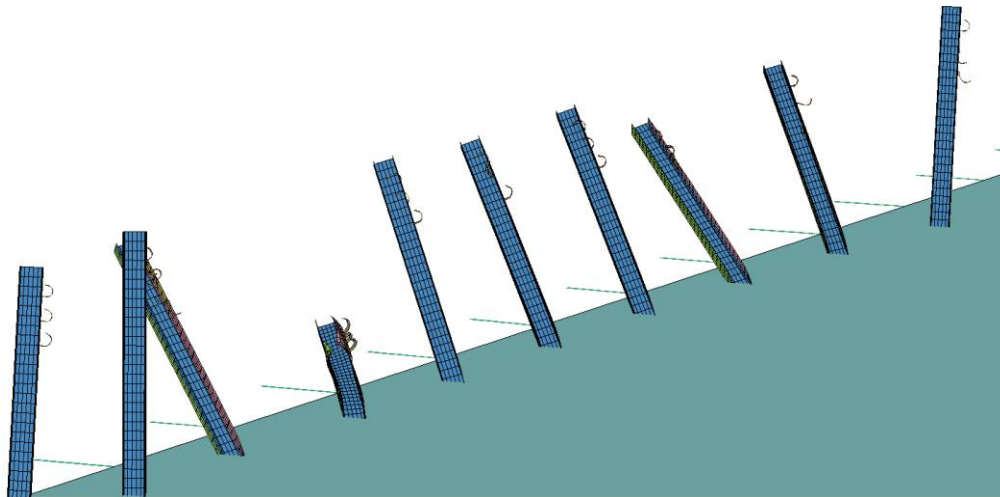


Figure 214. Post Deformation, Test and Simulation, Test No. CS-1

In the test, two posts were pulled out of the soil and deposited on the slope. This occurred due to the weak soil resistance caused by insufficient backfill behind the post due to the slope. Since the load curve was unknown and no physical testing was available to simulate the wire rope in soil, best estimates were used to determine the soil resistance curves.

In the full-scale test, the pickup was redirected and overrode the wire ropes at the rear wheels at 478 ms, whereas this did not occur in the simulation test until 570 ms. It was observed that the dynamic deflection of the pickup was greater in the simulation, because the wire rope had been stripped off of most posts downstream of impact. The wire ropes remained engaged to the simulated pickup truck for longer than the actual truck due to the release of the wire ropes from downstream posts from impact. This allowed a lower net overall lateral redirective force applied to the vehicle in the simulation than in the physical test. As a result of the lower net redirective force applied to the vehicle, vehicle roll and pitch motions experienced a delay, such that similar roll and pitch displacements occurred in the simulation at 720 ms and in the test at 560 ms.

Wire rope tensile loads measured in the test were compared with the recorded tensile loads in the simulation. The wire rope tensile loads are shown in Figure 215. Tensile loads for the first 200 ms were nearly identical, and followed a similar increase in load rate. After 220 ms, the test and simulated loads began to diverge, and the tested wire rope tensile load exceeded the simulated tensile loads. The maximum load recorded in the test was 24.36 kip (108.4 kN) at 460 ms, whereas the maximum tensile load in the simulation was 22.57 kip (100.4 kN) at 490 ms.

The sustained tensile loads of the test and simulation diverged, ranging between 20 and 24 kip (89 and 107 kN) and between 300 and 600 ms, whereas the tensile load in the simulations was typically between 10 and 18 kip (44 and 80 kN). However, the load trends for the first 200 ms were very similar between the full-scale test and the simulation. Results of the simulation and full-scale test were examined in greater detail to determine the cause of the differences.

Total Wire Rope Load at Upstream Anchor

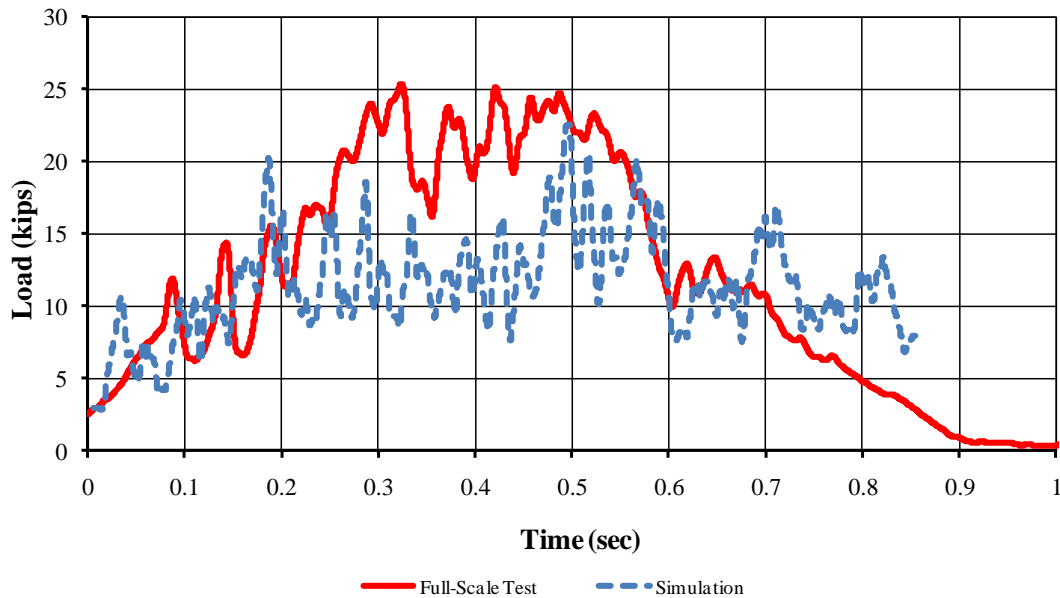


Figure 215. Total Wire Rope Tensile Loads, Three Ropes, Test and Simulation

It was observed that in the simulation, the wire rope released from the second, third, and fourth posts downstream of impact at 190, 240, and 295 ms, respectively. However, the post-release times for the wire rope in the full-scale test were 200, 376, and 610 ms, respectively. During these times, the post deformations were similar but the premature release of the wire ropes from the hook bolts allowed the wire ropes to slide up the post and deflect around the next adjacent post. By altering which post the wire rope is deflected around, the tension changes. This occurs because of a bulk increase in total wire rope strain if for the same pickup deflection, the slope of the wire rope bend around adjacent posts increases. The magnitude of the tensile force developed by a cable is related to the duration of time in which the cable remains attached to the post, and larger tensile loads in the cable create greater lateral loads on the vehicle. Wire rope retention on the post was evident in high tensile loads, and the release from the third post downstream of impact at 376 ms was clear as a slight dip in the tensile force curve.

A contact analysis study was conducted, and it was determined that the wire rope model cannot be defined with the true cross-sectional area of wire rope, if contact definitions are to be accurately captured. Using a cross-sectional area of 0.2395 in.² (154.5 mm²) in LS-DYNA resulted in an equivalent outer contact surface diameter of 0.55 in. (14.0 mm), which was too small and allowed the wire ropes to slide between the hook bolt opening and the post traffic-side flange under a low hook bolt pullout load.

When the wire rope was declared with a cross-sectional area of 0.4418 in.² (285.0 mm²), the contact surface diameter was determined to be 0.75 in. (19-mm) as was desired. The simulation was corrected and re-run with new density and modulus of elasticity parameters based on this observation, and the comparison of wire rope tension in the model and full-scale test was improved. In addition, hook bolt release times were much more similar in the updated model than in previous models. A comparison of the updated wire rope model tensile loads with full-scale load cell results is shown in Figure 216.

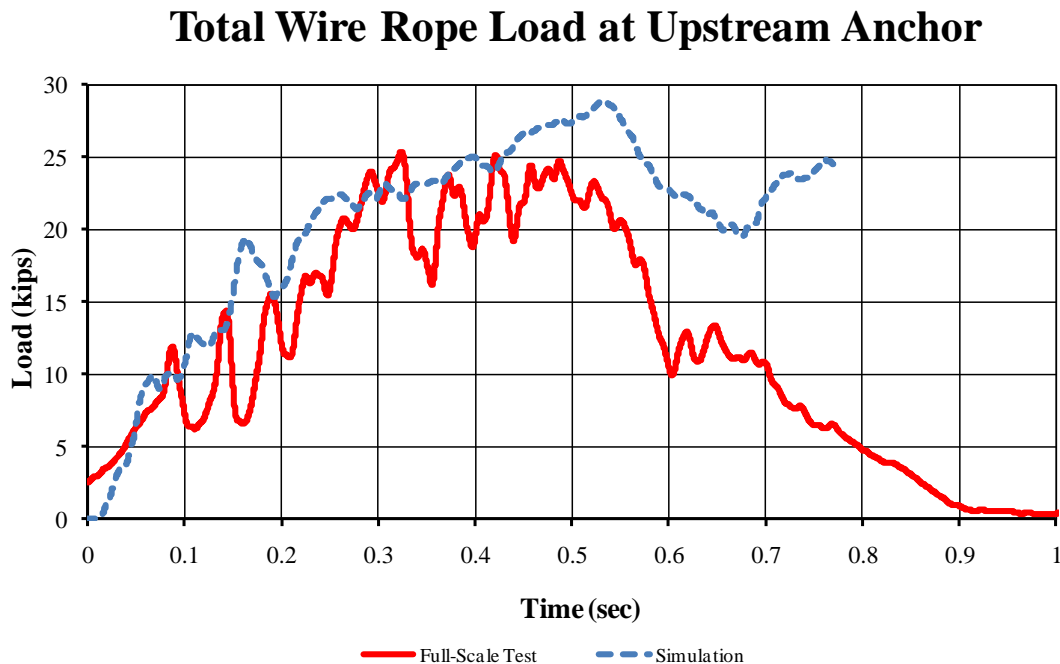


Figure 216. Wire Rope Tensile Load, Full-Scale Test and Updated Model, Test No. CS-1

Using the updated material properties, the wire rope model overestimated the tensile load on the anchors by between 5 and 10 percent. This was likely due to a combination of four factors.

(1) Wire rope testing conducted in this study was likely initially prestretched; thus the non-prestretched wire rope may have had a higher loading modulus of elasticity than the actual wire rope used in the test. Due to winding, thermal cycling, and extended relaxation prior to testing (which provided the non-prestretched effect), other truly non-prestretched wire ropes may have a lower loading modulus of elasticity.

(2) Vehicle geometries were not identical in the test and simulation since modeling each individual component in the pickup chassis and exterior would require significant effort and modeling resources. Gaps between the bumper and the left-front quarter panel allowed the wire ropes to slide between the pickup bumper and fender in the simulation, which did not occur in the full-scale test.

(3) Post models for the system were not validated against physical testing. The posts in the simulated system were meshed using shell elements though the actual flange shape of an S3x5.7 (S76x8.5) post are tapered to the web. This will affect post deflection properties and load intensities, and difficulties in modeling soil resistance increased modeling uncertainties. Furthermore, since the posts were embedded in soil near a slope, soil properties were even more difficult to estimate, and probably increased the stiffness of the system.

(4) Lastly, the modeled hook bolts have currently not been validated against physical testing. This could have contributed to differences in wire rope release times from posts.

The times of the peak force in the updated simulation were similar to the peak force in test no. CS-1, another force peak occurred after the pickup had begun to roll over. The additional force peak was caused by the wire ropes snagging on the left-front bumper corner and forcing the pickup to rotate around the wire rope trip point. It is believed that with better simulated pickup front-end geometry, the release of the wire ropes following vehicle redirection would have been smoother and a large reduction in force would have been observed after the pickup began to rollover.

Vehicle forward displacement, obtained from integration of the longitudinal velocity curve, was compared between physical test and simulation. The displacements were similar until 0.400 sec, after which the simulated vehicle forward displacement diverged from the test. Differences in the displacement curves of the vehicle were the result of the manner in which the accelerometer plotted displacements in the full-scale test.

Vehicle Longitudinal Displacement

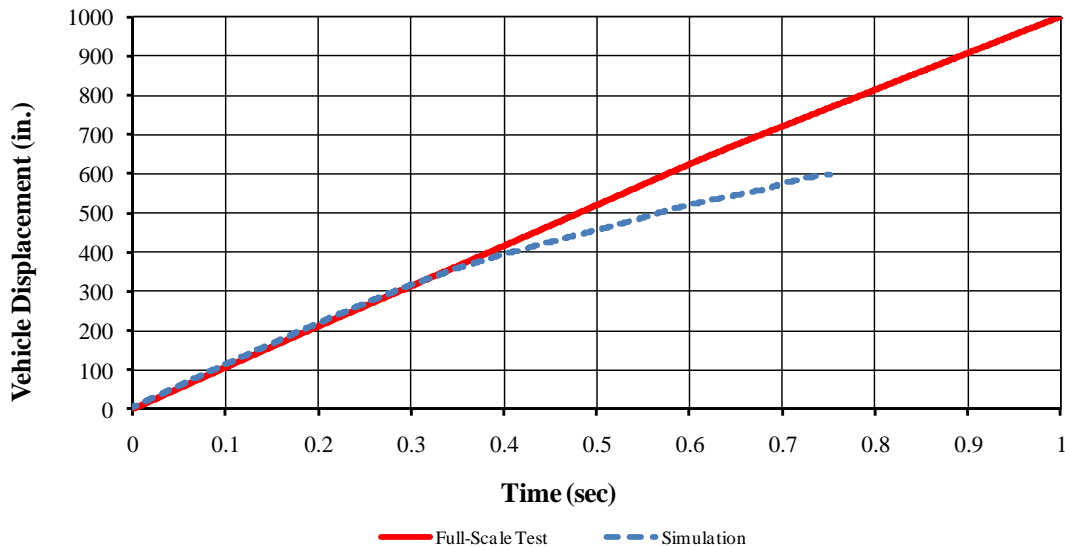


Figure 217. Vehicle Longitudinal Displacement, Test and Simulation, Test No. CS-1

During the full-scale test, the vehicle pitched forward and rolled with the left side leading. The accelerometers mounted in the vehicle were designed to measure accelerations in the vehicle in three principal directions. The vertical acceleration due to gravity in the accelerometer is subtracted from the vertical axis measurements, but may manifest in other axis directions if the vehicle pitches or rolls. During test no. CS-1, the vehicle pitched and rolled. Any rotational displacement of the vehicle which caused the longitudinal axis of the vehicle to have a non-orthogonal angle with a vertical line from the earth's surface will result in measured acceleration in that direction. This acceleration does not differentiate between static equilibrium or free acceleration of the vehicle because it is a body-centered force acting on the accelerometer and is not related to surface forces. Therefore, actual vehicle speed and displacement were not accurate beyond 300 ms.

In addition to wire rope load, the vehicle velocity curves, which were obtained via integration of the acceleration curves, were compared and are shown in Figure 218. Once again, the velocity curves were very similar through the first 300 ms, after which the velocity obtained by integration of the acceleration curves diverged. Whereas in the simulation, the velocity monotonically decreased, the velocity rose in the physical test. Once again, the velocity of the vehicle was deceptive because of an additional unbalanced acceleration related to the orientation of the vehicle was manifested in the longitudinal acceleration curve in addition to all longitudinal accelerations.

14.6 Summary, Discussion, and Future Work

Test no. CS-1 was simulated in full-scale impact conditions. Visual timelines were recorded to compare events simultaneously between test and simulation. Based on analysis of wire rope tensile loads and high-speed video analysis, it was determined that the differences in

wire rope tension were mostly caused by the premature release of the wire rope from the hook bolts in the simulation, whereas longer retention times were observed in the full-scale test.

Vehicle Longitudinal Velocity

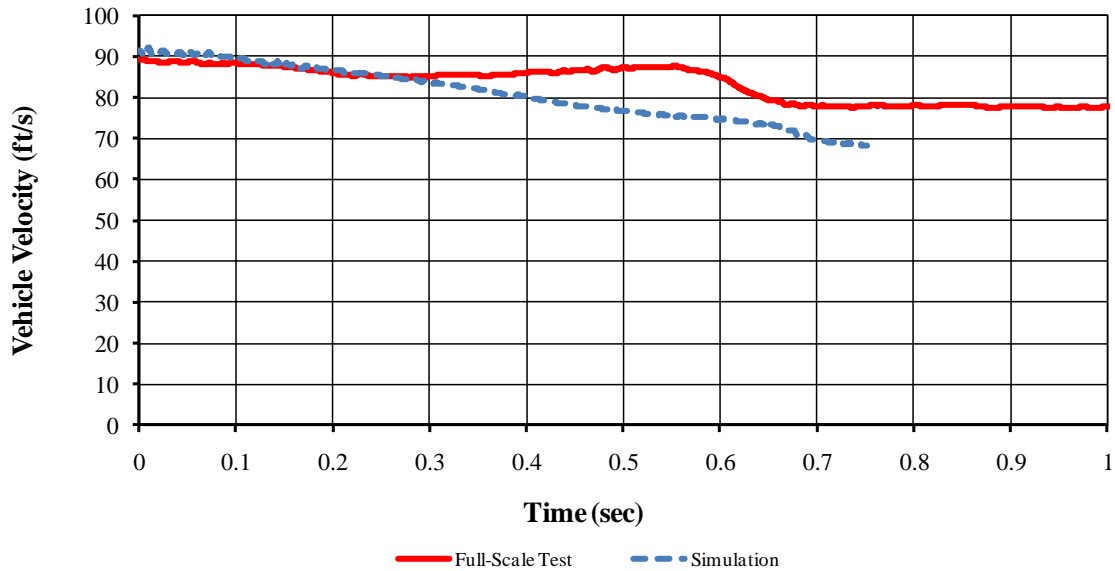


Figure 218. Vehicle Velocity, Test and Simulation, Test No. CS-1

Performance of the wire rope in the full-scale simulation indicated good correlation of physical test data and simulation data until the pickup rolled over. Modifications to the original section properties of the wire rope improved contact definitions and allowed the wire ropes to be retained on the posts until more accurate times in the simulation, compared to the full-scale test. Though the tension in the wire ropes was greater in the simulation than in the full-scale test, this was believed to be closely related with the post and hook bolt resistance than wire rope properties, though a slightly higher simulated modulus of elasticity may have contributed to the overall stiffer system response.

Vehicle velocity and displacement curves, obtained from integration of the accelerometer data, were very similar and indicated good agreement of vehicle orientation, reaction, and

motion. Integration of vehicle acceleration curves beyond 0.300 sec were deceptive due to the influence of gravity on the physical accelerometers which was not replicated in the simulation. Nonetheless, the actual vehicle motion was similar during flat-ground redirection, and thus the wire rope model was believed to be representative of the wire rope in the full-scale test.

The following three improvements to modeled cable barrier system are recommended. (1) An improved model of the hook bolts used to retain the wire ropes on the posts is necessary. (2) An improved post-soil interaction and modeling is necessary to accurately capture post-soil interaction on the slope. (3) Improvements to the geometry of the pickup may be necessary, since the generic C2500 model did not incorporate the geometrically unique features found on the test pickup. Each contribution to cable barrier modeling will improve the state of the art in simulation. It is believed that accurate soil modeling efforts will be the most rewarding, in terms of application to alternative systems, of the three options presented.

15 DISCUSSION

One critical aspect that became apparent as the project progressed is the strength of wire rope epoxy end terminations. As previously mentioned, epoxied end terminations are not generally recommended for applications involving dynamic loading [2]. However, cable barrier impacts are definitely dynamic loading applications, with varying tension during impact. In addition, though warm-weather testing indicated good bonding between the epoxy and the wire rope, cold-weather testing resulted in much less bonding strength of the wire rope with the epoxy, and a more brittle response of the epoxy. Furthermore, the epoxy in the sockets will have a different coefficient of thermal expansion than the wire rope, which may cause internal shear and tensile stresses to develop in situations of large temperature fluctuations. Dynamic stress waves in the epoxy may activate brittle response in cold temperatures which do not occur either in static conditions or warm environments.

Furthermore, it was pointed out that epoxied end terminations are good for 6x19 wire ropes, which have more than 5 times the number of wires as a 3x7 wire rope. By considering surface area, a 6x19 wire rope will have more than 3 times the bonding area, and potentially up to 6 times the bonding area of the 3x7 wires. However, the breaking strength of the 6x19 wire rope with similar material properties is only 15% more on average. Thus, the stress in epoxy end terminations used with 3x7 wire rope is potentially much higher than the stress in equivalent terminations using 6x19 wire rope.

Lastly, based on the wire rope pullout of test nos. DTC-2 and DBC-3, wire distribution within the epoxy can also have a very strong effect on the bonding strength. Inadequate wire distribution within the socket may cause wire rope release under a relatively low load.

Furthermore, since epoxy sockets act as a significant increase in stiffness at a concentrated location, they may be subject to fatigue, whereas the remainder of the rope is largely unaffected.

As a result, the use of epoxy end terminations is not currently recommended. Further study is necessary in order to prove the crashworthiness of these sockets in a variety of physically representative applications. Applying epoxy end terminations to wire rope cable barriers could potentially result in catastrophic consequences, if conditions are not favorable for use. However, swaged sockets, which have been recommended in dynamic applications, will likely be a better selection for wire rope terminations.

Beam elements are very useful for modeling many simplified components where the bulk reaction of the component is known and controllable. Beam elements may be applied accurately to the response of wire rope, if the tensile, bending, and torsional properties are accurately known. The beam element assumptions are also accurate for wire rope: (1) cross-sectional distortions in wire rope are minimal; (2) small relative angular and axial displacements occur between adjacent beam elements; (3) very little change in cross-sectional area occurs in any loading condition; and (4) warping and out-of-plane bending do not occur.

At the onset of the testing, an investigation into possible material use for wire rope models was conducted. It became clear that, in order to use the simplified beam element model, a material which allowed independent control of bending, tensile, and torsional properties, in addition to dynamic effects, was required. Because wire rope has a very low flexural strength relative to a solid bar of equivalent diameter, most of the cross-sectional integration sections for beam elements were not applicable; furthermore, many people have looked into the actual stress distribution within wires, and non-linearities were evident in every wire [e.g. 4, 25-27]. Furthermore, the "plastic" bending of wire rope represents plastic and elastic stress contributions

from many wires in the cross-section. This has not been analytically modeled accurately yet. The ability to independently control multi-axial contributions to the wire rope response was considered an important contribution for modeling wire rope using beam elements, and *MAT_166 was a material model capable of fulfilling the desired material model qualities.

It should be reiterated that the dynamic bending waves present in test no. DBC-6 had an unexpected response. As the untensioned wire rope deflected, the bending wave pulse itself acted as a tension-release boundary to the wire rope at the outer edge. This tension-release boundary did not propagate waves back toward the bogie, but instead allowed the tension between the propagating bends of the wire rope to increase within the constrained bends propagating from the bogie. This effect was not witnessed in the full-scale test modeled, test no. CS-1, and has not been witnessed in any other full-scale test analyzed. The effect is likely constrained to the untensioned wire rope in high-curvature test applications, since the excess slack allowed large bend radii to form before the wire rope became taut.

Causes for the difference in the model and component test are currently uncertain. One explanation is that the resultant Belytshcko-Schwer beam element may propagate tension across the bend diameter based on the constitutive assumptions used in deriving the beam element responses. An alternative explanation is that material model *MAT_166 may propagate tension at the tensile wave speed calculated from tensile properties in the material model independently of the bending response of the rope. Further, since only one moment-curvature bending curve was generated for wire rope at effectively no tensile load, higher tensions may result in stiffer rope response due to increased shear load transmission between the wires. With improved high-tension moment-curvature curves, this response may be better captured in the wire rope model.

High-curvature moment bending properties were approximated for the wire rope since testing was not conducted at curvatures as large as 0.254 in.^{-1} (0.010 mm^{-1}). The simulation of test no. DBC-1 gave a very similar bend appearance and residual plastic bend in the rope to the modeled "plastic" bend, but the static curvature resulting in the simulation was impossible to determine without waiting for the modeled wire rope to return to an undeformed state. This was computationally very expensive and time consuming, and plagued by compounding numerical error. However, since large bending curvatures are not witnessed in full-scale tests, further analysis and testing in large curvature bending was not conducted. The loss of accuracy of the bending moment-curvature curve past a bending moment of 0.35 kip-in. (40 kN-mm) is believed to be insignificant in comparison with other sources of error at these large bend radii.

Test no. CS-1 was selected for preliminary full-scale test evaluation with the wire rope model because unique characteristics of $\frac{3}{4}$ -in. (19-mm) diameter 3x7 wire rope were evident in the test. Wire rope release times from the posts, wire rope – post interactions, and engagement of the wire ropes with the pickup truck could be compared using this test. Furthermore, it was felt that the tripping mechanism witnessed in test no. CS-1, which was caused by the rear wheels overriding the wire ropes as the ropes in the front of the vehicle were pulled below the bumper, would provide a very critical evaluation of the response of the modeled wire rope. Nonetheless, further full-scale modeling will be completed using the new wire rope model, and will consist of flat-ground low-tension and cable barrier termination models.

Additionally, the tension-torsion coupling witnessed in the dynamic bending and tension tests was not modeled in the new wire rope model. There is no option using *MAT_166 for a failure strain from a combination of tension, torsion, and bending. However, the breaking strength of wire rope in the model is only to be used as a first approximation to the actual

fracture conditions of wire rope. If fracture occurs using the new wire rope model, further investigation with a more detailed model may be necessary to accurately capture the fracture event. Since the torsion has little contribution to the response of wire rope except in the breaking strength, the torsional effects were neglected.

The non-linear non-prestretched wire rope tensile curve was created in such a way that the wire rope unloaded along the slope of the prestretched wire rope, though the rope itself was linear-elastic. Low-speed impacts with cable barrier systems may not cause this transition between the tensile response of the softer non-prestretched wire rope to the stiffer prestretched rope. However, hysteresis in loading will almost always occur, and the difference between the prestretched modulus and non-prestretched modulus is not significant except at loads above the "prestretching" load. If concern remains that the unloading strain is too small, the linearized non-prestretched wire rope tension curve may be used.

Though damping was only briefly discussed in this project, it was used in every dynamic impact simulation. However, the damping coefficients used in the test were usually insufficient to cause significant differences in the wire rope response after filtering test load and acceleration data. This is because the damping coefficient corresponding to the fundamental natural frequency mode was measured experimentally to be 12% of critical. This damping coefficient was applied via a natural frequency analysis. In the dynamic bending tests, the wire rope underwent three kinds of dynamic bending oscillations: (1) propagating stiffness-related bending waves; (2) propagating tension-related bending waves; and (3) combined modal bending waves.

The first two kinds of waveforms visibly propagated along the length of the wire rope and were visible in the accelerometer traces. The combined effect of these waves was to establish standing waves in modal patterns with the bogie at a node and the rotator pipe as a mass-

weighted free-end. As the tension increased, however, the load frame rotator pipe tended toward a fixed end condition.

Based on this analysis and the analysis of a cantilever section of rope allowed to oscillate, a simple method of generating the approximate damping from the primary mode of bending and tension of wire rope was created. Based on the different dynamic bending tests conducted at varying speeds, a characteristic bending wave speed was determined to be approximately 1,030 ft/s (314 m/s). This characteristic bending wave speed was closely associated with the stiffness bending wave propagation speed. Using the characteristic bending wave speed, a characteristic damping frequency was defined, such that

$$f = \frac{c^*k}{2\pi} = \frac{2c^*}{d}$$

where c^* = characteristic bending wave speed
 k = wave number
 d = distance between bending constraints (e.g., posts)

The distance d in the dynamic bending tests was approximately the distance between the bogie and the load frames; the distance in cantilever beam tests was approximately twice the length of the beam, and the distance in full-scale tests is approximately the length between adjacent posts. This method was briefly described in the dynamic bending sections.

The reason for using the characteristic bending wave speed to damp bending stiffness is because no constant true bending wave speed is present during a full-scale impact. Though the tension wave speed is nearly constant for linearly-elastic response at a given tension, bending waves are propagated at varying speeds based on tension, wave number, and frequency. However, analysis of several full-scale cable barrier full-scale impacts revealed that frequency modes between 40-80 Hz were present. Since the wire rope is internally damped and a damping coefficient of 12% was empirically determined to be accurate for the combined range of tension

and bending, using a frequency range corresponding to tension wave propagation between two adjacent posts is currently recommended for damping both the tension and bending waves. Further study should be conducted on internal damping to determine the axial damping coefficient that is most accurate for wire rope simulations; this damping coefficient would likely replace the use of *DAMPING_PART_STIFFNESS in future modeling applications.

The damping term *DAMPING_PART_STIFFNESS was used to reduce the effect of high-frequency bending oscillations in the wire rope. Currently, a 2% stiffness damping coefficient is recommended based on quality of fit for wire rope dynamic bending component test simulations. However, despite the low coefficient for the part stiffness damping and the assumption that high-frequency oscillations would be damped, it was observed that a significant dynamic softening occurred using even a small coefficient for the stiffness-based damping. This nonetheless had a beneficial effect on the model.

Finally, limitations on the use of the new wire rope model should be noted. These limitations include restrictions on fracture loading, high-angle high-velocity impacts, pre-existing damage and mesh density.

The breaking strength of wire rope was determined based on testing, but the fracture occurred in the model through the deletion of the entire beam element. However, in every wire rope fracture witnessed, including quasi-static tensile testing, the wire rope fractured two strands and a single strand remained after fracture. Because this occurred both dynamically and statically, it is believed to be likely to occur in most wire rope fracture situations. However, the new wire rope model cannot simulate this with beam elements. Furthermore, the dynamics of fracture are not replicated using simplified beam elements; therefore, more detailed models should be used in cases where wire rope fractures are important.

This wire rope model does not account for damage to wire ropes caused by vehicle impacts, corrosion, prestresses, plastic deformations, or fatigue cracking. These effects may contribute to a lower overall wire rope strength, and may result in variations in the new wire rope model and actual tested wire ropes. If defects are found in the wire ropes to be compared with the model, potential rectifications should be identified to account for differences in the response.

Lastly, mesh density is always an important consideration when evaluating a model. In all dynamic simulations conducted in support of this project, the wire rope was modeled using 0.500-in. (12.7-mm) long elements. Mesh density studies indicated that the use of 1.0-in. (25-mm) long elements may be acceptable, particularly in impacts in which the wire rope is not deflected to a large curvature. It was observed that the fine mesh density used in this study did not cause a 2x reduction in computational speed for large models since the beam elements were inherently more efficient than the shell and solid elements, but an increase in speed may be obtained using larger element sizes.

16 CONCLUSIONS

A wire rope model was tested and evaluated against component and full-scale testing. The wire rope model was found to replicate many of the characteristics of physical wire rope used in cable barrier systems very well, including tension, moment-bending, dynamic bending wave propagation, and density. In addition, the wire rope model demonstrated improvement over the existing wire rope models used in highway barrier simulations when evaluated in component test modeling.

The tensile response of the wire rope was recorded from quasi-static tensile testing. The quasi-static tensile test curves were used to generate force-strain curves for use with *MAT_166 and a type 2 beam element to represent the wire rope. The quasi-static tensile test curves were observed to have some dynamic strain rate dependence which cannot currently be simulated, but the strain rate dependence was small and in many cases could be ignored. The fracture load of wire rope was determined to be approximately 40 kip (178 kN), which led to a fracture strain of approximately 2.17%.

The bending strength of wire rope was determined empirically from data and collaboration with simulations. The bending curves were used to replicate bending stiffness in the dynamic bending tests, and were observed to accurately represent the dynamic bending tests. Comparison of the new model with the pre-existing models indicated that the other models were stiffer than the non-prestretched wire rope tests, and tended to cause bogie rebound at approximately the same speed as the bogie impact.

Full-scale impact modeling using the new wire rope model provided a means of testing the wire rope model against external physical tests not part of this research project. Accurate bending wave propagation, tensile response, and wire rope-vehicle interactions were noted. To

improve the model, it is necessary to use a cross-sectional area consistent with a solid $\frac{3}{4}$ -in. (19-mm) diameter rod, instead of the actual wire rope cross-sectional area of approximately 0.2395 in.^2 (154.5 mm^2). In order to maintain advantageous timestep and accurate mass density, both the modulus of elasticity E and the density ρ_0 were scaled by the inverse of the cross-sectional area scale factor.

However, the accuracy of the model was limited to the accuracy of the soil, post, vehicle, and hook bolt models. Further improvements in each of these areas will eventually lead to more accurate and sophisticated models of vehicle interactions with cable guardrail systems.

17 RECOMMENDATIONS

Based on the optimization and evaluation of the wire rope model in quasi-static and dynamic impact conditions, three recommendations are made: (1) hook bolt, post, and soil modeling should be improved in order to better evaluate the new wire rope model in simulations of full-scale tests; (2) the new wire rope model should be substituted into any future cable guardrail models for design optimization; and (3) more detailed models of vehicles should be utilized to ensure proper geometrical interaction of simulated vehicle and cable barrier system. In endless pursuit of better models, areas in which the new model demonstrates deficiency should be noted for future improvement studies to ensure continuing progress on wire rope simulations.

18 FUTURE WORK

Wire rope is a complex system of interactions, and its response was approximated in this research by single beam elements along the length of the wire rope. Additional exploration into the moment-bending curve of high-curvature bends may be necessary in the future to capture bend-yielding behavior. In addition, moment-bending curves determined at different axial tensions may be necessary to ensure accurate moment-bending behavior in high-tension conditions.

Viscoelastic response of the wire rope may be important for further refinement of the model. Treatment of the internal friction of the wire rope with viscoelastic characterization may prove to be advantageous. Further research considering modeling wire rope as viscoelastic may be advantageous.

One full-scale crash test evaluated using the new wire rope model was met with overall good behavior of the wire rope, but the comparison of the wire rope reaction in the model with the full-scale crash test was limited by accuracy of the other modeled components. Further analysis on the test no. CS-1 model requires an improved hook bolt model to accurately capture the deformation of the hook bolts under the applied loads, improved post models to capture post deflection, improved vehicle geometry to prevent the wire ropes from sliding between the bumper and fender, and validated soil material models to replicate soil resistance forces as a function of post rotation. With these improvements, the wire rope model will become more versatile and advantageous for prediction of the reaction of the barrier to vehicle impact.

Additional vehicle crash tests with cable barrier systems should be pursued to further validate the model or identify weaknesses and potential for improvement. Many cable barrier

crash tests, recorded through the year 2009, have been tabulated in literature review reports [e.g., 45].

19 REFERENCES

1. Costello, George. Theory of Wire Rope. 2nd ed. New York: Springer Publishing, 1990. Print.
2. Wire Rope User's Manual. Wire Rope Technical Board. 1993. Print.
3. Rochinha, Fernando, and Costa Mattos, Heraldo. "Numerical Modeling of the Extension-Torsion Coupling in Cables." Mechanics Research Communications. Volume 23 No. 5. (1996): 511-517. Print.
4. Jiang, W.G., Henshall, J.L., and Walton, J.M. "A Concise Finite Element Model for Three-Layered Straight Wire Rope Strand." International Journal of Mechanical Sciences. Vol 42 Issue 1. (1999): 63-86. March 2009. <www.sciencedirect.com>
5. Costello, George. "Mechanics of Wire Rope", Presented to the Wire Association International. Georgia. May 2003. Print.
6. Graham, M.D., et al. "New Highway Barriers: The Practical Application of Theoretical Design." Highway Research Record No. 174., New York: New York State Department of Transportation. (1967): 88-167. Print.
7. Whitmore, J.L., Picciocca, R.G., and Snyder, W.A. Testing of Highway Barriers and Other Safety Accessories. Research Report No. NYSDOT-ERD-76-RR 38. New York: New York State Department of Transportation, December, 1976. Print.
8. Wijk, M.C., and Pinkney, H.F.L. A Single Camera Method for the 6-Degree of Freedom Sprung Mass Response of Vehicles Redirected by Cable Barriers. Ontario: National Aeronautical Establishment of Canada, November 1972. Print.
9. Pinkney, H.F.L., Basso, G.L., and Fraser, I.J. The NAE Model of the Highway Cable Barrier for Parametric Studies of Vehicle Redirection using Digital Simulation. Research Report No. NRC No. 12694. Ottawa: National Aeronautical Establishment of Canada, May 1972. Print.
10. Bateman, M.B., Howard, I.C., Johnson, A.R., and Walton, J.M., "Computer Simulation of the Impact Performance of a Wire Rope Safety Fence." International Journal of Impact Engineering, Volume 25: University of Sheffield (2001): 67-85. Print.
11. Nelson, Ryan, et al. Evaluation of Alternative Cable Anchor Designs and Three-Cable Guardrail Adjacent to Steep Slope. Transportation Research Report No. TRP-03-155-05. Lincoln, Nebraska: Midwest Roadside Safety Facility, University of Nebraska-Lincoln, February 2005. Print.
12. Hitz, Rebecca, et al. Design and Evaluation of a Low-Tension Cable Guardrail End Terminal System. Transportation Research Report No. TRP-03-131-08. Lincoln, Nebraska: Midwest Roadside Safety Facility, University of Nebraska-Lincoln, July 2008. Print.
13. Reid, John., and Coon, Brian. "Finite Element Modeling of Cable Hook Bolts." LS-DYNA Users Conference. 7th International Meeting. (2002): 17-11-17-23. Print.

14. Reid, John, and Hiser, Nick. "Friction Modeling Between Solid Elements." IJ Crash 2004. Vol 9 No. 1. (2004): 65-72. Print.
15. Reid, John, and Hiser, Nick. "Detailed Modeling of Bolted Joints with Slippage." Finite Elements in Analysis and Design. Vol 41. (2004): 547-562. Print.
16. Reid, John, and Hiser, Nick. "Modeling Slip Base Mechanisms." IJ Crash 2005. Vol 10 No. 5. (2005): 463-472. Print.
17. Reid, John, Paulsen, T.J., and Hiser, Nick. "Simulation and Bogie Testing of a New Cable Barrier Terminal." Crashworthiness, Occupant Protection and Biomechanics in Transportation Systems Conference 2003. Paper No. IMECE2003-55104. (2003). Print.
18. Hiser, Nick. Slip Base Modeling for Cable Guardrail Systems. April 2003. Master's Thesis.
19. Reid, John, and Hiser, Nick. Cable Guardrail End Terminal Simulation. Transportation Research Report No. TRP-03-142-03. Lincoln, Nebraska: Midwest Roadside Safety Facility, University of Nebraska-Lincoln, 2003. Print.
20. Reid, John. "LS-DYNA Simulation Influence on Roadside Hardware." Transportation Research Record No. 1890. Washington, D.C. (2004): 34-41. Print.
21. Marzougui, D., et al. "Performance Evaluation of Low-Tension Three-Strand Cable Median Barriers." Transportation Research Record No. 2025. (2007): 34-44. Print.
22. Marzougui, D., et al. Performance Evaluation of Low-Tension, Three-Strand Cable Median Barriers on Sloped Terrains. Research Report No. 2007-R-003. Washington, D.C.: National Crash Analysis Center, George Washington University, April 2007. Print.
23. Marzougui, D. Effects of End Anchor Spacing and Initial Tension on Cable Barrier Deflection. Washington, D.C.: National Crash Analysis Center, George Washington University, 2008. Print.
24. Berg, F.A., et al. "Motorcycle Impacts into Roadside Barriers – Real World Accident Studies, Crash Tests, and Simulations Carried Out in Germany and Australia." Proc. 19th International Technical Conference on the Enhanced Safety of Vehicles. Washington, D.C. June 2005. Print.
25. Chiang, Y.J. "Characterizing Simple-Stranded Wire Cables Under Axial Loading." Finite Elements in Analysis and Design. Vol 24. (2006): 49-66. Print.
26. Jun, M.A., Shi-rong, G.E., and Zhang, D. "Distribution of Wire Deformation Within Strands of Wire Ropes." Journal of China University of Mining and Technology. Vol 18, Issue 3. (2008): 475-478. Web March 2009. <www.elsevier.com>
27. Jiang, W.G., Henshall, J.L., and Walton, J.M. "A Concise Finite Element Model for Three-Layered Straight Wire Rope Strand." International Journal of Mechanical Sciences, Volume 42, 2000, pp. 63-86. Print.

28. Stolle, Cody, Reid, John, and Coon, Brian. Review of LS-DYNA Beam Elements. Lincoln, Nebraska: Midwest Roadside Safety Facility, University of Nebraska-Lincoln, 2010. Internal report.
29. Battini, J.M. Co-Rotational Beam Elements in Instability Problems. Stockholm, Sweden: Department of Mechanics, Royal Institute of Technology. December 2001. Master's Thesis.
30. Gere, J.M. Mechanics of Materials. 6th ed. Belmont, California: Thomson Brooks/Cole, 2004. Print.
31. Schwer, Len. "LS-DYNA Beam Elements: Default and User-Defined Cross-Section Integration." 4th European LS-DYNA User's Conference. May, 2003. Web, October 2008. <www.dynalook.com>
32. LS-DYNA Keyword User's Manual. Version 971 Release 4. Livermore Software Technology Corporation. Livermore, California: 2009.
33. "Standard Test Method for Tension Testing of Wire Ropes and Strand." ASTM Standards. Designation A 931-96. 2002. Print.
34. "Standard Specifications for Zinc-Coated Steel Wire Rope and Fittings for Highway Guardrail." ASTM Standards. Designation A 741-98. 2003. Print.
35. "Wire Rope Selection Criteria for Gate Operating Devices." Manual Reference EM-1110-2-3200. US Army Corps of Engineers. Submitted September 30, 1998, Reapproved April 2, 2004. Print.
36. "Wire Ropes." Encyclopedia of Materials: Science and Technology. Elsevier Ltd. (2004): 1-10. Web October 2008. <www.elsevier.com>
37. "Wire Rope and Strand." Federal Specification RR-W-410E. February 7, 2002. Accessed January 14, 2010. <<http://www.wbdg.org/ccb/FEDMIL/rrw410e.pdf>>.
38. Boresi, A., and Schmidt, R. Advanced Mechanics of Materials. 6th ed. Danvers, Massachusetts: John Wiley and Sons, 2005. Print.
39. Kenyon, W.D. Cable-Guiderail Tension. Transportation Research Report No. FHWA/NY/RR-85/124. New York: New York State Department of Transportation, July 1985. Print.
40. Yang, W., et al. "Performance of Cable Guiderail in New York." Transportation Research Record No. 1419. Washington D.C. (1993): 9-20. Print.
41. Arrington, D.R., Alberson, D.C., and Menges, W.L. Development of Field-Applied Fittings for Cable Barrier and Conversion to High-Tension. TTI Research Report No. 405160-11-1. College Station, Texas: Texas Transportation Institute, Texas A&M University, 2008.
42. Fish, Jacob, and Belytschko, Ted. A First Course in Finite Elements. Chichester, West Sussex, England: John Wiley and Sons Ltd, 2007. Print.

43. Kinsler, L.E., et al. Fundamentals of Acoustics. 4th ed. New York: John Wiley and Sons, 2000. Print.
44. Nelson, Ryan, et al. Evaluation of Alternative Cable Anchor Designs and Three-Cable Guardrail Adjacent to Steep Slope. MwRSF Research Report No. TRP-03-155-05. Lincoln, Nebraska: Midwest Roadside Safety Facility, University of Nebraska-Lincoln, 2005.
45. Stolle, Cody, Reid, John, and Lechtenberg, Karla. Update to Cable Barrier Literature Review. MwRSF Research Report No. TRP-03-222-10. Lincoln, Nebraska: Midwest Roadside Safety Facility, University of Nebraska-Lincoln, 2010. Report in Progress.

20 APPENDICES

LS-DYNA Modeling Parameters for New Wire Rope Model


```

$$$$$$ MATERIAL
$
*MAT_MOMENT_CURVATURE_BEAM
$
$ DENSITY:
$ Based on measurements in lab for linear density of cable
$ Cross-sectional area assumed to be 154.5 mm^2 (from above)
$ Mass per in. length is 0.06877 lb/in., per mm is 0.00122804 kg/mm
$ Converting to 19-mm bar equivalency for contact, mass is reduced from
$ actual density (7.9480E-6) to 19-mm bar density (4.3085E-6)
$
$ MODULUS OF ELASTICITY:
$ Modulus determined from non-prestretched cable is 75.952 kN/mm^2
$ Prestretched cable has a modulus of 115.072 kN/mm^2
$ Both determined from tensile test data
$ Since it is used for tensile wave speed calculation, should scale by the same
$ factor as density to maintain timestep
$ Recommended modulus of elasticity (unchanged) should be increased to 104 GPa
$ and 116 GPa for non-prestretched and prestretched ropes; thus the new moduli
$ will be 56.3773 GPa for non-prestretched and 62.8824 GPa for prestretched
$
$ TENSILE CURVE:
$ Tensile curve generated from tensile test results
$
$ MOMENT BENDING CURVE:
$ Moment bending curve generated from quasi-static bending analysis
$ and bending curve simulations
$ Currently only have one moment-curvature curve corresponding to zero load
$ Apply to all tensions until more representative properties can be determined
$
$ TORSION CURVE:
$ Torsion curve estimated by engineering judgment, is equal to 1/4 stiffness of
$ circular rod
$ Torsion currently uncoupled from tension, but coupling is known to exist
$
$ ADDITIONAL NOTES
$ elaf is the tensile curve
$ fpflg is 1.0 for multi-linear plastic (0.0 for non-linear elastic)
$ mid ro e elaf fpflg cta ctb ctt
  20009 4.3085-6 56.3773 20001 1.0
$ n1 n2 n3 n4 n5 n6 n7 n8
  0.000 10.000
$
$$$ lcms is the bending curve in the s-s direction
$ lcms1 lcms2 lcms3 lcms4 lcms5 lcms6 lcms7 lcms8
  20002 20002
$
$$$ lcmt is the bending curve in the t-t direction
$ lcmt1 lcmt2 lcmt3 lcmt4 lcmt5 lcmt6 lcmt7 lcmt8
  20002 20002
$
$$$ lct is the torsional resistance curve
$ lct1 lct2 lct3 lct4 lct5 lct6 lct7 lct8
  20003 20003
$
$$$ cfa = 0.970 because it has best correlation, some physical sense
$$$ cfb = 1.0 since can't determine what it should be
$$$ cft = 1.0 since is not related to wire rope performance now
$$$ hrule = 0.0 (isotropic hardening) -> doesn't go into compression, so doesn't
$ matter
$$$ reps = 0.0215 based on NON-LINEAR NON-PRESTRETCHED CURVE; prestretched 0.010625
$$$$$ note, reps will change if the above is not true
$$$ other r values set to never fail in practical conditions
$ NOTE: could also use *MAT_ADD_EROSION to maintain correct failure load
$ cfa cfb cft hrule reps rbeta rcapay rcapaz
  0.970 1.000 1.000 0.0 0.0215 1.0E+20 1.0E+20 1.0E+20
$
$

```

\$ This tension curve is for non-linear non-prestretched wire rope.

*DEFINE_CURVE_TITLE

Tension Curve

\$ lcid sidr sfa sfo offa offo dattyp
20001 0 1.000000 1.000000

\$ a1 o1
0 0
0.0000099591 0.157
0.0001699855516374 0.8
0.0003699315668796 1.78434589496708
0.00045 2.19817175090707
0.00058 2.91013021273932
0.00069 3.59539023225286
0.001 6.1183930313709
0.00117 7.6891513877883
0.00129 9.02407350372377
0.009496593389826 110.398594105285
0.0104238654686602 121.813154169461
0.0118405973058221 133.028541129822
0.0121237029769039 135.088068132534
0.0130533434144995 140.537140655908
0.0156255558750551 151.413044590316
0.0174473158361913 157.585950323564
0.020166743837246 162.477820470892
0.0275346773170982 175.003839658753

\$

\$ This curve is for moment-bending of wire rope, but the last point was
\$ estimated for completeness.

*DEFINE_CURVE_TITLE

Moment Bending Curve

\$ lcid sidr sfa sfo offa offo dattyp
20002 0 1.000000 1.000000

\$ a1 o1
0.00000 0.000
0.00030 9.800
0.00175 30.000
0.00500 58.000
0.00950 80.000

\$

\$ The torsion curve was estimated by taking the torsional stiffness
\$ of 21 independent wires, then increasing the total torsional strength
\$ by 20%

*DEFINE_CURVE_TITLE

Torsion Bending Curve

\$ lcid sidr sfa sfo offa offo dattyp
20003 0 1.000000 1.000000

\$ a1 o1
0.000 0.000
0.0010000 0.1668652
0.0050000 0.333730499

\$

END OF DOCUMENT